Dynamics in Low-Dimensional Correlated Quantum Systems

Von der Fakultät für Mathematik, Informatik und Naturwissenschaften der RWTH Aachen University zur Erlangung des akademischen Grades eines Doktors der Naturwissenschaften genehmigte Dissertation

vorgelegt von

Dante Marvin Kennes, M.Sc.

aus Neuss

Berichter:	**Universitätsprofessor Dr. rer. nat. Volker Meden**
	Universitätsprofessor Stefan Weßel, Ph.D.
Tag der mündlichen Prüfung:	**30. September 2014**

Diese Dissertation ist auf den Internetseiten der Hochschulbibliothek online verfügbar.

Contact Information:

Dante Marvin Kennes

Institut für Theorie der Statistischen Physik
Physikzentrum, RWTH Aachen
52056 Aachen

phone: +49 241 8027032
email: Dante.Kennes (at) physik.rwth-aachen.de

Berichter:	**Universitätsprofessor Dr. rer. nat. Volker Meden**
	Universitätsprofessor Stefan Weßel, Ph.D.
Tag der mündlichen Prüfung:	**30. September 2014**

Preface

First of all, I would like to express my gratitude to numerous colleagues, who helped me in the course of my Ph.D. studies. Certainly, their helpful thoughts and insights improved my work to a great deal.

Above all, I appreciate that Volker Meden gave me the opportunity to study the fascinating subject of quantum many-body physics under his supervision and guidance. As actions speak louder than words: after doing already my bachelor and master thesis with him, I once more asked him if he could be my supervisor as I could not imagine a better tutor. I have learned enormously from him throughout these past years.

Furthermore, I am very glad that Stefan Weßel agreed to referee this thesis. Also I want to specifically thank Herbert Schoeller for igniting my interest in quantum many-body theory by his intriguing lectures. In general, the very friendly atmosphere at the institute gave room to productive exchange.

The study of open quantum systems benefited greatly from Oleksiy Kashuba, Mikhail Pletyukhov and Herbert Schoeller not only in respect to deriving the corresponding RTRG equations, but even more so from their enlightening insights.

Regarding the study of thermoelectric transport through quantum dots it is more than a mere obligation to thank Dirk Schuricht, Matti Laakso and Severin G. Jakobs for valuable discussion and benchmarking data.

Last but not least, I would like to thank my colleague and, above all, good friend Christoph Karrasch. He helped me in numerous ways. Especially, I would like to thank him and also the University of California, Berkeley for the opportunity to visit during the summer 2013.

Financial support from the Forschergruppe 723 of the DFG is gratefully acknowledged.

Contents

Preface iii

Introduction 1

1. Short Summary 3

2. Introduction 5

3. Models 11
- 3.1. Ab Initio Model of Solid-State Physics . . . 11
- 3.2. One-Dimensional Lattice Models . . . 12
  - 3.2.1. Equilibrium Correlation Physics: Luttinger Liquids . . . 13
  - 3.2.2. Jordan-Wigner Transformations . . . 15
- 3.3. Single Impurity Anderson Model . . . 15
  - 3.3.1. One Word on Experiments . . . 15
  - 3.3.2. Hamiltonian . . . 16
  - 3.3.3. Equilibrium Correlation Physics: Kondo Physics . . . 16
- 3.4. Single Impurity Anderson-Holstein Model . . . 17
  - 3.4.1. Hamiltonian . . . 18
  - 3.4.2. Equilibrium Correlation Physics: Kondo Physics . . . 18
- 3.5. Interacting Resonant Level Model . . . 19
  - 3.5.1. Hamiltonian . . . 19
  - 3.5.2. Equilibrium Correlation Physics: Renormalization of Hybridization . . . 21
- 3.6. Spin-Boson Model . . . 21
  - 3.6.1. Hamiltonian . . . 22
  - 3.6.2. Correlation Effects: Dynamical Regimes . . . 23
  - 3.6.3. Mapping to IRLM . . . 23

Methods 25

4. Functional Renormalization Group 27
- 4.1. Green's Functions . . . 29
  - 4.1.1. Equilibrium vs. Non-Equilibrium: Matsubara vs. Keldysh . . . 30
  - 4.1.2. Non-Interacting Green's Function: An Exact Starting Point . . . 34
  - 4.1.3. From Green's Function to Observables . . . 37
- 4.2. Generating Functionals . . . 40
  - 4.2.1. Functional Integral Representation of the Many-Body Problem . . . 41
  - 4.2.2. Functional Reformulating of the Keldysh Green's Functions . . . 42
  - 4.2.3. Functional Reformulating of the Matsubara Green's Functions . . . 44
  - 4.2.4. Generating Functional of (Connected) Green's Functions . . . 45
  - 4.2.5. Generating Functional of Vertex Functions . . . 45
- 4.3. Flow Equations . . . 47

4.3.1. Flow of Generating Functional of Connected Green's Functions 47
4.3.2. Flow of Vertex Functions 48
4.3.3. Truncation Schemes and Initial Conditions 50
4.4. Cut-Off Schemes 52
4.4.1. Sharp Cut-Off Scheme: Equilibrium Problems 52
4.4.2. Reservoir Cut-Off Scheme: Non-Equilibrium Problems 52
4.4.3. Initial Conditions Vol. II 53
4.5. Symmetries and Their Conservation 54
4.5.1. Symmetries... 54
4.5.2. ... and Their Conservation 55

5. Density Matrix Renormalization Group 57
5.1. Matrix Product States 58
5.1.1. From a Quantum State to a MPS: Singular Value Decomposition 58
5.1.2. Left, Right and Mixed Canonical Forms 60
5.1.3. Γ-Λ Notation 61
5.2. Matrix Product Operator 62
5.3. Symmetries 64
5.4. From MPS and MPO to Observables 65
5.5. Iterative Ground State Calculations 66
5.5.1. The Crucial Ingredient: The Update 67
5.5.2. Explicit Algorithm 67
5.5.3. One- vs. Two-Site DMRG: Advantages and Possible Pitfalls 68
5.6. Real and Imaginary Time Evolution 68
5.6.1. Trotter and co. 69
5.6.2. Ground States Revisited 71
5.6.3. Finite Temperatures and Purification 71
5.7. From Finite Size to Infinite Size DMRG 75
5.7.1. Ground States of Infinite Systems 75
5.7.2. Real and Imaginary Time Evolutions 76
5.8. DMRG: Success and Failure 76

6. Alternative Methods 79
6.1. Perturbation Theory 80
6.2. Hartree-Fock 80
6.3. Bosonization 81
6.3.1. Basics 81
6.3.2. Exact Solution in One Dimension 82
6.3.3. ...Expectation Values including the Fermionic Operators? 83
6.4. Real Time Renormalization Group 84
6.4.1. Introduction 84
6.4.2. Liouville-Laplace Space 85
6.4.3. Setting up Diagrammatics 85
6.4.4. Upgrading to a Renormalization Group 86
6.5. Numerical Renormalization Group 86
6.5.1. Introduction 86
6.5.2. Iterative Diagonalization 86
6.5.3. Dynamics? 87

Questions 89

7. Dynamics in Open Quantum Systems 91
7.1. Thermodynamic Limit and Pitfalls 92
7.1.1. Recurrence in Finite Systems 92

7.1.2. Wilson Chains as Reservoirs? . . . 94
7.1.3. $N \to \infty$ . . . 94
7.2. Transient Dynamics of the IRLM . . . 96
7.2.1. Warm-up: Single-Level ($U = 0$) . . . 96
7.2.2. FRG Treatment at Finite U . . . 99
7.2.3. Transport at Finite Temperature . . . 106
7.3. Dynamics of Dissipative Quantum Systems . . . 110
7.3.1. Dynamics at $T = 0$ . . . 111
7.3.2. Dynamics at $T > 0$ . . . 120
7.3.3. Quenches and the Role of Non-Markovian Memory . . . 125
7.4. Biased ($V \neq 0$) IRLM $\leftrightarrow$ Spin-Boson Model . . . 128
7.5. Conclusion . . . 129

8. Thermoelectric Transport **131**
8.1. Basics and Definitions . . . 132
8.1.1. Linear Response . . . 132
8.1.2. Non-Equilibrium Beyond Linear Response . . . 134
8.2. Thermoelectric Transport in the IRLM . . . 135
8.2.1. IRLM: Finite Temperature an FRG Analysis . . . 135
8.2.2. RLM case: $U = 0$ . . . 137
8.2.3. IRLM: $U \neq 0$ . . . 141
8.2.4. Application: Charging . . . 142
8.3. Thermoelectric Transport in the AHM . . . 144
8.3.1. First order perturbation theory . . . 144
8.3.2. AHM: FRG Analysis . . . 145
8.3.3. AHM: Thermoelectric Properties in Linear Response . . . 152
8.4. Conclusion . . . 156

9. Dynamics in Closed Quantum Systems **159**
9.1. Basics and Definitions . . . 160
9.1.1. Thermalization and Non-Thermal Steady-States . . . 160
9.1.2. Models . . . 162
9.2. Reminder of Luttinger Liquid Physics . . . 163
9.3. Real-Time FRG for Closed Quantum Systems . . . 165
9.3.1. Efficiently Evaluating Keldysh Green's Function Using GPU... . . . 167
9.3.2. ... or Trotter Decompositions . . . 168
9.3.3. Benchmark: Dynamics of Interacting Fermions . . . 168
9.4. Luttinger Liquid properties in Non-Thermal Steady-States . . . 169
9.4.1. The Tomonaga-Luttinger Model . . . 170
9.4.2. Lattice Model: Spinless Fermions . . . 175
9.5. Thermalization in One Dimension . . . 179
9.5.1. Models and Method . . . 179
9.5.2. Time Evolution of Observables . . . 181
9.5.3. A Single Measure of Thermalization . . . 182
9.5.4. Chaos Induced Thermalization . . . 183
9.6. Conclusion . . . 184

Conclusions & Outlook **187**

10. Conclusion **189**
10.1. Updated Status Report: Transient Time FRG . . . 189
10.2. Summaries of the Results . . . 189
10.2.1. Dynamics in Open Quantum Systems . . . 190
10.2.2. Thermoelectric Transport . . . 190

10.2.3. Dynamics in Closed Quantum Systems 191

11. Outlook **193**

A. List of Acronyms **I**

Supplements **III**

List of Publications **XIX**

Curriculum Vitae **XXI**

Thank You! **XXIII**

Introduction

Chapter 1

Short Summary

We study the dynamics in low dimensional correlated quantum systems. Advances in this thesis are three-fold.

First, as a methodical point we extend the real-time formulation of the functional renormalization group approach introduced in [Ken11].

Method Development

Describing the transient time dependence of a given microscopic model prepared in an initial non-equilibrium state poses a formidable challenge in the presence of interaction. We successfully extend the functional renormalization group approach of [Ken11] to finite temperature as well as extended interacting geometries. Furthermore, for both extensions we test the validity of the perturbatively motivated treatment by explicitly benchmarking to complementary methods and find that for not too large interactions the functional renormalization group proves to be quantitatively accurate.

Second, we examine the non-equilibrium dynamics of open as well as closed quantum systems in the presence of correlations.

Dynamics in Open Systems

We study a prominent prototype model for coherence in small quantum systems coupled to dissipative environments, namely the spin-boson model. We reveal that prevailing literature does not cover the full complexity of the dynamics encountered. The relaxation dynamics formerly classified as coherent and incoherent should be refined according to the results presented in this thesis: we propose a subdivision of the coherent regime into partially and asymptotically coherent. For the former the coherence signature of the dynamics is restricted only to intermediate times, while in the latter it extends in the asymptotic regime. Interestingly, we explicitly show that elevating temperature might be conducive to coherence, which is opposite to the expected behavior.

Dynamics in Closed Systems

For those closed quantum systems known to fall into the so called Luttinger Liquid universality class in equilibrium, we provide evidence that the equilibrium concept of universality seemingly carries over to the non-equilibrium steady-state. This is rather counter-intuitive, as universality is usually attributed to the low energy degrees of freedom only.

Third, we study the thermoelectric transport properties of quantum dots.

Thermoelectric Transport

Quantum dots are promising candidates for highly efficient thermoelectric devices as they are not bounded by the Wiedemann-Franz law which strongly limits the efficiency of ordinary bulk systems. For this we study a charge fluctuating model and a model which additionally allows for spin fluctuations and phononic degrees of freedom. We find that in certain regimes quantum dots show very high efficiency when operated as power engines.

Chapter 2

Introduction

We are interested in studying the dynamics in low dimensional correlated quantum systems in the following. Correlations have proven to lead to fascinating physics. Even in equilibrium, despite major advances in understanding the correlation physics, many aspect are still subject of current research. Rather recently describing the interplay of correlations and non-equilibrium has emerged as an intriguing novel challenge. We will motivate our study of non-equilibrium physics in correlated systems by considering two subjects of current interest.

Quantum Computing

Quantum computing, i.e. the processing of information by using the fundamental concepts of quantum mechanics, is a vivid field of theoretical as well as experimental research. Building on these concepts quantum computers are envisioned to give rise to accelerated algorithms for certain prominent tasks of conventional information processing, such as integer factorization (cryptography), searching databases and evaluating NAND (negated AND) gate trees. Interestingly, they would also allow to simulate/compute the physical properties of a quantum many-body Hamiltonian in polynomial instead of exponential[1] time. However, quantum computers are still in their infancy and so far experiments have only been conducted with a small number of qubits[2]. Besides the technical challenges, such as the controlled preparation, manipulation and read-out of qubits, decoherence is still one of the major obstacles to overcome on the road to applied quantum computing. Therefore, understanding the key physics of these devices is of utter relevance and motivates the study of so called quantum dots. Those are prototype models of (in general more complicated) nano-devices used for quantum information processing. Quantum dot models constitute quasi-zero dimensional structures coupled to extended reservoirs and feature very intriguing physics in the presence of strong correlations: e.g. the repulsive interaction between the electrons, manifesting in Coulomb blockade or Kondo screening [GG98, vdW00]. This gives rise to unexpected (and maybe exploitable) behavior, but also renders quantum dots difficult to treat theoretically. Quantum dots were therefore extensively studied within equilibrium, while their non-equilibrium behavior is a newly emerging field of research. In particular, in contrast to examining solely the equilibrium or non-equilibrium steady-state, understanding the dynamics encountered in these systems is of major importance to take into account, e.g. the application of manipulation gates within a quantum computing process.

Ultra-Cold Atoms

Another field of intense study that recently became very popular is the physics of ultra-cold atoms. Holding atoms in a magnetic or optical trap at low temperature was found to give rise to quantum systems under unmatched experimental control [Blo08]. With this it became possible to realize model Hamiltonians in real physical systems suffering from almost no external influences. Thus, these highly coherent and isolated systems can be used to examine the intriguing physics encountered at low dimensions, which in the presence of correlation, i.e. particle interaction, feature a wealth

[1] Although there is no proof that solving a general quantum many-body problem cannot be done in sub-exponential time, this is at least plausible, due to the exponential Hilbert space as well as by considering nowadays available methods.

[2] Qubits constitute the quantum processing counterparts to conventional bits.

of peculiar and fascinating behavior. For one dimensional systems the origin of this behavior is particularly easy to envision: particles cannot bypass each other without interacting, rendering their excitations collective. Due to this collective behavior, the Fermi Liquid paradigm, describing successfully bulk materials, breaks down and has to be replaced by the so called Luttinger Liquid theory. Ultra-cold atoms allow to test this theory of low-dimensional systems in a very controlled way and have reignited also the interest in non-equilibrium questions, i.e. regarding the dynamics and equilibration. Non-equilibrium setups can be realized, for example, in release experiments, where after preparation, a trap is suddenly switched off or changed and the subsequent dynamics is studied. By repetitively preparing and releasing the cloud of ultra-cold atoms and measuring certain observables after different times a real time signal showing the relaxation process of these observables can be found.

The Stage: Dynamics in the Presence of Correlations

In both of the aforementioned systems (quantum dots and one-dimensional systems) correlations play a significant role. A perturbation theory approach in the two-particle interaction is straightforward, but loses its reliability when correlations get too large or even worse often breaks down altogether due to the appearance of logarithmic divergences in low-dimensional systems. This behavior motivated the renormalization group idea [Wil75], which can be used to resum divergences by subsequently addressing all energy scales from high to low. We will focus here mainly on the functional renormalization group as one implementation of the general renormalization group idea, which was recently extended to address the non-equilibrium steady-state properties [Jak09] and afterwards also to describe the transient time regime [Ken11]. We will complement this method by the time dependent density matrix renormalization group[3] [Whi04], which in the last decade has evolved to one of the most powerful tools to handle one-dimensional systems. Besides of those there exist a few additional methods which can be used to tackle dynamics of correlated quantum systems, such as the time dependent numerical renormalization group [And05, And06, Ngh14], non-interacting blib approximation [Wei12], the real time renormalization group [Sch00, Sch09], Hamilton flow equations [Hac08] and field theoretical approaches [Les98] as well as bosonization [Sch05a]. Recently, also continuous time quantum Monte Carlo methods were applied to extract the dynamics in low dimensional quantum systems as well [Sch08a]. In the following we want to give a very rough overview of the applicability of these methods.

Naturally, every of the above mentioned methods has its own advantages and short comes. A functional renormalization group approach being essentially analytic is not as numerically demanding as other quantum many-body approaches and thus can be used to easily investigate entire parameter regimes. Furthermore, it can easily be applied to open as well as closed quantum systems. On the downside such an approach is well controlled only up to a certain order in the interaction, because truncations of the functional renormalization group equations are necessary in practice. The density matrix renormalization group, in contrast, is non-perturbative, but when aiming at dynamics is severely restricted in the time scales which can be reached. Due to the spread of entanglement in the system a time dependent formulation of this approach "runs into a wall", after which, further progressing in time space is numerically exponentially expensive. Additionally, the density matrix renormalization group can only be applied to infinite systems in the translational invariant case and thus treating impurity problems is impractical if huge reservoirs are needed to resolve the relevant physics. The numerical renormalization group on the other hand is also non-perturbative, but solves the full interacting system after logarithmically discretizing the conductance band. This discretization leads to severe artefacts in the time evolution, which are very difficult to control. The non-interacting blib approximation was used to tackle the time evolution of quantum systems as well, but the approximations made are strictly controlled only at short times. In practice the real time renormalization group can be applied to impurity problems only. It then works complementary to the functional renormalization group approach. Whereas typically within the real time renormalization

[3] Although this method's name suggests the implementation of Wilson's renormalization group idea as well, this is actually a historical artefact. Modern density matrix renormalization group approaches are not build on this concept.

group one incorporates the local interaction exactly and treats the influence of the leads perturbatively this is opposite in the functional renormalization group. A remarkable advantage of the real time renormalization group approach is that it is often possible to extract analytical expressions even for the time-evolution. Field theoretical approaches excel in exact analytical predictions, but can only be applied to a few specific models which sometimes turn out to be non-generic. In general, they cannot incorporate correctly the high-energy physics, which determines the time evolution at short times as well as the crossover from short to long times. Similarly, Bosonization can only be applied for models meeting certain criteria. Continuous time quantum Monte Carlo suffers from the so called sign problem, rendering this method difficult to apply for general problems. Finally, Hamilton flow equations are a technique with a similar validity range than functional renormalization group, but of course differs in its implementation.

In the following we want to concentrate mainly on the functional and density matrix renormalization group, but in parts also compare to results from a real time renormalization group approach. We deem this choice of methods useful as they supplement each other in range of validity and applicability.

Scope of this Thesis

The goal of this thesis is three-fold. First, as a methodical point we aim at extending the real-time formulation of the functional renormalization group approach introduced in [Ken11] to tackle quantum dots at zero temperature by (a) deriving expressions for finite temperature and (b) applying it also to the non-equilibrium dynamics in closed one-dimensional quantum systems. Second, we want to examine the non-equilibrium dynamics of open quantum systems, in particular the interacting resonant level model and the spin-boson model, as well as closed quantum systems, such as spinless fermions with (next-)nearest neighbor interaction and the Hubbard model, in the presence of correlations. Third, we study the thermoelectric transport properties of quantum dots focusing on the interacting resonant level model and the single impurity Anderson-Holstein model.

The models named above will be introduced in more detail in the following chapter, where we will also give a brief overview of the correlation physics encountered within them. This following model chapter is similar in spirit to an introduction and thus should be understood to supplement this chapter. Next, we will go into more detail of the declared sub-goals, separately.

Method Development: Real-Time Formulation of the Functional Renormalization Group

Describing the transient time evolution of a given microscopic model poses a formidable challenge in the presence of interaction. In [Ken11] we outlined the general framework with which such a study can be conducted within the functional renormalization group. In this framework explicit formulae were restricted to the zero temperature case and quantum dots (open quantum systems) featuring only a few correlated quantum degrees of freedom. In this thesis we broaden the application range of the general procedure to finite temperature as well as extended interacting geometries (closed quantum systems). Due to the perturbative motivation of the functional renormalizaiton group it is a priori not clear how large the interaction parameter can be chosen before the approximate treatment looses its significance, but throughout this thesis we are in the fortunate position that at least some benchmark results are available.

For open quantum systems those will be constituted by the real time renormalization group, which although motivated perturbatively as well, provides an independent check. For small times we can also compare to perturbative non-interacting blib approximations. Finding reliable non-perturbative results in this case is rather difficult as each method (see above) copes with its own difficulties.

For one dimensional closed quantum systems the density matrix renormalization group, can be used to extract numerically exact benchmarking results. For this we coded our own implementation of this method and compare the time evolution after so called quantum quenches in one dimension.

This provides us with a rather stringent test of the developed method in either case: for not too large interactions it turns out that the functional renormalization group proves to be quantitatively accurate.

Key Interest: Dynamics in Open and Closed Systems

In a next step, we apply the developed functional renormalization group and the well established density matrix renormalization group to open and closed quantum systems. For open systems we will concentrate on the former method[4], while closed systems are treated by both. In the later chapters we take a close look at different aspects of the dynamics.

As a prototype model of an open quantum system we consider the so called spin-boson model. For this prominent model of quantum coherence we reveal that prevailing literature [Wei12] does not cover the full complexity of the dynamics encountered. The relaxation dynamics formerly classified as coherent and incoherent should be refined according to the results of chapter 7. We also show that the non-pertutbative results of conformal field theory [Les98] actually do not describe the leading, but the sub-leading behavior of this model in certain parameter regimes. Furthermore, we find that elevating temperature might be conducive to coherence, which is opposite to the expected behavior.

As a common model of a closed quantum system we consider spinless fermions on a lattice, which feature a nearest neighbor hopping and interaction. For appropriately chosen parameters this model is well known to fall into the so called Luttinger Liquid universality class in equilibrium. We show that the equilibrium concept of universality seemingly carries over to the non-equilibrium steady-state. This is highly non-trivial and even counter-intuitive, as universality is usually attributed to the low energy degrees of freedom only.

A New Route to an Old Problem: Thermoelectric Transport through Quantum Dots

It is a distinct advantage of the functional renormalization group that parameter regimes can be sampled rather quickly. This renders this method an ideal candidate to study thermoelectric properties, where usually multiple parameters need to be optimized iteratively. Quantum dots could be promising structures for highly efficient thermoelectric devices as they are not bounded by the Wiedemann-Franz law which strongly limits the efficiency of ordinary bulk systems. For this we study (1) the charge fluctuating interacting resonant level model and (2) the single impurity Anderson-Holstein model, which additionally allows for spin fluctuations and phononic degrees of freedom. For the former the functional renormalization group was already successfully applied to tackle the steady-state non-equilibrium regime [Kar10d, Kar10b] at zero temperature. The extension to finite temperature is straightforward and the entire parameter regime can be sampled excluding large interactions. For the single impurity Anderson-Holstein model this is less clear a priori and we will first have to check the functional renormalization group approach's range of validity.

We aim at presenting the following results accessible assuming only a basic expertise when dealing with the concept of (equilibrium) Green's functions as well as strongly correlated equilibrium physics. Throughout the thesis we will have to introduce a multitude of special functions, which, if not stated explicitly otherwise, are defined as in [Abr70].

Outline

The rest of this thesis is structured as follows. In the next chapter we will introduce the models of relevance throughout the remainder of this work. We will give a brief overview of the literature, discuss which physical degrees of freedom are modelled and sum up the known correlation physics. This provides a prerequisite for the non-equilibrium physics studied in the following. This chapter should be understood as part of the introduction.

Next, we concentrate on the methodical points of this thesis. First, the functional renormalization group is introduced. We will give the explicit formulae needed to apply this general framework to interacting quantum many-body problems. Afterwards, our second method of choice, the density matrix renormalization group is outlined. The vantage point in this chapter is to concentrate on the details of code implementation of a density matrix renormalization group approach, which is used from thereon. In a short section we discuss some more fundamental relations of physical properties to the success and failure of this method. To sum up this method oriented part, we also introduce

[4] Open systems can be treated within the density matrix renormalization group only if appropriate large reservoirs can be treated (see e.g. [Ken14b]).

some alternative methods, which were not in the center of attention for this work, but are used throughout this thesis, for comparison or benchmarking reasons.

Finally, we turn to the results. In a first chapter we sum up our findings for the dynamics in open quantum systems. We will study the finite temperature transport regime of the interacting resonant level model, which also paves the way to the thermoelectric transport study presented in the following chapter. Next, we study the dynamics of the spin-boson model with a distinct focus on how interactions affect the dynamics at zero and finite temperature. Then we turn to the aforementioned thermoelectric transport study, where we again begin with the interacting resonant level model. Afterwards, we additionally study the more complicated single impurity Anderson-Holstein model. In a last chapter we also consider closed quantum systems, where the interaction acts on an extended spatial regime. We concentrate on systems, which classify as Luttinger Liquids in equilibrium and study their out-of-equilibrium dynamics. An outlook-like overview of results of our current research about thermalization concludes this result oriented part.

In the two final chapters, we briefly sum up our findings as well as give an overview of possible future avenues of research.

Chapter 3

Models

Contents

3.1. Ab Initio Model of Solid-State Physics **11**
3.2. One-Dimensional Lattice Models **12**
3.2.1. Equilibrium Correlation Physics: Luttinger Liquids 13
3.2.2. Jordan-Wigner Transformations 15
3.3. Single Impurity Anderson Model **15**
3.3.1. One Word on Experiments 15
3.3.2. Hamiltonian 16
3.3.3. Equilibrium Correlation Physics: Kondo Physics 16
3.4. Single Impurity Anderson-Holstein Model **17**
3.4.1. Hamiltonian 18
3.4.2. Equilibrium Correlation Physics: Kondo Physics 18
3.5. Interacting Resonant Level Model **19**
3.5.1. Hamiltonian 19
3.5.2. Equilibrium Correlation Physics: Renormalization of Hybridization 21
3.6. Spin-Boson Model **21**
3.6.1. Hamiltonian 22
3.6.2. Correlation Effects: Dynamical Regimes 23
3.6.3. Mapping to IRLM 23

Introduction

In the course of this thesis we will consider different standard models of solid-state physics, which we want to briefly introduce, motivate and set in the context of existing literature in this chapter. We focus on one-dimensional lattice models or models of quantum dots. As we are mainly interested in (strong) correlations, we also give a short overview of what is known about the effects of the correlations in each model separately. For this discussion we will mainly concentrate on the more transparent case of equilibrium. This has to be contrasted with the general setting of this thesis, which aims at describing the non-equilibrium dynamics of such systems. Understanding the equilibrium physics, however, is a natural first step. To explain the connection of the models used to the general problem faced in solid-state physics we start with the description of an...

3.1 Ab Initio Model of Solid-State Physics

Generally, a model of a solid must include different relevant degrees of freedom. In a first step we can distinguish between electrons on the one, and cores on the other hand. The bonding type

determines which fraction of the electrons is strongly bound to the cores forming so called ions[1]. These ions are usually aligned in a periodic structure, while the remaining weakly bound electrons are more or less delocalized. The corresponding Hamiltonian describing the total system

$$H = T_C + T_e + V_{CC} + V_{Ce} + V_{ee} \tag{3.1.1}$$

decomposes into five parts. From left to right the contributions on the right hand side of Eq. (3.1.1) read: kinetic energy of ions, kinetic energy of electrons, ion-ion interaction, ion-electron interaction and electron-electron interaction. The Hilbert space of combined electrons and ions of Eq. (3.1.1) is immense. Luckily, the masses of the ions are usually $10^4 - 10^5$ times larger than the ones of the electrons. This makes it feasible to employ a so called *Born-Oppenheimer approximation* [Czy08] to separate the dynamics of ions and electrons. Concentrating solely on the quickly moving electrons and keeping the ions' positions constant on the underlying lattice, one can focus on the electrons moving in some effective potential (generated by the stationary ions)[2]. To tackle this Hamiltonian ab initio methods have been devised. One of the most prominent ones is the density functional theory, in which a variational optimization of the (approximate) density functional is performed to describe the ground state.

However, it is very difficult in general to include strong correlations in an ab initio treatment. They are usually handled effectively only on the mean field level, neglecting quantum fluctuation, which is only reasonable for higher dimension ($d \geq 3$). Including correlations beyond this approach is difficult and one needs to resort to simpler models. To do so one can (still under the assumption of a Born-Oppenheimer approximation) motivate the description of solids via so called *lattice models*

3.2 One-Dimensional Lattice Models

So far we have considered the electrons as moving in continuous space. The periodic potential of the ions defines a lattice creating a rather strong[3] potential. It is well known that the periodic potential gives rise to a certain class of wave functions as eigenfunctions of the underlying Hamiltonian, namely the *Bloch states*. Bloch states are nice in the sense that only their phase changes when their spacial argument is shifted exactly by one period of the lattice, but not very practical in the sense that they are highly non-local in space. A better choice is to construct from the Bloch states, a new orthonormal set of states, whose elements are localized around the lattice sites. Those new states, called *Wannier functions*, can be used to derive the effective tight-binding Hamiltonian

$$H_{\mathrm{TBM}} = \sum_{k,k'} t_{k,k'} c_k^\dagger c_{k'} + \mathrm{H.c.} + \sum_{k,k'} U_{k,k'} c_{k'}^\dagger c_{k'} c_k^\dagger c_k \ , \tag{3.2.1}$$

which describes fermions created (annihilated) by $c_k^\dagger (c_k)$ hopping from one Wannier state labelled $k = (n, b, \sigma)$ to another labelled $k' = (n', b', \sigma')$ with amplitude $t_{k,k'}$ and interacting with one another with strength $U_{k,k'}$. Here we restrict ourself to density-density type interactions and k and k' are understood as multi-indices incorporating site n, band b and spin σ index[4]. The parameters $t_{k,k'}$ and $U_{k,k'}$ are determined (approximately) by the matrix elements of the kinetic energy and interaction operators in the basis of the Wannier functions.

In this thesis we want to consider low-dimensional systems, where correlation effects are especially prominent and therefore focus on *one-dimensional* lattice models in the following. Furthermore, we concentrate on a single band and consequently drop the index b from now on. Due to the strong localization (by construction of the Wannier functions), usually only a few elements of $t_{k,k'}$ and

[1] These ions are the constituents of the crystal structure of the solid. They contain atoms including their strongly bound inner electrons.

[2] One can improve on this approximation of keeping the ions' positions perfectly constant by including so called *phonons*. These new (in general highly delocalized) quasi-particles describe lattice distortions in form of vibrations and ultimately their interactions with the electrons.

[3] How strong is strong enough to motivate the following discussion is non-trivial, but shall not be elaborated on in much detail now.

[4] Depending on the problem additional indices can be included.

$U_{k,k'}$ carry significant weight. Therefore, one often considers only a few (nearest neighbor) hopping and interaction terms. Let us start with only $t_{n,\sigma} = t_{(n,\sigma),(n+1,\sigma)}$ and $U_n = U_{(n,\uparrow),(n,\downarrow)}$ being non-zero in Eq. (3.2.1). This yields the so called *Hubbard model*

$$H = \sum_{n=1}^{N-1} \left[\sum_{\sigma=\uparrow,\downarrow} t_{n,\sigma} c_{n,\sigma}^\dagger c_{n+1,\sigma} + \text{H.c.} \right] + \sum_{n=1}^{N} U_n c_{n,\uparrow}^\dagger c_{n,\uparrow} c_{n,\downarrow}^\dagger c_{n,\downarrow} \quad . \tag{3.2.2}$$

The translation invariant case $t = t_{n,\sigma}$ and $U = U_n$ constitutes the prototype model to describe strongly correlated systems. It is, e.g., studied in the context of the metal-(Mott)insulator transition as well as itinerant magnetism. Furthermore, (depending on the parameter regime) it exhibits interesting Luttinger Liquid physics (see below). We do not dwell further on the rich physics of this model, as it plays a minor role for what follows. We will encounter it again only when discussing thermalization ($\rightarrow$ Section 9.5). In this context it is more interesting to us to scrutinize the model's integrability. Here integrability shall be understood as the property of a system of being Bethe ansatz solvable. With this an exact solution of the model exists: calculating eigenenergies is then usually rather easy, while calculating wavefunctions beyond the energetically lowest ones and from them correlators, despite of having obtained a (formally) exact solution, is a close to impossible task [Gia03]. The model defined via Eq. (3.2.2) is in this sense integrable and to contrast it with a similar but non-integrable one we also consider (one variant) of the extended Hubbard model, by including a finite nearest neighbor interaction $V_{n,\sigma} = U_{(n,\sigma),(n+1,\sigma)}$

$$H = \sum_{n=1}^{N-1} \left[\sum_{\sigma=\uparrow,\downarrow} t_{n,\sigma} c_{n,\sigma}^\dagger c_{n+1,\sigma} + \text{H.c.} + V_{n,\sigma} c_{n,\sigma}^\dagger c_{n,\sigma} c_{n+1,\sigma}^\dagger c_{n+1,\sigma} \right] + \sum_{n=1}^{N} U_n c_{n,\uparrow}^\dagger c_{n,\uparrow} c_{n,\downarrow}^\dagger c_{n,\downarrow} \quad . \tag{3.2.3}$$

$V_{n,\sigma}$ can then be used to tune the integrability of the model away from its integrable point $V_{n,\sigma} = 0$.

An even simpler model is obtained if we disregard the spin-degree of freedom. The resulting model of *spinless fermions with nearest neighbor interaction* still shows very interesting correlation physics [Gia03]. We define the spinless Hamiltonian

$$H = \sum_{n=1}^{N-1} t_n c_n^\dagger c_{n+1} + \text{H.c.} + \sum_{n=1}^{N-1} U_n c_n^\dagger c_n c_{n+1}^\dagger c_{n+1} + \sum_{n=1}^{N} h_n c_n^\dagger c_n \ , \tag{3.2.4}$$

where we have additionally included an onsite energy h_n and concentrate in the following on the translational invariant case $t_n = t$, $h_n = h$ and $U_n = U$. For $U = 0$ the Hamiltonian describes a Fermi Liquid (non-interacting theory), while for $-2|t| < U < 2|t| \wedge U \neq 0 \wedge h = 0$ (half-filling) the system turns to a so called *Luttinger Liquid*. At $|U| = 2|t| \wedge h = 0$ a phase transition to a charge-density wave or phase separation (depending on the relative sign of t and U) occurs. If we consider a finite h one finds (by e.g. Bethe ansatz or density matrix renormalization group) the phase diagram of Fig. 3.1 [DC66]. In the following the ungapped Luttinger Liquid phase is of special interest to us. Here correlations lead to a particularly peculiar behavior as outlined next.

3.2.1 Equilibrium Correlation Physics: Luttinger Liquids

In one dimension the consequences arising from correlations in a fermionic system are especially severe. In equilibrium, they lead to a break down of the Fermi Liquid paradigm, signalled by the logarithmically divergent reduction of the quasi-particle weight at the Fermi surface within second order perturbation theory. This breakdown of Fermi Liquid theory is not only a feature of the model of Eq. (3.2.4), which is the one of major interest for the remainder of this thesis, but rather encountered generically in interacting one-dimensional fermionic systems. It was found that a large class of those models are described by the same universal physics at low energies, dubbed Luttinger Liquid physics [Hal80]. Its most prominent hallmark is the emergence of generic critical power-law decay of correlation functions. A renormalization group flow analysis revealed that in equilibrium

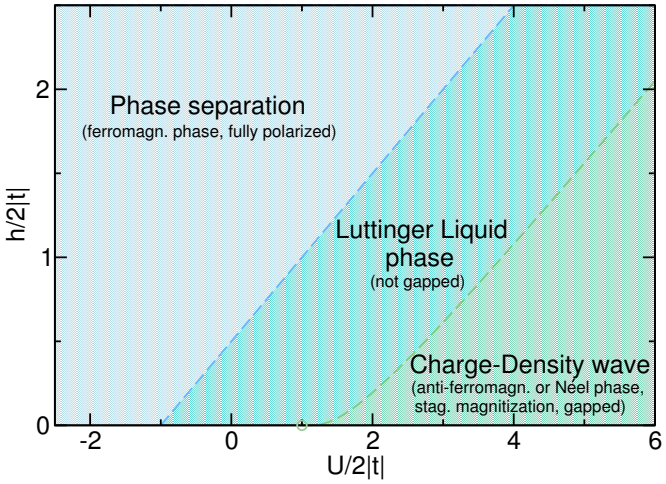


Figure 3.1.: Phase diagram of spinless fermions with nearest neighbor interaction as given in the Hamiltonian of Eq. (3.2.4). The names of the ferromagnetic and Néel (anti-ferromagnetic) phases become evident only via considering spins instead of spinless fermions employing the transformation of section 3.2.2.

the exactly solvable Tomonaga-Luttinger model [Gia03, Sch05b]

$$H = \sum_{n>0} \left[k_n \left(v_F + \frac{g_4(k_n)}{2\pi} \right) \left(b_n^\dagger b_n + b_{-n}^\dagger b_{-n} \right) + k_n \frac{g_2(k_n)}{2\pi} \left(b_{-n}^\dagger b_n^\dagger + b_{-n} b_n \right) \right], \tag{3.2.5}$$

with bosonic ladder operators $b_n^{(\dagger)}$ associated to the densities of left- and right-moving fermions, the Fermi velocity v_F, and $k_n = 2\pi n/L$, $n \in \mathbb{Z}$, is the infrared fixed point model of many interacting one-dimensional models in their ungapped phase [Sól79]. In analogy to Fermi Liquid systems the low-energy physics is completely characterized by only a few parameters. For spinless models [like the one given in Eq. (3.2.4)] these parameters are (1) the velocity v of the elementary excitations and (2) the Luttinger Liquid parameter K, which enters exponents of the algebraically decaying correlation functions. For the Tomonaga-Luttinger model of Eq. (3.2.5) those parameters are given by

$$K = \left[\frac{1 + g_4(0)/(2\pi v_F) - g_2(0)/(2\pi v_F)}{1 + g_4(0)/(2\pi v_F) + g_2(0)/(2\pi v_F)} \right]^{1/2}, \tag{3.2.6}$$

$$v = v_F \left[\left(1 + \frac{g_4(0)}{2\pi v_F} \right)^2 - \left(\frac{g_2(0)}{2\pi v_F} \right)^2 \right]^{1/2}. \tag{3.2.7}$$

Due to the availability of a Bethe ansatz solution of the model defined in Eq. (3.2.4) the values of K and v for this lattice model are also known analytically at half-filling

$$K = \frac{\pi}{4\eta}, \quad v = J \frac{\pi \sin(2\eta)}{\pi - 2\eta}, \quad 2\eta = \arccos\left(-\frac{U}{2J} \right). \tag{3.2.8}$$

The Luttinger Liquid regime found for the model of Eq. (3.2.4) (as well as other models out of the Luttinger Liquid universality class) is then distinctively different from a Fermi Liquid system, as it features (among others) a

1. continuous bulk momentum distribution function $n(k)$ even at zero temperature [quasi-particle weight $Z = 0$, instead of the finite quasi-particle weight Z of Fermi Liquids. Here Z is given by the jump of $n(k)$ at k_F and $T = 0$].

2. single-particle bulk density of states which vanishes as $|\omega|^{\alpha(K)}$ with $\alpha(K) = (K - K^{-1} - 2)/2$, where ω is the energy measured relative to the Fermi energy ϵ_F.

3. particular sensitivity to impurities. For repulsive interactions even a single weak impurity acts as a strong perturbation. The homogeneous system (perfect chain) corresponds to an unstable fixed point in the renormalization group sense [Kan92, And04, Ens05b]. The system always flows towards an open chain, which constitutes the stable fixed point.

Points 1. and 2. signal that fermionic quasi-particles do not exist in one dimension due to correlations [Gia03], which is in sharp contrast to Fermi Liquid theory. At this point this concludes our condensed presentation of the fascinating correlation physics encountered in one dimension, further details are postponed to chapter 9. Last but not least, we outline a particularly useful transformation for one-dimensional lattice models.

3.2.2 Jordan-Wigner Transformations

For the one-dimensional tight-binding models discussed above there exists a simple transformation[5], namely a *Jordan-Wigner transformation* [Gia03], which maps the fermionic language ($c_k^{(\dagger)}$) used above to a spin one ($S^{x/y/z}$) or vice versa. For different methods the one or the other[6] is preferred and thus being able to map the two is highly beneficial[7]. We will explain the mapping by exemplification for the simplest case of a spinless fermion tight-binding model with nearest neighbor interaction as given in Eq. (3.2.4).

We want to write the Hamiltonian into a form including only spins $S^{x/y/z}$ or equivalently $S^{+/-/z}$. Fermionic operators anticommute $[c_n^\dagger, c_n]_+ = 1 \quad \wedge \quad [c_n^\dagger, c_{n'}]_+ = 0$ (for $n \neq n'$). Spins on the other hand fulfil the commutation relation $[S_n^+, S_n^-]_+ = 1 \quad \wedge \quad [S_n^+, S_{n'}^-]_- = 0$ (for $n \neq n'$). Thus the commutation relation are "almost" the same. One can fix the difference in commutation relations by attaching a *Jordan-Wigner string* to the spins

$$\begin{aligned} c_n &= e^{i\phi_n} S_n^- \ , \qquad c_n^\dagger = e^{-i\phi_n} S_n^+ \ , \qquad \text{with: } \phi_n = \pi \sum_{j<n} S_j^+ S_j^- \ . \\ e^{\pm i\phi_n} &= \prod_{j<n} \left(-2S_j^z\right) \ , \qquad S_n^+ S_{n+1}^- = c_n^\dagger c_{n+1} \ , \qquad S_n^z = S_n^+ S_n^- - \frac{1}{2} = c_n^\dagger c_n - \frac{1}{2}, \end{aligned} \tag{3.2.9}$$

which completes the mapping of fermions to spins and vice versa. A similar mapping as outlined above can be found for the Hubbard model [Bar02].

3.3 Single Impurity Anderson Model

As a next step we further reduce the above mentioned one-dimensional models and confine the interaction to a very small spatial region, which can be done to describe so called *quantum dots*. Since their experimental realization became possible due to improved micro-fabrication technologies[8], quantum dots have attracted a lot of research interest [GG98, Los98, Eng05].

3.3.1 One Word on Experiments

We want to recall briefly the peculiar behavior found in quantum dot transport experiments, assoziated to strong correlations. By depositing metallic electrodes on top of semiconducting heterostructures and cleverly applying gate voltages it became possible to effectively fabricate a quantum dot

[5] In higher dimensions Jordan-Wigner transforms induce long-ranged operator strings, complicating calculations in practice.

[6] as we will see later the functional renormalization group is formulated for fermions ($\rightarrow$ Chapter 4), while the density matrix renormalization group is most easily set up with spins ($\rightarrow$ Chapter 5).

[7] Also an exact solution might be possible in the one formulation, while being far from obvious in the other, as for example the XY Heisenberg chain, which maps to free fermions.

[8] If the physics is dominated by s-wave scattering, the dimensionality of the Fermi Liquid reservoirs is irrelevant.

experimentally [GG98]. In those the quantum-mechanical level spacings Δ are typically very large. Additionally, one usually encounters a rather large charging energy U, attributed to the Coulomb interaction, if an additional electron is harbored by the quantum dot. In the presence of some (higher dimensional) source and drain, by applying an external gate voltage ϵ on the dot one would thus naively expect distinct resonance in the conductance, whenever one of the quantum dot levels, spaced by $\Delta + U$, is tuned through the chemical potential of source and drain. Given that the temperature T is not very small, this so called "Coulomb blockade" regime can actually be investigated in experiments [vdW00]. However, approaching very low T leads to a significant decrease in conductance or the development of wide conductance plateaus for an even or odd number of electrons residing on the droplet [GG98, vdW00], respectively. Strikingly, the spectral function of the quantum dot (accessed by the differential conductance experimentally) is found to exhibit a very narrow resonance, for a regime of odd dot occupation, of width given by a newly emergent energy scale (called T_K later on) rather than by the "bare" strength of the tunnel barriers. This intriguing physics became known as the Kondo effect in quantum dots which has triggered a huge amount of theoretical and further experimental works.

3.3.2 Hamiltonian

A minimal model of such an experimental realization of a quasi-zero dimensional structure including spin and charge fluctuations is the single impurity Anderson model (SIAM)

The Hamiltonian of the SIAM reads

$$H = \sum_{\sigma} (\tilde{\epsilon} n_\sigma + \sigma B n_\sigma) + U n_\uparrow n_\downarrow + \sum_{\alpha=\mathrm{R,L}} (H^\alpha_{\mathrm{res}} + H^\alpha_{\mathrm{tun}}) \,, \tag{3.3.1}$$

$$H^\alpha_{\mathrm{res}} = \sum_{k_\alpha,\sigma} \epsilon_{k_\alpha} c^\dagger_{k_\alpha\sigma} c_{k_\alpha\sigma} \,, \tag{3.3.2}$$

$$H^\alpha_{\mathrm{tun}} = \sum_{k_\alpha,\sigma} \gamma_{k_\alpha\sigma} c^\dagger_{k_\alpha\sigma} d_\sigma + \mathrm{H.c.} \,, \tag{3.3.3}$$

where

$$n_\sigma = d^\dagger_\sigma d_\sigma \,, \qquad \tilde{\epsilon} = \epsilon - \frac{U}{2}. \tag{3.3.4}$$

The fermionic operators d_σ and $c_{k_r\sigma}$ refer to electrons on the dot and in the reservoir $r = \mathrm{R, L}$, respectively. Concerning the remaining parameters, ϵ is the gate voltage and U the strength of the repulsive interaction between electrons on the dot. Finally, B denotes a magnetic field, lifting the spin degeneracy. With this definition, $\epsilon = B = 0$ corresponds to half-filling of the dot in equilibrium. In the following we will consider the limit, where the details of the reservoirs are unimportant and their influence can be described effectively by some hybridization Γ, which is determined by $\gamma_{k_\alpha\sigma}$ and the density of state of the reservoirs at zero frequency only. More details on this so called wide-band limit can be found in section 4.1.2.

3.3.3 Equilibrium Correlation Physics: Kondo Physics

The SIAM is particularly fascinating as it describes the intriguing (strongly correlated) Kondo physics found experimentally in quantum dots outlined above: close to the particle-hole symmetric point, or equivalently odd average occupation, the dot spin-degree of freedom is screened by the bath, giving rise to a highly correlated ground state of combined lead and dot electrons. It governs the physics below some (exponentially small) temperature called *Kondo temperature* T_K. One can define this scale

$$T_K = -\frac{2}{\pi \chi_s} \,, \tag{3.3.5}$$

via the spin susceptibility

$$\chi_s = \left. \frac{d(\langle n_\uparrow \rangle - \langle n_\downarrow \rangle)}{dB} \right|_{B=0}. \tag{3.3.6}$$

In the strong interaction limit $U \gg \Gamma$ one finds that the Kondo temperature indeed features exponential behavior [Hew93]

$$T_K \sim \sqrt{|U|/\Gamma/2}\exp\left[-\frac{\pi}{8|U|\Gamma}\left|U^2-4\epsilon^2\right|\right]. \tag{3.3.7}$$

The universal scale T_K describes the low energy behavior of the SIAM and should thus show up in different zero-energy properties (such as, e.g., the effective mass → Section 8.3.2). The spectral density of the dot at $U = \epsilon = B = 0$ is given by a Lorentzian of width $\sim \Gamma$. If we increase U to large values the central resonance narrows to width $\sim T_K$ (but remains at the same height) and Hubbard satellites (broader features) positioned at $\omega \sim U$ appear With this the central resonance becomes exponentially narrow. For finite ϵ and large $U \gg \epsilon$ the spectral density is said to be *pinned* to the chemical potential of the reservoirs, meaning that the position of the central resonance depends only weakly on ϵ. This gives rise to a broad conductance plateau of perfect conductance in $G(\epsilon)$ of width $\sim U$. The Kondo effect promotes transport in a regime naively associated to Coulomb blockade (as observed in experiments see section 3.3.1). On the other hand turning on B at $\epsilon = 0$ and $U \gg B$ leads to a rapid collapse of the conductance. $G(B)$ is of width $\sim T_K$. Therefore, the strong correlation limit of large U is (to us) the most fascinating one as the correlation induce very prominent effects.

As a side note, adding to this brief introduction of the Kondo effect, we point out at that the Kondo effect was actually first measured in bulk materials long before being able to fabricate quantum dots. The resistivity of gold [dH34] increases at small temperatures. Later it was realized, that this effect can be explained within the SIAM [And61], which at this point was used rather as a simple model of magnetic impurities in such bulk materials. Furthermore, it was soon realized that the Kondo effect can be attributed to the spin-degree of freedom, and the yet simpler Kondo model, neglecting charge fluctuations was introduced to explain the resistivity anomaly. The latter can be treated rather efficiently [Kon64], but will not be of interest throughout the rest of this work.

Although the SIAM is certainly a model of great experimental as well as theoretical interest, we want to focus in what follows on a model including additionally phonons. Therefore we will not discuss further the physics of the SIAM (for more information consult [Hew93]) and rather move on to the ...

3.4 Single Impurity Anderson-Holstein Model

The single impurity Anderson-Holstein model (AHM) is studied as a simple impurity model that includes spin, charge as well as *phononic* degrees of freedom. It is commonly used to model electronic transport through individual molecules contacted between two leads. Within this quantum dot model the lowest unoccupied molecular orbital is described as a single level featuring a two-fold spin-degree of freedom with a Coulomb repulsion between electrons of opposite spin. So far this is identical to the SIAM. In contrast, the molecule additionally can vibrate at some characteristic frequency ω_0 and electrons residing on the quantum dot interact with the polarization field generated by this vibration.

The intriguing interplay of electronic degrees of freedom and phonons led to an intense interest in and extensive research on the AHM. The equilibrium properties (linear conductance, spectral density, susceptibility, ...) of the Anderson–Holstein model have been studied perturbatively [Mit04, Gal07], and nonperturbatively using numerical renormalization group techniques [Hew02, Cor04]. In the limit of weak lead-dot coupling, using a Lang–Firsov transformation together with a generalized Schrieffer–Wolff transformation one obtains an effective Kondo model, which allows for a more traditional renormalization group ansatz [Paa05].

The AHM is experimentally relevant as it is can be realized e.g. in suspended carbon nanotubes, where the principal vibration mode of the tube is described by a local phonon mode [Let09]. The strength of the electron–phonon coupling in this setup is rather high (with the ratio between the coupling constant and the phonon frequency, $\lambda/\omega_0 \geqslant 5$ [Let09]).

3.4.1 Hamiltonian

The system is described by the Hamiltonian of the SIAM given in Eq. (3.3.1)-(3.3.3) by adding the local phonon mode

$$H = \sum_{\sigma} (\tilde{\epsilon} n_\sigma + \sigma B n_\sigma) + U n_\uparrow n_\downarrow + \sum_{\alpha=\mathrm{R,L}} (H^\alpha_{\mathrm{res}} + H^\alpha_{\mathrm{tun}}) + \omega_0 b^\dagger b + \lambda (b^\dagger + b)(n_\uparrow + n_\downarrow), \tag{3.4.1}$$

$$H^\alpha_{\mathrm{res}} = \sum_{k_\alpha,\sigma} \epsilon_{k_\alpha} c^\dagger_{k_\alpha\sigma} c_{k_\alpha\sigma}, \tag{3.4.2}$$

$$H^\alpha_{\mathrm{tun}} = \sum_{k_\alpha,\sigma} \gamma_{k_\alpha\sigma} c^\dagger_{k_\alpha\sigma} d_\sigma + \mathrm{H.c.}, \tag{3.4.3}$$

where

$$n_\sigma = d^\dagger_\sigma d_\sigma \ , \qquad \tilde{\epsilon} = \epsilon - \frac{U}{2} + U_{\mathrm{epe}} \ , \qquad U_{\mathrm{epe}} = \frac{2\lambda^2}{\omega_0}. \tag{3.4.4}$$

Additionally to the operators defined above, the bosonic operator b refers to a phonon mode with frequency ω_0 and coupling constant λ. With this choice again $\epsilon = B = 0$ corresponds to half-filling of the dot in equilibrium. Once more we focus on structureless reservoirs, inducing hybridization Γ, as will be introduced in Section 4.1.2.

3.4.2 Equilibrium Correlation Physics: Kondo Physics

The AHM displays especially interesting strongly correlated Kondo physics. First of all, as the SIAM is reproduced after decoupling the phonons $\lambda = 0$, we recover the full SIAM's physics including the emergence of the low energy scale T_K. If we now turn on λ, but consider the limit $\omega_0 \to \infty$, the AHM reduces to an effective SIAM with $U^{\mathrm{eff}} = U - U_{\mathrm{epe}}$, which is easy to see by integrating out exactly the phonon modes ([Tsa05] and → Section 8.3.2). For $U \ll U_{\mathrm{epe}}$ and $U^{\mathrm{eff}} \gg \Gamma$ the spin induced Kondo effect described above turns to a charge Kondo effect instead. Magnetic field B and gate voltage ϵ switch roles, where now analogous statements about the conductance can be adopted from section 3.3.3.

Furthermore, in the to us more interesting limit $U_{\mathrm{epe}} \gg U$ and $\epsilon = B = 0$, but with a general ω_0, the problem is described effectively by the anisotropic Kondo model [Laa14]. We do not discuss details of the mapping here, but only outline the results. The Kondo temperature T_K, found by this mapping, features a rich behavior depending on the initial parameters Γ/ω_0, $[\lambda/\omega_0]^2$ and $U/[2\omega_0]$ of the AHM, which is determined by the anisotropic Kondo model's coupling constants

$$J_\parallel D \approx \frac{4\Gamma}{\pi\omega_0} e^{-(\lambda/\omega_0)^2} \gamma_+([\lambda/\omega_0]^2, U/[2\omega_0]), \tag{3.4.5}$$

$$J_\perp D \approx \frac{4\Gamma}{\pi\omega_0} e^{-(\lambda/\omega_0)^2} \gamma_-([\lambda/\omega_0]^2, U/[2\omega_0]), \tag{3.4.6}$$

where

$$\gamma_\pm(x,y) = \int_0^1 dt\ t^{x-y-1} e^{\pm xt}, \tag{3.4.7}$$

is the *incomplete gamma function*. Different limits can then be addressed analytically: (1) For $J_\perp \ll J_\parallel$,

$$T_K \sim \left(\frac{J_\parallel}{J_\perp}\right)^{-\frac{1}{J_\parallel D}}, \tag{3.4.8}$$

while for (2) $J_\perp \approx J_\parallel$

$$T_K \sim \exp\left(-\frac{1}{J_\parallel D}\right). \tag{3.4.9}$$

In practice, one can now use Eq. (3.4.5) and (3.4.6) to find T_K for a given set of the parameters U, λ and ω_0. However, for additionally $\lambda \gg \omega_0$ we further approximate $J_\parallel/J_\perp \sim \exp[2(\lambda/\omega_0)^2]$, and with this

$$T_K \sim \exp\left[-\frac{\pi\omega_0}{\Gamma}\left(\frac{\lambda}{\omega_0}\right)^4\right]. \tag{3.4.10}$$

To sum up, for small U, but large U_{epe} and $\epsilon = B = 0$ one therefore finds an exponentially small emergent low energy scale T_K, for $w_0 \gg \lambda$ given by Eq. (3.3.7) with $U \to U - U_{\text{epe}}$ and for $w_0 \ll \lambda$ given by Eq. (3.4.10). The latter shows an exponential behavior in λ^4 (instead of λ^2 in the former), a regime of very strong renormalization due to correlations with respect to λ. We will aim at this intriguing behavior in section 8.3.

3.5 Interacting Resonant Level Model

In the previous section we outlined an extension of the SIAM. Now, as a last quantum dot model we introduce a simplification of it by neglecting the spin-degree of freedom[9]. This leads to the so called *interacting resonant level model* (IRLM). Almost half a century ago the IRLM was introduced in the context of studying equilibrium properties of mixed-valence compounds. Within this question a wealth of interesting behavior was found, either by a mapping to the anisotropic Kondo model or directly by perturbative renormalization group calculations [Noz69, Fil81, Sch80b, Sch82a, Sch82b, Sch82c]. Only later the two-reservoir IRLM, which can be viewed as a simple prototype model for non-equilibrium physics gained considerable interest [Meh06, Bor07, Doy07, Bor08, Bou08, Bor10]. The general idea is to focus on spinless fermions, which tunnel (by amplitude t_{imp}) through a very constrained geometry, namely a single level, from one lead to the other. Electrons residing on the level might be subjected to some gate voltage ϵ. The model is supplemented by a two-particle interaction of a density-density type, coupling electrons residing on the single level to those (spatially) nearby in the reservoirs. Although one might suspect that this model can be realized experimentally for spin polarized electrons, in some quantum dot setups (resembling the single-level), here we view it only from the perspective of theoretical interest. It poses an ideal "play ground" to study the interplay of correlations and transport in charge-fluctuating systems.

3.5.1 Hamiltonian

We put the aforementioned description of the IRLM in a formal form by considering the microscopic Hamiltonian

$$H = \epsilon n_0 + \sum_{\alpha=\text{R,L}} U_\alpha \left(n_0 - \frac{1}{2}\right)\left(n_{1_\alpha} - \frac{1}{2}\right) + \sum_{\alpha=\text{R,L}} (H^\alpha_{\text{res}} + H^\alpha_{\text{tun}}), \tag{3.5.1}$$

$$H^\alpha_{\text{res}} = \sum_{i_\alpha} \tau_{i_\alpha} c^\dagger_{i_\alpha} c_{i_\alpha}, \tag{3.5.2}$$

$$H^\alpha_{\text{tun}} = t_{\text{imp},\alpha} c^\dagger_{1_\alpha} d_0 + \text{H.c.}, \tag{3.5.3}$$

where for simplicity of depiction we have chosen nearest neighbor hoping tight-binding chains as a description of the leads. Furthermore, we use $n_0 = d^\dagger_0 d_0$ and $n_{i_\alpha} = c^\dagger_{i_\alpha} c_{i_\alpha}$, for the occupancies corresponding to the fermionic operators d_0 and c_{i_α}, which describe the spinless fermions on the dot and in reservoir $r = \text{R, L}$, respectively.

Scaling Limit

We are mainly interested in the limit, where the details of the reservoirs are unimportant. This is the so called *scaling limit*, also describable by a field theoretical approach to the IRLM [Meh06, Bor07, Doy07, Bor08, Bou08, Bor10]. Later we will see that for the functional renormalization group method used to tackle the IRLM in the scaling limit, it is vital, that the region where the interaction

[9] Complementary to what was hinted above for the Kondo model.

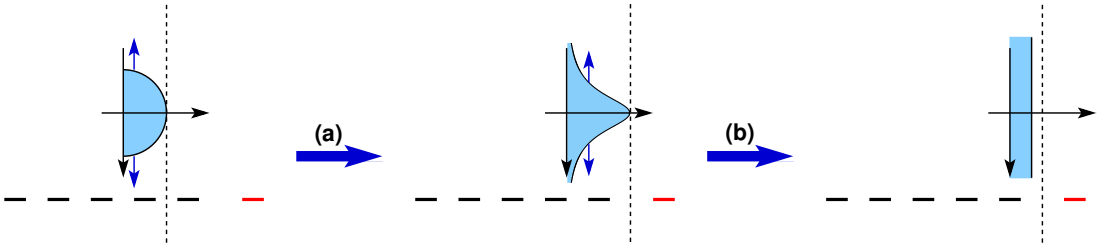


Figure 3.2.: Within the functional renormalization group treatment the structureless reservoirs of the IRLM are established in a two step procedure. We treat the first site of each reservoir explicitly and first perform the limit of infinite bandwidth to the left and right of these sites (a). With this the central site is coupled to baths featuring a Lorentzian density of states. Second, we perform the limit of the width of this Lorentzian going to infinity (b), effectively modelling structureless reservoirs for the central level.

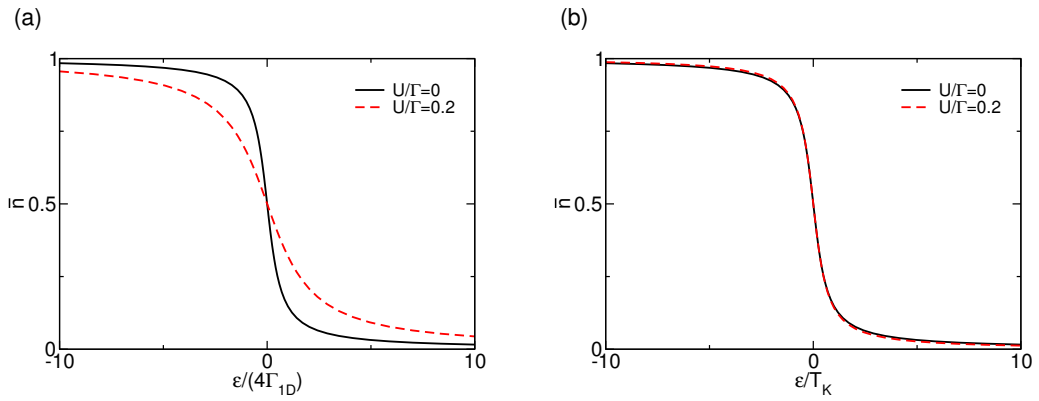


Figure 3.3.: FRG results for the occupancy of the central level of the IRLM in equilibrium at $T = \mu = 0$ in dependency of the gate voltage ϵ. Details on how to calculate the occupancy are outlined later ($\rightarrow$ chapter 4 and 7). We demonstrate by this example that T_K indeed governs the low energy physics, as the curves for the occupancy do collapse if every energy scale is taken with respect to T_K (b) instead of the non-universal "bare" scale $4\Gamma_{1D}$ (a).

acts is treated explicitly, while the non-interacting reservoirs can be integrated out exactly. The microscopic lattice model falls into the scaling regime by a two step procedure. First, we take the limit in which $\tau_{1_\alpha} = \tau_1$, $\tau_{i_\alpha} = \tau_2$ for all $i > 1$ and $\tau_{1/2} \to \infty$ while $\Gamma = \tau_1^2/\tau_2$ remains constant. This way a structureless reservoir (with constant density of states) coupled to the first site of both leads can be established. For the single level in between these two first sites of the leads the hybridization ($\sim$ density of states on sites next to central one) takes the form of a Lorentzian of width $\sim \Gamma$ [compare Fig. 3.2(a)]. Subsequently, taking $t_{\mathrm{imp},\alpha} \to \infty$ and $\Gamma \to \infty$, with constant $\Gamma_{1D} = t_{\mathrm{imp},\alpha}^2/\Gamma$ and $g_1 = 2U/(\pi\Gamma)$ relates the above described model to the IRLM in the scaling limit[10] [compare Fig. 3.2(b)]. The frequency independent hybridization (corresponding to a structureless reservoirs) of the central level is then $\sim \Gamma_{1D}$. The different limits are summarized in Fig. 3.2. Further details on structureless reservoirs can be found in Section 4.1.2.

[10] The index 1 at g_1 signals that this is the first order expansion of a more "general" $g = 2U/(\pi\Gamma) - [U/(\pi\Gamma)]^2$. This g is the more natural choice than U/Γ itself for describing the IRLM physics. However, higher orders in U are generally difficult to capture by our functional renormalization group approach employed later for the IRLM ($\rightarrow$ Section 7.2).

3.5.2 Equilibrium Correlation Physics: Renormalization of Hybridization

Interestingly, in the scaling limit the IRLM shows a strong renormalization of the hopping amplitude coupling the level and the leads t_{imp}. More precisely, in the scaling limit, the renormalization of this hopping amplitude is characterized by a universal power-law, which also manifests in the dot observables [Bor07, Doy07, Bor08]. Considering the problem in equilibrium and at $\epsilon = 0$ provides valuable analytical insights into the problem. With a simple first order perturbation theory approach in U [Noz69, Fil81, Sch80b, Sch82a, Sch82b, Sch82c, Kar10a, Ken11] one finds that the Fock term gives the effective hopping

$$\frac{t_{\text{imp}}^{\text{pert}}}{t_{\text{imp}}} = 1 - \frac{U}{\pi}\frac{1}{\sqrt{\Gamma^2 - 8t_{\text{imp}}^2}} \ln\left(\frac{1-\sqrt{1-\frac{8t_{\text{imp}}^2}{\Gamma^2}}}{1+\sqrt{1-\frac{8t_{\text{imp}}^2}{\Gamma^2}}}\right) \overset{t_{\text{imp}}\ll\Gamma}{\longrightarrow} \frac{t_{\text{imp}}^{\text{pert}}}{t_{\text{imp}}} = 1 - \frac{U}{\Gamma\pi}\ln\left(\frac{2t_{\text{imp}}^2}{\Gamma^2}\right), \quad (3.5.4)$$

between lead and impurity. Its logarithmic divergence signals the onset of strong renormalization. The range of validity of a perturbative approach vanishes as the scaling limit $\Gamma \to \infty$ is approached. The artificial logarithmic divergence in this parameter can be lifted by a renormalization group procedure. In equilibrium we find analytically, that the renormalized hopping amplitude $t_{\text{imp}}^{\Lambda=0}$ is described by ($t_{\text{imp}} \ll \Gamma$)

$$\left(\frac{t_{\text{imp}}^{\Lambda=0}}{t_{\text{imp}}}\right)^2 = 2^{-\frac{2U}{\pi\Gamma}}\left(\frac{t_{\text{imp}}}{\Gamma}\right)^{-\frac{4U}{\pi\Gamma}}, \quad (3.5.5)$$

within the functional renormalization group treatment employed later on. The logarithmic divergence is resummed to a power-law (where only the leading term of the exponent can be trusted in this approach).

The renormalization of the hopping amplitude reveals the emergence of a renormalized effective low energy scale, which governs the low energy physics of the IRLM in the scaling limit similar to the SIAM. We want to define this emergent scale microscopically

$$T_K = -\frac{2}{\pi\chi_c} \quad (3.5.6)$$

by the charge susceptibility

$$\chi_c = \left.\frac{d\langle n\rangle}{d\epsilon}\right|_{\epsilon=0}. \quad (3.5.7)$$

It was shown [And05, Kar10b, And11b, Ken12a] that this definition is useful in the sense that it leads to a correct universal scale T_K, meaning that low energy observables collapse if every energy scale is taken with respect to T_K. This is exemplified for the central level's occupancy $\bar{n}(\epsilon)$ for reservoirs at $\mu = T = 0$ in Fig. 3.3. We note however that alternative definitions, be it field theoretical ones or other microscopic linear response quantities like the conductance can be used equivalently. In passing we note that within the IRLM accounting correctly for the power-law renormalization of the hybridization to the leads is the most essential component to describe accurately not only the equilibrium, but also the non-equilibrium steady-state properties [Kar10a] as well as transient dynamics [Ken11].

The relation between all the presented quantum dot models is finally summarized in Fig. 3.4.

3.6 Spin-Boson Model

Quantum coherence is especially interesting in the context of quantum computing. For this it is essential to understand how the coherence of a small quantum system (zero-dimensional quantum dot) is influenced by its environment. A prototype model to study this is a two-state model, as realized in any system effectively described by the two lowest-lying states of a double well potential with respect to some generalized coordinate, coupled to some large environment. Famous examples of such systems include the inversion resonance of NH_3 molecules, strangeness oscillations of K-meson beams, and coherent tunneling of light interstitials in tunneling centers [Wei12]. As such

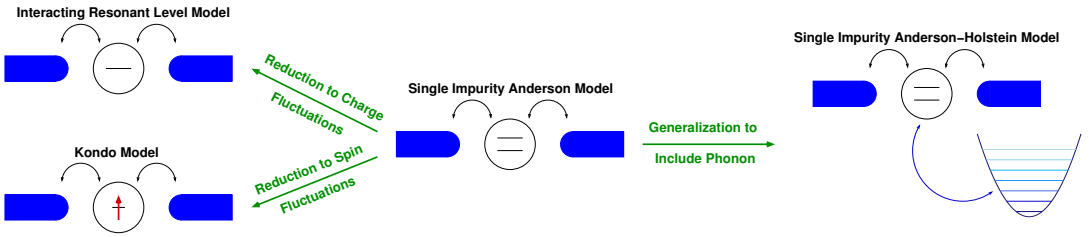


Figure 3.4.: Different quantum dot models and their relations among each other, with respect to how they can be obtained starting from the SIAM by including further or reducing to certain degrees of freedom.

they span over different major fields of physics (and chemistry). In any real system effects of the large surrounding environment have severe influence on the small quantum system. From a modern standpoint effective two-state systems are also interesting from a quantum information's point of view. Superconducting circuits based on tunnel junctions (Josephson junctions) could be ideal candidates for qubits as they are easily contactable, controllable, as well as scalable to large numbers using recent integrated-circuit fabrication technology [Wei12]. A rf SQUID is a simple design of such a superconducting circuit and can be effectively described by a two-level system (coupled to an environment) in the appropriate limit. The two-levels of the system can be viewed as a spin-$1/2$ particle, while the effect of the bath can be modelled by some bosonic bath. This description leads to the so called *spin-boson model* (SBM) [Leg87, Wei12].

3.6.1 Hamiltonian

The SBM is described by the Hamiltonian

$$H = \frac{\epsilon}{2}\sigma_z - \frac{\Delta}{2}\sigma_x - \sum_k \frac{\lambda_k}{2}\sigma_z\left(b_k^\dagger + b_k\right) + \sum_k \omega_k b_k^\dagger b_k, \tag{3.6.1}$$

where $\sigma_{x,y,z}$ are the Pauli-matrices. ϵ describes a Zeeman splitting term of the up- and down-spin configuration and Δ gives the tunneling amplitude between the two states. The environment is described by an (infinite) set of oscillators with different eigenfrequencies ω_k. The term λ_k couples the k-th oscillator to the spin-direction and thus the two-state system to its environment [compare Fig. 3.5(a)]. In a very pictorial description the environment can be viewed to be sensitive to the spin orientation, thus *measuring* its direction. From quantum mechanics it is then plausible to conclude that the coupling to the environment will compete with the coherence encountered in the isolated SBM.

Ohmic Case

Alternatively to Eq. (3.6.1), the system can also be completely characterized by the part of the Hamiltonian describing the spin as well as giving the spectral function, incorporating all effects from the environment

$$J(\omega) = \sum_k \lambda_k^2 \delta(\omega - \omega_k). \tag{3.6.2}$$

Here we concentrate on the so called *ohmic case* with

$$J(\omega) = 2\alpha\omega\Theta(\omega_c - \omega), \tag{3.6.3}$$

where ω_c is considered to be much larger than any other energy scale. The sub-ohmic (super-ohmic) case with $J(\omega) \sim \omega^s$, $s < 1$ ($s > 1$) will not be of interest here, because the ohmic case (1) features the richest physics and (2) shows universal signatures (just as the field-theoretical IRLM, also compare Section 3.6.3).

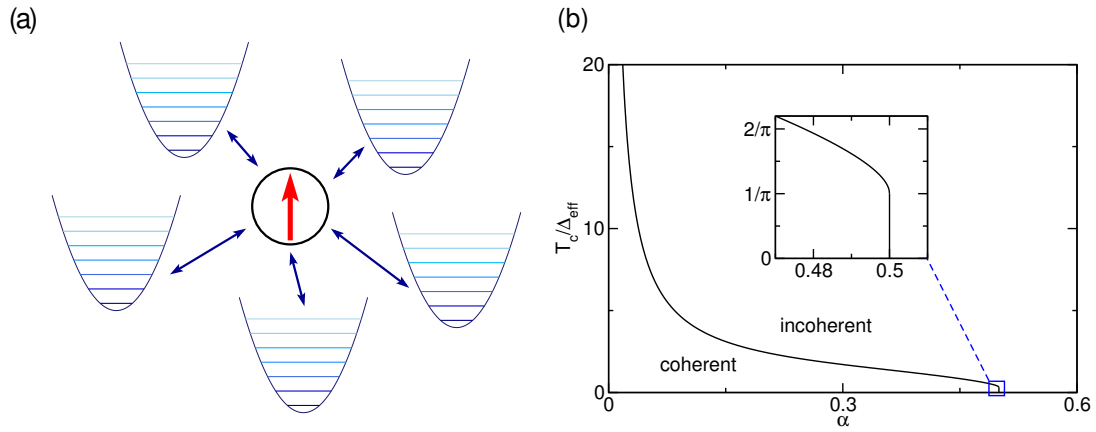


Figure 3.5.: Left: Depiction of the SBM. Right: "transition" line from coherent to incoherent dynamics in the unbiased ohmic SBM following from Eq. (22.20) of [Wei12]. We will see in Section 7.3 that this result actually has to be refined.

3.6.2 Correlation Effects: Dynamical Regimes

To dwell some more on (1) we will recapitulate some of the physics found in the ohmic SBM [Leg87, Wei12]. First of all, similar to the IRLM, within the SBM an interaction α dependent effective low energy scale Δ_{eff} emerges, which can be treated correctly employing renormalization group ideas. For α close to $1/2$ we will analyze this scale in the following section. In this section we want to consider the correlation effects on the dynamics instead of only on the equilibrium properties as done before, because the effect studied now (and later on $\rightarrow$ Section 7.3) manifest only in the dynamics. Without bias $\epsilon = 0$ the dynamics of the spin expectation value $\langle \sigma_z \rangle$ at $T = 0$ are damped oscillatory (coherent) for $\alpha < 1/2$, whereas it turns monotonic (incoherent) for $1/2 < \alpha < 1$. Finally, for $\alpha = 1$ a quantum phase transition from delocalized to localized occurs. The *interaction strength* α thus determines the relaxation dynamics found. Tuning the temperature T in the oscillators one finds that the coherent behavior vanishes for $T_c(\alpha)$ even in the regime $\alpha < 1/2$. A reconstruction of the "transition" line taken from [Wei12] is shown in Fig. 3.5(b). We will see in section 7.3 that this picture has to be refined following the results presented in this thesis.

3.6.3 Mapping to IRLM

We are mainly interested in the coherent-incoherent "transition" around $\alpha = 1/2$, when considering the SBM. Around this special point bosonization ($\rightarrow$ Section 6.3) allows to map the low energy degrees of freedom of the ohmic SBM to the one of the IRLM discussed in the previous section [Leg87], but with only one structureless lead instead of two. The two Hamiltonians are then mapped exactly, which relates their parameters as

$$\epsilon = \epsilon \,, \tag{3.6.4}$$

$$\Gamma_{1\text{D}} = \Delta^2/\omega_c \,, \tag{3.6.5}$$

$$g = 2U/(\pi\Gamma) - [U/(\pi\Gamma)]^2 = 1 - 2\alpha. \tag{3.6.6}$$

Similarly, the observables in the one can be related to the ones in the other. For the only observable of interest in this thesis, the spin expectation value $\langle \sigma_z \rangle (t)$, this is achieved by

$$\langle \sigma_z \rangle (t) = 1 - 2\bar{n}(t), \tag{3.6.7}$$

where $\bar{n}(t)$ is the expectation value of the occupancy of the central level. The huge advantage of this mapping, as were are concerned with the above mentioned transition, is that at $\alpha = 1/2$ it targets a non-interaction model, since $g(\alpha = 1/2) = U(\alpha = 1/2) = 0$ (Toulouse limit). For this exact

solutions are known. Furthermore, this exact point can be used as the starting point for the later used perturbatively motivated renormalization group procedures, i.e. the functional renormalization group and the real time renormalization group. From the mapping also the necessity of such a renormalization group procedure becomes evident: around $\alpha = 1/2$, the entire strong renormalization physics encountered in the IRLM (compare section 3.5.2) will be inherited.

Methods

Chapter 4

Functional Renormalization Group

Contents

4.1. Green's Functions **29**
- 4.1.1. Equilibrium vs. Non-Equilibrium: Matsubara vs. Keldysh 30
- 4.1.2. Non-Interacting Green's Function: An Exact Starting Point 34
- 4.1.3. From Green's Function to Observables 37

4.2. Generating Functionals **40**
- 4.2.1. Functional Integral Representation of the Many-Body Problem 41
- 4.2.2. Functional Reformulating of the Keldysh Green's Functions 42
- 4.2.3. Functional Reformulating of the Matsubara Green's Functions 44
- 4.2.4. Generating Functional of (Connected) Green's Functions 45
- 4.2.5. Generating Functional of Vertex Functions 45

4.3. Flow Equations **47**
- 4.3.1. Flow of Generating Functional of Connected Green's Functions 47
- 4.3.2. Flow of Vertex Functions 48
- 4.3.3. Truncation Schemes and Initial Conditions 50

4.4. Cut-Off Schemes **52**
- 4.4.1. Sharp Cut-Off Scheme: Equilibrium Problems 52
- 4.4.2. Reservoir Cut-Off Scheme: Non-Equilibrium Problems 52
- 4.4.3. Initial Conditions Vol. II 53

4.5. Symmetries and Their Conservation **54**
- 4.5.1. Symmetries... 54
- 4.5.2. ... and Their Conservation 55

Introduction

In this chapter we introduce one of the two methods mainly used in this thesis, which is called the *functional renormalization group* (FRG) [Met12]. Within the FRG one aims at treating a quantum many-body problem in terms of the so called vertex functions. Within FRG those are determined by an exact hierarchy of renormalization group dressed differential equations. Although this exact hierarchy cannot be solved in its entity[1] and is thus approximated (truncated), the FRG is a valuable tool to: (1) devise powerful new approximation schemes with the renormalization group structure built in (2) treat microscopic models (including high energies), instead of only effective low energy ones (3) gain physical insights into the problems as the (truncated) flow equations are usually very transparent (4) obtain approximate *analytical* solutions in certain cases. Where the latter is not

[1] excluding some rare cases where other methods can be used to obtain an exact solution in a more straightforward fashion.

possible, a [compared to other methods of quantum many-body physics (see e.g. chapter 5)] rather fast numerical treatment can be employed . We will apply the FRG to a variety of different (zero- and one-dimensional, open and closed) systems in different physical contexts (equilibrium, non-equilibrium steady-state and dynamics). Having said so already indicates an additional advantage of the method; its flexibility.

Fundamental Idea

Models of solid state physics usually exhibit a very different behavior on different energy scales. Orders of magnitude typically separate, e.g., "bare Coulomb" interactions, "bare" kinetic energy, the mediated short-ranged magnetic interaction and those scales associated to ordering phenomena such as superconductivity. On the one hand, this diversity of scales is difficult to handle with straightforward numerical solutions of microscopic models, as the most intriguing effects show up at low temperatures and for large systems only. On the other hand perturbative many-body methods treating all these scales at once, are often (especially in low dimensions) plagued by infrared divergences, rendering a perturbative expansion inappropriate, even if the expansion parameter is small. This lead to the notion that treating energy scales successively from high to low, might be suited better for these type of problems, which is the central idea behind the *renormalization group* scheme [Wil75]. The FRG outlined here is one way of implementing this general renormalization group idea.

To be more precise: we will present in the following a fermionic formulation of the FRG in which the renormalization group idea is included on the level of the generating *functional*[2] of the one-particle irreducible vertex functions [Sal98]. To this end, first, a so called *cut-off* is introduced into the non-interacting single-particle Green's functions G_0 to address different energy scales successively

$$G_0 \to G_0^\Lambda \qquad \text{with :} \quad G_0^{\Lambda=\infty} = 0 \qquad G_0^{\Lambda=0} = G_0, \tag{4.0.1}$$

where loosely speaking at intermediate Λ only energy scales above Λ contribute in G_0.[3] This (artificial) Λ dependency is in turn inherited by the generating functional of the one-particle irreducible vertex functions and therefore also by the vertex functions γ_m themselves. Taking the derivative of the generating functional with respect to Λ and expanding in its external fields eventually results in an infinite hierarchy of differential equations for the vertex functions

$$\partial_\Lambda \gamma_m^\Lambda = f_m(\{\gamma_n^\Lambda : n \leq m+1\}) \,, \tag{4.0.2}$$

with the form of the functions f_m known. The set of differential equations of Eq. (4.0.2) is called *flow equations* and incorporates (due to the dressing of G_0 described above) energy scale by energy scale. As a final step these flow equations for the vertex functions are integrated from $\Lambda = \infty$, where only high energy physics is included and all expressions are regular (infrared, low energy divergences not present), all the way down to $\Lambda = 0$, where the introduced cut-off is removed and the full physical problem we started with is restored. The full (infinite) set of flow equations, being just an exact reformulation of the full-fledged quantum many-body problem, cannot be handled in practice and the need for truncation arises. The truncation is usually carried out by neglecting the flow of all vertex functions above a certain order m_c

$$\gamma_{m_c+1}^\Lambda = \gamma_{m_c+1}^{\Lambda=\infty} \;\Rightarrow\; \partial_\Lambda \gamma_{m\leq m_c}^\Lambda = f(\{\gamma_n^\Lambda : n \leq m_c\}, \gamma_{m_c+1}^{\Lambda=\infty}) \;, \qquad \partial_\Lambda \gamma_{m>m_c}^\Lambda = 0 \,, \tag{4.0.3}$$

which is appropriate only if those terms are and "remain" small at the beginning as well as throughout the flow[4]. This renders the FRG approximate, but the successive treatment of energy scales is still included. It has been applied successfully to many different aspects of strongly correlated physics [Met12].

In two-dimensional models competing instabilities can be analyzed in an unbiased way. The presence of such an instability (phase transition) is signalled by a divergence of some parts of the

[2] hence the functional in the FRG.

[3] We will see, that depending on the cut-off used this does not necessarily mean $G_0^\Lambda(\omega < \Lambda) = 0$.

[4] which is of course difficult to determine as only the truncated problem can be solved.

vertex functions. In the FRG, the precursor to such a singularity is the growth of a certain part of the vertex functions (called "flow to strong coupling"). As we truncated the flow equations the flow has to be stopped, at some finite scale $\Lambda = \Lambda^s$, before the singularity actually occurs. Thus one cannot recover the cut-off free setup ($\Lambda = 0$), but at the scale Λ^s can determine the dominant part of the two-particle vertex (and try to infer from this a first approximation to a phase diagram).

In contrast, in this thesis we concentrate on $d \leq 1$ dimensions. Here perturbative approaches frequently break down at low temperatures due to arising logarithmic divergences [Hew93, Kan92, Gia03]. Those are artefacts of the approach in the sense that logarithmic divergences would show up in all orders of perturbation theory with such prefactors that they could be re-sumed, e.g., into a power-law (in practice however doing so within ordinary perturbation theory is difficult, as it involves insights into the expression upto arbitrarily high order). We want to separate two different "types" of these divergences: (1) divergences in the frequency or momentum dependency of the quantities of interest at low energies, signalling that perturbation theory can not be applied at all (compare studies of Luttinger Liquids → Chapter 9). (2) "parametric" divergences which restrict the applicability range of plain perturbation theory to essentially zero in certain limits as explained for the IRLM in section 3.5.2 (compare also chapter 7 and section 8.2). In the presence of either of these logarithmic divergences the (often justified) hope is that the FRG can be used to re-sum them to power-laws, by the feed-back of the vertex functions to their own flow equations. By this contributions in all orders of the interaction are incorporated. As a final motivation of a FRG approach we note that FRG results are often quantitatively significantly better[5] than those from perturbation theory. For these problems one might view the FRG as a *renormalizationg group enhanced perturbation theory* (compare studies of the AHM → Section 8.3).

Outline

The rest of this chapter is structured as follows. First, we review some basic ideas of the Green's function formalism, which lies at heart of the FRG approach. Here we also give the explicit expressions needed for the rest of this thesis. Afterwards, we change perspective to the functional integral representation from which in the subsequent section the hierarchy of flow equations of the FRG is derived. Finally, we dwell some more on the subject of how cut-off schemes are introduced as well as the subject of physical symmetries and their conservation within the approximate FRG treatment. The presentation is similar to that of [Kar10a] (mainly equilibrium and steady-state) as well as [Ken11] (mainly dynamics).

4.1 Green's Functions

Before being able to describe the FRG approach used in this thesis we need to cover some basics [Neg88]. We will start with the concept of Green's functions, which will be a crucial ingredient to what follows. Let us concentrate on a quantum many-body Hamiltonian of the general form

$$H = H_0 + U = \sum_{k_1,k_2} \epsilon_{k_1,k_2} c^\dagger_{k_1} c_{k_2} + \frac{1}{4} \sum_{k_1,k_2,k_3,k_4} \bar{v}_{k_1,k_2,k_3,k_4} c^\dagger_{k_1} c^\dagger_{k_2} c_{k_3} c_{k_4} . \tag{4.1.1}$$

Here the indices k_i reference an appropriate set of single-particle quantum numbers and ϵ_{k_1,k_2} denotes the corresponding single-particle matrix elements. ϵ_{k_1,k_2} determines the single-particle part H_0 of H which of course can be treated easily by exact diagonalization. U on the other hand renders a solution difficult as it entails the two-particle interaction, generically rendering an exact treatment infeasible. The term $\bar{v}_{k_1,k_2,k_3,k_4}$ denotes the properly (anti-)symmetrized[6] matrix elements of the two-particle interaction in the single-particle basis $\{k_i\}$. For such a system the n-point Green's functions are functions of n different operators as

$$\begin{aligned} G_{A_1,A_2,\ldots,A_n}(t_1, t_2, \ldots, t_n) &= -i \mathrm{Tr}\left[A_1[t_1]_H A_2[t_2]_H \ldots A_n[t_n]_H \, \rho\right] \\ &= -i \left\langle A_1[t_1]_H A_2[t_2]_H \ldots A_n[t_n]_H \right\rangle_\rho , \end{aligned} \tag{4.1.2}$$

[5] known by comparing to (numerically) exact results obtained with different methods.
[6] As usual symmetrized for bosons, anti-symmetrized for fermions.

where the statistical operator ρ will be specified later and times in square brackets denote the Heisenberg picture $A[t]_H = \exp(iHt)A\exp(-iHt)$. Here we are exclusively concerned with two-point Green's functions, which e.g. include the important cases of certain *observables, correlation functions and single-particle functions* (such as single-particle spectra). Equilibrium and non-equilibrium Green's functions are calculated in the so called Matsubara or Keldysh framework, respectively. This finally brings us to the question regarding ρ.

4.1.1 Equilibrium vs. Non-Equilibrium: Matsubara vs. Keldysh

Usually treating systems in thermal equilibrium with their environment is much simpler than handling the full-fledged time dependency of a system out of equilibrium. With Green's functions this simplification becomes quite clear.

Equilibrium

If we assume the system to be in a thermal equilibrium state described by the grand canonical ensemble with temperature $T = 1/\beta$ and chemical potential μ the density matrix is given by $\rho_{\text{eq}} = \exp(-\beta\tilde{H})/\text{Tr}[\exp(-\beta\tilde{H})]$ with $\tilde{H} = H - \mu N$ and N the particle number operator. If $[H, N] = 0$, any two-point Green's function

$$\begin{aligned} G_{AB}(t,t') &= -i\left\langle A[t]_H B[t']_H\right\rangle_{\rho_{\text{eq}}} = -i\text{Tr}\left[e^{iHt}Ae^{-iH(t-t')}Be^{-iHt'}\rho_{\text{eq}}\right] \\ &= -i\text{Tr}\left[e^{i\tilde{H}(t-t')}Ae^{-i\tilde{H}(t-t')}B\rho_{\text{eq}}\right] = -i\left\langle A[t-t']_{\tilde{H}}B\right\rangle_{\rho_{\text{eq}}} = G_{AB}(t-t'), \end{aligned} \tag{4.1.3}$$

depends only on the time difference $t - t'$ of the two operators. This is a consequence of the time translational invariance encountered in equilibrium. We introduced the time evolution operator with respect to $\tilde{H}$ instead of H, which is convenient to set up diagrammatics. As a consequence every energy is measured with respect to μ. In equilibrium the time evolution and the density operator can be treated on equal footing if we introduce imaginary times τ [Neg88]. We define

$$G_{AB}(\tau) = -\left\langle T_\tau A[\tau]_{\tilde{H}}B\right\rangle_{\rho_{\text{eq}}} = \begin{cases} -\left\langle A[\tau]_{\tilde{H}}B\right\rangle_{\rho_{\text{eq}}} & \tau > 0 \\ -\zeta\left\langle BA[\tau]_{\tilde{H}}\right\rangle_{\rho_{\text{eq}}} & \tau \leq 0 \end{cases}, \tag{4.1.4}$$

where $\zeta = 1(=-1)$ for bosons (fermions).

As usually, it is in practice impossible to solve for the interacting Green's function in the presence of two-particle interaction[7]. Therefore, in a next step, we set up a diagrammatic theory. In this we can expand the problem (in theory) in an infinite Taylor series. Although such a diagrammatic approach frequently breaks down for low-dimensional systems at low temperatures, if truncated to any order, it can still be used to motivate more elaborate methods (like a FRG approach) for handling these types of systems. If we formally integrate the differential equation

$$\partial_\tau\left[e^{\tau\tilde{H}_0}e^{-(\tau-\tau')\tilde{H}}e^{-\tau'\tilde{H}_0}\right] = e^{\tau\tilde{H}_0}(\tilde{H}_0 - \tilde{H})e^{-(\tau-\tau')\tilde{H}}e^{-\tau'\tilde{H}_0}, \tag{4.1.5}$$

we arrive at

$$e^{-(\tau-\tau')\tilde{H}} = e^{-\tau\tilde{H}_0}\left\{\begin{matrix} T_\tau e^{-i\int_{\tau'}^{\tau}U[\tau'']_{\tilde{H}_0}d\tau''} & \tau > \tau' \\ \tilde{T}_\tau e^{-i\int_{\tau'}^{\tau}U[\tau'']_{\tilde{H}_0}d\tau''} & \tau \leq \tau' \end{matrix}\right\}e^{\tau'\tilde{H}_0}. \tag{4.1.6}$$

The (anti-)time ordering operator $T_\tau(\tilde{T}_\tau)$ makes all operators commute and the Green's function (4.1.4) takes the simple form

$$G_{AB}(\tau) = -\frac{\left\langle T_\tau e^{-\int_0^\beta U[\tau'']_{\tilde{H}_0}d\tau''}A[\tau]_{\tilde{H}_0}B\right\rangle_{\rho_{\text{eq},0}}}{\left\langle T_\tau e^{-\int_0^\beta U[\tau'']_{\tilde{H}_0}d\tau''}\right\rangle_{\rho_{\text{eq},0}}}, \tag{4.1.7}$$

[7] We will see that in the framework of functional integrals (see section 4.2) this can be understood in the language of scalar integrals. Determining Green's functions belonging to Hamiltonians featuring no two-particle interactions amounts to solving Gaußian integrals, while with two-particle interactions an additional quartic term in the exponent prohibits an analytic treatment.

which involves only a single forward propagation in imaginary time. The expectation values are taken with respect to the grand canonical ensemble of the non-interacting Hamiltonian $\rho_{\mathrm{eq},0} = \exp(-\beta\tilde{H}_0)/\mathrm{Tr}[\exp(-\beta\tilde{H}_0)]$. Then expression (4.1.7) can be calculated order by order in a perturbative approach by the evaluation of Gaußian integrals. Furthermore, employing Wick's theorem (which again can be done due to the quadratic nature of $\rho_{\mathrm{eq},0}$) one can set up a diagrammatic language. For the single-particle Green's functions ($A = c$, $B = c^\dagger$) the corresponding *Dyson equation* reads

$$G_{12} = [G_0]_{12} + \sum\!\!\!\!\!\!\int_{34} [G_0]_{13}\Sigma_{34}G_{42}, \tag{4.1.8}$$

where Σ is the *one-particle irreducible self-energy* (describing the influence of U) and the $\sum\!\!\!\!\!\!\int$ is an integral or sum for a continuous or discrete variable, respectively. All indices are multi-indices in imaginary time as well as in the appropriate single-particle basis $(i) = (\tau_i, k_i)$. In equilibrium it is most useful to perform a Fourier transform from imaginary time to imaginary frequencies (energy space) [Neg88]. This entails

$$(G \text{ or } \Sigma)_{k_1,k_2}(i\omega_1, i\omega_2) = \delta(i\omega_1 - i\omega_2)(G \text{ or } \Sigma)_{k_1,k_2}(i\omega_1)\,, \tag{4.1.9}$$

which is a consequence of energy conservation. It renders the solution of the Dyson equation to be determined by a mere matrix inversion in the single-particle index space

$$G_{k_1,k_2}(i\omega) = \left[\frac{1}{G_0^{-1}(i\omega) - \Sigma(i\omega)}\right]_{k_1,k_2}. \tag{4.1.10}$$

Non-Equilibrium

Now we turn to non-equilibrium. The situation is more complicated in this case, because it is not possible to write down straight away the analogue of Eq. (4.1.7) involving only a single propagation in time. For this reason we employ a trick introduced by Keldysh in [Kel65], which basically reduces the "new" non-equilibrium problem to the "old" one of equilibrium, where the (minor) price to pay is only a doubling of the degrees of freedom.

In the out-of-equilibrium setup one is usually interested in the dynamics which follows after a certain preparation of the quantum system, described by the density matrix ρ, at $t = t_0$. The time evolution is performed with a Hamiltonian H, which generally does not commute with ρ. Often the question whether a, and if so which, steady-state is reached in the limit $t \to \infty$ is of particular interest. Therefore, generally in non-equilibrium it is useful to consider the Green's functions directly in real-time and define

$$\text{Chronological}: \quad G_{AB}^{--}(t,t') = -i\,\langle T_t A[t]_H B[t']_H\rangle_\rho\,, \tag{4.1.11}$$

$$\text{Lesser}: \quad G_{AB}^{-+}(t,t') = -\zeta i\,\langle B[t']_H A[t]_H\rangle_\rho\,, \tag{4.1.12}$$

$$\text{Larger}: \quad G_{AB}^{+-}(t,t') = -i\,\langle A[t]_H B[t']_H\rangle_\rho\,, \tag{4.1.13}$$

$$\text{Anti}-\text{Cronological}: \quad G_{AB}^{++}(t,t') = -i\left\langle \tilde{T}_t A[t]_H B[t']_H\right\rangle_\rho. \tag{4.1.14}$$

Instead of one equilibrium Green's function, now four different functions are needed.

But how can we reduce the problem to a simple forward time evolution analogue to Eq. (4.1.7), which allows for setting up a diagrammatic treatment? The answer is to introduce a back-folded time contour [Kel65] as shown in Fig. 4.1. With respect to this new contour γ the propagation from t_0 first to t', then to t and finally back to t_0 can be expressed by a forward propagation (along γ) only. We assign a new index $\nu = +/-$ to the operators and introduce a new time ordering operator T_γ, which first orders operators associated with $\nu = +$ left of those with $\nu = -$ and subsequently acts as the usual (anti)time ordering operator $T_t(\tilde{T}_t)$ within the sector of $\nu = -$ ($\nu = +$). This allows us to compactify the four Green's functions defined in (4.1.11)-(4.1.14) into a single one

$$G_{AB}^{\nu\nu'-}(t,t') = -i\left\langle T_\gamma A^\nu[t]_H B^{\nu'}[t']_H\right\rangle_\rho, \tag{4.1.15}$$

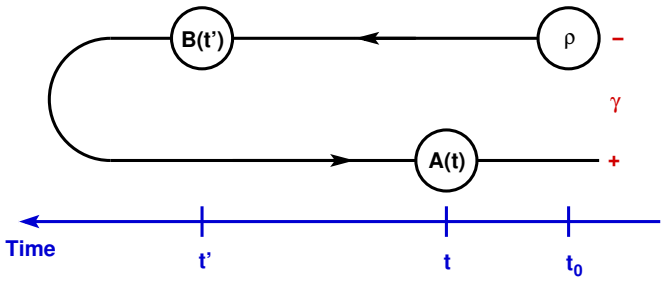


Figure 4.1.: The Keldysh contour introduced to tackle the non-equilibrium problem [Kel65]. It consists of an upper (-) and a lower (+) branch. With respect to this back-folded contour a mixed forward- and backward-propagation along the time axis can be treated as a single propagation along the contour γ.

which is the perfect analogue of (4.1.4). Now the doubling of degrees of freedom becomes apparent. *Under the action* of T_γ the annihilation c_k and the creation $c^\dagger_{k'}$ operator fulfil the commutation relation

$$[c_k^\nu, c_{k'}^{\nu'}]_{-\zeta} = 0 \qquad [c_k^\nu, c_{k'}^{\nu'\dagger}]_{-\zeta} = \delta_{kk'}\delta_{\nu\nu'} \,, \tag{4.1.16}$$

which shows that indeed ν can be regarded as an additional independent single-particle index. Now we can proceed completely analogous to the equilibrium case and first rewrite the time evolution operator as above, by formally integrating its derivative and obtain

$$e^{-iH(t-t_0)+iH(t'-t_0)} = e^{-iH_0(t-t_0)} \begin{Bmatrix} T_\gamma e^{-i\int_{t'}^{t} U^+[t'']_{H_0}dt''} & t > t' \\ T_\gamma e^{-i\int_{t'}^{t} U^-[t'']_{H_0}dt''} & t \leq t' \end{Bmatrix} e^{iH_0(t'-t_0)}. \tag{4.1.17}$$

Following the procedure for equilibrium we can now re-express the Green's function (4.1.15), where we concentrate on the single-particle case

$$\begin{aligned} G^{\nu\nu'}_{kk'}(t,t') &= -i\Big\langle T_\gamma \left[T_\gamma\, e^{-i\int_t^{t_0} U^+ dt} e^{iH_0(t-t_0)}\right] c_k^\nu \left[e^{-iH_0(t-t_0)}\, T_\gamma\, e^{-i\int_{t'}^{t} U^\mp dt} e^{iH_0(t'-t_0)}\right] \\ &\quad \times c_{k'}^{\nu'}\left[e^{-iH_0(t'-t_0)}\, T_\gamma\, e^{-i\int_{t_0}^{t'} U^- dt}\right]\Big\rangle_\rho \\ &= -i\Big\langle T_\gamma\, e^{-i\int_{t_0}^{\max\{t,t'\}}\left\{U^-[t'']_{H_0} - U^+[t'']_{H_0}\right\}dt''} c_k^\nu[t]_{H_0} c_{k'}^{\nu'\dagger}[t']_0\Big\rangle_\rho \\ &= -i\Big\langle T_\gamma\, e^{-i\int_{t_0}^{\infty} U[t'']_{H_0}dt''} c_k^\nu[t]_{H_0} c_{k'}^{\nu_2\dagger}[t']_{H_0}\Big\rangle_\rho \quad \text{for} \quad \begin{matrix} t > t' \\ t \leq t'. \end{matrix} \end{aligned} \tag{4.1.18}$$

Here we introduce the two-particle interaction U in Keldysh space by absorbing the Keldysh index as

$$\bar{v}_{\{k_1\nu_1\}\{k_2\nu_2\}\{k_3\nu_3\}\{k_4\nu_4\}} = \bar{v}_{k_1k_2k_3k_4} \times (-\nu_1)\delta(\nu_1 = \nu_2 = \nu_3 = \nu_4), \tag{4.1.19}$$

in the two-particle term $\bar{v}$ of the Hamiltonian H.

Since (4.1.18) contains a single forward propagation[8] only, just like in equilibrium, this again serves as a starting point for employing Wick's theorem[9] and setting up diagrammatics. Adopted from equilibrium we find the same Dyson equation (4.1.8), where the new single-particle index $(i) = (\nu, k, t)$ now also contains the Keldysh index. If the existence of a steady-state for $t_0 \to -\infty$ is *assumed*[10] and we consider this limit the Green's functions depend on time differences only. Thus

[8] Under T_γ which though more complicated is structurally equivalent to the usual time ordering.

[9] For this the initial density matrix ρ needs to be quadratic, i.e. should not contain any correlations. When solving the full time dependent problem however one could combine the equilibrium and non-equilibrium frameworks to first perform an imaginary time evolution into a (correlated) equilibrium state and then calculate the real-time dynamics out of this initial state.

[10] Tackling the full transient dynamics sheds light on this assumptions, which will be the issue of a later discussion (see section 7.1.3).

it is again more convenient to work in energy space (Fourier transform of the time differences to the real frequency ω), which gives the analogue of Eq. (4.1.10)

$$\begin{aligned}&(G \text{ or } \Sigma)_{\{\nu_1,k_1\},\{\nu_2,k_2\}}(\omega_1,\omega_2) = \delta(\omega_1-\omega_2)(G \text{ or } \Sigma)_{\{\nu_1,k_1\},\{\nu_2,k_2\}}(\omega_1)\\ &\Rightarrow G_{\{\nu_1,k_1\},\{\nu_2,k_2\}}(\omega) = \left[\frac{1}{G_0^{-1}(\omega)-\Sigma(\omega)}\right]_{\{\nu_1,k_1\},\{\nu_2,k_2\}},\end{aligned} \tag{4.1.20}$$

in non-equilibrium, where the single-particle index reads $(i) = (\nu, k, \omega)$.

In the Dyson equation as written above all the different Green's functions and self-energies mix with respect to the Keldysh indices. However, one can find a more clever representation by exploiting that the four Green's functions defined in (4.1.11)-(4.1.14) are not independent, but rather obey

$$\sum_{\nu,\nu'}(\nu)(\nu')G^{\nu,\nu'} = 0, \tag{4.1.21}$$

which is a consequence of causality [Ken11, Sch11a]. We have suppressed all other than the Keldysh indices to improve readability. A similar relation holds for the self-energy

$$\sum_{\nu,\nu'}\Sigma^{\nu,\nu'} = 0. \tag{4.1.22}$$

Performing a rotation in Keldysh space

$$\begin{aligned}\begin{pmatrix} G^{\mathrm{R}} & G^{\mathrm{K}} \\ 0 & G^{\mathrm{A}}\end{pmatrix} &= \underbrace{\frac{1}{\sqrt{2}}\begin{pmatrix}1 & 1\\ 1 & -1\end{pmatrix}}_{A}\begin{pmatrix} G^{--} & G^{-+} \\ G^{+-} & G^{++}\end{pmatrix}\underbrace{\frac{1}{\sqrt{2}}\begin{pmatrix}1 & 1\\ -1 & 1\end{pmatrix}}_{B},\\ \begin{pmatrix} \Sigma^{\mathrm{R}} & \Sigma^{\mathrm{K}} \\ 0 & \Sigma^{\mathrm{A}}\end{pmatrix} &= B^{-1}\begin{pmatrix} \Sigma^{--} & \Sigma^{-+} \\ \Sigma^{+-} & \Sigma^{++}\end{pmatrix}A^{-1},\end{aligned} \tag{4.1.23}$$

decouples two Green's functions (retarded and advanced) completely from the other ones and reduces the total number of Green's functions to be calculated by one. The simpler Dyson equation takes the form

$$G^{\mathrm{R}} = G_0^{\mathrm{R}} + G_0^{\mathrm{R}}\Sigma^{\mathrm{R}}G^{\mathrm{R}}\ ,\ , \tag{4.1.24}$$

$$G^{\mathrm{K}} = G_0^{\mathrm{K}} + G_0^{\mathrm{R}}\Sigma^{\mathrm{R}}G^{\mathrm{K}} + G_0^{\mathrm{R}}\Sigma^{\mathrm{K}}G^{\mathrm{A}} + G_0^{\mathrm{K}}\Sigma^{\mathrm{A}}G^{\mathrm{A}}\ ,\ , \tag{4.1.25}$$

$$G^{\mathrm{A}} = G_0^{\mathrm{A}} + G_0^{\mathrm{A}}\Sigma^{\mathrm{A}}G^{\mathrm{A}}. \tag{4.1.26}$$

Therefore usually it is easier to work within the basis of retarded, Keldysh and advanced Green's function (RKA-basis)

$$\text{retarded}: \quad G^{\mathrm{R}}_{k,k'}(t,t') = -i\Theta(t-t')\left\langle\left[c_k[t]_H, c^\dagger_{k'}[t']_H\right]_{-\zeta}\right\rangle_\rho \tag{4.1.27}$$

$$\text{Keldysh}: \quad G^{\mathrm{K}}_{k,k'}(t,t') = -i\left\langle\left[c_k[t]_H, c^\dagger_{k'}[t']_H\right]_{\zeta}\right\rangle_\rho \tag{4.1.28}$$

$$\text{advanced}: \quad G^{\mathrm{A}}_{k,k'}(t,t') = i\Theta(t'-t)\left\langle\left[c_k[t]_H, c^\dagger_{k'}[t']_H\right]_{-\zeta}\right\rangle_\rho, \tag{4.1.29}$$

rather than in the $(+-)$-basis introduced earlier. For the non-equilibrium steady-state the Dyson equation of the retarded and advanced Green's function can be rewritten explicitly (as in the equilibrium case) as

$$G^{\mathrm{R/A}}(\omega) = \frac{1}{\left[G_0^{\mathrm{R/A}}(\omega)\right]^{-1} - \Sigma^{\mathrm{R/A}}(\omega)}. \tag{4.1.30}$$

Also the Keldysh part can then be brought into the more convenient form

$$G^{\mathrm{K}}(\omega) = G^{\mathrm{R}}(\omega)\Sigma^{\mathrm{K}}(\omega)G^{\mathrm{A}}(\omega)\,, \tag{4.1.31}$$

as long as the assumption of an initial-state independent steady-state remains true. If the transient dynamics are kept and thus t instead of ω is included in the multi-index, retarded and advanced Green's function are given by integral equations (Volterra equation of the second type) given in Eqs. (4.1.24) and (4.1.26). The Keldysh Green's function can again be simplified to [Ken11]

$$G^{\mathrm{K}}(t,t') = -iG^{\mathrm{R}}(t,0)(1+2\zeta\bar{n})G^{\mathrm{A}}(0,t') + (G^{\mathrm{R}}\Sigma^{\mathrm{K}}G^{\mathrm{A}})(t,t'), \tag{4.1.32}$$

where $\bar{n}$ is the matrix with entries $\bar{n}_{k_1k_2} = \mathrm{Tr}\left[d^\dagger_{k_2}d_{k_1}\rho\right]$. This reduces its determination from a Volterra equation of the second type to a simple integral, with known integrand.

So far, we considered bosonic or fermionic degrees of freedom everywhere. For the sake of simplicity, and because this is the only case of relevance later on, we focus in the remaining part on fermions only. A generalization to bosons however is easily possible.

4.1.2 Non-Interacting Green's Function: An Exact Starting Point

Closed Systems

If we – for the time being – forget about the two-particle interaction U in (4.1.1), we can evaluate the corresponding Green's functions explicitly. To this end let us first consider the diagonal non-interacting Hamiltonian

$$H_0 = \sum_k \epsilon_k c^\dagger_k c_k. \tag{4.1.33}$$

In the Heisenberg picture creation and annihilation operators then take the simple form

$$c^{(\dagger)}_k[t]_{H_0} = \left(e^{-i\epsilon_k(t-t_0)}\right)^{(*)} c^{(\dagger)}_k, \tag{4.1.34}$$

which gives the non-interacting Green's functions

$$G^{\mathrm{R}}_{k,k'}(t,t') = -ie^{-i\epsilon_k(t-t')}\Theta(t-t')\delta_{k,k'} = \left[G^{\mathrm{A}}_{k',k}(t',t)\right]^*\,, \tag{4.1.35}$$

$$G^{\mathrm{K}}_{k,k'}(t,t') = -ie^{-i\epsilon_k(t-t_0)}e^{i\epsilon_{k'}(t'-t_0)}\left(\delta_{k,k'} - 2\left\langle c^\dagger_{k'}c_k\right\rangle_\rho\right). \tag{4.1.36}$$

From this the corresponding expressions in an arbitrary (non-diagonal) single-particle basis $H_0 = \sum_{k,k'}\epsilon_{k,k'}c^\dagger_k c_{k'}$ can be deduced by a simple rotation in the single-particle space. In an equilibrium or steady-state analysis these expressions Fourier transform to

$$G^{\mathrm{eq}}_{k,k'}(i\omega) = \left[\frac{1}{i\omega-\mu-\epsilon}\right]_{k,k'}\,,\quad G^{\mathrm{R}}_{k,k'}(\omega) = \left[\frac{1}{\omega-\epsilon+i\eta}\right]_{k,k'} = \left[G^{\mathrm{A}}_{k',k}(\omega)\right]^*, \tag{4.1.37}$$

with ϵ being a matrix with entries $\epsilon_{k,k'}$ and where we had to introduce some infinitesimal η (convergence factor) to perform the Fourier transform. For G^{K} the Fourier transform cannot be given, because in general it does not depend on time differences only. This is reminiscent of the fact that closed finite systems generally do not equilibrate to a steady-state for any time. If however we assume an (uncorrelated) initial density ρ such that $\left\langle c^\dagger_{k'}c_k\right\rangle_\rho = \delta_{k,k'}n_k$ is diagonal in k,k' (system already equilibrated at t_0), a Fourier transform yields

$$G^{\mathrm{K}}_{k,k'}(\omega) = 2\pi i\delta(\omega-\epsilon_k)\delta_{k,k'}(1-2n_k)\,. \tag{4.1.38}$$

This assumption is trivially true for initial density matrices given by a grand canonical density matrix to the same Hamiltonian under which the time evolution is performed (and $[H_0,N]=0$), with $n_k = f(\epsilon_k)$ and f being the Fermi function

$$f(\epsilon) = \frac{1}{e^{\beta(\epsilon-\mu)}+1}. \tag{4.1.39}$$

Open Systems

So far we have considered an isolated system. It is an distinct advantage of the Green's function framework that also open quantum system, i.e. of infinite size, can be treated explicitly. To this end let us generalize our Hamiltonian (4.1.1) by adding a reservoir and tunnelling term to it

$$H = H_0 + U + H_{\text{res}} + H_{\text{tun}}. \tag{4.1.40}$$

The reservoir is described by an arbitrary number of non-interacting[11] leads (index α) of unspecified dimensions, which are fully characterised by the dispersion $\epsilon_{\alpha,i}$

$$H_{\text{res}} = \sum_{\alpha,i} \epsilon_{\alpha,i} c^\dagger_{\alpha,i} c_{\alpha,i}. \tag{4.1.41}$$

The tunnelling which connects the leads to the system under consideration reads

$$H_{\text{tun}} = \sum_{\alpha,i,k} t_{\alpha,i,k} c^\dagger_{\alpha,i} c_k + \text{H.c.} \quad . \tag{4.1.42}$$

We have not included a direct link between the different reservoirs, which would render what follows slightly more complicated. Whenever we are treating open systems in non-equilibrium, we will assume a product form $\rho(0) = \rho_0 \prod_\alpha \rho_{\text{res},\alpha}$ for the initial density matrix in the following. Here $\rho_{\text{res},\alpha}$ is the grand canonical density matrix (characterized by temperature T_α and chemical potential μ_α) of reservoir α and ρ_0 the initial (uncorrelated) density matrix of the system described by $H_0 + U$.

Again focussing on $U = 0$ for now [12] we can incorporate the (non-interacting) reservoirs exactly, by integrating out those degrees of freedom[13]. To perform this task one can, e.g., employ the projection technique based on [Tay72]. First, we divide the full system into the local part (described by H_0) and the reservoirs (given by H_{res}). The influence of the remaining tunnelling term H_{tun}, describing how the two are connected, can be put in terms of a one-particle irreducible self-energy Σ. The general Dyson equation (leaving implicit single-particle indices, times or frequencies as well as possibly the Keldysh indices) reads

$$1G1 = 1G_0 1 + 1G_0 1\, 1\Sigma 1\, 1G1, \tag{4.1.43}$$

where we have introduces identities, which in a subsequent step can be rewritten as sums over projectors $1 = P + Q$ onto the local system (P) and the reservoirs (Q). Carrying out the partial trace over Q yields

$$G_{PP} = G^0_{PP} + G^0_{PP}\Sigma_{PP}G_{PP} + G^0_{PP}\Sigma_{PQ}G_{QP}\ , \tag{4.1.44}$$

$$G_{QP} = G^0_{QQ}\Sigma_{QP}G_{PP}, \tag{4.1.45}$$

because $G^0_{PQ} = G^0_{QP} = \Sigma_{QQ} = 0$. The indices P or Q denote that the single-particle indices are supported on the part of the system projected on by P or Q respectively. In the current set up ($U = 0$), actually also $\Sigma_{PP} = 0$, but as a finite value will be introduced by incorporating the interaction, we keep this term explicit at this point to reuse this result later on. Existence of inversion with respect to all implicit indices assumed[14], we can solve for the Green's function of the local system of interest

$$G_{PP} = \left[(G^0_{PP})^{-1} - \Sigma_{PQ}G^0_{QQ}\Sigma_{QP} - \Sigma_{PP}\right]^{-1}. \tag{4.1.46}$$

The term $-\Sigma_{PQ}G^0_{QQ}\Sigma_{QP}$ describes the changes induces due to the presence of the reservoirs, and if one defines the sum $\left[G^0_{PP})^{-1} - \Sigma_{PQ}G^0_{QQ}\Sigma_{QP}\right]^{-1}$ as a novel non-interacting Green's function we recover an effective Dyson equation for the local system only. This Dyson equation is formally

[11] ...,in the case of fermions, Fermi Liquid,...

[12] finite U will be treated using the FRG approach later on (see section 4.3).

[13] as one is usually not interested in observables local to the reservoirs, loosing the explicit handle on those degrees of freedom is unimportant.

[14] In time space this is tricky, see [Ken11] and (for an explicit application) chapter 7.

invariant to Eq. (4.1.10), but now is set up with the still non-interacting, but *reservoir dressed* Green's functions. Starting from those reservoir dressed Green's functions (GF) the FRG can be set up to additionally treat interactions supported fully on the local system in terms of Σ_{PP}. To this end we employ the terminology

decoupled, non-interacting local GF ($H = H_0$):
$$(g)_{PP} = G^0_{PP} \ ,$$

decoupled, non-interacting reservoir GF ($H = H_{\text{res}}$):
$$(g_{\text{res}})_{QQ} = G^0_{QQ} \ ,$$

reservoir dressed, non-interacting local GF ($H = H(U = 0)$):
$$(G^0)_{PP} = \left\{ [(g)_{PP}]^{-1} - \Sigma_{PQ}(g_{\text{res}})_{QQ}\Sigma_{QP} \right\}^{-1} \ ,$$

full (reservoir dressed, interacting) local GF ($H = H(U)$):
$$(G)_{PP} = \left\{ [(g)_{PP}]^{-1} - \Sigma_{PQ}(g_{\text{res}})_{QQ}\Sigma_{QP} - \Sigma_{PP} \right\}^{-1} \ ,$$

in the following. Also we will denote the part $-\Sigma_{PQ}(g_{\text{res}})_{QQ}\Sigma_{QP}$ and Σ_{PP} (to incorporate finite U with FRG) as reservoirs self-energy Σ_{res} and as two-particle interaction induced self-energy (Σ) respectively.

To be more explicit on how to calculate the reservoir dressed, non-interacting Green's functions, which constitute the exact starting point of our FRG treatment of open systems, we need to find the reservoir self-energy. Generally, the reservoir self-energy can be calculated by

$$[\Sigma^{\text{eq}}_{\text{res}}]_{k,k'} = \sum_{\alpha,i,i',k,k'} t^*_{\alpha,i,k} \, [g^{\text{eq}}_{\text{res}}]_{\alpha,i,i'} \, t_{\alpha,i',k'} \ , \tag{4.1.47}$$

$$\begin{pmatrix} [\Sigma^{\text{R}}_{\text{res}}]_{k,k'} & [\Sigma^{\text{K}}_{\text{res}}]_{k,k'} \\ 0 & [\Sigma^{\text{A}}_{\text{res}}]_{k,k'} \end{pmatrix} = \sum_{\alpha,i,i',k,k'} t^*_{\alpha,i,k} \begin{pmatrix} [g^{\text{R}}_{\text{res}}]_{\alpha,i,i'} & [g^{\text{K}}_{\text{res}}]_{\alpha,i,i'} \\ 0 & [g^{\text{A}}_{\text{res}}]_{\alpha,i,i'} \end{pmatrix} t_{\alpha,i',k'} . \tag{4.1.48}$$

From Tight-Binding Chains as Reservoirs...

If we assume the reservoirs to be given by several ($H_{\text{res}} = \sum_\alpha H_{\text{res},\alpha}$) one-dimensional tight-binding chains each described by

$$H_{\text{res},\alpha} = -\tau_\alpha \sum_{n=0}^{\infty} c^\dagger_n c_{n+1} + \text{H.c.} \quad , \tag{4.1.49}$$

we can proceed analytically. If we are interested in coupling the local system solely to the site $n = 0$ where the chain terminates, we are only in need of the "boundary" Green's functions $g_{\text{res}} = (g_{\text{res}})_{n=0,n=0}$. As shown in [Jak09] we arrive at

$$g^{\text{R}}_{\text{res},\alpha}(\omega) = \frac{1}{2\tau_\alpha^2} \left\{ \begin{array}{ll} -\text{sign}(\omega)\sqrt{\omega^2 - 4\tau_\alpha^2} & |\omega| > 2\tau_\alpha \\ \omega - i\sqrt{4\tau_\alpha^2 - \omega^2} & |\omega| \leq 2\tau_\alpha \end{array} \right\} = \left[g^{\text{A}}_{\text{res},\alpha}(\omega) \right]^* \ , \tag{4.1.50}$$

$$g^{\text{K}}_{\text{res},\alpha}(\omega) = [1 - 2f_\alpha(\omega)] \left[g^{\text{R}}_{\text{res},\alpha}(\omega) - g^{\text{A}}_{\text{res},\alpha}(\omega) \right] \ , \tag{4.1.51}$$

$$g^{\text{eq}}_{\text{res},\alpha}(i\omega) = \frac{1}{2\tau_\alpha^2} \left[i\omega + \mu - i\text{sign}(\omega)\sqrt{4\tau_\alpha^2 + \omega^2} \right] \ , \tag{4.1.52}$$

where we have concentrated on the case of real or imaginary frequencies only, because the isolated reservoirs are always in equilibrium initially. When dealing with reservoirs (or open systems in general) one frequently encounters a characterization of the reservoirs in terms of their *density of states* $\rho_{\text{res}}(\omega)$ instead of their Green's functions. The former determines the latter uniquely

by [Neg88]

$$g^{\mathrm{R/A}}_{\mathrm{res},\alpha}(\omega) = \mp i\pi\rho_{\mathrm{res},\alpha}(\omega) + \fint \frac{\rho_{\mathrm{res},\alpha}(\omega')}{\omega-\omega'}d\omega' \,, \tag{4.1.53}$$

$$g^{\mathrm{eq}}_{\mathrm{res},\alpha}(i\omega) = \int \frac{\rho_{\mathrm{res},\alpha}(\omega')}{i\omega-\omega'}d\omega'. \tag{4.1.54}$$

$$\tag{4.1.55}$$

In the case of a tight-binding chain, the boundary density of states thus reads

$$\rho_{\mathrm{res},\alpha}(\omega) = \frac{1}{2\pi\tau_\alpha^2}\sqrt{4\tau_\alpha^2-\omega^2}\Theta(2\tau_\alpha-|\omega|). \tag{4.1.56}$$

... to the Wide-Band Limit

The most important case however, is the one, where the details of the reservoirs (i.e. their band structure) are unimportant to the physics under scrutiny. We can investigate this important set up as a limit of the tight-binding chains as reservoirs. If we couple the first site of reservoir α to the site i of the local system by amplitude $t_{\alpha,i}$ we perform the limit $\tau_\alpha \to \infty$ (bandwidth becomes infinitely large), such that the ratio of any $\Gamma_{\alpha,i,i'} = t_{\alpha,i}t^*_{\alpha,i}/\tau_\alpha$ remains constant. In this limit the details of the band disappear, while physical quantities remain well defined and characterized by the hybridization $\Gamma_{\alpha,i,i'}$. The reservoir Green's functions then simplify to

$$g^{\mathrm{R}}_{\mathrm{res},\alpha}(\omega) = -i/\tau_\alpha = -i\pi\rho_{\mathrm{res}} = \left[g^{\mathrm{A}}_{\mathrm{res},\alpha}(\omega)\right]^* \,, \tag{4.1.57}$$

$$g^{\mathrm{K}}_{\mathrm{res},\alpha}(\omega) = [1-2f_\alpha(\omega)]\left[g^{\mathrm{R}}_{\mathrm{res},\alpha}(\omega) - g^{\mathrm{A}}_{\mathrm{res},\alpha}(\omega)\right] \,, \tag{4.1.58}$$

$$g^{\mathrm{eq}}_{\mathrm{res},\alpha}(i\omega) = -i/\tau_\alpha \mathrm{sign}(\omega), \tag{4.1.59}$$

where the (vanishing) density of states is now indeed a constant $\rho_{\mathrm{res}} = 1/(\pi\tau_\alpha)$. It is only for this prominent case, where the explicit time dependent problem can be solved efficiently (details see [Ken11] and chapter 7). The corresponding equations in real-time space read

$$g^{\mathrm{R}}_{\mathrm{res},\alpha}(t,t') = -i/\tau_\alpha \delta(t-t') \,, \tag{4.1.60}$$

$$g^{\mathrm{K}}_{\mathrm{res},\alpha}(t,t') = -1/\tau_\alpha T_\alpha \exp(-i\mu_\alpha(t'-t))\sum_{\pm}\frac{1}{\sinh[\pi T_\alpha(t'-t\pm i\delta)]}, \tag{4.1.61}$$

with an infinitesimally small chosen δ and μ_α and T_α the chemical potential and temperature, respectively. For the derivation of Eq. (4.1.61) we exploited the expansion

$$1-2f_\alpha(\epsilon_{k_\alpha}) = -2T_\alpha\sum_{\omega_m}\frac{1}{i\omega_m-\epsilon_{k_\alpha}+\mu_\alpha} \,, \tag{4.1.62}$$

where the fermionic Matsubara frequencies ω_m are the odd multiples of πT_α, and the series is to be evaluated as a principal value for $|\omega_m| \to \infty$. To obtain the self-energy contribution from these expressions, one just has to multiply the Green's function by the corresponding couplings $t_{\alpha,i}t^*_{\alpha,i'}$, the reservoir self-energies are thus just given by replacing $1/\tau_\alpha \to \Gamma_{\alpha,i,i'}$ everywhere in $g^X_{\mathrm{res},\alpha}$ above.

4.1.3 From Green's Function to Observables

We are usually not interested in the Green's functions themselves, but rather in some physical observables, which can be deduced from them.

Occupancy

The occupancy of the single-particle level labelled by k is nothing but (modulo some trivial prefactor) the corresponding lesser Green's function

$$n_k(t) = \left\langle c_k^\dagger[t]c_k[t]\right\rangle_{\rho_{t_0}} = \frac{1}{i}G^{-+}_{kk}(t,t). \tag{4.1.63}$$

Rotating to the 'RKA'-basis this can be reformulated by

$$G^{-+}_{kk}(t,t) = \lim_{\eta\to 0^+} \frac{1}{2}\left[-G^{\mathrm{R}}_{kk}(t,t-\eta) + G^{\mathrm{K}}_{kk}(t,t-\eta)\right] \tag{4.1.64}$$

$$= \lim_{\eta\to 0^+} \frac{1}{2}\left[G^{\mathrm{A}}_{kk}(t,t+\eta) + G^{\mathrm{K}}_{kk}(t,t+\eta)\right], \tag{4.1.65}$$

where we have to perform $\eta \to 0$ to retrieve the correct boundary conditions.

In a steady-state formulation ($t_0 \to -\infty$) the analogous expression reads

$$n_j = \frac{1}{2\pi}\int_{-\infty}^{\infty} e^{-i\omega t - |\omega|\eta}\frac{1}{i}G^{-+}_{jj}(\omega)d\omega\Big|_{t=0} = \frac{1}{2\pi i}\int_{-\infty}^{\infty} e^{-|\omega|\eta}G^{-+}_{jj}(\omega)d\omega. \tag{4.1.66}$$

Charge Current

Another physical observable of interest is the charge current, which can be calculated following the ideas presented in [Mei92, Kar10a]. For the following we divide the total system in real space into "two reservoirs" $\alpha = \mathrm{L/R}$ and a "central region". This assignment then defines where in space the current is calculated. For open systems this division is always chosen by the definition of the model (compare section 4.1.2). Only a single level (labelled $\mathrm{L},1$ and $\mathrm{R},1$) of each "reservoir" is assumed to be coupled to a, in general different, single level of the central region via hoppings $T_{\mathrm{L/R}}$. We label the two levels which are coupled to the reservoirs by 1 and N, respectively. The current leaving one of the reservoirs is then given by the change of particles in it

$$J_{\mathrm{L/R}}(t) = \mp\partial_t n_{\mathrm{L/R}}(t),. \tag{4.1.67}$$

We concentrate on J_{L} in the following, but J_{R} follows analogously. To reformulate equation (4.1.67) such that it contains only Green's functions one considers

$$J_{\mathrm{L}}(t) = -i\left\langle[H(t), n_{\mathrm{L}}]\,[t]\right\rangle_{\rho_{t_0}} = -iT^*_{\mathrm{L}}\left\langle\left[c^\dagger_1 c_{\mathrm{L},1}, c^\dagger_{\mathrm{L},1}c_{\mathrm{L},1}\right][t] - \mathrm{h.c.}\right\rangle_{\rho_{t_0}} = -T^*_{\mathrm{L}}G^{-+}_{\mathrm{L},1;1}(t,t) + \mathrm{c.c.}, \tag{4.1.68}$$

which holds as long as the interaction term of the Hamiltonian fulfils $[U, n_{\mathrm{L}}] = 0$. This expressions involves a full Green's function being non-local with respect to the central region. For open systems (non-interacting reservoirs integrated out) it is necessary to employ the projection technique once more to recast the current to

$$\begin{aligned} J_{\mathrm{L}}(t) &= -T^*_{\mathrm{L}}\int_{t_0}^{\infty}\begin{pmatrix} g^{--}_{\mathrm{res,L}}(t,t') & g^{-+}_{\mathrm{res,L}}(t,t') \\ g^{+-}_{\mathrm{res,L}}(t,t') & g^{++}_{\mathrm{res,L}}(t,t')\end{pmatrix}\begin{pmatrix} T_{\mathrm{L}} & 0 \\ 0 & -T_{\mathrm{L}}\end{pmatrix}\begin{pmatrix} G^{--}_{11}(t',t) & G^{-+}_{11}(t',t) \\ G^{+-}_{11}(t',t) & G^{++}_{11}(t',t)\end{pmatrix}\Bigg|_{-+} dt' + \mathrm{c.c.} \\ &= -|T_{\mathrm{L}}|^2\int_{t_0}^{\infty}\left[g^{--}_{\mathrm{res,L}}(t,t')G^{-+}_{11}(t',t) - g^{-+}_{\mathrm{res,L}}(t,t')G^{++}_{11}(t',t)\right]dt' + \mathrm{c.c.} \\ &= -|T_{\mathrm{L}}|^2\int_{t_0}^{\infty}\left[g^{\mathrm{R}}_{\mathrm{res,L}}(t,t')G^{-+}_{11}(t',t) + g^{-+}_{\mathrm{res,L}}(t,t')G^{\mathrm{A}}_{11}(t',t)\right]dt' + \mathrm{c.c.}\quad. \end{aligned} \tag{4.1.69}$$

This form includes full Green's functions of the central system only as well as known functions $g^{-+}_{\mathrm{res,L}}$ and $g^{\mathrm{R}}_{\mathrm{res,L}}$. Explicitly in the wide-band limit one finds

$$|T_L|^2 g^{\mathrm{R}}_{\mathrm{res},L}(t,t')_{i,j} = -i\Gamma_{\mathrm{L}}\delta(t-t'), \tag{4.1.70}$$

$$|T_L|^2 g^{-+}_{\mathrm{res},L}(t,t')_{i,j} = -\frac{\Gamma_{\mathrm{L}}}{2}\left(\frac{1}{\beta_L}e^{-i\mu_L(t-t')}\sum_{\pm}\frac{1}{\sinh\left(\frac{\pi(t-t'\pm i\delta)}{\beta_L}\right)} - i\delta(t-t')\right), \tag{4.1.71}$$

and thus that in (4.1.69) again (as for the occupancy) only the equal-time Keldysh Green's function of the central region is needed.

For the steady-state we can transform (4.1.69) to frequency space

$$\begin{aligned} J_{\mathrm{L}} &= -\frac{|T_{\mathrm{L}}|^2}{2\pi}\int_{-\infty}^{\infty}\left[g^{\mathrm{R}}_{\mathrm{res,L}}(\omega)G^{-+}_{11}(\omega)+g^{-+}_{\mathrm{res,L}}(\omega)G^{\mathrm{A}}_{11}(\omega)+\mathrm{c.c.}\right]d\omega \\ &= i|T_{\mathrm{L}}|^2\int_{-\infty}^{\infty}\rho_{\mathrm{res,L}}(\omega)\left\{G^{-+}_{11}(\omega)+f_{\mathrm{L}}(\omega)\left[G^{\mathrm{R}}_{11}(\omega)-G^{\mathrm{A}}_{11}(\omega)\right]\right\}d\omega. \end{aligned} \tag{4.1.72}$$

For the last equality we have anticipated some symmetry relations explicitly given in section 4.5. In the case of a single impurity ($1 = N$) and symmetric reservoir spectral functions $a|T_{\mathrm{L}}|^2\rho_{\mathrm{res,L}}(\omega) = |T_{\mathrm{R}}|^2\rho_{\mathrm{res,R}}(\omega)$ this equation can be further simplified to the famous form [Mei92]

$$J_{\mathrm{L}} = 2\pi|T_{\mathrm{L}}|^2\frac{a}{1+a}\int\rho_{\mathrm{res,L}}(\omega)\left[f_{\mathrm{L}}(\omega)-f_{\mathrm{R}}(\omega)\right]\rho_{11}(\omega)\,d\omega\ . \tag{4.1.73}$$

with the impurity's spectral function $\rho_{11}(\omega) = -1/\pi\mathrm{Im}\left[G^{\mathrm{R}}_{11}(\omega)\right]$.

Heat Current

The heat current is slightly more complicated and as we could not find an analogue calculation to the one for the charge current presented above in the literature[15], we will give more details here. Again we separate our system in a left, central and right part. We aim at the change in energy of the left reservoir

$$\begin{aligned} Q_{\mathrm{L}}(t) &= -i\left\langle[H(t),H_{\mathrm{L}}]\,[t]\right\rangle_{\rho_{t_0}} = -i\sum_i T^*_{\mathrm{L},i}\epsilon_{\mathrm{L},i}\left\langle\left[c_1^\dagger c_{\mathrm{L},i},c^\dagger_{\mathrm{L},i}c_{\mathrm{L},i}\right][t]-\mathrm{H.c.}\right\rangle_{\rho_{t_0}} \\ &= -\sum_i T^*_{\mathrm{L},i}\epsilon_{\mathrm{L},i}G^{-+}_{\mathrm{L},i;1}(t,t)+\mathrm{c.c.}, \end{aligned} \tag{4.1.74}$$

where we have again concentrated on the reservoir being coupled to a single level of the central region only (labelled 1) and have used the eigenbasis of the left lead i. As above we employ the projection technique to rewrite the expression in terms of full Green's functions of the central region

$$\begin{aligned} Q_{\mathrm{L}}(t) &= -\sum_i T^*_{\mathrm{L},i}\epsilon_{\mathrm{L},i}\int_{t_0}^{\infty}\begin{pmatrix} g^{--}_{\mathrm{res,L},i}(t,t') & g^{-+}_{\mathrm{res,L},i}(t,t') \\ g^{+-}_{\mathrm{res,L},i}(t,t') & g^{++}_{\mathrm{res,L},i}(t,t')\end{pmatrix}\begin{pmatrix} T_{\mathrm{L},i} & 0 \\ 0 & -T_{\mathrm{L},i}\end{pmatrix} \\ &\qquad\times\begin{pmatrix} G^{--}_{11}(t',t) & G^{-+}_{11}(t',t) \\ G^{+-}_{11}(t',t) & G^{++}_{11}(t',t)\end{pmatrix}\Bigg|_{-+}dt'+\mathrm{c.c.} \\ &= -\sum_i|T_{\mathrm{L},i}|^2\epsilon_{\mathrm{L},i}\int_{t_0}^{\infty}\left[g^{--}_{\mathrm{res,L},i}(t,t')G^{-+}_{11}(t',t)-g^{-+}_{\mathrm{res,L},i}(t,t')G^{++}_{11}(t',t)\right]dt'+\mathrm{c.c.} \\ &= -\sum_i|T_{\mathrm{L},i}|^2\epsilon_{\mathrm{L},i}\int_{t_0}^{\infty}\left[g^{\mathrm{R}}_{\mathrm{res,L},i}(t,t')G^{-+}_{11}(t',t)+g^{-+}_{\mathrm{res,L},i}(t,t')G^{\mathrm{A}}_{11}(t',t)\right]dt'+\mathrm{c.c.}\quad. \end{aligned} \tag{4.1.75}$$

The term $\epsilon_{\mathrm{L},i}$ in $\sum_i|T_{\mathrm{L},i}|^2\epsilon_{\mathrm{L},i}g^{X}_{\mathrm{res,L},i}(t,t')$ prohibits a simple resumation in terms of a self-energy (as it was possible for the charge current). Luckily there is a way around this, by considering the differential form of the Dyson equation [Ken11]. For the retarded and lesser Green's functions of the non-interacting reservoirs it reads

$$i\frac{\partial}{\partial t}g^{\mathrm{R}}_{\mathrm{res,L},i}(t,t') = \epsilon_{\mathrm{L},i}g^{\mathrm{R}}_{\mathrm{res,L},i}(t,t')+\delta(t-t')\,, \tag{4.1.76}$$

$$i\frac{\partial}{\partial t}g^{-+}_{\mathrm{res,L},i}(t,t') = \epsilon_{\mathrm{L},i}g^{-+}_{\mathrm{res,L},i}(t,t'). \tag{4.1.77}$$

[15] Note however that there has been work in a very similar direction [Wan06, Oja08].

Therefore we find

$$Q_{\mathrm{L}}(t) = -\int_{t_0}^{\infty} \left\{ \left[i\frac{\partial}{\partial t}\Sigma^{\mathrm{R}}_{\mathrm{res,L}}(t,t') \right] G_{11}^{-+}(t',t) + \left[i\frac{\partial}{\partial t}\Sigma^{-+}_{\mathrm{res,L}}(t,t') \right] G^{\mathrm{A}}_{11}(t',t) \right\} dt' + \text{c.c.} \quad , \tag{4.1.78}$$

where the delta-function contribution of Eq. (4.1.76) vanishes with the corresponding part of the +c.c. term.

The Fourier transform for the steady-state trivially reads ($\frac{\partial}{\partial t} \to -i\omega$)

$$Q_{\mathrm{L}} = -\frac{1}{2\pi}\int_{-\infty}^{\infty} \omega \left[\Sigma^{\mathrm{R}}_{\mathrm{res,L}}(\omega) G_{11}^{-+}(\omega) + \Sigma^{-+}_{\mathrm{res,L}}(\omega) G^{\mathrm{A}}_{11}(\omega) + \text{c.c.} \right] d\omega \ . \tag{4.1.79}$$

Generally, in the steady-state we thus recapture all formulas for the charge current with $\int d\omega \to \int d\omega\, \omega$. Especially, for the single impurity case coupled to symmetric reservoirs (see above) we find

$$Q_{\mathrm{L}} = 2\pi |T_{\mathrm{L}}|^2 \frac{a}{1+a} \int \omega \rho_{\mathrm{res,L}}(\omega) \left[f_{\mathrm{L}}(\omega) - f_{\mathrm{R}}(\omega) \right] \rho_{11}(\omega)\, d\omega \ . \tag{4.1.80}$$

As we aim at the *heat* current one must subtract the "particle part" of the energy transported and thus consider

$$H_\alpha = Q_\alpha - \mu_\alpha J_\alpha . \tag{4.1.81}$$

Linear Conductances

In the context of thermoelectric transport ($\to$ section 8) we will consider the four linear response coefficients given as the matrix elements of the matrix $\hat{G}$ in

$$\begin{pmatrix} J \\ H \end{pmatrix} = \hat{G} \begin{pmatrix} \Delta V \\ \Delta T \end{pmatrix} = \begin{pmatrix} G_{\mathrm{c},V} & G_{\mathrm{c},\Delta T} \\ G_{\mathrm{h},V} & G_{\mathrm{h},\Delta T} \end{pmatrix} \begin{pmatrix} \Delta V \\ \Delta T \end{pmatrix} . \tag{4.1.82}$$

Here $V/2 = \mu_L = -\mu_R$ and $\Delta T = T_L - T_R$ are infinitesimally small. The three independent (see chapter 8 for details) elements can be calculated for a single impurity by Eqs. (4.1.73) and (4.1.80) considering infinitesimal differences in chemical potential or temperature in the two reservoirs. A leading order expansion in $V, \Delta T$ yields

$$G_{\mathrm{c},V} = 2\pi |T_{\mathrm{L}}|^2 \frac{a}{1+a} \int \rho_{\mathrm{res,L}}(\omega)[-f'(\omega)]\rho_{11}(\omega)\, d\omega \ , \tag{4.1.83}$$

$$G_{\mathrm{c},\Delta T} = 2\pi |T_{\mathrm{L}}|^2 \frac{a}{1+a} \int \rho_{\mathrm{res,L}}(\omega) \frac{\omega}{T}[-f'(\omega)]\rho_{11}(\omega)\, d\omega = \frac{G_{\mathrm{h},V}}{T} \ , \tag{4.1.84}$$

$$G_{\mathrm{h},\Delta T} = 2\pi |T_{\mathrm{L}}|^2 \frac{a}{1+a} \int \rho_{\mathrm{res,L}}(\omega) \frac{\omega^2}{T}[-f'(\omega)]\rho_{11}(\omega)\, d\omega \ . \tag{4.1.85}$$

All conductances are thus determined by *transport integrals* of the type

$$I_n = 2\pi |T_{\mathrm{L}}|^2 \frac{a}{1+a} \int \rho_{\mathrm{res,L}}(\omega) \omega^n [-f'(\omega)]\rho_{11}(\omega)\, d\omega \ , \tag{4.1.86}$$

with $n \in \mathbb{N}_0$.

4.2 Generating Functionals

To set up the right framework to derive the FRG flow equations (in the next section) we recapitulate first how Green's functions can be deduced from generating functionals.

4.2.1 Functional Integral Representation of the Many-Body Problem

Before we can tackle the generating functionals of Green's functions themselves, we first must understand how one can translate the operator-based language underlying any quantum many-body problem to the of Grassmann (complex) fields. Following pioneering ideas of Feynman [Ste93] we aim first at reformulating the Green's functions given in Eq. (4.1.7) and (4.1.18) in terms of functionals [Hon10]. For fermions, for this cause the concept of Grassman variables needs to be introduced [Neg88]. A set of independent Grassmann variables are the collection of elements ψ_{k_i} following the algebra, containing the complex numbers x, in which the ψ_{k_i} pairwise anticommute, but on the other side commute with all x. Claiming that

$$[\psi_{k_1}, \psi_{k_2}]_+ = \left[\psi_{k_1}, \bar{\psi}_{k_2}\right]_+ = \left[\psi_{k_1}, c_{k_2}^{(\dagger)}\right]_+ = 0 \,, \tag{4.2.1}$$

holds for the Grassmann variables ψ_{k_i} and $\bar{\psi}_{k_i}$ allows to define fermionic *coherent states*

$$|\psi\rangle = |\psi_{k_1}, \psi_{k_2}, \dots\rangle = e^{-\sum_k \psi_k c_k^\dagger} |\mathrm{vac}\rangle \,, \tag{4.2.2}$$

$$\langle\psi| = \langle\psi_{k_1}, \psi_{k_2}, \dots| = \langle\mathrm{vac}| \, e^{-\sum_k c_k \bar{\psi}_k} . \tag{4.2.3}$$

These are called coherent (compare to harmonic oscillator), as they fulfil (with $\psi_k^2 = 0$)

$$c_k |\psi\rangle = \psi_k |\psi\rangle \,, \quad \langle\psi| c_k^\dagger = \langle\psi| \bar{\psi}_k, \quad \langle\psi|\phi\rangle = e^{\sum_k \bar{\psi}_k \phi_k} = 1 + \sum_k \bar{\psi}_k \phi_k . \tag{4.2.4}$$

In Fock space one additionally finds

$$1 = \int \prod_k d\bar{\psi}_k d\psi_k \, |\psi\rangle \langle\psi| \, e^{-\sum_k \bar{\psi}_k \psi_k} \,, \tag{4.2.5}$$

$$\mathrm{Tr} O = \int \prod_k d\bar{\psi}_k d\psi_k \, \langle -\psi| \, O \, |\psi\rangle \, e^{-\sum_k \bar{\psi}_k \psi_k} \,, \tag{4.2.6}$$

for the unity operator as well as the trace of an arbitrary operator O, by exploiting the Grassmann variables' algebra. Furthermore, 'Gaußian type integrals' are easily calculated [Kar10a] using

$$\int \prod_k d\bar{\psi}_k d\psi_k e^{-\sum_{k_1,k_2} \bar{\psi}_{k_1} O_{k_1,k_2} \psi_{k_2} + \sum_k \bar{\psi}_k \phi_k + \bar{\phi}_k \psi_k} = \det O \;\; e^{\sum_{k_1,k_2} \bar{\phi}_{k_1} \left[O^{-1}\right]_{k_1,k_2} \phi_{k_2}} . \tag{4.2.7}$$

To reformulate the Green's function there is only a single ingredient missing. This ingredient is the idea condensed in the simple Trotter decomposition [Neg88]

$$e^{-\lambda H} = \lim_{N\to\infty} \left(: e^{-\lambda H/N} : \right)^N \,, \tag{4.2.8}$$

which lies at heart of any functional approach. H is an arbitrary normal ordered Hamilton operator and $: A :$ denotes normal ordering of A. Placing unities as in Eq. (4.2.5) in between two adjacent exponentials, allows for turning the operators into ordinary variables (eigenvalues). This way an arbitrary real- or imaginary-time ($\lambda \in \mathbb{R}$ or $i\lambda \in \mathbb{R}$) evolution can be evaluated by integrals, which in the limit $N \to \infty$ turns to a functional integral. In the case where $U = 0$ those integrals are of 'Gaußian type', while for finite U an additional quartic term shows up. A perturbative approach can be set up right away by expanding the part of the exponential containing the interaction term in a simple Taylor series. We proceed by deriving a functional integral representation of the full Green's functions. We will start with the more complicated non-equilibrium Keldysh Green's functions, because then the simpler equilibrium case of the Matsubara Green's function follows quickly.

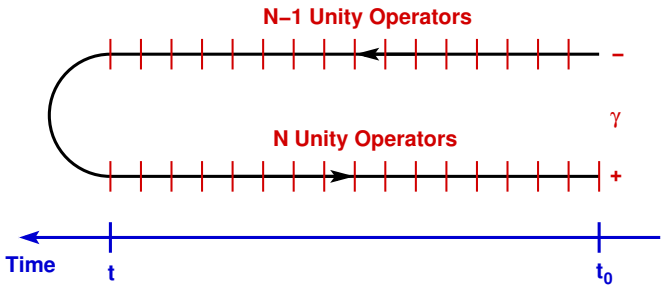


Figure 4.2.: Within the Trotter decomposition, the unity operators are inserted on the Keldysh contour as shown. $N-1$ operators are inserted on the upper and in total N unities are inserted on the lower part of the contour.

4.2.2 Functional Reformulating of the Keldysh Green's Functions

The starting point is Eq. (4.1.18), which we cast into

$$G^{\nu,\nu'}_{k,k'}(t,t') = -i\left\langle T_\gamma\, c^\nu_k[t] c^{\dagger\,\nu'}_{k'}[t']\right\rangle = -i\left\langle T_\gamma\, c^{\{t,\nu\}}_\alpha c^{\dagger\,\{t',\nu'\}}_{\alpha'}\, e^{-i\oint_\gamma d\tau H(\tau)}\right\rangle_{\rho_{t_0}}, \tag{4.2.9}$$

where the superscript $\{t,\nu\}$ is needed only to indicate the appropriate ordering. The integral

$$\oint_\gamma dt_i = \sum_{\nu=\pm}(-\nu)\int_{t_0}^{t} dt_i \;\Big|_{t_i\in\gamma_\nu}. \tag{4.2.10}$$

runs along the entire γ contour. The H in the integrand has no Keldysh index, as this is contained in the integral of Eq. (4.2.10), but is time-ordered appropriately by its τ argument. We define

$$c^{\max}_k = \begin{cases} c^{\{t,\nu\}}_k & \text{if } t_\nu >_\gamma t'_{\nu'} \\ -c^{\dagger\,\{t',\nu'\}}_{k'} & \text{if } t_\nu \leq_\gamma t'_{\nu'} \end{cases}, \qquad c^{\min} = \begin{cases} c^{\{t,\nu\}}_k & \text{if } t_\nu \leq_\gamma t'_{\nu'} \\ c^{\dagger\,\{t',\nu'\}}_{k'} & \text{if } t_\nu >_\gamma t'_{\nu'} \end{cases}, \tag{4.2.11}$$

$$t^{\max} = \begin{cases} t_\nu & \text{if } t_\nu >_\gamma t'_{\nu'} \\ t'_{\nu'} & \text{if } t_\nu \leq_\gamma t'_{\nu'} \end{cases}, \qquad t^{\min} = \begin{cases} t_\nu & \text{if } t_\nu \leq_\gamma t'_{\nu'} \\ t'_{\nu'} & \text{if } t_\nu >_\gamma t'_{\nu'} \end{cases}, \tag{4.2.12}$$

where we have introduced an ordering $>_\gamma$ or $<_\gamma$ with respect to the contour γ[16]. This turns (4.2.9) to

$$G^{\nu,\nu'}_{k,k'}(t,t') = -i\mathrm{Tr}\left[T_\gamma\, e^{-i\int_{t^{\max}}^{\{t_0,+\}} d\tau H(\tau)} c^{\max} T_\gamma\, e^{-i\int_{t^{\min}}^{t^{\max}} d\tau H(\tau)} c^{\min} T_\gamma\, e^{-i\int_{\{t_0,-\}}^{t^{\min}} d\tau H(\tau)} \rho^-_{t_0}\right]. \tag{4.2.13}$$

Using (4.2.6) yields

$$\begin{aligned} G^{\nu,\nu'}_{k,k'}(t,t') = -i\int\prod_{k''} d\bar\psi^-_{k'',0} d\psi^-_{k'',0} \left\langle -\psi^-_0\right| T_\gamma\, e^{-i\int_{t^{\max}}^{\{t_0,+\}} d\tau H(\tau)} c^{\max} T_\gamma\, e^{-i\int_{t^{\min}}^{t^{\max}} d\tau H(\tau)} c^{\min} \\ \times T_\gamma\, e^{-i\int_{\{t_0,-\}}^{t^{\min}} d\tau H(\tau)} \rho^-_{t_0} \left|\psi^-_0\right\rangle e^{-\sum_{k''}\bar\psi^-_{k'',0}\psi^-_{k'',0}}. \end{aligned} \tag{4.2.14}$$

Now we employ the above mentioned Trotter decomposition and insert in total $2N-1$ unity operators given as in Eq. (4.2.5). $N-1$ are inserted equidistantly on the upper and N on the lower part of the contour[17] (see Fig. 4.2). Ultimately we take the $N\to\infty$ limit. Now one can evaluate the Green's

[16] following the ordering established by T_γ.

[17] One unity operator less is inserted on the upper part, because the trace was evaluated to give the missing $\left|\psi^-_0\right\rangle$.

function to

$$G^{\nu,\nu'}_{k,k'}(t,t') = -i \lim_{N\to\infty} \int \prod_{n=0}^{N-1} \prod_{\nu''=\pm} \prod_{k''} d\bar{\psi}^{\nu''}_{k'',n} d\psi^{\nu''}_{k'',n} \psi^{\nu}_{k,n_t} \psi^{\nu'}_{k',n_{t'}} \left\langle \psi^-_1 \right| \rho^-_{t_0} \left| \psi^-_0 \right\rangle$$
$$\times \exp\left\{ -\sum_{n=1}^{N-1} \left[\sum_{k''} \bar{\psi}^-_{k'',n+1} \left(\psi^-_{k'',n+1} - \psi^-_{k'',n} \right) + i\Delta t \mathcal{H}\left(\left\{ \bar{\psi}^- \right\}_{n+1}, \left\{ \psi^- \right\}_n \right) \right] \right.$$
$$- \sum_{n=0}^{N-1} \left[\sum_{k''} \bar{\psi}^+_{k'',n+1} \left(\psi^+_{k'',n+1} - \psi^+_{k'',n} \right) - i\Delta t \mathcal{H}\left(\left\{ \bar{\psi}^+ \right\}_{n+1}, \left\{ \psi^+ \right\}_n \right) \right]$$
$$\left. - \sum_{k''} \bar{\psi}^-_{k'',1} \psi^-_{k'',1} + \sum_{k''} \bar{\psi}^+_{k'',N} \psi^+_{k'',N} - \sum_{k''} \bar{\psi}^-_{k'',0} \psi^-_{k'',0} \right\} , \tag{4.2.15}$$

with boundary conditions

$$\psi^-_N \equiv \psi^+_0 , \qquad \psi^+_N \equiv -\psi^-_0 . \tag{4.2.16}$$

We used explicitly that all operators involve an even number of creation and annihilation operators. The function $\mathcal{H}\left(\left\{ \bar{\psi}^\pm \right\}_{n+1}, \left\{ \psi^\pm \right\}_n \right)$ is defined by

$$\mathcal{H}\left(\left\{ \bar{\psi}^\pm \right\}_{n+1}, \left\{ \psi^\pm \right\}_n \right) = H(c^\dagger_k \to \bar{\psi}^\pm_{k,n+1}, c_k \to \psi^\pm_{k,n}). \tag{4.2.17}$$

Using[18] [Kar10a]

$$\begin{aligned}
\langle\psi|\,\rho\,|\psi'\rangle = \langle\psi|\, e^{\sum_{k''} \rho_{k''} c^\dagger_{k''} c_{k''}} \,|\psi'\rangle &= \langle\psi| \prod_{k''} \left[1 + \sum_{m=1}^{\infty} \frac{\rho^m_{k''}}{m!} \underbrace{(c^\dagger_{k''} c_{k''} \ldots c^\dagger_{k''} c_{k''})}_{\text{m-pairs}} \right] |\psi'\rangle \\
&= \langle\psi| \prod_{k''} \left[1 + \bar{\psi}_{k''} \psi'_{k''} \sum_{m=1}^{\infty} \frac{\rho^m_{k''}}{m!} \underbrace{(c_{k''} \ldots c^\dagger_{k''})}_{\overset{(*)}{\to} 1} \right] |\psi'\rangle \\
&= \langle\psi| \prod_{k''} \left[1 + e^{\rho_{k''}} \bar{\psi}_{k''} \psi'_{k''} - \bar{\psi}_{k''} \psi'_{k''} \right] |\psi'\rangle \\
&= \prod_{k''} \left[1 + e^{\rho_{k''}} \bar{\psi}_{k''} \psi'_{k''} - \bar{\psi}_{k''} \psi'_{k''} \right] \left(1 + \sum_{\tilde{k}''} \bar{\psi}_{\tilde{k}''} \psi'_{\tilde{k}''} \right) \\
&= e^{\sum_{k''} \exp(\rho_{k''}) \bar{\psi}_{k''} \psi'_{k''}} ,
\end{aligned} \tag{4.2.18}$$

which can be derived by employing $\psi^2_k = 0$, after permuting the first and last $c_{k''}$ and $c^\dagger_{k''}$ with their neighbor at $(*)$. One can recast the Green's functions[19] to the continuous representation

$$G^{\nu,\nu'}_{k,k'}(t,t') = -i \int \mathcal{D}\bar{\psi}\psi \psi^\nu_k(t) \bar{\psi}^{\nu'}_{k'}(t')$$
$$\times \exp\left\{ i \int_{t_0}^{\infty} d\tau \sum_{k_1 k_2} \sum_{p_1 p_2} \bar{\psi}^{\nu_1}_{k_1}(\tau+\eta) \left[\hat{G}_0(\tau,\tau)^{-1} \right]^{\nu_1,\nu_2}_{k_1,k_2} \psi^{\nu_2}_{k_2}(\tau) - iS_{\text{int}} \right\} . \tag{4.2.19}$$

Here, all quadratic contributions, those from $\mathcal{H}$ and from the initial density matrix $\exp(\rho_{k''})$, were condensed in $\hat{G}_0$. The remaining terms are included in S_{int}. Eq. (4.2.19) is again an ideal point for employing a perturbative expansion of the term containing S_{int} as all the rest then just amounts to

[18] Without loss of generality one can employ a rotation of the single-particle basis k'' such that the density matrix is diagonal.

[19] Once again, assuming an uncorrelated initial density matrix is vital at this point.

solving Gaußian integrals. This is the route to a diagramatic expansion, in which all prefactors as in Wick's theorem follow from the properties of the aforementioned Gaußian integrals. For the most relevant situation, where the Hamiltonian contains single- and two-particle terms only, S_{int} reads

$$S_{\text{int}} = \frac{1}{4} \sum\!\!\!\!\!\!\int_{1,2,1',2'} v^{\sigma}_{1,2,1',2'} \bar{\psi}_1 \bar{\psi}_2 \psi_{2'} \psi_{1'}, \tag{4.2.20}$$

with the multi-index $1 = \{t, k, \nu\}$ and the explicitly four-times dependent interaction

$$v^{\sigma}_{1,2,1',2'} = \delta(t_1 - t_1')\delta(t_1 - t_2)\delta(t_1 - t_2') \times v^{\sigma}_{\{k_1\nu_1\},\{k_2\nu_2\},\{k_1'\nu_1'\},\{k_2'\nu_2'\}}(t_1). \tag{4.2.21}$$

Time dependence is now hidden in the multi-index and derivation in the real-frequency (aiming at the steady-state) or real-time (aiming at transient dynamics) space can be presented in a single calculation[20]. From now on we use the shorthand notation

$$(\psi, \phi) = i \sum\!\!\!\!\!\!\int_{1} \psi_1 \phi_1 \ , \ (\bar{\psi}, X\psi) = \{i\} \sum_{12} \bar{\psi}_1 X_{12} \psi_2 \ , \tag{4.2.22}$$

$$S_0 = \left(\bar{\psi}, \left[\hat{G}_0\right]^{-1}, \psi\right) = i \sum\!\!\!\!\!\!\int_{1,2} \bar{\psi}_1 \left[\left[\hat{G}_0\right]^{-1}\right]_{1,2} \phi_2 \ , \tag{4.2.23}$$

where the bracketed $\{i\}$ is absent in the Matsubara case discussed later ($\rightarrow$ see section 4.2.3). A priori, the symbol defined by $\hat{G}_0$ must not somehow relate to the free Green's function G^0 defined above, but using (4.2.7) one shows for $S_{\text{int}} = 0$

$$\begin{aligned}
\left[G^0\right]^{\nu,\nu'}_{k,k'}(t,t') &= -i \int \mathcal{D}\bar{\psi}\psi \psi^{\nu}_{k}(t) \bar{\psi}^{\nu'}_{k'}(t') \exp\left\{ i \int_{t_0}^{\infty} d\tau \sum_{k_1 k_2} \sum_{\nu_1\nu_2} \bar{\psi}^{\nu_1}_{k_1}(\tau+\eta) \left[\hat{G}_0(\tau,\tau)^{-1}\right]^{\nu_1,\nu_2}_{k_1,k_2} \psi^{\nu_2}_{k_2}(\tau) \right\} \\
&= \left[\frac{\delta}{\delta \bar{\phi}^{\nu'}_{k'}(t')} \frac{\delta}{\delta \phi^{\nu}_{k}(t)} - i \int \mathcal{D}\bar{\psi}\psi \exp\left\{ i \int_{t_0}^{\infty} d\tau \sum_{k_1 k_2} \sum_{\nu_1\nu_2} \bar{\psi}^{\nu_1}_{k_1}(\tau+\eta) \left[\hat{G}_0(\tau,\tau)^{-1}\right]^{\nu_1,\nu_2}_{k_1,k_2} \psi^{\nu_2}_{k_2}(\tau) \right.\right. \\
&\quad \left.\left. + \int_{t_0}^{\infty} d\tau \sum_{k_1,\rho_1} \left[\bar{\psi}^{\nu_1}_{k_1}(\tau)\phi^{\nu_1}_{k_1}(\tau) + \bar{\phi}^{\nu_1}_{k_1}(\tau)\psi^{\nu_1}_{k_1}(\tau) \right] \right\} \right]_{\bar{\phi}=\phi=0} \\
&= \left[\hat{G}_0\right]^{\nu,\nu'}_{k,k'}(t,t').
\end{aligned} \tag{4.2.24}$$

This proves that, as our naming convention suggested all along, the two objects agree. Eq. (4.2.19) provides the representation of the Green's functions in terms of a functional we were searching for. As we have covered the more complicated Keldysh case rather extensively, we can now proceed with the Matsubara analogue rather quickly.

4.2.3 Functional Reformulating of the Matsubara Green's Functions

We perform analogous steps as above, but additionally consider the (finite temperature) partition function, as in contrast to the Keldysh case it is non-trivial in Matsubara space. To this end we can formulate

$$\begin{aligned}
Z &= \text{Tr}\left[e^{-\beta\tilde{H}}\right] \\
&= \lim_{N\to\infty} \int \prod_{n=0}^{N} \prod_{k} d\bar{\psi}_{k,n} d\psi_{k,n} \exp\left\{ -\sum_{n=0}^{N-1} \left[\sum_{k} \bar{\psi}_{k,n+1} \left(\psi_{k,n+1} - \psi_{k,n}\right) + \Delta\tau \mathcal{H}(\{\bar{\psi}_{n+1}\},\{\psi_n\}) \right] \right\} \\
&= \int \mathcal{D}\bar{\psi}\psi \exp\left\{ -\int_{0}^{\beta} d\tau \left[\sum_{k} \bar{\psi}_k(\tau+\eta) \frac{d\psi_k(\tau)}{d\tau} + \mathcal{H}\left(\{\bar{\psi}\},\{\psi\}\right) \right] \right\} \ ,
\end{aligned} \tag{4.2.25}$$

[20] However evaluating expressions in real-time space is still more cumbersome.

with $\Delta\tau = \beta/N$ and

$$\mathcal{H}(\{\bar{\psi}\},\{\psi\}) = \tilde{H}(c_k^\dagger \to \bar{\psi}_k(\tau+\eta), c_k \to \psi_k(\tau)). \tag{4.2.26}$$

The fields obey the boundary conditions

$$\psi_k(\beta) \equiv -\psi_k(0)\,, \qquad \bar{\psi}_k(\beta) \equiv -\bar{\psi}_k(0). \tag{4.2.27}$$

Likewise, we find for the single-particle Green's function in Eq. (4.1.7)

$$G_{12} = -\left\langle T_\tau c_{k_1}[t=\tau_1-\tau_2]_{\tilde{H}} c_{k_2}^\dagger \right\rangle_{\rho_{\text{eq}}} = -\frac{1}{Z}\int \mathcal{D}\bar{\psi}\psi\psi_{k_1}(\tau)\bar{\psi}_{k_2}\exp\left\{(\bar{\psi},\hat{G}_0^{-1}\psi) - iS_{\text{int}}\right\}, \tag{4.2.28}$$

with $\hat{G}_0$ as above and S_{int} analogously defined to Eq. (4.2.20). Again this is the functional representation of the Green's function, now for the equilibrium case of Eq. (4.1.7) and the ideal starting point for a (diagramatic) perturbative expansion in the term S_{int}. A simple calculation shows $G^0 = \hat{G}_0$ also for the Matsubara case.

4.2.4 Generating Functional of (Connected) Green's Functions

We now want to introduce the so called *generating functional of Green's function*, which is another intermediate step to functional renormalization group, which will be build on an analogue generating functional, but of the vertex functions. To this end we generalize the single-particle Green's functions of Eqs. (4.1.4) and (4.1.18) to m-particle Green's functions

$$G_m(1\ldots m;1'\ldots m') = \begin{cases} (-1)^m \left\langle T_\tau c_{k_1'}[\tau_1']_{\tilde{H}} \ldots c_{k_m'}[\tau_m']_{\tilde{H}} c_{k_m}^\dagger[\tau_m]_{\tilde{H}} \ldots c_{k_1}^\dagger[\tau_1]_{\tilde{H}} \right\rangle \\ (-i)^m \left\langle T_\gamma c_{k_1'}^{\nu_1'}[t_1']_H \ldots c_{k_m'}^{\nu_m'}[t_m']_H c_{k_m}^{\nu_m,\dagger}[t_m]_H \ldots c_{k_1}^{\nu_1\dagger}[t_1]_H \right\rangle . \end{cases} \tag{4.2.29}$$

We define a generating functional[21]

$$\mathcal{W}(\{\bar{\eta}\},\{\eta\}) = \frac{1}{Z}\int \mathcal{D}\bar{\psi}\psi \exp\left\{S_0 - \{i\}S_{\text{int}} - (\bar{\psi},\eta) - (\bar{\eta},\psi)\right\}\,, \tag{4.2.30}$$

from which (by construction) the m-particle Green's function can be deduced as

$$G_m^{(c)}(1\ldots m;1'\ldots m') = \{-i\}^m \frac{\delta^m}{\delta\bar{\eta}_{1'}\ldots\delta\bar{\eta}_{m'}} \frac{\delta^m}{\delta\eta_1\ldots\delta\eta_m} \mathcal{W}^{(c)}(\{\bar{\eta}\},\{\eta\})\Big|_{\eta=\bar{\eta}=0}\,, \tag{4.2.31}$$

where the curly bracketed expressions $\{\ldots\}$ are present for the Keldysh case only and the optional (c) is explained below. For the FRG usually one is more interested in the connected part of the Green's function. When setting up a diagramatic language this part of the Green's functions contains all contributions arising from diagrams that are connected by a single graph. Their generating functional [Neg88] is given by

$$\mathcal{W}^c(\{\bar{\eta}\},\{\eta\}) = \ln\left[\mathcal{W}(\{\bar{\eta}\},\{\eta\})\right]. \tag{4.2.32}$$

The connected Green's functions are generated from this by reading (4.2.31) with the bracketed c in place.

4.2.5 Generating Functional of Vertex Functions

Finally, we consider the m-particle vertex functions (the quantity of our main interest), which in a diagrammatic context correspond to the sum of all connected *one-particle irreducible* diagrams,

[21] For a calculation in Keldysh space $Z = 1$.

i.e. the sum of all diagrams with $2m$ amputated external legs, which cannot be split into two disconnected parts by cutting a single contraction. It is well known [Neg88] that the functional

$$\Gamma(\{\bar{\phi}\},\{\phi\}) = -\mathcal{W}^c(\{\bar{\eta}\},\{\eta\}) - (\bar{\phi},\eta) - (\bar{\eta},\phi) + (\bar{\phi},[G_0]^{-1},\phi)\,, \tag{4.2.33}$$

given by the Legendre transformation of $\mathcal{W}^c$ generates the m-particle vertex functions

$$\gamma_m(1\dots m,1'\dots m') = (-i)^m \frac{\delta^m}{\delta\bar{\phi}_1\dots\delta\bar{\phi}_m}\frac{\delta^m}{\delta\phi_{m'}\dots\delta\phi_{1'}}\Gamma(\{\bar{\phi}\},\{\phi\})\Big|_{\phi=\bar{\phi}=0}\,. \tag{4.2.34}$$

Here the conjugated fields are

$$\phi = -\{-i\}\frac{\delta}{\delta\bar{\eta}}\mathcal{W}^c(\{\bar{\eta}\},\{\eta\}) \qquad \bar{\phi} = \{-i\}\frac{\delta}{\delta\eta}\mathcal{W}^c(\{\bar{\eta}\},\{\eta\})\,. \tag{4.2.35}$$

The last term in the sum is added for convenience only [Med01]. In general it is thus possible to find a relation between the general m-particle connected Green's functions and the vertex functions (the interested reader is referred to [Neg88]) by virtue of Eqs. (4.2.33) and (4.2.35). At this point we concentrate on the simplest of those relation, namely the one for the single-particle vertex. Before doing so we need to outline some simple, but very helpful formulas, which can be proven trivially [Kar10a]:

$$\begin{aligned}\frac{\delta\Gamma}{\delta\phi_1} &= \sum_2\left[-\frac{\delta\mathcal{W}^c}{\delta\eta_2}\frac{\delta\eta_2}{\delta\phi_1} - \frac{\delta\mathcal{W}^c}{\delta\bar{\eta}_2}\frac{\delta\bar{\eta}_2}{\delta\phi_1} + \{i\}\left(\bar{\phi}_2\frac{\delta\eta_2}{\delta\phi_1} - \frac{\delta\bar{\eta}_2}{\delta\phi_1}\phi_2 - \bar{\phi}_2\left[\left(G^0\right)^{-1}\right]_{21}\right)\right] + \{i\}\bar{\eta}_1 \\ &= \{i\}\left[\;\bar{\eta}_1 - \sum_2\bar{\phi}_2\left[\left(G^0\right)^{-1}\right]_{21}\right]\,,\end{aligned} \tag{4.2.36}$$

$$\begin{aligned}\frac{\delta\Gamma}{\delta\bar{\phi}_1} &= \sum_2\left[-\frac{\delta\mathcal{W}^c}{\delta\eta_2}\frac{\delta\eta_2}{\delta\bar{\phi}_1} - \frac{\delta\mathcal{W}^c}{\delta\bar{\eta}_2}\frac{\delta\bar{\eta}_2}{\delta\bar{\phi}_1} + \{i\}\left(\bar{\phi}_2\frac{\delta\eta_2}{\delta\bar{\phi}_1} - \frac{\delta\bar{\eta}_2}{\delta\bar{\phi}_1}\phi_2 + \left[\left(G^0\right)^{-1}\right]_{12}\phi_2\right)\right] - \{i\}\eta_1 \\ &= \{i\}\left[-\eta_1 + \sum_2\left[\left(G^0\right)^{-1}\right]_{12}\phi_2\right]\,.\end{aligned} \tag{4.2.37}$$

Note the additional minus signs which is a consequence of taking the derivative with respect to Grassmann variables. The fields $\bar{\phi}$ and ϕ of the Legendre transform Γ are independent, which implies $\delta\phi/\delta\bar{\phi} = 0$. Next, we derive

$$\begin{aligned}\{i\}\delta_{11'} =& \{i\}\frac{\delta\phi_1}{\delta\phi_{1'}} = -\frac{\delta}{\delta\phi_{1'}}\frac{\delta\mathcal{W}^c}{\delta\bar{\eta}_1} = -\sum_2\left[\frac{\delta\eta_2}{\delta\phi_{1'}}\frac{\delta^2\mathcal{W}^c}{\delta\eta_2\delta\bar{\eta}_1} + \frac{\delta\bar{\eta}_2}{\delta\phi_{1'}}\frac{\delta^2\mathcal{W}^c}{\delta\bar{\eta}_2\delta\bar{\eta}_1}\right] \\ =& \sum_2\left[\left(\frac{\{-i\}\delta^2\Gamma}{\delta\phi_{1'}\delta\bar{\phi}_2} - \left[\left(G^0\right)^{-1}\right]_{21'}\right)\frac{\delta^2\mathcal{W}^c}{\delta\eta_2\delta\bar{\eta}_1} - \frac{\{-i\}\delta^2\Gamma}{\delta\phi_{1'}\delta\phi_2}\frac{\delta^2\mathcal{W}^c}{\delta\bar{\eta}_2\delta\bar{\eta}_1}\right]\,.\end{aligned} \tag{4.2.38}$$

In the last step we have used the derivative of Eqs. (4.2.36) and (4.2.37) with respect to ϕ and $\bar{\phi}$, respectively. Starting with $\delta\bar{\phi}_1/\delta\bar{\phi}_{1'} = \delta_{1,1'}$ and $\delta\bar{\phi}_1/\delta\phi_{1'} = \delta\phi_1/\delta\bar{\phi}_{1'} = 0$, leads to analogue formulas. Combining all these relations gives

$$\begin{pmatrix}\{-i\}\frac{\delta^2\Gamma}{\delta\bar{\phi}\delta\phi} + \left(G^0\right)^{-1} & \{-i\}\frac{\delta^2\Gamma}{\delta\bar{\phi}\delta\bar{\phi}} \\ \{-i\}\frac{\delta^2\Gamma}{\delta\phi\delta\phi} & \{-i\}\frac{\delta^2\Gamma}{\delta\phi\delta\bar{\phi}} - \left(G^0\right)^{-1,T}\end{pmatrix} \times \begin{pmatrix}\{-i\}\frac{\delta^2\mathcal{W}^c}{\delta\bar{\eta}\delta\eta} & -\{-i\}\frac{\delta^2\mathcal{W}^c}{\delta\bar{\eta}\delta\bar{\eta}} \\ -\{-i\}\frac{\delta^2\mathcal{W}^c}{\delta\eta\delta\eta} & \{-i\}\frac{\delta^2\mathcal{W}^c}{\delta\eta\delta\bar{\eta}}\end{pmatrix} = 1\,, \tag{4.2.39}$$

where the derivatives $\delta^2/\delta x_1 \delta y_2$ are used as the matrix indices. When deriving the FRG flow equations we will also make use of the definition

$$\begin{aligned}\mathcal{V}(\{\bar{\phi}\},\{\phi\}) &= \begin{pmatrix} \{-i\}\frac{\delta^2\mathcal{W}^c}{\delta\bar{\eta}\delta\eta} & -\{-i\}\frac{\delta^2\mathcal{W}^c}{\delta\bar{\eta}\delta\bar{\eta}} \\ -\{-i\}\frac{\delta^2\mathcal{W}^c}{\delta\eta\delta\eta} & \{-i\}\frac{\delta^2\mathcal{W}^c}{\delta\eta\delta\bar{\eta}} \end{pmatrix} \\ &= \begin{pmatrix} \{-i\}\frac{\delta^2\Gamma}{\delta\bar{\phi}\delta\phi} + \left[G^0\right]^{-1} & \{-i\}\frac{\delta^2\Gamma}{\delta\bar{\phi}\delta\bar{\phi}} \\ \{-i\}\frac{\delta^2\Gamma}{\delta\phi\delta\phi} & \{-i\}\frac{\delta^2\Gamma}{\delta\phi\delta\bar{\phi}} - \left[G^0\right]^{-1,T} \end{pmatrix}^{-1} .\end{aligned} \tag{4.2.40}$$

With this we can establish a link between the connected Green's functions and the vertex functions, explicitly at least for the single-particle case. Using Eq. (4.2.40) at vanishing external fields, the matrix $\mathcal{V}$ becomes diagonal,[22] where the first element reads

$$G_1(1';1) \overset{(*)}{=} G_1^c(1';1) = \{-i\}\frac{\delta^2\mathcal{W}^c}{\delta\bar{\eta}_{1'}\delta\eta_1}\Big|_{\eta=\bar{\eta}=0} = \left[\{-i\}\frac{\delta^2\Gamma}{\delta\bar{\phi}\delta\phi}\Big|_{\phi=\bar{\phi}=0} + \left(G^0\right)^{-1}\right]^{-1}_{1'1} . \tag{4.2.41}$$

The identity $(*)$ is a consequence of the so called linked *cluster theorem* [Neg88]. As G_1 is the single-particle propagator (called G above) also obeying the Dyson equation (4.1.8) a comparison yields

$$\gamma_1 = \{-i\}\frac{\delta^2\Gamma}{\delta\bar{\phi}\delta\phi}\Big|_{\phi=\bar{\phi}=0} = -\Sigma . \tag{4.2.42}$$

With this, upto a sign, we found that γ_1 corresponds to the self-energy Σ.

4.3 Flow Equations

Finally, we have accomplished all the preliminary tasks to present the FRG framework. At the heart of this method lie the flow of equations, which describe the action induced by the two-particle interaction in terms of the vertex functions. We turn to the flow equations of the connected Green's function first, only to facilitate the derivation of the same for the vertex functions. We will delay a specification of how the cut-off Λ is introduced in the non-interacting part of the Green's function G_0 to the next section ($\rightarrow$ see section 4.4). We follow closely the logic outlined in [Med01, Kar10a, Ken11]. For an alternative diagramatic approach see [Jak09].

4.3.1 Flow of Generating Functional of Connected Green's Functions

Next, we take a look at

$$\mathcal{W}^\Lambda(\{\bar{\eta}\},\{\eta\}) = \frac{1}{Z_0^\Lambda}\int \mathcal{D}\bar{\psi}\psi \exp\left\{S_0^\Lambda - \{i\}S_{\text{int}} - (\bar{\psi},\eta) - (\bar{\eta},\psi)\right\} , \tag{4.3.1}$$

where we have changed Z to Z_0 in the denominator for convenience[23] and introduced the cut-off controlled by parameter Λ in the non-interacting part of the action

$$S_0^\Lambda = \left(\bar{\psi}, \left[G^{0,\Lambda}\right]^{-1}\psi\right) , \tag{4.3.2}$$

via $G^{0,\Lambda}$ as in Eq. (4.0.1). Taking the derivative of the logarithm of this functional yields the flow equation

$$\dot{\mathcal{W}}^{c,\Lambda} = \frac{1}{\mathcal{W}^\Lambda}\partial_\Lambda\left[\frac{1}{Z_0^\Lambda}\int \mathcal{D}\bar{\psi}\psi \exp\left\{S_0^\Lambda - \{i\}S_{\text{int}} - (\bar{\psi},\eta) - (\bar{\eta},\psi)\right\}\right] , \tag{4.3.3}$$

[22] The off-diagonal elements are zero unless we are in a phase of broken symmetry.

[23] This changes the $\mathcal{W}^c$ and Γ only by a constant and thus leaves higher order connected Green's and vertex functions $G^c_{m\geq 1}$ and $\gamma_{m\geq 1}$ unaffected.

which in this implicit form is of minor use. We further evaluate the derivative by

$$\begin{aligned}\partial_\Lambda \frac{e^{S_0^\Lambda}}{\mathcal{Z}_0^\Lambda} &= \frac{e^{S_0^\Lambda}}{\mathcal{Z}_0^\Lambda}\left[(\bar\psi, \partial_\Lambda[G^{0,\Lambda}]^{-1}\psi) - \{i\}\sum_{1,1'}\left\{\int \frac{\mathcal{D}\bar\psi\psi}{\mathcal{Z}_0^\Lambda}\bar\psi_1\psi_{1'}e^{S_0^\Lambda}\left[\partial_\Lambda[G^{0,\Lambda}]^{-1}\right]_{1,1'}\right\}\right] \\ &= \frac{e^{S_0^\Lambda}}{\mathcal{Z}_0^\Lambda}\left\{(\bar\psi, \partial_\Lambda[G^{0,\Lambda}]^{-1}\psi) - \mathrm{Tr}\left[G^{0,\Lambda}\partial_\Lambda[G^{0,\Lambda}]^{-1}\right]\right\}.\end{aligned} \tag{4.3.4}$$

With this Eq. (4.3.3) can be recast in the simple form

$$\dot{\mathcal{W}}^{c,\Lambda} = -\mathrm{Tr}\left[G^{0,\Lambda}\partial_\Lambda[G^{0,\Lambda}]^{-1}\right] - \{-1\}\frac{1}{\mathcal{W}^\Lambda}\left(\frac{\delta}{\delta\eta}, \left\{\partial_\Lambda[G^{0,\Lambda}]^{-1}\right\}\frac{\delta}{\delta\bar\eta}\right)\mathcal{W}^\Lambda. \tag{4.3.5}$$

As a last step we eliminate $\mathcal{W}$ from this expression, by

$$\begin{aligned}\frac{1}{\mathcal{W}^\Lambda}\left(\frac{\delta}{\delta\eta}, \partial_\Lambda[G^{0,\Lambda}]^{-1}\frac{\delta}{\delta\bar\eta}\right)\mathcal{W}^\Lambda &= e^{-\mathcal{W}^{c,\Lambda}}\left(\frac{\delta}{\delta\eta}, \partial_\Lambda[G^{0,\Lambda}]^{-1}\frac{\delta}{\delta\bar\eta}\right)e^{\mathcal{W}^{c,\Lambda}} \\ &= \left(\frac{\delta\mathcal{W}^{c,\Lambda}}{\delta\eta}, \partial_\Lambda[G^{0,\Lambda}]^{-1}\frac{\delta\mathcal{W}^{c,\Lambda}}{\delta\bar\eta}\right) + \left(\frac{\delta}{\delta\eta}, \partial_\Lambda[G^{0,\Lambda}]^{-1}\frac{\delta}{\delta\bar\eta}\right)\mathcal{W}^{c,\Lambda} \\ &= \left(\frac{\delta\mathcal{W}^{c,\Lambda}}{\delta\eta}, \partial_\Lambda[G^{0,\Lambda}]^{-1}\frac{\delta\mathcal{W}^{c,\Lambda}}{\delta\bar\eta}\right) + \{i\}\sum_{1,1'}\left[\frac{\delta^2\mathcal{W}^{c,\Lambda}}{\delta\eta_1\delta\bar\eta_{1'}}[\partial_\Lambda[G^{0,\Lambda}]^{-1}]_{1,1'}\right] \\ &= \left(\frac{\delta\mathcal{W}^{c,\Lambda}}{\delta\eta}, \partial_\Lambda[G^{0,\Lambda}]^{-1}\frac{\delta\mathcal{W}^{c,\Lambda}}{\delta\bar\eta}\right) - \{i\}\mathrm{Tr}\left[\partial_\Lambda[G^{0,\Lambda}]^{-1}\frac{\delta^2\mathcal{W}^{c,\Lambda}}{\delta\bar\eta\delta\eta}\right],\end{aligned} \tag{4.3.6}$$

and arrive at the flow equation of the generating functional of the connected Green's functions

$$\begin{aligned}\dot{\mathcal{W}}^{c,\Lambda} = &-\mathrm{Tr}\left[G^{0,\Lambda}\partial_\Lambda[G^{0,\Lambda}]^{-1}\right] + \{-i\}\,\mathrm{Tr}\left[\partial_\Lambda[G^{0,\Lambda}]^{-1}\frac{\delta^2\mathcal{W}^{c,\Lambda}}{\delta\bar\eta\delta\eta}\right] \\ &- \{-1\}\left(\frac{\delta\mathcal{W}^{c,\Lambda}}{\delta\eta}, \partial_\Lambda[G^{0,\Lambda}]^{-1}\frac{\delta\mathcal{W}^{c,\Lambda}}{\delta\bar\eta}\right).\end{aligned} \tag{4.3.7}$$

4.3.2 Flow of Vertex Functions

In the FRG framework used in this thesis one proceeds one step further and considers the flow of the Legendre transformation of this quantity, namely the flow of the vertex functions. Taking the derivative ∂_Λ of Eq. (4.2.33), where now $\bar\phi$ and ϕ acquire a Λ dependency via Eq. (4.2.35), we arrive at

$$\begin{aligned}\dot\Gamma^\Lambda(\{\bar\phi\},\{\phi\}) &= -\frac{d}{d\Lambda}\mathcal{W}^{c,\Lambda}\left(\{\bar\eta^\Lambda\},\{\eta^\Lambda\}\right) - (\bar\phi, \dot\eta^\Lambda) - (\dot{\bar\eta}^\Lambda, \phi) + (\bar\phi, \partial_\Lambda[G^{0,\Lambda}]^{-1}\phi) \\ &= -\dot{\mathcal{W}}^{c,\Lambda} - \sum_1\left[\dot\eta_1^\Lambda\frac{\delta\mathcal{W}^{c,\Lambda}}{\delta\eta_1^\Lambda} + \dot{\bar\eta}_1^\Lambda\frac{\delta\mathcal{W}^{c,\Lambda}}{\delta\bar\eta_1^\Lambda}\right] - (\bar\phi, \dot\eta^\Lambda) - (\dot{\bar\eta}^\Lambda, \phi) + (\bar\phi, \partial_\Lambda[G^{0,\Lambda}]^{-1}\phi) \\ &= -\dot{\mathcal{W}}^{c,\Lambda}\left(\{\bar\eta^\Lambda\},\{\eta^\Lambda\}\right) + (\bar\phi, \partial_\Lambda[G^{0,\Lambda}]^{-1}\phi) \\ &= \mathrm{Tr}\left[G^{0,\Lambda}\partial_\Lambda[G^{0,\Lambda}]^{-1}\right] \mp \{i\}\,\mathrm{Tr}\left[\partial_\Lambda[G^{0,\Lambda}]^{-1}\frac{\delta^2\mathcal{W}^{c,\Lambda}}{\delta\bar\eta^\Lambda\delta\eta^\Lambda}\right] \\ &= \mathrm{Tr}\left[G^{0,\Lambda}\partial_\Lambda[G^{0,\Lambda}]^{-1}\right] - \quad \mathrm{Tr}\left[\partial_\Lambda[G^{0,\Lambda}]^{-1}\mathcal{V}_{11}^\Lambda(\{\bar\phi\},\{\phi\})\right].\end{aligned} \tag{4.3.8}$$

Here the symbol $\mathcal{V}_{11}$ denotes the upper right element of the matrix defined in Eq. (4.2.40), which generally relates the derivative of Γ to that of $\mathcal{W}^c$. This concludes the flow equation for the generating functional of the vertex functions and we can finally turn to the flow of the vertex functions themselves.

For the flow equations of the vertices we aim at a Taylor expansion of (4.3.8) and compare it to the series expansion around $\phi = \bar{\phi} = 0$

$$\Gamma^\Lambda(\{\bar{\phi}\},\{\phi\}) = \sum_{m=0}^{\infty} \frac{(-1)^m\{i\}^m}{(m!)^2} \sum_{1\dots m} \sum_{1'\dots m'} \gamma_m^\Lambda(1\dots m, 1'\dots m')\bar{\phi}_1 \dots \bar{\phi}_m \phi_{m'} \dots \phi_{1'}, \tag{4.3.9}$$

of the generating functional or to be more precise its derivative

$$\partial_\Lambda\Gamma^\Lambda(\{\bar{\phi}\},\{\phi\}) = \sum_{m=0}^{\infty} \frac{(-1)^m\{i\}^m}{(m!)^2} \sum_{1\dots m} \sum_{1'\dots m'} \partial_\Lambda\gamma_m^\Lambda(1\dots m, 1'\dots m')\bar{\phi}_1 \dots \bar{\phi}_m \phi_{m'} \dots \phi_{1'}, \tag{4.3.10}$$

from which the flow equations can be read off. First, we recast Eq. (4.2.40) to

$$\begin{aligned}
\mathcal{V}^\Lambda &= \begin{pmatrix} \{-i\}\frac{\delta^2\Gamma^\Lambda}{\delta\bar{\phi}\delta\phi} + [G^{0,\Lambda}]^{-1} & \{-i\}\frac{\delta^2\Gamma^\Lambda}{\delta\bar{\phi}\delta\bar{\phi}} \\ \{-i\}\frac{\delta^2\Gamma^\Lambda}{\delta\phi\delta\phi} & \{-i\}\frac{\delta^2\Gamma^\Lambda}{\delta\phi\delta\bar{\phi}} - [G^{0,\Lambda}]^{-1,T} \end{pmatrix}^{-1} \\
&= \left[\begin{pmatrix} [G^\Lambda]^{-1} & 0 \\ 0 & -[G^\Lambda]^{-1,T} \end{pmatrix} + \begin{pmatrix} \mathcal{U}^\Lambda & \{-i\}\frac{\delta^2\Gamma^\Lambda}{\delta\bar{\phi}\delta\bar{\phi}} \\ \{-i\}\frac{\delta^2\Gamma^\Lambda}{\delta\phi\delta\phi} & -\mathcal{U}^\Lambda \end{pmatrix} \right]^{-1} \\
&= -\underbrace{\left[1 - \begin{pmatrix} -G^\Lambda & 0 \\ 0 & [G^\Lambda]^T \end{pmatrix} \cdot \begin{pmatrix} \mathcal{U}^\Lambda & \{-i\}\frac{\delta^2\Gamma^\Lambda}{\delta\bar{\phi}\delta\bar{\phi}} \\ \{-i\}\frac{\delta^2\Gamma^\Lambda}{\delta\phi\delta\phi} & -\mathcal{U}^\Lambda \end{pmatrix} \right]^{-1}}_{=\hat{\mathcal{V}}^\Lambda} \cdot \begin{pmatrix} -G^\Lambda & 0 \\ 0 & [G^\Lambda]^T \end{pmatrix},
\end{aligned} \tag{4.3.11}$$

where we have defined $\mathcal{U}^\Lambda$ as the difference of the one-particle vertex function and the second derivative of Γ^Λ with respect to its fields

$$\mathcal{U}^\Lambda = \{-i\}\frac{\delta^2\Gamma^\Lambda}{\delta\bar{\phi}\delta\phi} - \{-i\}\frac{\delta^2\Gamma^\Lambda}{\delta\bar{\phi}\delta\phi}\Big|_{\phi=\bar{\phi}=0} = \{-i\}\frac{\delta^2\Gamma^\Lambda}{\delta\bar{\phi}\delta\phi} - \gamma_1^\Lambda = \{-i\}\frac{\delta^2\Gamma^\Lambda}{\delta\bar{\phi}\delta\phi} - [G^\Lambda]^{-1} + [G^{0,\Lambda}]^{-1}\ . \tag{4.3.12}$$

With $\tilde{\mathcal{V}}^\Lambda = \hat{\mathcal{V}}^\Lambda_{11}$ we rewrite (4.3.8) as

$$\dot{\Gamma}^\Lambda = \mathrm{Tr}\left[G^{0,\Lambda}\partial_\Lambda[G^{0,\Lambda}]^{-1}\right] - \mathrm{Tr}\left[G^\Lambda\partial_\Lambda[G^{0,\Lambda}]^{-1}\tilde{\mathcal{V}}^\Lambda\right]\ . \tag{4.3.13}$$

Which amounts to simply relabelling the variables in Eq. (4.3.8), but allows to expand in form of a geometric series

$$\tilde{\mathcal{V}}^\Lambda = 1 - G^\Lambda\mathcal{U}^\Lambda + \left[G^\Lambda\mathcal{U}^\Lambda G^\Lambda\mathcal{U}^\Lambda - G^\Lambda\frac{-i\delta^2\Gamma^\Lambda}{\delta\bar{\phi}\delta\bar{\phi}}[G^\Lambda]^T\frac{-i\delta^2\Gamma^\Lambda}{\delta\phi\delta\phi} + \dots \right]\ . \tag{4.3.14}$$

Using this expansion in (4.3.13) and comparing powers in the external fields to (4.3.10) one can read off the flow equations of the vertices. This procedure yields an infinite hierarchy of flow equation, which is just an exact reformulation of the many-particle problem we started with[24]. The explicit flow equations for the two lowest order vertex functions (disregarding the free energy described by γ_0) $\gamma_{1/2}$ are given below.

Flow of γ_1: Self-energy

The flow equation of γ_1^Λ can be obtained by the part of $\mathcal{U}^\Lambda$ that is linear in $\bar{\phi}\phi$:

$$\mathcal{U}^{\Lambda,\mathrm{lin}} = \frac{\{-i\}\{i\}^2}{(2!)^2}\frac{\delta^2}{\delta\bar{\phi}_{3'}\delta\phi_3}\sum_{1'2'12}\gamma_2^\Lambda(1'2';12)\bar{\phi}_{1'}\bar{\phi}_{2'}\phi_2\phi_1 = -\{i\}\sum_{2'2}\gamma_2^\Lambda(2'3';23)\bar{\phi}_{2'}\phi_2\ , \tag{4.3.15}$$

where we exploited that

$$\gamma_2^\Lambda(1'2';12) = -\gamma_2^\Lambda(2'1';12) \qquad \gamma_2^\Lambda(1'2';12) = -\gamma_2^\Lambda(1'2';21)\ , \tag{4.3.16}$$

[24]...and thus calls for the truncation of this hierarchy at some level.

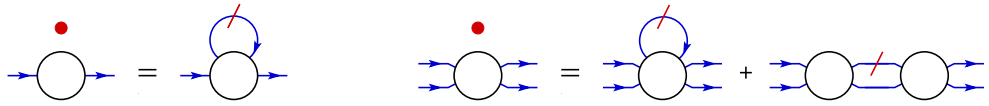


Figure 4.3.: Diagrammatic representation of the flow equations given in Eqs. (4.3.17) and (4.3.19).

for the anti-symmertrized two-particle vertex. The flow equation follows as

$$\partial_\Lambda \gamma_1^\Lambda(1';1) = \sum_{22'} \left[G^\Lambda \partial_\Lambda [G^{0,\Lambda}]^{-1} G^\Lambda\right]_{22'} \gamma_2^\Lambda(1'2';12) = \sum_{22'} S^\Lambda_{22'} \gamma_2^\Lambda(1'2';12). \tag{4.3.17}$$

In the former expression we defined the *single-scale propagator*[25]

$$S^\Lambda_{1'1} = S^\Lambda(1';1) = \sum_{22'} G^\Lambda_{1'2} \left[\partial_\Lambda [G^{0,\Lambda}]^{-1}\right]_{22'} G^\Lambda_{2'1} = -\partial^*_\Lambda G^\Lambda_{1'1} = -\partial^*_\Lambda G^\Lambda(1';1)\ . \tag{4.3.18}$$

Here the star partial derivative ∂^*_Λ is understood as to act on the explicit cut-off dependence in G_0^Λ (not in γ_1 itself) only. The diagramatic representation of this flow equation is shown in the left part of Fig. 4.3, where the derivative with respect to Λ is indicated by a red dot and the single-scale propagator by a red slanted line. Importantly, although having a high resemblance to the diagram of first order perturbation theory, the self-energy γ_1^Λ is feed back directly into Eq. (4.3.17) by G^Λ, and it is thus reasonable to hope that logarithmic divergences in perturbation theory can be re-sumed even if a truncation of the hierarchy of flow equations is introduces (as in section 4.3.3).

Flow of γ_2: Effective Two-Particle Interaction

As in the previous section one can proceed for the effective two-particle interaction γ_2, but by comparing to all terms on the right hand site of Eq. (4.3.13) containing four field terms. This yields

$$\begin{aligned}
\partial_\Lambda \gamma_2^\Lambda(1'2';12) = \quad & \sum_{33'} S^\Lambda_{33'} \gamma_3^\Lambda(1'2'3';123) \\
& - \sum_{33'44'} S^\Lambda_{33'} \gamma_2^\Lambda(3'4;12) G^\Lambda_{4'4} \gamma_2^\Lambda(1'2';4'3) \\
& - \Bigg[\sum_{33'44'} S^\Lambda_{33'} \gamma_2^\Lambda(1'3';14) G^\Lambda_{44'} \gamma_2^\Lambda(2'4';23) \\
& \qquad - (1' \leftrightarrow 2') - (1 \leftrightarrow 2) + (1' \leftrightarrow 2', 1 \leftrightarrow 2) \Bigg]\ .
\end{aligned} \tag{4.3.19}$$

If the initial two-particle vertex is anti-symetrized, this symmetry is respected by the flow explicitly as shown in Eq. (4.3.19). Again a simple diagrammatic representation can be given; see the right site of Fig. 4.3.

4.3.3 Truncation Schemes and Initial Conditions

With the procedure, exemplified above for γ_1^Λ and γ_2^Λ, one can derive in principle the infinite hierarchy of flow equations for all vertex functions γ_m^Λ. In practice however, only quite a small number of vertex functions ($m \leq 2$ in this thesis) can be treated explicitly and the need for truncation arises. Before justifying this approximation, we take a closer look at the structure of the flow equations of higher order vertex functions. As for the cases $\gamma_{1/2}^\Lambda$ shown explicitly the flow equation of the vertex function γ_m^Λ contains one vertex function γ_{m+1}^Λ as well as contributions from all lower ones (for a

[25] A name originating from the fact that when the sharp cut-off scheme is used ($\rightarrow$ Section 4.4), the quantity $S^\Lambda(\omega)$ is only non-zero for a single energy scale $\omega = \pm\Lambda$. The flow equation then indicates that only a single energy scale is incorporated during the flow at a given Λ. When a different cut-off scheme is used this renders this name somewhat a misnomer, which we will ignore for the sake of simplicity.

very instructive way of understanding this by the use of diagrams see [Jak09]). At the beginning of the flow, where following Eq. (4.0.1) $G^{0,\Lambda=\infty} = 0$, all contributions containing G^0 are suppressed. In this simple language, the initial conditions[26] complementing the flow equations are given by

$$\Gamma^{\Lambda=\infty}\left(\{\bar{\phi}\},\{\phi\}\right) = \{i\}S_{\text{int}} = \{i\}\,\frac{1}{4}\sum_{1'2'12}\bar{v}_{1'2'12}\bar{\psi}_{1'}\bar{\psi}_{2'}\psi_2\psi_1\ , \tag{4.3.20}$$

which translates to the initial conditions for the flow equations of the vertex functions

$$\gamma_2^{\Lambda=\infty}(1'2';12) = \{-i\}\,\bar{v}_{1'2'12}\ , \quad \gamma_{m\neq 2}^{\Lambda=\infty} = 0\ . \tag{4.3.21}$$

If we concentrate on the prominent case of Coulomb interaction, U is of the density-density type $Ud_n^\dagger d_n d_m^\dagger d_m$ and thus

$$\bar{v}_{1'2'12} = U\times\tilde{\delta}\times\begin{cases}\beta^{-1} & \text{Matsubara}\\ (-i)(-\nu_1)\delta(\nu_1'=\nu_2'=\nu_1=\nu_2) & \text{Keldysh}\end{cases}\ , \tag{4.3.22}$$

for each pair of coupled neighbors (i,j) and where $\tilde{\delta} = \delta(\omega_1'+\omega_2'-\omega_1-\omega_2)$ or $\tilde{\delta} = \delta(t_1'=t_2'=t_3=t_4)$ for frequencies or times, respectively. Rotating to the more practical RKA-basis gives (with all other indices suppressed)

$$\begin{aligned}\bar{v}_{n_1'n_2'n_1n_2} &= \sum_{\nu_1'\nu_2'\nu_1\nu_2}[B^{-1}]_{n_1'\nu_1'}[B^{-1}]_{n_2'\nu_2'}\times[(-\nu_1)\delta(\nu_1'=\nu_2'=\nu_1=\nu_2)]\times[A^{-1}]_{\nu_1n_1}[A^{-1}]_{\nu_2n_2}\\ &= \frac{\bar{v}}{2}\times\begin{cases}1 & n_1'=n_1\wedge n_2'\neq n_2\ \vee\ n_1'\neq n_1\wedge n_2'=n_2\\ 0 & \text{otherwise}\ .\end{cases}\end{aligned} \tag{4.3.23}$$

With this we can also give a hierarchy in terms of the two-particle interaction. A diagram contributing to the m-particle vertex function, which has to be irreducible with 2m external lines amputated, always includes at least m interaction vertices γ_2 [Jak09]. This renders the truncation, which consists in simply cutting the infinite hierarchy of flow equations at a certain order m_c by setting

$$\gamma_{m_c+1}^{\Lambda} = \gamma_{m_c+1}^{\Lambda=\infty} \Rightarrow \partial_\Lambda\gamma_{m\leq m_c}^{\Lambda} = f(\{\gamma_n^\Lambda : n\leq m_c\},\gamma_{m_c+1}^{\Lambda=\infty})\quad,\quad \partial_\Lambda\gamma_{m>m_c}^{\Lambda} = 0\ , \tag{4.3.24}$$

plausible, if γ_2 is chosen small to start with. Due to Eq. (4.3.24) the set of flow equations closes and can be integrated from $\Lambda=\infty$, where the exact values of the vertex functions are known [see Eq. (4.3.21)] down to $\Lambda = 0$, where the physical problem is recovered. In this thesis, whenever treating non-equilibrium problems we will restrict ourselves to the simplest truncation scheme $m_c = 1$. A restriction which can be lifted when scrutinizing the steady-state (see [Kar10a]), but in practice is very hard to circumvent when dealing with real times (i.e. to find transient behavior). In equilibrium, we will also use $m_c = 2$. Importantly, the FRG thus allows (in principle) for a *systematic* improvement of accuracy by including higher and higher orders. Although this improvement is systematic, it is not clear a priori, whether qualitative results found in some truncation order necessarily carry over to another. An instructive example of this is the exponential behavior in the *single impurity Anderson model* (see chapter 8 for details). While for $m_c = 1$ exponential behavior – albeit with slightly wrong exponents – are re-sumed correctly by the FRG (see [And08]), this re-summation is lost at a higher truncation level (see [Kar10a]), although quantitative agreement with exact methods (NRG) improve strongly. It is thus always important to remember the (perturbative) motivation of the FRG and keep the vertex functions below a certain threshold, whenever the validity of FRG results are in doubt. Nonetheless using FRG has proven to be an invaluable tool to tackle many equilibrium as well as non-equilibrium problems [Met12]. The renormalization procedure greatly improves the accuracy of the results found compared to those from a purely perturbative ansatz, or even allows to extract results, where perturbation theory fails altogether. Furthermore, it avoids spurious spontaneous symmetry breaking as found, e.g., in a self-consistent Hartree-Fock approach to the SIAM [Kar10a].

[26] which can also be deduced analytically more rigorously [Med01].

4.4 Cut-Off Schemes

In this section we will finally specify the cut-off schemes used in this thesis. Up to this point they were left completely generic only claiming Eq. (4.0.1), which of course still allows for a multitude of possible cut-off schemes. Without truncation the details of the cut-off would be entirely irrelevant, as in the end the FRG would always constitute an exact reformulation of the quantum many-body problem. But as truncations are essential to the method the natural question arises, whether different cut-offs lead to results agreeing among each other on a qualitative or even quantitative level. If this is not the case, one can further investigate whether certain cut-off, are better or worse suited to describe the problem at hand and why. In general after truncation it is absolutely unclear whether different cut-offs give consistent results, but some prominent realizations of cut-off schemes have been established, which are usually very convincing. Two of those realizations, the sharp cut-off and the reservoir cut-off scheme, will be used in equilibrium and non-equilibrium, respectively. The overall reason for this is that the former greatly simplifies the solution of the flow equations, while retaining accurate results in equilibrium. The latter, although in general more expensive from a numerical point of view, leads to results obeying causality relations, which are vital in non-equilibrium.

4.4.1 Sharp Cut-Off Scheme: Equilibrium Problems

We first concentrate on the case of finite temperature T. The zero temperature limit can then be properly deduced. The multiplicative *sharp cut-off scheme* then reads

$$\begin{aligned} G^0(i\omega) \to G^{0,\Lambda}(i\omega) &= \Theta_\Lambda(|\omega| - \Lambda) G^0(i\omega) \,, \\ \Theta_\Lambda(x) &= \begin{cases} 0 & -\pi T > x \\ 1/2 + \frac{x}{2\pi T} & -\pi T \leq x \leq \pi T \\ 1 & x > \pi T \end{cases} \,, \end{aligned} \tag{4.4.1}$$

and was successfully employed to quantum impurity problems in [And04, Ens05b, Med05, Kar08]. As we will also use this scheme in a similar context, this justifies its choice for equilibrium. With this the single-scale propagator

$$S^\Lambda(i\omega) = \begin{cases} \frac{1}{2\pi T} G^\Lambda(i\omega) G^0(i\omega)^{-1} G^\Lambda(i\omega) & -\pi T \leq |\omega| - \Lambda \leq \pi T \\ 0 & \text{otherwise,} \end{cases} \tag{4.4.2}$$

for a given Λ vanishes at any frequency but a single pair of Matsubara frequencies $|\omega| = \omega_c$. After accounting for frequency conservation, this property cancels the only trace over imaginary frequencies remaining in the flow of the self-energy as well as the effective two-particle interaction and renders this cut-off scheme particularly suited in equilibrium.

In the limit $T \to 0$ imaginary frequencies turn continuous and the above definition becomes

$$G^{0,\Lambda}(i\omega) = \Theta(|\omega| - \Lambda) G^0(i\omega) \quad \to \quad S^\Lambda = -\partial_\Lambda G^\Lambda = \delta(|\omega| - \Lambda) \partial_\Theta G^\Lambda \,, \tag{4.4.3}$$

with the usual Heaviside step function Θ. Products of distributions, such as δ distributions with Heaviside step function are evaluated as usual by virtue of the Morris' Lemma [Mor94]

$$\delta_\epsilon(x - \Lambda) f\left[\Theta_\epsilon(x - \Lambda)\right] \;\to\; \delta(x - \Lambda) \int_0^1 f(t)\, dt \,, \tag{4.4.4}$$

with some artificial broadening $\epsilon \to 0$.

4.4.2 Reservoir Cut-Off Scheme: Non-Equilibrium Problems

In non-equilibrium it has proven useful to introduce the cut-off scheme on the level of the Hamiltonian, because only then it is straightforward that physically important conservation laws (e.g. causality) remain fulfilled. A very useful member of such a class of cut-off schemes was introduced

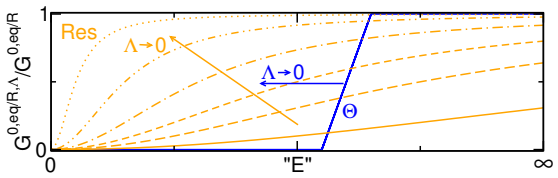


Figure 4.4.: Pictorial representation of how the two cut-off schemes, sharp and auxiliary reservoir, suppress "low energy degrees of freedom" in the non-interacting Green's function. The plot should be understood schematically rather than rigorously.

in [Jak10b, Jak10a] and dubbed the *reservoir cut-off scheme*. It consists in coupling additional structureless auxiliary reservoirs to the local system in such a way that each single-particle level couples to its own structureless auxiliary reservoir. The statics of those auxiliary reservoirs are still free and different configurations can be tested. While in [Jak09, Kar10a] reservoirs with $T_{\text{aux}} = \mu_{\text{aux}} = 0$ were proposed, we want to concentrate on $T_{\text{aux}} = \infty$, where μ_{aux} becomes irrelevant. This was exemplified to lead to the same results for certain models in [Ken11, Ken13d], and facilitates calculations during the flow. Each level is coupled to its respective reservoir with the same hybridization Λ. In total this cut-off scheme simply introduces another self-energy contribution

$$\text{real-frequency space:} \quad \Sigma^{\text{R}}_{\text{cut}} = -i\Lambda\,\mathbb{1} = \left(\Sigma^{\text{A}}_{\text{cut}}\right)^{\dagger} \;, \quad \Sigma^{\text{K}}_{\text{cut}} = 0 \;, \quad \mathbb{1} = \sum_k |k\rangle\langle k| \;. \tag{4.4.5}$$

$$\text{real-time space:} \quad \Sigma^{\text{R}}_{\text{cut}} = -i\Lambda\,\mathbb{1}\delta(t-t') = \left(\Sigma^{\text{A}}_{\text{cut}}\right)^{\dagger} \;, \quad \Sigma^{\text{K}}_{\text{cut}} = 0 \;. \tag{4.4.6}$$

to the Green's function G^0. It is easy to see that this corresponds to a multiplicative scheme, but in real-time instead of frequency space, where large time differences are suppressed exponentially with prefactor Λ

$$G^{0,\text{R/A}} \quad \rightarrow \quad e^{\mp\Lambda(t-t')}\,G^{0,\text{R/A}} \;, \tag{4.4.7}$$

Both cut-off schemes, the sharp cut-off and reservoir cut-off are schematically analyzed in Fig. 4.4. For frequency space it is shown how the cut-off incorporates energy scales[27] E from high to low as $\Lambda = \infty \rightarrow \Lambda = 0$. In the sharp cut-off scheme a perfect suppression of smaller energy scales is used, while higher energies are completely taken into account. The step crossing from high to low energies is continuously moved to smaller energy scales as $\Lambda \rightarrow 0$. In the case of the reservoir cut-off scheme this is more subtle. At any Λ all energy scales carry some weight ($\propto G^{0,\Lambda}/G^0$), but smaller energies are heavily suppressed $\propto (E/\Lambda)^2$. As $\Lambda \rightarrow 0$ more weight is contiguously shifted also to smaller energies as shown.

4.4.3 Initial Conditions Vol. II

Although the initial conditions given in Eq. (4.3.21) are mathematically correct there exists a subtle point about the convergence of the self-energy flow equation, which effectively alters the initial condition of this vertex function. This is due to the fact, that the flow of the self-energy for very high Λ is so slow, that it always needs to be addressed analytically. We consider first the sharp

[27] Of course defining this energy scale model independently is complicated. For the sharp cut-off ω itself was taken. For the reservoir cut-off we used $\omega - \epsilon_k$ and assumed a diagonal basis for k everywhere. The plot should be understood schematically rather than rigorously.

cut-off scheme, for which

$$\begin{aligned}
&\lim_{\Lambda_0\to\infty}\int_{\infty}^{\Lambda_0} d\Lambda\,\partial_\Lambda\gamma_1^\Lambda(1';1)\\
&= \frac{1}{2\pi}\lim_{\Lambda_0\to\infty}\int_{\infty}^{\Lambda_0} d\Lambda\sum_{\omega=\pm\Lambda}\sum_{k_2k_2'} e^{i\omega\eta}\frac{\delta_{k_2k_2'}}{i\omega}\bar{v}_{1'2'12}+O(\Lambda_0^{-1})\\
&= \frac{1}{\pi}\lim_{\Lambda_0\to\infty}\sum_q \bar{v}_{k_1'qk_1q}\int_{\infty}^{\Lambda_0} d\Lambda\left\{\frac{\sin(\Lambda\eta)}{\Lambda}\right\}+O(\Lambda_0^{-1})\\
&= \frac{1}{\pi}\lim_{\Lambda_0\to\infty}\sum_q \bar{v}_{k_1'qk_1q}\left[\underbrace{\int_0^{\Lambda_0} d\Lambda\left\{\frac{\sin(\Lambda\eta)}{\Lambda}\right\}}_{=0}-\underbrace{\int_0^{\infty} d\Lambda\left\{\frac{\sin(\Lambda\eta)}{\Lambda}\right\}}_{=\frac{\pi}{2}}\right]+O(\Lambda_0^{-1})\\
&= -\frac{1}{2}\sum_q \bar{v}_{k_1'qk_1q}\ ,
\end{aligned} \tag{4.4.8}$$

where we have used the large frequency asymptote of the Green's functions $G\propto 1/(i\omega)$ [Neg88]. For real-frequency space and using the reservoir cut-off one can find the same result apart from some changes in signs due to the Keldysh structure [Jak09]. But instead of presenting the calculation we want to rather explain the appearance of this shift in initial conditions by an argument from real-time space. The self-energy is the only vertex function, which contains a self-contracted diagram (similar to the one on the left of Fig. 4.3). This diagram contains the free equal-time Green's function $G^0(t,t)$. For Eq. (4.3.21) we assumed, that *all* G^0 are suppressed, but actually following Eq. (4.4.7) this is not the case for the equal-time Green's function. A simple diagramatic argument [Ken11] then a shift analogue to the Matsubara case. In total the changed initial condition of the self-energy reads

$$\gamma_1^{\Lambda\to\infty}(1';1) = -\{-\nu_1\delta_{\nu_1'\nu_1}\}\frac{1}{2}\sum_q \bar{v}_{k_1'qk_1q}. \tag{4.4.9}$$

4.5 Symmetries and Their Conservation

Symmetries play a major role in any branch of physics. They cannot only be exploited to find simpler analytical or speed up numerical solutions, but also provide valuable insights into the problem at hand, including which approximations might be suited better or worse. To this end the aim of this section is to outline symmetries for the Green's and vertex functions and also discuss their conservation if the FRG treatment outlined above is employed. In a slight abuse of the word "symmetry" we will discuss here any relationship linking the Green's or vertex functions to one another, even if this relationship might not be accredited to a symmetry in its conventional meaning. We will take a pragmatic vantage point and concentrate on single-particle Green's functions and one- and (in exceptions) two-particle vertex functions (self-energy and effective two-particle interaction) only, as those are the only relevant ones throughout this thesis. For a broader view see [Jak09, Jak10b].

4.5.1 Symmetries...

Equilibrium

From the very definition of Eq. (4.1.4) (and a Fourier transform) follows a symmetry under *complex conjugation* as

$$G(i\omega) = G(-i\omega)^\dagger, \tag{4.5.1}$$

which carries over to the self-energy

$$\Sigma(i\omega) = \Sigma(-i\omega)^\dagger. \tag{4.5.2}$$

Furthermore we can Wick rotate the equilibrium Green's functions (of imaginary frequencies) to find their corresponding counterparts on the real frequency axis

$$G(i\omega \to \omega \pm i\eta) = G^{\mathrm{R/A}}(\omega). \tag{4.5.3}$$

In equilibrium (characterized by $\beta = 1/T$) the Keldysh Green's functions and self-energies (of real frequencies) are related by a *dissipation-fluctuation theorem*[28]

$$G^{\mathrm{K}}(\omega) = \left[G^{\mathrm{R}}(\omega) - G^{\mathrm{A}}(\omega)\right] \tanh(\beta\omega/2)\,, \tag{4.5.4}$$
$$\Sigma^{\mathrm{K}}(\omega) = \left[\Sigma^{\mathrm{R}}(\omega) - \Sigma^{\mathrm{A}}(\omega)\right] \tanh(\beta\omega/2). \tag{4.5.5}$$

Non-Equilibrium

For the non-equilibrium steady-state we find analogously

$$G^{\mathrm{R}}(\omega) = G^{\mathrm{A}}(\omega)^\dagger\,, \quad G^{\mathrm{K}}(\omega) = -G^{\mathrm{K}}(\omega)^\dagger\,, \quad G^{\nu,\nu'}(\omega) = -G^{-\nu',-\nu}(\omega)^\dagger\,, \tag{4.5.6}$$
$$\Sigma^{\mathrm{R}}(\omega) = \Sigma^{\mathrm{A}}(\omega)^\dagger\,, \quad \Sigma^{\mathrm{K}}(\omega) = -\Sigma^{\mathrm{K}}(\omega)^\dagger\,, \quad \Sigma^{\nu,\nu'}(\omega) = -\Sigma^{-\nu',-\nu}(\omega)^\dagger\,, \tag{4.5.7}$$

under *complex conjugation*. For real times this amounts to

$$G^{\mathrm{R}}(t,t') = G^{\mathrm{A}}(t',t)^\dagger\,, \quad G^{\mathrm{K}}(t,t') = -G^{\mathrm{K}}(t',t)^\dagger\,, \quad G^{\nu,\nu'}(t,t') = -G^{-\nu',-\nu}(t',t)^\dagger\,, \tag{4.5.8}$$
$$\Sigma^{\mathrm{R}}(t,t') = \Sigma^{\mathrm{A}}(t',t)^\dagger\,, \quad \Sigma^{\mathrm{K}}(t,t') = -\Sigma^{\mathrm{K}}(t',t)^\dagger\,, \quad \Sigma^{\nu,\nu'}(t,t') = -\Sigma^{-\nu',-\nu}(t',t)^\dagger. \tag{4.5.9}$$

A central relation between the Green's functions and self-energies, briefly commented on above[29], is *causality*. We re-iterate it in this symmetry section for completeness

$$\sum_{\nu,\nu'=\pm} (\nu)(\nu') G^{\nu,\nu'} = 0\,, \qquad \sum_{\nu,\nu'=\pm} \Sigma^{\nu,\nu'} = 0. \tag{4.5.10}$$

Beside the mentioned symmetries there are of course a multitude of additional potential symmetries, which depend on details of the system (e.g. particle-hole symmetry). To discuss those and their conservation within the FRG treatment (under the assumption that the original system inherits them) we scrutinize them separately in the following section.

4.5.2 ... and Their Conservation

Conservation due to Diagramatic Structure

The FRG treatment outlined above inherits some trivial symmetry conservations from its diagrammatic motivation. Among those are the *anti-symmetry* of the effective two-particle interaction

$$\gamma_2^\Lambda(1',2',1,2) = -\gamma_2^\Lambda(1',2',2,1) = -\gamma_2^\Lambda(2',1',1,2)\,, \tag{4.5.11}$$

and the *frequency (energy) conservation* of $\gamma_{1/2}$ if the above truncation schemes are applied. Furthermore, conserved *single-particle degrees of freedoms* and *symmetries under rotations of the former* are preserved in any truncation order. Popular examples of those two symmetries are conserved spin-degrees of freedom or the symmetry under rotation of the spin sectors. Furthermore, in equilibrium[30] certain parameter points in ϵ can often be distinguished in the sense that

$$G^\epsilon(i\omega) = -G^{\epsilon\to\tilde{\epsilon}}(i\omega)^*\,, \quad \Sigma^\epsilon(i\omega) = -\Sigma^{\epsilon\to\tilde{\epsilon}}(i\omega)^*\,, \quad \gamma_2^\epsilon(1',2',1,2) = \gamma_2^{\epsilon\to\tilde{\epsilon}}(1',2',1,2)\,, \tag{4.5.12}$$

which will be called *particle-hole symmetry* in the following. This symmetry is likewise conserved for the approximate FRG treatment.

[28] This is e.g. useful when reproducing the equilibrium limit within the Keldysh framework or when calculating reservoirs' properties initially held at equilibrium.

[29] It was used to make explicit that of the four Green's functions in the (+-)-basis only three are actually independent and motivated the rotation to the RKA-basis.

[30] Similar statements carry over to the Hamiltonian of a non-equilibrium problem, but not to the Green's functions in general (where also statics are involved).

Complex Conjugation and Causality

It is also quite easy to see that the symmetries under complex conjugation, outlined above, are always conserved in the truncated FRG treatment used here (first or second order truncation scheme) [Jak09, Kar10a]. More complicated is the case of causality in non-equilibrium problems. Its conservation depends on the cut-off used. While the sharp cut-off scheme preserves causality only to the truncation order, the reservoir cut-off scheme preserves it to arbitrary order. This explains why the latter is always the cut-off scheme of choice for non-equilibrium. As only first order truncation schemes are used in this case, it is trivial to show, that from $\Sigma^{\mathrm{R},\Lambda} = \Sigma^{\mathrm{A},\Lambda}$ and $\Sigma^{\mathrm{K},\Lambda} = 0$,

$$\partial_\Lambda \sum_{\nu,\nu'=\pm} \Sigma^{\nu,\nu',\Lambda} = 0 \,, \tag{4.5.13}$$

follows for real-time [Ken11] as well as real-frequency space [Jak09, Kar10a] (and which is nothing but the conservation of causality). As a by-product one also finds that the equilibrium limit dissipation-fluctuation theorem of Eq. (4.5.5) remains conserved in this case.

Finally, more complicated symmetries, e.g. time-reversal, Martin-Kubo-Schwinger relations and so on could be analyzed, but since this is of minor relevance in what follows the interested reader is simply referred to [Kar10a] for equilibrium as well as to [Jak09] for non-equilibrium setups.

Chapter 5

Density Matrix Renormalization Group

Contents

5.1. Matrix Product States **58**
5.1.1. From a Quantum State to a MPS: Singular Value Decomposition 58
5.1.2. Left, Right and Mixed Canonical Forms 60
5.1.3. Γ-Λ Notation 61
5.2. Matrix Product Operator **62**
5.3. Symmetries **64**
5.4. From MPS and MPO to Observables **65**
5.5. Iterative Ground State Calculations **66**
5.5.1. The Crucial Ingredient: The Update 67
5.5.2. Explicit Algorithm 67
5.5.3. One- vs. Two-Site DMRG: Advantages and Possible Pitfalls 68
5.6. Real and Imaginary Time Evolution **68**
5.6.1. Trotter and co. 69
5.6.2. Ground States Revisited 71
5.6.3. Finite Temperatures and Purification 71
5.7. From Finite Size to Infinite Size DMRG **75**
5.7.1. Ground States of Infinite Systems 75
5.7.2. Real and Imaginary Time Evolutions 76
5.8. DMRG: Success and Failure **76**

Introduction

In the following chapter the *density matrix renormalization group* (DMRG) approach used in this thesis will be outlined briefly. Over the last decade DMRG has proven to be an invaluable tool to tackle low-dimensional – in practice mostly one-dimensional – interacting quantum systems with extreme accuracy. Starting from its original invention in 1992 by S. White [Whi92,Whi93] DMRG was reformulated in various ways. Originally, completely unrelated research let to the discovery of matrix product states as a fascinating subclass of quantum states which, e.g., can be used to represent states of interacting one-dimensional systems very cleverly (e.g. see [Bax68] and references therein). Only later in a two step development, first for infinite [Öst95] and later also for finite [Duk98] system sizes, it was realized that DMRG, when applied in one-dimension, can be very naturally formulated in terms of these matrix product states. Since in this thesis we will focus exclusively on one-dimensional systems the convenient matrix product states formulation of DMRG will be employed and all subsequent statements are implicitly made in this one-dimensional context.

Fundamental Idea

For a generic quantum many-body system the dimension of the underlying Hilbert space scales exponentially in the number of particles, which makes an exact solution (via diagonalization) impractical. In fact only systems with very few particles [$N \sim \mathcal{O}(10)$] can be treated this way. On the other hand, depending on the questions under examination, not every of these exponentially many quantum states is equally relevant. For example, qua their very definition, the ground state properties depend on only a single of such states, namely the ground state itself. DMRG is inspired by the numerical renormalization group developed by K. Wilson to tackle the Kondo problem [Wil75] and similarly aims to retain only the relevant part of the exponentially large Hilbert space. Originally set up for examining ground state properties the DMRG thus retains only the energetically low-lying states, while disregarding all highly excited ones. By iteratively bi-partitioning the full system into different subsystems and reservoirs the optimal density matrix – with the lowest energy – is found. Put simple the idea is to optimize iteratively different parts of the system, instead of trying to look at the full system at once. This way one (as seen in many application justifiably) hopes that the algorithm converges to the ground state of the full system. Today, and also in this thesis, DMRG is applied in a much wider range, than only in the context of describing ground states, and is used successfully to tackle also (thermo)dynamical questions. This is possible due to the ability of stating precisely which part of the quantum states needs to be kept and which part can be safely neglected as will be explained below. How much numerical effort is needed to describe a quantum system accurately increases drastically with the amount of entanglement in the system. Employing area laws for entanglement shows that one-dimensional systems are thus natural candidates for a DMRG treatment.

Outline

The remainder of this chapter is strongly based on the presentation of [Sch11b]. First, we introduce the general concept of matrix product states and operators in the first two sections (compare section 4 and 5 of [Sch11b], respectively). Those will be the framework underlying everything that follows. Afterwards, we will explain how Abelian symmetries and their conservation can be used to significantly speed up numerics. Then, we will show how observables can be calculated efficiently within the matrix product state representation. Next, we turn to the core algorithms needed in a DMRG treatment. We describe in more detail (a) iterative ground state calculations (compare section 6 of [Sch11b]) and (b) (either real or imaginary) time evolutions (compare section 7 of [Sch11b]). Finally, we describe how systems in the thermodynamic limit can be tackled (compare section 10 of [Sch11b]) as well as sum up briefly why and when DMRG succeeds or fails to describe a given quantum systems.

5.1 Matrix Product States

The Hilbert space of a system on a lattice of even length L with d local degrees of freedom scales exponentially as d^L. It is impossible in practice to handle this immense Hilbert space for $L \gtrapprox 40$, but luckily usually only a tiny corner of it is relevant for the questions one tries to answer. In one dimension a very efficient way of parametrizing this tiny corner is given by the so called *matrix product states* (MPS). Throughout this thesis we will adopt a graphical notation from [Sch11b] in which a MPS is represented as in Fig. 5.1. The details of this representation will become clear later.

5.1.1 From a Quantum State to a MPS: Singular Value Decomposition

First we want to examine how an arbitrary quantum state can be expressed in terms of a MPS. Let us again focus on a quantum state on a lattice of L sites and with a d dimensional local state space $\{\sigma_i\}$ on sites $i = 1 \dots L$

$$|\psi\rangle = \sum_{\sigma_1,\dots,\sigma_L} c_{\sigma_1,\dots,\sigma_L} |\sigma_1, \dots, \sigma_L\rangle . \tag{5.1.1}$$

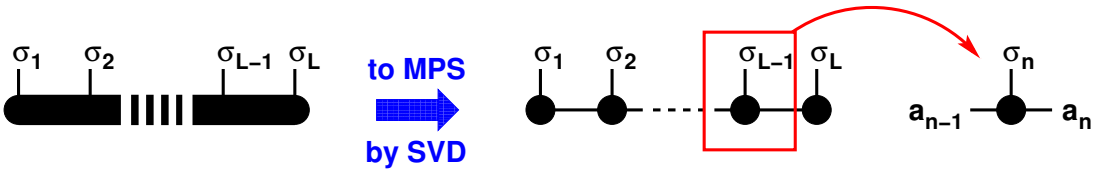


Figure 5.1.: Any quantum state can be decomposed into a MPS via employing SVDs successively. A MPS is represented by a line of filled circles with three legs attached to each of them, corresponding to the two unphysical (left and right) and single physical (top) degree of freedom. A single matrix of the MPS is shown in the very right.

The quantum state is characterized by the d^L coefficients $c_{\sigma_1,\ldots,\sigma_L}$. We reshape this tensor by grouping together all indices but the first as $c_{\sigma_1,\ldots,\sigma_L} = \Psi_{(\sigma_1),(\sigma_2,\ldots,\sigma_L)}$ and subsequently perform a *singular value decomposition* (SVD) of the resulting matrix $\Psi_{(\sigma_1),(\sigma_2,\ldots,\sigma_L)} \in \mathbb{C}^{d\times d^{L-1}}$. For any matrix $M \in \mathbb{C}^{N_A\times N_B}$ by employing a SVD one can construct a decomposition of the form $M = USV^\dagger$ with the following properties:

1. $U \in \mathbb{C}^{N_A\times \min(N_A,N_B)}$ and $U^\dagger U = 1$.
2. $S \in \mathbb{C}^{\min(N_A,N_B)\times\min(N_A,N_B)}$. S is diagonal with the so called *singular values* $S_{n,n} = s_n \geq 0$ being the diagonal entries. The number of non-zero singular values is called Schmidt rank r of M. All non-zero singular values are chosen to be arranged in descending order $s_1 \geq s_2 \geq s_3 \geq \cdots \geq s_r > 0$.
3. $V \in \mathbb{C}^{\min(N_A,N_B)\times N_B}$ and $V^\dagger V = 1$.

This way one achieves the form

$$c_{\sigma_1,\ldots,\sigma_L} = \underbrace{\Psi_{(\sigma_1),(\sigma_2,\ldots,\sigma_L)}}^{\text{SVD}} = \sum_{a_1=1}^{r_1} U_{\sigma_1,a_1} S_{a_1,a_1} (V^\dagger)_{a_1,(\sigma_2,\ldots,\sigma_L)} = \sum_{a_1=1}^{r_1} A^{\sigma_1}_{a_1} c_{a_1,\sigma_2,\ldots,\sigma_L}, \tag{5.1.2}$$

where we have reshaped $U_{\sigma_1,a_1} = A^{\sigma_1}_{a_1}$ and $S_{a_1,a_1}(V^\dagger)_{a_1,(\sigma_2,\ldots,\sigma_L)} = c_{a_1,\sigma_2,\ldots,\sigma_L}$ in the last step. Next, concentrating on $c_{a_1,\sigma_2,\ldots,\sigma_L}$, we once more reshape $c_{a_1,\sigma_2,\ldots,\sigma_L}$ into the matrix $\Psi_{(a_1,\sigma_2),(\sigma_3,\ldots,\sigma_L)}$. Again performing an SVD of this matrix leads to

$$\begin{aligned} c_{\sigma_1,\ldots,\sigma_L} &= \sum_{a_1=1}^{r_1} A^{\sigma_1}_{a_1} \underbrace{\Psi_{(a_1,\sigma_2),(\sigma_3,\ldots,\sigma_L)}}^{SVD} = \sum_{a_1=1}^{r_1}\sum_{a_2=1}^{r_2} A^{\sigma_1}_{a_1} U_{(a_1,\sigma_2),a_2} S_{a_2,a_2} (V^\dagger)_{a_2,(\sigma_3,\ldots,\sigma_L)} \\ &= \sum_{a_1=1}^{r_1}\sum_{a_2=1}^{r_2} A^{\sigma_1}_{a_1} A^{\sigma_2}_{a_1,a_2} c_{a_2,\sigma_3,\ldots,\sigma_L}, \end{aligned} \tag{5.1.3}$$

with analogous reshaping of matrices $U_{(a_1,\sigma_2),a_2} = A^{\sigma_2}_{a_1,a_2}$ and $S_{a_2,a_2}(V^\dagger)_{a_2,(\sigma_3,\ldots,\sigma_L)} = c_{a_2,\sigma_3,\ldots,\sigma_L}$. Because of the form $A^{\sigma_2}_{a_1,a_2}$ a single matrix of the MPS is represented as in the right part of Fig. 5.1 by a circle with one physical index σ_n and two unphysical indices a_{n-1}, a_n sticking out to the top and left and right respectively. One can reiterate this procedure until all indices have been expressed in terms of A-matrices[1] as

$$c_{\sigma_1,\ldots,\sigma_L} = \sum_{\{a_i\}} A^{\sigma_1}_{a_1} A^{\sigma_2}_{a_1,a_2} \ldots A^{\sigma_{L-1}}_{a_{L-2},a_{L-1}} A^{\sigma_L}_{a_{L-1}}. \tag{5.1.4}$$

We have successfully recast the quantum state (5.1.1) into a MPS form (compare Fig. 5.1)

$$|\psi\rangle = \sum_{\{a_i\}} A^{\sigma_1}_{a_1} A^{\sigma_2}_{a_1,a_2} \ldots A^{\sigma_{L-1}}_{a_{L-2},a_{L-1}} A^{\sigma_L}_{a_{L-1}} |\sigma_1,\ldots,\sigma_L\rangle, \tag{5.1.5}$$

[1] actually the objects A are of course higher order tensors and only each of the d elements given by $A^{\tilde{\sigma}_i}$ with $\tilde{\sigma}_i \in \{\sigma_i\}$ are matrices $\in \mathbb{C}^{r_{i-1}\times r_i}$. Nonetheless, in a slight abuse of the usage matrix we will still refer to these (and similar) objects as A-matrices also to stay consistent with the prevailing literature.

but what have we gained? Recasting the quantum state in an MPS like this is an exact reformulation and does not – a priori – yield any simplification. The dimensions labelled by the indices $(\sigma_i \times a_{i-1} \times a_i)$ of the A-matrices are $(d \times 1 \times d)(d \times d \times d^2)(d \times d^2 \times d^3) \dots (d \times d^{L/2-1} \times d^{L/2})(d \times d^{L/2} \times d^{L/2-1}) \dots (d \times d^3 \times d^2)(d \times d^2 \times d)(d \times d \times 1)$ along the lattice[2], which in no way is easier to handle than the original coefficients $c_{\sigma_1,\dots,\sigma_L}$. The gain of this representation lies in the way optimal approximations can be employed. To understand this in detail we need to talk about different normalizations first.

5.1.2 Left, Right and Mixed Canonical Forms

Left Normalized MPS

In the previous section we have recast a general quantum state into a MPS by (5.1.5). But there is more to this representation than apparent on first glance. From the SVD the A-matrices inherit the important property

$$\sum_{\sigma_i} (A^{\sigma_i})^\dagger A^{\sigma_i} = 1 \tag{5.1.6}$$

of *left normalization* and are said to be in left canonical form. We will use normalization properties extensively in the following.

Right Normalized MPS

Similarly as outlined in the previous part we could have started the procedure of recasting the quantum state (5.1.1) into a MPS from the right. Analogously reshaping the $V^\dagger$ matrices into B-matrices and grouping U and S one arrives at

$$|\psi\rangle = \sum_{\{a_i\}} B^{\sigma_1}_{a_1} B^{\sigma_2}_{a_1,a_2} \dots B^{\sigma_{L-1}}_{a_{L-2},a_{L-1}} B^{\sigma_L}_{a_{L-1}} |\sigma_1, \dots, \sigma_L\rangle . \tag{5.1.7}$$

The resulting B-matrices by virtue of the SVD fulfil *right normalization*

$$\sum_{\sigma_i} B^{\sigma_i} (B^{\sigma_i})^\dagger = 1. \tag{5.1.8}$$

The representation by B-matrices is called right canonical form.

Mixed form of a MPS

Besides of purely left and right canonical forms there is also a mixed form. For this form we stop the iterative procedure to establish a, lets say, left canonical form of a MPS after the n-th SVD

$$c_{\sigma_1,\dots,\sigma_L} = \sum_{\{a_i\}} A^{\sigma_1}_{a_1} A^{\sigma_2}_{a_1,a_2} \dots A^{\sigma_n}_{a_{n-1},a_n} S_{a_n,a_n} (V^\dagger)_{a_n,(\sigma_{n+1},\dots,\sigma_L)}. \tag{5.1.9}$$

Decomposing $(V^\dagger)_{a_n,(\sigma_{n+1},\dots,\sigma_L)}$ in the same fashion as for establishing the right canonical form of a MPS gives

$$(V^\dagger)_{a_n,(\sigma_{n+1},\dots,\sigma_L)} = \sum_{a_{n+1},\dots,a_{L-1}} U_{(a_n,\sigma_{n+1}),a_{n+1}} S_{a_{n+1},a_{n+1}} B^{\sigma_{n+2}}_{a_{n+1},a_{n+2}} \dots B^{\sigma_{L-1}}_{a_{L-2},a_{L-1}} B^{\sigma_L}_{a_{L-1}}. \tag{5.1.10}$$

[2] For simplicity we have introduced dummy indices of dimension one for the first and last A-matrix to cast all of them into the general form $A^{\sigma_i}_{a_{i-1},a_i}$.

$U_{(a_n,\sigma_{n+1}),a_{n+1}} S_{a_{n+1},a_{n+1}}$ can be reshaped itself to a B-matrix $U_{(a_n,\sigma_{n+1}),a_{n+1}} S_{a_{n+1},a_{n+1}} = B^{\sigma_{n+1}}_{a_n,a_{n+1}}$, because

$$\begin{aligned}\delta_{a_n,a_n'} &= \sum_{\sigma_{n+1},\ldots,\sigma_L} (V^\dagger)_{a_n,(\sigma_{n+1},\ldots,\sigma_L)} V_{(\sigma_{n+1},\ldots,\sigma_L),a_n'} \\ &= \left(\sum_{\sigma_{n+1},\ldots,\sigma_L} B^{\sigma_{n+1}} \underbrace{B^{\sigma_{n+2}} \ldots \underbrace{B^{\sigma_L - 1} \underbrace{B^{\sigma_L} (B^{\sigma_L})^\dagger} (B^{\sigma_L - 1})^\dagger} \ldots (B^{\sigma_{n+2}})^\dagger} (B^{\sigma_{n+1}})^\dagger \right)_{a_n,a_n'} \\ &= \left(\sum_{\sigma_{n+1}} B^{\sigma_{n+1}} (B^{\sigma_{n+1}})^\dagger \right)_{a_n,a_n'},\end{aligned} \tag{5.1.11}$$

as also V results of a SVD.

This finally yields the form

$$|\Psi\rangle = \sum_{\{a_i\}} A^{\sigma_1}_{a_1} A^{\sigma_2}_{a_1,a_2} \ldots A^{\sigma_n}_{a_{n-1},a_n} S_{a_n,a_n} B^{\sigma_{n+1}}_{a_n,a_{n+1}} \ldots B^{\sigma_{L-1}}_{a_{L-2},a_{L-1}} B^{\sigma_L}_{a_{L-1}} |\sigma_1, \ldots, \sigma_L\rangle , \tag{5.1.12}$$

which contains only left and right normalized A- or B-matrices left and right of the n-th bond, respectively.

Earlier it was advertised that the advantage of the DMRG framework (in MPS) is the exact knowledge of how to approximate in an optimal fashion the high dimensional Hilbert space, involved in any quantum many-body problem. In the MPS language this translates to the knowledge of how to deal with the – a priori – exponentially large dimensions of the unphysical, auxiliary indices a_n. Let us assume that we have expressed the quantum state in the mixed canonical form introduced in Eq. (5.1.12). In this case one can show [Ver06] that reducing the Schmidt rank r_n of S_{a_n,a_n} to $\chi_n = \tilde{r}_n < r_n$ by neglecting the $r_n - \tilde{r}_n$ smallest singular values yields the optimal approximation of $|\Psi\rangle$ under the 2-norm[3]. The truncation of singular values leads to a deviation of the approximated state $|\tilde{\Psi}\rangle$ from the exact one $|\Psi\rangle$ in the 2-norm proportional to the sum of the squared singular values neglected $\epsilon_n(\chi_n)$. By multiplying S_{a_n,a_n} to the A- or B-matrix to the left or right of it and subsequently performing a SVD one can shift the bond before which only A-matrices and after which only B-matrices appear by one site. After the SVD was performed we can once more employ the same truncation as above. By doing so for all sites, all indices a_n can be reduced in dimension which leads to a total error at worst given by [Ver06]

$$|| \, |\tilde{\Psi}\rangle - |\Psi\rangle \, ||_2 \leq 2 \sum_{n=1}^{L} \epsilon_n(\chi_n). \tag{5.1.13}$$

The crucial point here is the fact, that the singular values – arranged in descending order – of such a MPS for one-dimensional systems in most cases decrease in magnitude quite quickly (exponentially in practice). Thus a much smaller (than the originally exponentially large) Schmidt rank can be used, without appreciable loss of precision. In general when working with a MPS later on we will always renormalize the sum of squared singular values to one (by simply putting $S_{a_i,a_i} \to S_{a_i,a_i} / \sqrt{[\sum S^2_{a_i,a_i}]}$) after a truncation to respect the norm of the MPS.

5.1.3 Γ-Λ Notation

We have seen that when considering a certain bond it is advantageous that all matrices of the MPS left and right to that bond are left and right normalized, respectively. In the mixed form introduced this is true for a single bond (the n-th bond above) only. A natural question to ask is thus: Is there a simple representation in which for a single cut, bipartitioning the system into left and right subsystem, the left and right normalized A- and B-matrices can be read of directly? The question

[3] This is true if and only if all matrices to the left and right are left (A-matrices) and right (B-matrices) normalized respectively as is the case for the mixed canonical form.

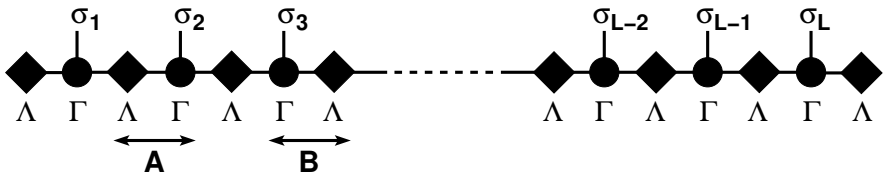


Figure 5.2.: A MPS in the Γ-Λ notation. Additionally, to the known object of Fig. 5.1, diagonal matrices (diamonds) are inserted to retain both left and right normalization simultaneously.

was positively answered in [Vid03]. The trick relies on introducing *diagonal* matrices Λ_n, such that each matrix of the MPS has two adjacent Λ-matrices as shown in Fig. 5.2. An arbitrary state can be written as

$$|\psi\rangle = \sum_{\{a_i\}} \Lambda_{a_0,a_0} \prod_{n=1}^{L} \Gamma^{\sigma_n}_{a_{n-1},a_n} \Lambda_{a_n,a_n} |\sigma_1, \dots, \sigma_L\rangle \,, \tag{5.1.14}$$

where $\Lambda_{a_0,a_0} = \Lambda_{a_L,a_L} = 1$ are dummy matrices with dimension 1×1 (scalar). Finally, we demand the correct left and right normalization for each $\sum_{a_{n-1}} \Lambda_{a_{n-1},a_{n-1}} \Gamma^{\sigma_n}_{a_{n-1},a_n} = A^{\sigma_n}_{a_{n-1},a_n}$ and $\sum_{a_n} \Gamma^{\sigma_n}_{a_{n-1},a_n} \Lambda_{a_n,a_n} = B^{\sigma_n}_{a_{n-1},a_n}$, respectively. How can one construct such a representation? Let us review the procedure to build a left normalized MPS from the coefficients $c_{\sigma_1,\dots,\sigma_L}$. After the first SVD we arrive at [compare Eq. (5.1.2)]

$$\begin{aligned} c_{\sigma_1,\dots,\sigma_L} &= \sum_{a_1} U_{\sigma_1,a_1} S_{a_1,a_1} (V^\dagger)_{a_1,(\sigma_2,\dots,\sigma_L)} = \sum_{a_1} \Lambda_{a_0,a_0} \Gamma^{\sigma_1}_{a_0,a_1} \Lambda_{a_1,a_1} (V^\dagger)_{a_1,(\sigma_2,\dots,\sigma_L)} \\ &= \sum_{a_1} \Lambda_{a_0,a_0} \Gamma^{\sigma_1}_{a_0,a_1} \Psi_{(a_1,\sigma_2),(\sigma_3\dots,\sigma_L)}, \end{aligned} \tag{5.1.15}$$

where we have introduced a dummy index a_0 as well as dummy Λ-matrix $\Lambda_{a_0,a_0} = 1$, relabelled and reshaped $U_{\sigma_1,a_1} = \Gamma^{\sigma_1}_{a_0,a_1}$ and $S_{a_1,a_1} = \Lambda_{a_1,a_1}$ and store Λ_{a_1,a_1} before it is multiplied to the right $\Lambda_{a_1,a_1}(V^\dagger)_{a_1,(\sigma_2,\dots,\sigma_L)} = \Psi_{(a_1,\sigma_2),(\sigma_3\dots,\sigma_L)}$. In the next step we proceed similarly

$$\begin{aligned} c_{\sigma_1,\dots,\sigma_L} &= \sum_{a_1,a_2} \Lambda_{a_0,a_0} \Gamma^{\sigma_1}_{a_0,a_1} A^{\sigma_2}_{a_1,a_2} \Lambda_{a_2,a_2} (V^\dagger)_{a_2,(\sigma_3,\dots,\sigma_L)} \\ &= \sum_{a_1,a_2} \Lambda_{a_0,a_0} \Gamma^{\sigma_1}_{a_0,a_1} \Lambda_{a_1,a_1} \Gamma^{\sigma_2}_{a_1,a_2} \Lambda_{a_2,a_2} (V^\dagger)_{a_2,(\sigma_3,\dots,\sigma_L)} \\ &= \sum_{a_1,a_2} \Lambda_{a_0,a_0} \Gamma^{\sigma_1}_{a_0,a_1} \Lambda_{a_1,a_1} \Gamma^{\sigma_2}_{a_1,a_2} \Psi_{(a_2,\sigma_3),(\sigma_4\dots,\sigma_L)}, \end{aligned} \tag{5.1.16}$$

calling $S_{a_2,a_2} = \Lambda_{a_2,a_2}$ and crucially replacing the $A-$matrix resulting out of the SVD by $A^{\sigma_2}_{a_1,a_2} = \Lambda_{a_1,a_1} \Gamma^{\sigma_2}_{a_1,a_2}$ for which storing Λ_{a_1,a_1} was necessary[4]. This step can be reiterated until the last site is reached, where we additionally introduce the dummy Λ-matrix $\Lambda_{a_L,a_L} = 1$. By Construction of course $A^{\sigma_n}_{a_{n-1},a_n} = \Lambda_{a_{n-1},a_{n-1}} \Gamma^{\sigma_n}_{a_{n-1},a_n}$ is then left normalized. The fact that also all $B^{\sigma_n}_{a_{n-1},a_n} = \Gamma^{\sigma_n}_{a_{n-1},a_n} \Lambda_{a_n,a_n}$ are right normalized can be checked in perfect analogy to the short calculation presented in Eq. (5.1.11).

Thus for any bond the A (B)-matrices left (right) of it can be read of as $\Lambda\Gamma$ ($\Gamma\Lambda$). This representation therefore largely simplifies handling the MPS and will be our usual choice in the following.

5.2 Matrix Product Operator

With the concept of matrix product states at hand we have completed almost all the preliminary work. Only one – quite analogous concept –, namely the concept of *matrix product operators* (MPO) needs to be introduced before we can dive into some concrete DMRG algorithms. A MPO

[4] The involved inversion of singular values should be handled with care. Very small singular values (albeit close to machine precision) should be neglected to avoid numerical instabilities.

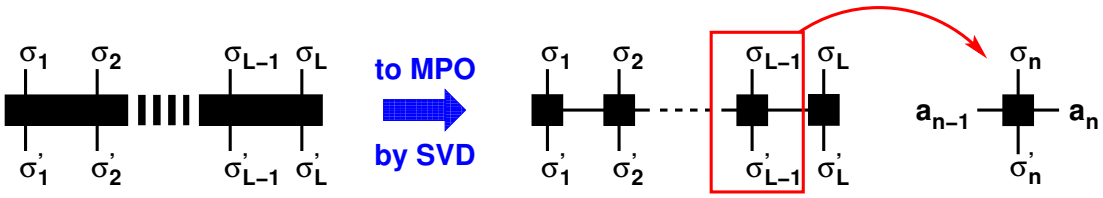


Figure 5.3.: The same decomposition as shown in Fig. 5.1 now done for the MPO. The decomposition leads to elementary matrices (squares) which compared to their MPS counterparts (circles of Fig. 5.1) obtain an additional physical index (pointing to the bottom).

is quite similar to a MPS, the crucial difference being though that two, not one, physical indices are assigned to each constituent of the MPO, because it describes an operator instead of a wave function (compare Fig. 5.3). The most instructive way to understand the MPO representation of arbitrary operators might be to consider an example. Let us look at the operator[5] (where $S^i = 1/2\ \sigma^i$ and $i = x, y, z$)

$$\begin{aligned} H =& J \sum_{n=1}^{L-1} S_n^x S_{n+1}^x + S_n^y S_{n+1}^y + \Delta S_n^z S_{n+1}^z + h \sum_{n=1}^{L} S_n^z \\ =& J \sum_{n=1}^{L-1} \frac{1}{2} \left(S_n^+ S_{n+1}^- + S_n^- S_{n+1}^+ \right) + \Delta S_n^z S_{n+1}^z + h \sum_{n=1}^{L} S_n^z \\ =& J/2\ \ (S_1^+ \otimes S_2^- \otimes 1 \otimes 1 \otimes 1 \otimes \dots) + J/2\ \ (1 \otimes S_2^+ \otimes S_3^- \otimes 1 \otimes 1 \otimes \dots) + \dots \\ & J/2\ \ (S_1^- \otimes S_2^+ \otimes 1 \otimes 1 \otimes 1 \otimes \dots) + J/2\ \ (1 \otimes S_2^- \otimes S_3^+ \otimes 1 \otimes 1 \otimes \dots) + \dots \\ & J\Delta\ \ (S_1^z \otimes S_2^z \otimes 1 \otimes 1 \otimes 1 \otimes \dots) + J\Delta\ \ (1 \otimes S_2^z \otimes S_3^z \otimes 1 \otimes 1 \otimes \dots) + \dots \\ & h\ \ (S_1^z \otimes 1 \otimes 1 \otimes 1 \otimes 1 \otimes \dots) + h\ \ (1 \otimes S^z \otimes 1 \otimes 1 \otimes 1 \otimes \dots) + \dots \quad . \end{aligned} \tag{5.2.1}$$

which is to be decomposed into a product of matrices (with two additional indices per matrix) $H_{\sigma_1,\dots,\sigma_n;\sigma_1',\dots,\sigma_n'} = W^{[1]}_{\sigma_1,\sigma_1'} W^{[2]}_{\sigma_2,\sigma_2'} \dots W^{[L-1]}_{\sigma_{L-1},\sigma_{L-1}'} W^{[L]}_{\sigma_L,\sigma_L'}$ just like a quantum state was decomposed into a MPS (see Fig. 5.3). We introduce the additional superscript $[n]$ only for shorthand notation later on. Although successively employing SVDs, now to the many-body operator instead of the many-body wave function, guarantees the existence of such a decomposition, for operators of the given type of Eq. (5.2.1) a more straightforward approach can be used [McC07]. In fact it becomes surprisingly easy to see the decomposition when considering an arbitrary chosen operator string of H from the right to the left. From the last representation in Eq. (5.2.1) one can see that from the right one encounters unities until one hits one of four[6] non-trivial operators. If one first encounters $S^+(S^-)$ the next operator is $S^-(S^+)$ followed by only unity operators. The same is true for the $S_n^z S_{n+1}^z$-term for which after the first S^z a second one follows and then only unity operators again. The field term $\propto h$ takes an even simpler form as after the S^z directly only unity operators can show up. For book-keeping reasons we thus introduce 5 states:

- state 1: Only unity operators to the right.
- states 2,3 and 4: one S^+,S^- or S^z, respectively, just to the right.
- state 5: completed interaction- (S^+S^-,S^-S^+ or S^zS^z) or field term ($-hS^z$) to the right, which corresponds to only unity operators to the left.

In this auxiliary state space only very few possible transitions can be induced by the operators. Starting in state 1, those are $1 \to 1$ by 1, $1 \to 2$ by S^+, $1 \to 3$ by S^-, $1 \to 4$ by S^z and $1 \to 5$

[5] This is the Hamilton operator of a spin-1/2 anisotropic Heisenberg chain (XXZ), which (among other ones) is a standard model for a DMRG treatment.

[6] different operators of course contain a different number of non-trivial operators to be encountered, but this does not alter the general procedure.

by $-hS^z$. To complete the interaction part transitions $2 \to 5$ by $J/2\ S^-$, $3 \to 5$ by $J/2\ S^+$ and $4 \to 5$ by $J\Delta\ S^z$, must follow. After this to complete the string to the left only unities giving trivial transitions from $5 \to 5$ are allowed. Since one needs to start at state 1 (interaction- or field term will follow as one moves from right to left) and end at state 5 (completed interaction- or field term) the MPO, based on the allowed transitions mentioned above, reads

$$
\begin{aligned}
H &= \prod_{n=1}^{L} W^{[n]}, \\
W^{[n]} &= \begin{pmatrix} 1 & 0 & 0 & 0 & 0 \\ S^+ & 0 & 0 & 0 & 0 \\ S^- & 0 & 0 & 0 & 0 \\ S^z & 0 & 0 & 0 & 0 \\ -hS^z & (J/2)\ S^- & (J/2)\ S^+ & J\Delta\ S^z & 1 \end{pmatrix} \qquad \forall\ 1 < n < L, \\
W^{[1]}_{k,l} &= W^{[2]}_{5,l} \quad \text{and} \quad W^{[L]}_{g,h} = W^{[L-1]}_{g,1},
\end{aligned}
\tag{5.2.2}
$$

where we have introduced dummy indices k, h (of dimension one) for convenience. Note the tremendous reduction in the dimensionality of the operator from originally ($d = 2$ in this example) $2^L \times 2^L$ to roughly $L \times (5 \times 2) \times (5 \times 2)$. The exemplified procedure works also for longer-ranged interactions by introducing unity operators also in the center of $W^{[n]}$, which "carry" the interaction over uninvolved sites. Very long-ranged interactions, when treated this way, however tend to lead to a significant increase in the dimensions of the auxiliary state space. On the other hand, it is known [Frö10, Cro08] that for certain types of long-ranged interaction a more clever – meaning more compact – form for the MPO can be found differently.[7] In this thesis we will consider rather short ranged interaction only such that the procedure exemplified above will completely suffice.

5.3 Symmetries

It is yet another advantage of the MPS and MPO representation that symmetries can be included in a particularly instructive fashion. We will concentrate here on additive Abelian symmetries which are incorporated rather easily[8]. Let us assume that for our physical system we have identified an additive symmetry, which defines a good quantum number M. This good quantum number has to be preserved in all operations applied to the MPS within our DMRG treatment for it to be useful. We will focus on iterative ground state searches as well as time evolutions in the following. For both of those one can easily see that (as one is basically only applying the system's Hamiltonian) the good quantum numbers are conserved in an exact treatment. On the other hand, we employ truncations. This however does not jeopardize the use of good quantum numbers because states kept or thrown away can always be associated one-to-one with a well defined value of the good quantum number to the left (and via fixed global value of the quantum number also to the right) of the truncated bond under scrutiny. Why this is the case will become clear in the following.

Usage of the Abelian symmetry manifests in a block structure of the MPS and MPO matrices. We concentrate on MPSs in the following, while MPOs can be treated analogously. Starting from the left (where we set $M = 0$) we move through the chain one site at a time. First, we assign to the (dummy) index a_0 of the first matrix the value 0 of the good quantum number. For the MPS to exploit the good quantum number, elements of $A^{\sigma_1}_{a_0,a_{a_1}}$ must be non-zero (block structure) only for

$$
M(|a_{i-1}\rangle) + M(|\sigma_i\rangle) = M(|a_i\rangle), \tag{5.3.1}
$$

which assigns the possible values of the magnetization $[M(|a_0\rangle) + M(|\sigma_1\rangle)]$ to the left of the bond of a_1 uniquely to certain entries of a_1. This can be continued for all a_i.

[7] E.g. for $H = J \sum_{n,r} \lambda^r S^z_n S^z_{n+r}$ the auxiliary state space can be chosen to only be three dimensional.

[8] while others such as SU(2) symmetries are much more difficult to handle. Note however that those can, and in certain works actually already are, taken into account explicitly.

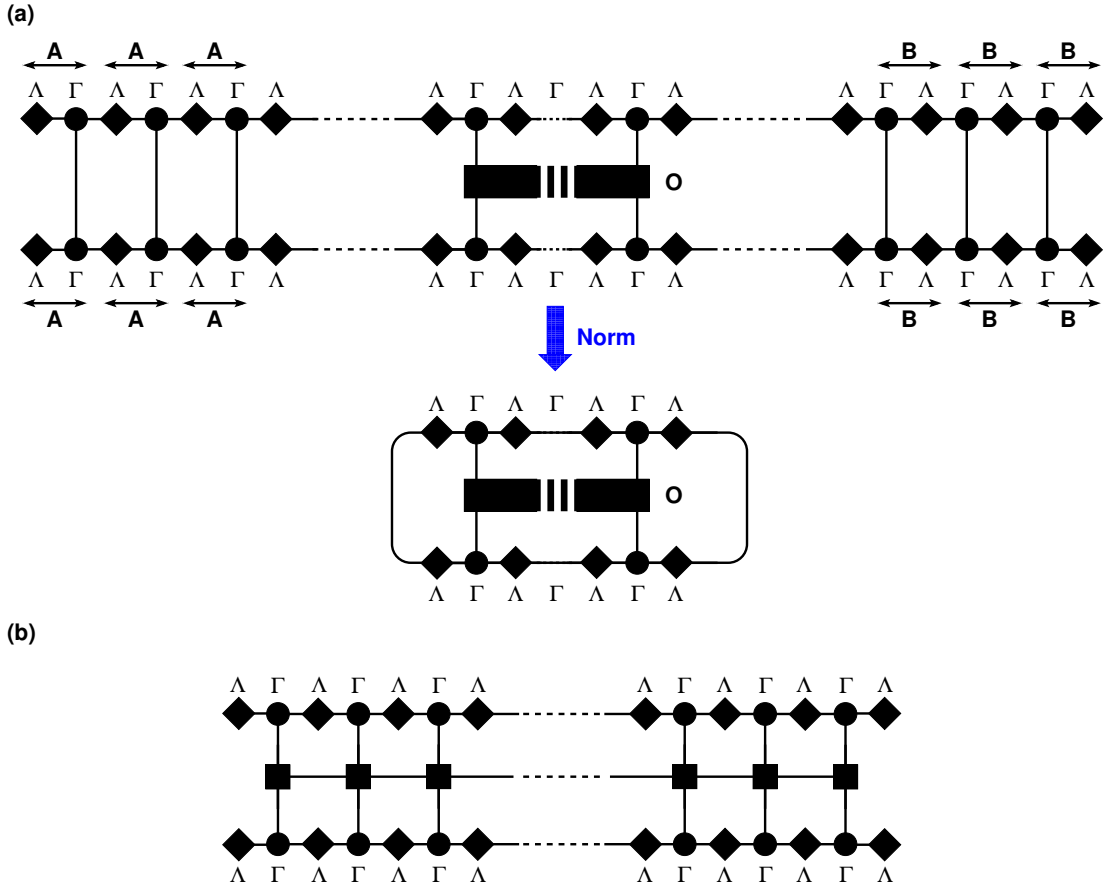


Figure 5.4.: Top: Evaluation of local observables in the Γ-Λ notation. Due to the normalization the evaluation of local observables only involves the contraction of the much smaller network shown in the lower part. Bottom: Evaluation of global observables in the Γ-Λ notation. Calculating the contraction successively from left to right makes the evaluation feasible.

An example will shed light on this issue. Let us consider a MPS of an XXZ model defined in Eq. (5.2.1), where the adjacent sites are pairwise in a single state. The MPS then reads

$$A^{2i+1} = \begin{matrix}\uparrow: \\ \downarrow:\end{matrix}\begin{bmatrix}1 & 0 \\ 0 & -1\end{bmatrix} \qquad A^{2i} = \begin{matrix}\uparrow: \\ \downarrow:\end{matrix}\begin{bmatrix}0 & 1/\sqrt{2} \\ 1/\sqrt{2} & 0\end{bmatrix}^T, \tag{5.3.2}$$

in left canonical form. If we assign quantum numbers 1 and -1 to $\uparrow$ and $\downarrow$, respectively, the first index of a_1 (non-zero only for $\sigma_1 = \uparrow$) would consequently be assigned to $M = 1$ and the second index (non-zero only for $\sigma_1 = \downarrow$) to $M = -1$. We continue with the next site. The ingoing index a_1 is associated with $M = 1$ or $M = -1$, respectively, and therefore, following Eq. (5.3.1), the single entry of a_2 is then associated with $M = 0$ (as it should in this simple singlet example). This carries over periodically to all further sites. The block structure (given above) will obviously get much more complicated during the DMRG treatment (sweeps or applications of time evolution operators, see below), but always retain its block diagonal form. It is by using this block diagonal form in all costly operations (eigenvalue solver, SVD, multiplications) that immense speed ups can be achieved.

5.4 From MPS and MPO to Observables

So far we have seen how any quantum state (or operator) can be put into MPS (or MPO) form. But what can we do with this? A whole lot, as will become clear in the following sections. Here we

show the first useful application of the MPS language; calculating observables, which is of course the ultimate goal of any inquiry. We have put our quantum state $|\Psi\rangle$ into the form of the Γ-Λ-notation shown in Eq. (5.2) and now we want to calculate the expectation value of some local observable $O_{\sigma_r \dots \sigma_{r+s}, \sigma'_r \dots \sigma'_{r+s}}$. For the moment we will not reformulate the operator O into a MPO, because we assume s to be rather small, such that one can still handle O easily. Technically we have to calculate $\langle\Psi| O |\Psi\rangle$, which in our pictorial representation corresponds to a contraction of the form shown in Fig. 5.4(a). Now the full power of our MPS representation can be used: All the contractions over all $\Lambda\Gamma$ left and all $\Gamma\Lambda$ right of the block containing O are trivially unities due to left and right normalization of theses matrices, respectively. One just needs to evaluate the much smaller contraction including the sites r to $r+n$ [compare Fig. 5.4(a)].

But not only rather local observables can be calculated efficiently. Given the worst case scenario of a global operator $O_{\sigma_1 \dots \sigma_L, \sigma'_1 \dots \sigma'_L}$ we can still make progress. Using MPS for the state and translating O to a MPO we can contract the network shown in Fig. 5.4(b) all the way from left to right while the numerical effort remains manageable. A task numerically hopelessly expensive for larger systems without the representations as MPS and MPO. The overlap of two different quantum states $\langle\psi|\phi\rangle$ can be viewed as a special case of this contraction without the MPO in the middle of the two states and is thus evaluated best by just calculating the corresponding network successively from left to right.

5.5 Iterative Ground State Calculations

Let us finally put the outlined framework of MPS and MPO to some practical use by showing how to efficiently implement ground state searches within DMRG. There are of course different ways of finding the ground state properties (e.g. numerical renormalization group [Hew02], density functional theory [Dre90], FRG [Met12], ...) of an arbitrary quantum system, but the iterative DMRG procedure has proven to be one of the ultimate tools for this task considering one-dimensional systems. Besides of an iterative ground state search one could also employ an imaginary time evolution from some random MPS within DMRG, which will be covered in the next section. However, in terms of performance and stability the iterative search is the state-of-the-art algorithm and therefore our favourite method of choice.

The problem of finding the ground state $|\Psi_0\rangle$ of a system can be seen as the variational problem of minimizing the energy

$$E = \frac{\langle\Psi| H |\Psi\rangle}{\langle\Psi|\Psi\rangle} , \tag{5.5.1}$$

with respect to $|\Psi\rangle$ under a given Hamilton operator H. Straightforwardly, varying the wave function $|\Psi\rangle$ in its parameters σ_i gives d^L configurations, which for $L \propto \mathcal{O}(10)$ already becomes a numerically challenging task. DMRG formulated in MPS in addition to having decomposed H as an MPO helps. The key idea is to move through the chain optimizing (in the sense of minimizing E) one matrix or two matrices of the MPS at a time. We will call the algorithms which handle one matrix or two matrices at a time one- or two-site DMRG, respectively. In the following we will focus on outlining the one-site version, but discuss advantages and pitfalls of each at the end.[9] We will move from the left most matrix in steps of one to the right until we reach the end of the chain, where we reverse the direction of update and move back from right to left. These so called right and left sweeps can be repeated until E has converged and one has (hopefully) found a good approximation to the ground state $|\Psi_0\rangle$. As can be seen the integral component of the algorithm is the update which moves the site under consideration by one. We will work with the mixed canonical form of the MPS in such a way that all the matrices to the left of the matrix to be updated are left normalized and similarly all matrices to the right of it are right normalized. The normalization of the matrix at the site under consideration itself is irrelevant. After the update the MPS with respect to the next (previous) site will fulfil this condition during a right(left) sweep.

[9] Implementation of both algorithm can be done analogously.

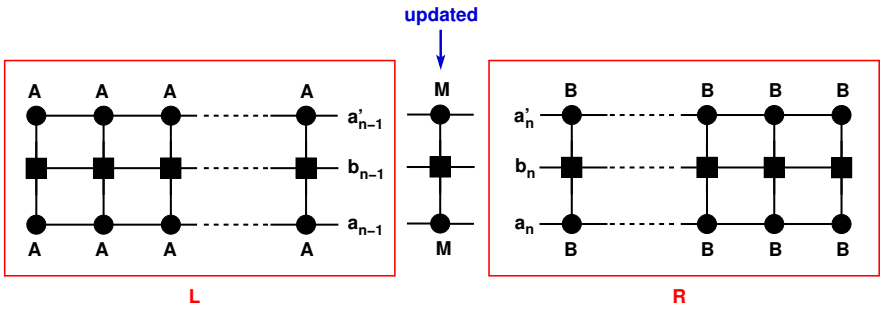


Figure 5.5.: Visualization of the iterative ground state algorithm. A single site is updated using explicitly only the shown tensors L and R (see text for further information).

5.5.1 The Crucial Ingredient: The Update

One can quite cleverly implement the main routine needed for an iterative ground state search update, which optimizes a single site and shifts the site under consideration by one. As the updates for the right and left sweeps work analogously (only reverse direction), we will concentrate on the one used within a right sweep only. During the update we will rely on the knowledge of the tensors called $L^{a_{n-1},a'_{n-1}}_{b_{n-1}}$ and $R^{a_n,a'_n}_{b_n}$ for all n which store the part of the overlap of the MPS-MPO-MPS contraction to the left and to the right of the n-th site to be updated, and which are shown in Fig. 5.5. Now we reformulate the initial problem of optimizing Eq. (5.5.1) trivially to the Lagrangian optimization problem

$$\langle\Psi|\,H\,|\Psi\rangle - E\langle\Psi|\,\Psi\rangle = 0, \tag{5.5.2}$$

where we simply have

$$\langle\Psi|\,H\,|\Psi\rangle = \sum_{\sigma_n,\sigma'_n} \sum_{a_{n-1},a'_{n-1},b_{n-1}} \sum_{a_n,a'_n,b_n} L^{a_{n-1},a'_{n-1}}_{b_{n-1}} W^{[n]\sigma_n,\sigma'_n}_{b_{n-1},b_n} R^{a_n,a'_n}_{b_n} M^{\sigma_n *}_{a_{n-1},a_n} M^{\sigma'_n}_{a'_{n-1},a'_n}\,, \tag{5.5.3}$$

$$\langle\Psi|\Psi\rangle = \sum_{\sigma_n,a_{n-1},a_n} M^{\sigma_n *}_{a_{n-1},a_n} M^{\sigma_n}_{a_{n-1},a_n}\,, \tag{5.5.4}$$

due to proper normalization.

In a next step the derivative with respect to $M^{\sigma_n *}_{a_{n-1},a_n}$ is taken in Eq. (5.5.2), leading to the simple extremal condition

$$\sum_{\sigma_n,\sigma'_n} \sum_{a_{n-1},a'_{n-1},b_{n-1}} \sum_{a_n,a'_n,b_n} L^{a_{n-1},a'_{n-1}}_{b_{n-1}} W^{[n]\sigma_n,\sigma'_n}_{b_{n-1},b_n} R^{a_n,a'_n}_{b_n} M^{\sigma'_n}_{a'_{n-1},a'_n} - E M^{\sigma_n}_{a_{n-1},a_n} \stackrel{!}{=} 0, \tag{5.5.5}$$

in form of an eigenvalue problem for the matrix $M_{(\sigma_n,a_{n-1}),a_n}$. After the optimal matrix $M_{(\sigma_n,a_{n-1}),a_n}$ is found, one can perform a singular value decomposition

$$M_{(\sigma_n,a_{n-1}),a_n} = A^{\sigma_n}_{a_{n-1},a'_n} S_{a'_n,a'_n} (V^\dagger)_{a'_n,a_n}. \tag{5.5.6}$$

The A-matrix is stored for site n, while $S_{a'_n,a'_n}(V^\dagger)_{a'_n,a_n}$ is multiplied to the right B-matrix at site $n+1$ calling it $M^{\sigma_{n+1}}$ for the next step. At this point the truncation of small singular values as described in section 5.1.2 can be employed to keep the problem manageable. As a last step we also update L by multiplying the new A-matrix as well as the n-th part of the MPO H to it to restore the tensor shown in Fig. 5.5 but with $n \to n+1$.

5.5.2 Explicit Algorithm

Most of the work goes in developing the update function described in the previous section. With this function at hand an iterative ground state search can be implemented by the following steps.

We start with some initial guess for the MPS to be optimized. Naively one can start from a product state (bond dimension $\chi = 1$) of some sort, but as the speed of the algorithm crucially relies (a) on the number of sweeps needed and (b) on quickly solving the eigenvalue problem of Eq. (5.5.5) one should try to provide good starting points to the routines. Concerning (b) as we are only interested in the lowest-lying eigenvalue E of Eq. (5.5.5), one should use implementations of eigensolvers such as Jacobi-Davidson or Lanczos[10] [Sch08c, Lan50]. The convergence speed of these solvers as well as the performance with respect to (a) crucially relies on the initial guess offered, such that taking a product state at the start of the algorithm might not be the most efficient thing to do. Luckily, there is a constructive way of finding a particularly good initial guess for the MPS, which will be discussed in section 5.7.

Subsequent steps can use the matrix M, which is stored for site n, as a good starting point of optimization. The routine starts from an MPS (initial guess before sweeping) which must be right normalized (B-matrices only) and we need to initialize the tensors R on all sites[11]. Next we can simply employ the update outlined above successively for sites 1 to $L-1$. This is the first right sweep. Afterwards, we reverse the direction of sweeping and perform a left sweep starting from site L going all the way back to site 2. Afterwards another right sweep follows and so on and so forth. The sweeping process is stopped when the energy E and the wave function $|\Psi\rangle$ have sufficiently converged to their respective ground state values. One has a very good tool at hand to measure how well the state has converged to the true ground state, by simply calculating

$$\Delta E^2 = \langle \Psi | H^2 | \Psi \rangle - (\langle \Psi | H | \Psi \rangle)^2. \tag{5.5.7}$$

In general $\Delta E^2 = 0$ only for an eigenstate of H, so if ΔE^2 vanishes (to a given tolerance) one has found (to this tolerance) a good approximation to the true ground state, jeopardized only by the unlikely scenario that by accident another eigenstate was targeted during the energy minimization procedure.

5.5.3 One- vs. Two-Site DMRG: Advantages and Possible Pitfalls

As mentioned two- and one-site implementation of the iterative ground state search algorithm are very similar. There are however performance and convergence differences to be discussed. The one-site algorithm outlined explicitly above is the fastest way of finding the ground state, because a two-site formulations involves finding the minimal eigenvalue at every update for a matrix which has dimension $d^2\chi^2 \times d^2\chi^2$ instead of $d\chi^2 \times d\chi^2$ as in the one-site case. This performance advantage of the one-site algorithm, however, has to be contrasted with the fact, that the one-site algorithm formulated above is quite prone to getting stuck in non-global energy minima. The two-site version is less plagued by this problem, which is founded in the fact, that in contrast to the one-site algorithm, it can mix more easily different symmetry sectors. Getting stuck in non-global minima can be circumvented in the one-site implementation very reliably by the procedure of White, which is outlined in detail in [Whi05] and will be employed here as well.

5.6 Real and Imaginary Time Evolution

For finding ground states DMRG was applied with much success, but actually more can be done. In MPS formulation the DMRG can be used very instructively to evolve an arbitrary pure state in (real or imaginary) time. This opens up the gateway to analyzing the dynamics and thermodynamics of arbitrary quantum systems and also provides an alternative – though usually less stable – route to the ground state properties.

[10] In all what follows we will restrict ourselves to using a Lanczos solver.

[11] For the first step only R is needed and L will be constructed on each site during the first sweep such that initially it can be set to dummy values.

5.6.1 Trotter and co.

We start with the Schrödinger equation for time independent H

$$i\frac{\partial}{\partial t}|\psi(t)\rangle = H|\psi(t)\rangle \quad \Rightarrow \quad |\psi(t)\rangle = e^{-iHt}|\psi(0)\rangle\,. \tag{5.6.1}$$

We thus need to apply the exponential of the Hamilton operator to the wave function to evolve it in time. Although, we have seen how to efficiently decompose and apply the many-particle Hamilton operator H to a wave function in section 5.2 we do not know how to this for its exponential, as the exponential turns sums of local terms into highly non-local ones. However using numerically controllable approximations to the exponential of H we can easily make progress. We note that [Hat05]

$$e^{-iHt} = \left(e^{-iHt/N}\right)^N = \left(e^{-iH\Delta t}\right)^N\,, \tag{5.6.2}$$

and

$$\begin{aligned} e^{-iH\Delta t} &= e^{-ih_1\Delta t}e^{-ih_3\Delta t}\ldots e^{-ih_{L-1}\Delta t}e^{-ih_2\Delta t}e^{-ih_4\Delta t}\ldots e^{-ih_{L-2}\Delta t} + \mathcal{O}(\Delta t^2) \\ &= e^{-iH_{\text{odd}}\Delta t}e^{-iH_{\text{even}}\Delta t} + \mathcal{O}(\Delta t^2), \end{aligned} \tag{5.6.3}$$

with $H = \sum_i h_i$, $H_{\text{odd/even}} = \sum_{i\ \text{odd/even}} h_i$ and $[h_i, h_j] = 0$ for i, j both odd or both even. This is called a first order *Trotter decomposition*, which allows to apply the exponential of H to order $\mathcal{O}(\Delta t^2)$, where we can choose Δt small enough[12] such that the Trotter decomposition poses an unimportant approximation. Importantly the approximation keeps $\exp(-iH\Delta t)$ unitary for $\Delta t \in \mathbb{R}$. We can systematically improve the order of the approximations, which allows for larger Δt. A second order Trotter decomposition reads

$$e^{-iH\Delta t} = e^{-iH_{\text{odd}}\Delta t/2}e^{-iH_{\text{even}}\Delta t}e^{-iH_{\text{odd}}\Delta t/2} + \mathcal{O}(\Delta t^3), \tag{5.6.4}$$

which will also be used in the following. Besides of the second order Trotter decomposition we also use the Trotter-Suzuki decomposition (fourth-order[13]) [Suz76]

$$\begin{aligned} e^{-iH\Delta t} =& e^{-iH_{\text{odd}}\Delta t_1/2}e^{-iH_{\text{even}}\Delta t_1}e^{-iH_{\text{odd}}\Delta t_1}e^{-iH_{\text{even}}\Delta t_1}e^{-iH_{\text{odd}}(\Delta t_1+\Delta t_2)/2}e^{-iH_{\text{even}}\Delta t_2} \\ & e^{-iH_{\text{odd}}(\Delta t_1+\Delta t_2)/2}e^{-iH_{\text{even}}\Delta t_1}e^{-iH_{\text{odd}}\Delta t_1}e^{-iH_{\text{even}}\Delta t_1}e^{-iH_{\text{odd}}\Delta t_1/2} + \mathcal{O}(\Delta t^5), \end{aligned} \tag{5.6.5}$$

where $\Delta t_1 = 1/(4 - \sqrt[3]{4})\Delta t$ and $\Delta t_2 = \Delta t - 4\Delta t_1$.

So far we have not specified the operators h_i, which are the constituents of the $H_{\text{even/odd}}$ terms, besides by the conditions $[h_i, h_j] = 0$ for i, j both odd or both even and that the sum is the full Hamilton operator. The details of how to choose these h_i of course depend on the model and situation studied and different choices render Trotter decompositions better or worse approximations, which in turn influence the Δt for which converged results are reached. Let us consider for the time being the standard model of spins interacting with nearest neighbors as outlined in Eq. (5.2.1). A standard choice[14] would render $h_i = J(S_i^x S_{i+1}^x + S_i^y S_{i+1}^y + \Delta S_i^z S_{i+1}^z) + h/2(S_i^z + S_{i+1}^z)$. Thus applying all odd or even $\exp(-ih_i\Delta t)$ involves updating pairs of neighboring sites only, which can be done successively for the whole lattice. Therefore, the two-site operator $\exp(-ih_i\Delta t)$ needs to be mutiplied to the Λ-Γ-matrices positioned at (for Γ-matrices) or next to (for Λ-matrices) the sites i and $i+1$ as

$$\Phi_{a_{i-1},\sigma_i,\sigma_{i+1},a_{i+1}} = \sum_{\sigma_i',\sigma_{i+1}'} \left(e^{-ih_i\Delta t}\right)_{\sigma_i,\sigma_{i+1},\sigma_i',\sigma_{i+1}'} \sum_{a_i} \Lambda_{a_{i-1},a_{i-1}}\Gamma^{\sigma_i}_{a_{i-1},a_i}\Lambda_{a_i,a_i}\Gamma^{\sigma_{i+1}}_{a_i,a_{i+1}}\Lambda_{a_{i+1},a_{i+1}}. \tag{5.6.6}$$

Φ is the updated part of the MPS and must now be decomposed back into Λ-Γ matrices. First we save the "old" $\Lambda_{a_{i-1},a_{i-1}}$ and $\Lambda_{a_{i+1},a_{i+1}}$ for future reference. They are not changed during the update.

[12] Raising the number of time steps, and thus the computational resources, needed to reach a given time t.

[13] Less symmetric formulations of a fourth-order decomposition lead to even smaller errors at approximately fixed numerical costs [McL95].

[14] We slightly change the magnetic field at the start and end of the lattice for simplicity.

Getting back to the Λ-Γ form can then be achieved by reshaping $\Phi_{(a_{i-1},\sigma_i),(\sigma_{i+1},a_{i+1})}$ and performing a SVD

$$\Phi_{(a_{i-1},\sigma_i),(\sigma_{i+1},a_{i+1})} = \sum_{a_i} U_{(a_{i-1,\sigma_i}),a_i} S_{a_i,a_i} (V^\dagger)_{a_i,(\sigma_{i+1},a_{i+1})}, \tag{5.6.7}$$

at this point once more the truncation of singular values can be performed to keep the bond dimension χ feasible. The updated Λ- and Γ-matrices of the MPS then read

$$\Gamma^{\sigma_i}_{a_{i-1},a_i} = (\Lambda)^{-1}_{a_{i-1},a_{i-1}} U_{(a_{i-1},\sigma_i),a_i}, \quad \Lambda_{a_i,a_i} = S_{a_i,a_i}, \quad \Gamma^{\sigma_{i+1}}_{a_i,a_{i+1}} = (V^\dagger)_{(a_i,\sigma_{i+1}),a_{i+1}} (\Lambda)^{-1}_{a_{i+1},a_{i+1}} \tag{5.6.8}$$

This concludes the elementary update function which (analogously to the iterative ground state search) only needs to be glued together at different sites to find the time evolution. To show how simply this elementary update can be implemented using python, we give it explicitly here (for the example we concentrated on above, generalizations are trivial)

```
import numpy as np

def bond(l0, G0, l1, G1, l2, d, chi1_max, O):

  # initial bond dimensions chi
  chi0=len(l0); chi2=len(l2)

  # step 1: form 2-site tensor
  Psi = np.tensordot( np.diag(l0), G0          , axes=(1,1) )
  Psi = np.tensordot( Psi        , np.diag(l1), axes=(2,0) )
  Psi = np.tensordot( Psi        , G1          , axes=(2,1) )
  Psi = np.tensordot( Psi        , np.diag(l2), axes=(3,0) )

  # step 2: apply local time evolution operator
  Phi = np.tensordot( Psi, O, axes=([1,2],[0,1]) )
  Phi = np.transpose( Phi, (2,0,3,1)      )
  Phi = np.reshape  ( Phi, (d*chi0,d*chi2) )

  # step 3: singular value decomposition
  U, S, V = np.linalg.svd(Phi,0)

  # step 4: truncate (to keep problem manageable, approximation
  # is optimal in the 2-norm, because of proper normalization
  # to the left and right)
  chi1 = min( len(S), chi1_max )

  discarded = np.sum(S[chi1:]**2) / np.sum(S**2)
  tilde_l1 = S[0:chi1] / np.sqrt(np.sum(S[0:chi1]**2))

  # step 5: reshape
  U        = np.reshape  ( U[:,0:chi1], (d,chi0,chi1) )
  U        = np.tensordot( U, np.diag(1.0/l0), axes=(1,0) )
  tilde_G0 = np.transpose( U, (0,2,1) )

  V        = np.reshape  ( (V.T)[:,0:chi1], (d,chi2,chi1)  )
  tilde_G1 = np.tensordot(  V, np.diag(1.0/l2), axes=(1,0) )

  return tilde_G0, tilde_l1, tilde_G1, discarded
```

where Λ^i and Γ^i are arrays of size χ_i and (d, χ_i, χ_{i+1}), respectively. The by far most time consuming parts of this algorithm are matrix multiplications ('np.tensordot') as well as the singular value decomposition ('np.linalg.svd'), which are wrapped to very efficient lapack routines through the 'numpy' package.

Depending on the Trotter decomposition one favours one can now apply the updates of even and odd bond with the local matrix exponentials as outlined and thus step by step propagate the MPS in time. The depicted algorithm of successively evolving odd and even sites of the MPS is summarized in Fig. 5.6. We have exemplified the procedure for a lattice model with nearest neighbor interaction terms. The general reasoning however can be applied also to longer-ranged interactions, as we shall see implicitly in section 5.6.3.

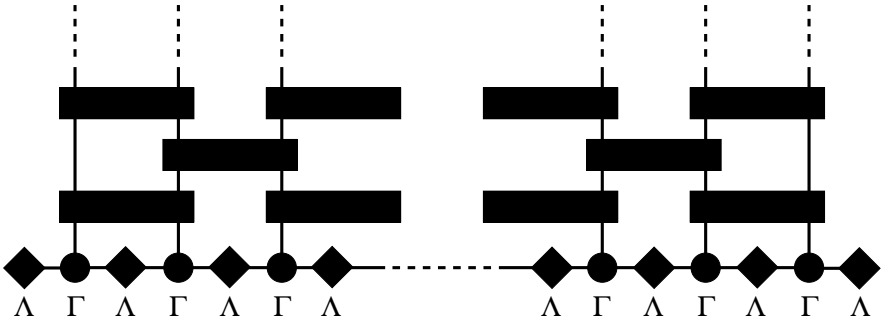


Figure 5.6.: For the example studied in the main text a Trotter decomposition of the global operator e^{-iHt} gives a sequence of elementary two-site updates as shown.

5.6.2 Ground States Revisited

The algorithm outlined to evolve a MPS in time works equally well for real as well as imaginary Δt, which means that a second route to finding the ground state of a quantum system can be employed; namely finding the ground state via an imaginary time evolution. For imaginary time evolution $\Delta t = -i\Delta\tau$ the time evolution operator $\exp(-iH\Delta t) = \exp(-H\Delta\tau)$ is not unitary. Thus an initially normalized MPS does not stay normalized. The norm can be restored either by exact methods (as outlined in section 5.1.3) or approximately by applying sufficiently often[15] Trotter evolutions with zero time steps (unities) in between [Sch11b, Kar12b]. To achieve optimal performance it is advisable to use decreasing $\Delta\tau$. One should converge the MPS for each $\Delta\tau$ chosen before decreasing it to the next smaller one. Starting with large $\Delta\tau$ allows to quickly reach large imaginary times, while the successive time evolution with decreased $\Delta\tau$ enhances the accuracy of the resulting MPS.

5.6.3 Finite Temperatures and Purification

So far we have discussed pure states. But what about *finite temperatures*? Of course, at finite temperatures in canonical equilibrium one faces the difficulty (from a DMRG standpoint) of mixed states. Thus our strategy will be to reduce the mixed states of such class of quantum states to a pure state again, for which the above outlines machinery can be applied right away. The key to this mapping of mixed states to pure states is called *purification* [Ver04]. Considering a general density matrix

$$\rho = \sum_{a=1}^{r} s_a^2 \left|a\right\rangle \left\langle a\right| , \tag{5.6.9}$$

which describes an arbitrary mixed state, we can see explicitly how purification works. First, we duplicate every degree of freedom of the physical system (index P) and thus introduce the ancillary system (index Q). Now it is easy to see that, with the *pure* state

$$\left|\Psi\right\rangle = \sum_{a=1}^{r} s_a \left|a\right\rangle_{\mathrm{P}} \left|a\right\rangle_{\mathrm{Q}} , \tag{5.6.10}$$

one can describe the density matrix of Eq (5.6.9) as $\rho_{\mathrm{P}} = \mathrm{Tr}_{\mathrm{Q}} \left[\left|\Psi\right\rangle \left\langle\Psi\right|\right]$. Let us turn our attention to the mixed states we are interested in; states describing finite temperatures. From statistical mechanics the canonical density matrix is given by $\rho_\beta = Z(\beta)^{-1} \exp(-\beta H)$ with $Z(\beta) = \mathrm{Tr}\left[\rho_\beta\right]$ the canonical partition function, H the Hamilton operator and $\beta = 1/T$ the inverse temperature. We note that $\rho_\beta = Z(\beta)^{-1} \exp(-\beta H/2) \cdot I \cdot \exp(-\beta H/2)$, where the identity I can be viewed as $I = Z(0)\rho_0$. If the purification for a thermal state at $\beta = 0$ is known to be $\left|\Psi_0\right\rangle$ the purifications

[15] How often classifies as "sufficiently" often depends on the problem considered and one's accuracy goals.

of thermal states with lower temperature can thus be reached by "cooling" via imaginary time evolutions

$$\begin{aligned}\rho_\beta &= \frac{Z(0)}{Z(\beta)} \exp(-\beta H/2)\mathrm{Tr}_\mathrm{Q}\left[|\Psi_0\rangle\langle\Psi_0|\right]\exp(-\beta H/2)\\ &= \mathrm{Tr}_\mathrm{Q}\left[\frac{Z(0)}{Z(\beta)}\exp(-\beta H/2)\,|\Psi_0\rangle\langle\Psi_0|\exp(-\beta H/2)\right]\\ &\to |\Psi_\beta\rangle = \sqrt{Z(0)/Z(\beta)}\exp(-\beta H/2)\,|\Psi_0\rangle\,.\end{aligned} \tag{5.6.11}$$

The evaluation of any physical observables can then be accessed as

$$\langle O\rangle = \mathrm{Tr}_\mathrm{P}\left[\rho_\beta O\right] = \langle\Psi_\beta|\,O\,|\Psi_\beta\rangle\,. \tag{5.6.12}$$

Thus as a last step we derive the purification of the canonical ensemble for $\beta = 0$, which is the the "worst case" in terms of how mixed the state is (all states contribute equally), but the "best case" for an analytical analysis. The purification here is trivial, because

$$\rho_0 = \frac{1}{d^L} I = \left(\frac{1}{d} I\right)^{\otimes L}\,, \tag{5.6.13}$$

and

$$\frac{1}{d} I = \mathrm{Tr}_\mathrm{Q}\left[\left(\sum_\sigma \frac{1}{\sqrt{d}}\,|\sigma\rangle_\mathrm{P}\,|\sigma\rangle_\mathrm{Q}\right)\left(\sum_{\sigma'}\frac{1}{\sqrt{d}}\,\langle\sigma'|_\mathrm{P}\,\langle\sigma'|_\mathrm{Q}\right)\right]. \tag{5.6.14}$$

The purified state at each physical plus ancillary site i can thus be read of as the maximally entangle state ($T\to\infty$)

$$|\Psi_{i,0}\rangle = \sum_\sigma \frac{1}{\sqrt{d}}\,|\sigma\rangle_\mathrm{P}\,|\sigma\rangle_\mathrm{Q}\,, \tag{5.6.15}$$

or any state connected to it via unitary transformations on P and Q, separately. One can exploit this gauge freedom to fix the quantities conserved by good quantum numbers (which thus allows the use of symmetries as explained in section 5.3). For our paradigmatic example of the Heisenberg chain (5.2.1) one can reach total $S = 0$ as well as $S^z = 0$ by putting locally the physical and its corresponding ancillary site into a singlet state

$$|\Psi_{i,0}\rangle = \frac{1}{\sqrt{2}}\left[|\uparrow\rangle_\mathrm{P}\,|\downarrow\rangle_\mathrm{Q} - |\downarrow\rangle_\mathrm{P}\,|\uparrow\rangle_\mathrm{Q}\right], \tag{5.6.16}$$

If one arranges physical and ancillary sites at odd and even sites[16], respectively, the correct Γ and Λ matrices read

$$\Lambda^{2i} = I \qquad \Gamma^{2i+1} = \begin{matrix}\uparrow:\\ \downarrow:\end{matrix}\begin{bmatrix}1 & 0\\ 0 & -1\end{bmatrix} \qquad \Lambda^{2i+1} = \frac{1}{\sqrt{2}} I \qquad \Gamma^{2i} = \begin{matrix}\uparrow:\\ \downarrow:\end{matrix}\begin{bmatrix}0 & 1\\ 1 & 0\end{bmatrix}^T, \tag{5.6.17}$$

where again I is shorthand for an identity matrix of the correct dimension (1×1 or 2×2).

Evolving the Ancillary System: A New Disentangler Vol. I

When subjecting purified states of higher temperatures to, e.g., subsequent real time evolutions numerical resources are usually exhausted very quickly. This is due to the fact that employing even trivial time evolutions $\exp(-iHt)$ to the purified state belonging to $\exp(-\beta H)$ leads to a substantial increase of the bond dimensions at *all* sites. Recently a powerful scheme for avoiding this problem was devised [Kar12a, Kar13]. The central idea is to exploit the fact that, when calculating any physical observable A_p, one can apply arbitrary unitary transformations of the form

$$\langle A_\mathrm{p}\rangle = \langle\Psi_\beta|\exp(iHt)A_\mathrm{p}\exp(-iHt)\,|\Psi_\beta\rangle = \langle\Psi_\beta|\exp(iHt)U_\mathrm{Q}^\dagger A_\mathrm{p} U_\mathrm{Q}\exp(-iHt)\,|\Psi_\beta\rangle\,, \tag{5.6.18}$$

[16] Such that the MPS reads $\Lambda^0\Gamma^1\Lambda^1\Gamma^2\Lambda^2\Gamma^3\Lambda^3\ldots$.

where U_Q acts on the ancillary system only, because $[A_p, U_Q] = 0$. The question arises, whether one can choose U_Q in a clever way, such that the artificial blow up of the bond dimension in the trivial time evolution mentioned above is removed. In [Kar12a] it was pointed out that choosing $U_Q = \exp(-iH_Q t)$ does the trick, if for example in the case of Heisenberg chains [defined by Eq. (5.2.2)], $H_Q(J, \Delta, h)$ is chosen as $H(-J, \Delta, h)$, which can be seen as to evolve the ancillary system with the same Hamiltonian, but backwards in time and the sign of the magnetic field term reversed.

The remarkable success of this *disentangler* has allowed to reach time scales for higher to intermediate temperatures, which are out of reach for "conventional" DMRG approaches. But why does this work? There are some insights into this question outlined in [Bar13], which will be focussed on in the next section. Here we want to propose a rather intuitive explanation. We consider for exemplification a Heisenberg chain (5.2.2), but different models follow analogously. What does $\exp(-iHt)\exp(-H_Q t)$ do to $|\Psi_\beta\rangle$? First we notice that $|\Psi_\beta\rangle = \sqrt{Z(0)/Z(\beta)}\exp(-\beta H/2)\,|\Psi_0\rangle$, where $\exp(-\beta H/2)$ and $\exp(-iHt)\exp(-H_Q t)$ commute. Thus we can exclusively focus on $|\Psi_0\rangle$. We combine physical site and ancillary site to one with squared degree of freedom, meaning that [given preparation (5.6.16)] the total MPS is actually a product state

$$\Lambda^i = I \qquad \Gamma^i = \begin{matrix} \uparrow\uparrow\text{: } [\ 0\ \ \ ] \\ \uparrow\downarrow\text{: } [\ 1/\sqrt{2}] \\ \downarrow\uparrow\text{: } [-1/\sqrt{2}] \\ \downarrow\downarrow\text{: } [\ 0\ \ \ ] \end{matrix} \tag{5.6.19}$$

in the appropriate basis. We also combine H and H_Q to an Hamilton operator $H_s = H \otimes 1 + 1 \otimes H_Q$ acting on the enlarged local Hilbert space. Trivially H_s is still the sum of local operators

$$\begin{aligned} h_i^s =& (J/2)\,(S^+ \otimes I)_i \otimes (S^- \otimes I)_{i+1} + (J/2)\,(S^- \otimes I)_i \otimes (S^+ \otimes I)_{i+1} \\ &+ J\Delta\,(S^z \otimes I)_i \otimes (S^z \otimes I)_{i+1} - h(S^z \otimes I)_i \\ &- (J/2)\,(I \otimes S^+)_i \otimes (I \otimes S^-)_{i+1} - (J/2)\,(I \otimes S^-)_i \otimes (I \otimes S^+)_{i+1} \\ &- J\Delta\,(I \otimes S^z)_i \otimes (I \otimes S^z)_{i+1} - h(I \otimes S^z)_i. \end{aligned} \tag{5.6.20}$$

First we take a look at the part of h_i^s acting on the physical sites (originating from $H \otimes 1$). Given a state as in Eq. (5.6.19) the action on two neighboring sites of this part of h_i^s induce transitions as

$$\begin{aligned} \downarrow\uparrow\,|\,\uparrow\downarrow \quad &\xrightarrow{(J/2)(S^+\otimes I)\otimes(S^-\otimes I)} \quad (J/2)\,\uparrow\uparrow\,|\,\downarrow\downarrow \\ \uparrow\downarrow\,|\,\downarrow\uparrow \quad &\xrightarrow{(J/2)(S^-\otimes I)\otimes(S^+\otimes I)} \quad (J/2)\,\downarrow\downarrow\,|\,\uparrow\uparrow \\ x|y \quad &\xrightarrow{(J\Delta)(S^z\otimes I)\otimes(S^z\otimes I)} \quad \mathrm{sign}_1(x)\mathrm{sign}_1(y)(J\Delta/4)\ \ x|y \\ x|y \quad &\xrightarrow{(-h)(S^z\otimes I)\otimes(I\otimes I)} \quad (-h/2)\mathrm{sign}_1(x)\ \ x|y, \end{aligned} \tag{5.6.21}$$

where $x, y \in \{\uparrow\downarrow, \downarrow\uparrow\}$, $\mathrm{sign}_1(\uparrow\downarrow) = 1$ and $\mathrm{sign}_1(\downarrow\uparrow) = -1$. All other transitions do not occur. The action of solely the physical part of h_i^s thus induces highly non-trivial transitions to a state not only with different prefactors ($\rightarrow$ phases), but completely different structure (e.g. finite weight is given to $\uparrow\uparrow\,|\,\downarrow\downarrow$). This leads to a non-trivial time evolution. Now we also include the evolution of the ancillary system (from $1 \otimes H_Q$). The transitions induced are

$$\begin{aligned} \downarrow\uparrow\,|\,\uparrow\downarrow \quad &\xrightarrow{(-J/2)(I\otimes S^-)\otimes(I\otimes S^+)} \quad (-J/2)\,\downarrow\downarrow\,|\,\uparrow\uparrow \\ \uparrow\downarrow\,|\,\downarrow\uparrow \quad &\xrightarrow{(-J/2)(I\otimes S^+)\otimes(I\otimes S^-)} \quad (-J/2)\,\uparrow\uparrow\,|\,\downarrow\downarrow \\ x|y \quad &\xrightarrow{(-J\Delta)(I\otimes S^z)\otimes(I\otimes S^z)} \quad [-\mathrm{sign}_1(x)][-\mathrm{sign}_1(y)](-J\Delta/4)\ \ x|y \\ x|y \quad &\xrightarrow{(-h)(I\otimes S^z)\otimes(I\otimes I)} \quad (-h/2)[-\mathrm{sign}_1(x)]\ \ x|y\ . \end{aligned} \tag{5.6.22}$$

We find that all transitions occur with reversed sign. The total time evolution of H_s including both terms H and H_Q thus becomes trivial. One could interpret this as follows. While the purified state is

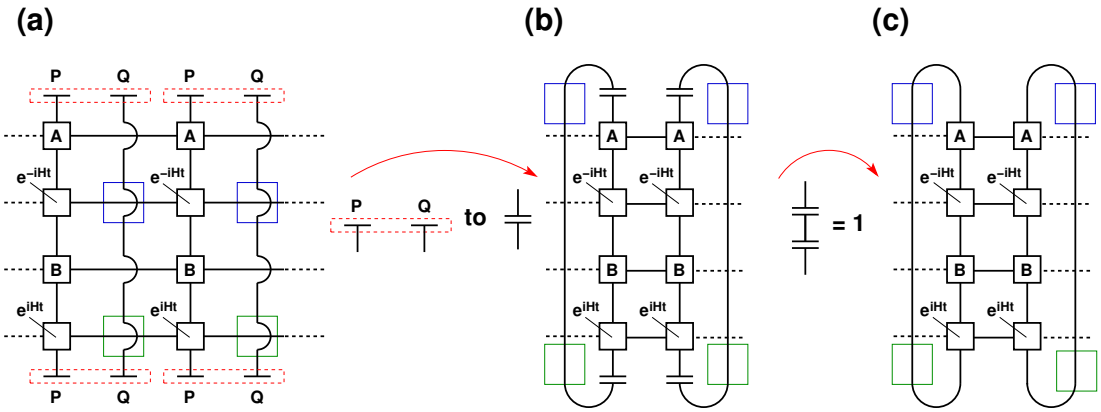


Figure 5.7.: When treating finite temperature via purification one encounters a general gauge freedom by inserting □ and □ in the contraction above (with $\square \cdot \square = 1$) (a). Reinterpreting the two sites P and Q as one (b) and the contraction from top to bottom as unity (c), shows that using $\square = e^{-iHt}$ the corresponding physical time evolution can be cancelled. We concentrated only on $\beta = 0$ explicitly, but all other cases follow from this.

not an Eigenstate of H alone, it is an Eigenstate of the Hamilton operator including H_Q. Of course this is only possible because at $\beta = 0$ the state is maximally entangled (product of local singlets of the physical and ancillary site) meaning that if the physical spin points upwards, the ancillary spin must point down and vice versa. This encodes the simple relation between H and H_Q for enforcing trivial time evolution.

Finite Temperature Response Functions: A New Disentangler Vol. II

With the above mentioned trick one can efficiently calculate dynamical finite temperature response functions of the form

$$\chi(\beta, t) = \frac{1}{Z_\beta} \mathrm{Tr}\left[e^{-\beta H} e^{iHt} B e^{-iHt} A\right], \tag{5.6.23}$$

where A and B are some "response" operators[17]. Usually in this context the Fourier transform $\chi(\beta, \omega)$ of $\chi(\beta, t)$ is studied. In [Bar13] the authors provide an alternative view on the issue of the gauge freedom U_Q outlined above. Their perspective involves to depict the purified MPS, with alternating physical and ancillary site, rather as an MPO of combined physical and ancillary site[18]. Again it suffices to concentrate on the case $\beta = 0$, where all finite β follow analogously. The transition from MPS to MPO for the state is schematically shown in Fig. 5.7. Blue and green boxes denote the (optional) unitary transformation, which can be inserted. For the above described disentangler they correspond to $\exp(-iH_Q t)$ and $\exp(iH_Q t)$.

The pictogram (a) is the MPS formulation. After combining physical and ancillary site to one MPO [shown in (b)], one can exploit the fact that the operator $|\Psi_0\rangle\langle\Psi_0|$ is the unity operator. Importantly, it became explicitly in (c), that the green box signalling $\exp(iH_Q t)$ and the physical $\exp(iHt)$ cancel, while the operator $\exp(-iH_Q t) A \exp(iH_Q t)$, becomes trivial if $A = 1$. In this fact founds the success of evolving the ancillary system (backwards in time).[19] But more can be gained. If one chooses to calculate $\chi(\beta, t)$ as

$$\chi(\beta, t) = \frac{1}{Z_\beta} \mathrm{Tr}\left[e^{-\beta H/2} \left\{e^{iHt/2} B e^{-iHt/2}\right\} \left\{e^{-iHt/2} A e^{iHt/2}\right\} e^{-\beta H/2}\right], \tag{5.6.24}$$

[17] Typically current operators of some form.

[18] The reasoning is in this respect thus similar to what we outlined above as combining physical and ancillary site into one site by doubling the local degrees of freedom. Then again the MPS is treated this is different in the following.

[19] Even if $A \neq 1$, if A is local large simplification occurs resulting in immense speed ups, because of the fact that the speed of spreading physical information is bound by the Lieb-Robinson bounds [Lie72].

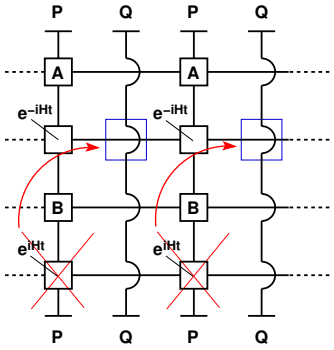


Figure 5.8.: Shifting the physical time evolution at the bottom of the contraction (following Fig. 5.7) to the ancillary system, realizes the new "disentangler" of [Kar12a] trivially. It additionally allows for exploiting the $t/2$-trick for correlators avoiding "mixed propagation" (see main text for details).

one only needs to evolve up to the largest time $t/2$ instead of t, which gives a "free" factor of two in reachable times, which is immense, given that the numerical effort usually grows exponentially in the time [Bar13]. In a naive MPS implementation the price to pay though is that one needs to calculate $\left\{e^{iHt/2}Be^{-iHt/2}\right\}|\Psi_\beta\rangle$ (and the conjugate of this with $B \to A$), which cannot be done in a simple forward time evolution[20]. In this thesis we want to present a very simple way around this. So far we have looked at the disentangler in views of schematic (a) of Fig. 5.7, only. But actually (c) tells us, that there is simple link between physical and ancillary site, which can be exploited. For example in the maximally entangled state of a Heisenberg chain Eq. (5.6.16) one could apply S^z to measure whether a spin is pointing up or down at a physical site. Equivalently one could apply $-S^z$ to the ancillary site belonging to it, to measure precisely the same. So obviously operators can be *shifted* from physical to ancillary and vice versa following given rules[21]. Let us forget about the gauge freedom (green and blue boxes) for a moment. If we start at (c), restore the state as in (b) and shift the physical time evolution e^{iHt} to the ancillary sites, we precisely get $\exp(-iH_Q t)$ for a state as in Eq. (5.6.16). $\exp(-iH_Q t)$ can then be arranged like the blue box in (a). This is depicted in Fig. 5.8. Now the disentangler and the $t/2$-trick can be exploited trivially with only a forward time evolution.

5.7 From Finite Size to Infinite Size DMRG

So far we have focussed on finite systems, but actually it is also possible to tackle systems in the thermodynamic limit directly as long as they are translational invariant. This is true for both ground state searches as well as real or imaginary time evolutions.

5.7.1 Ground States of Infinite Systems

Quite similarly to the iterative procedure outlined above one can implement an infinite ground state search. The essential idea is to grow the chain iteratively (instead of repeatedly sweeping through the chain). While growing the chain we call the left half of the system A and the right half B. The different sites will be uniquely labelled throughout the growing process by the two indices A or B as well as the iteration step they were inserted. We start with only two sites $|\Psi_1\rangle = \sum_{\sigma_1^A,\sigma_1^B} \Psi^{\sigma_1^A,\sigma_1^B} |\sigma_1^A\rangle |\sigma_1^B\rangle$, which can be recast into an MPS easily, by (1) optimizing with respect to H and (2) performing a singular value decomposition as always. We arrive at the MPS

[20] And thus involves doing the left time evolution over and over again for each time step, which is expensive.
[21] E.g. S^z on a physical site turns to $-S^z$ on an ancillary one.

representation $|\Psi_1\rangle = \sum_{\sigma_1^A,\sigma_1^B} A^{\sigma_1^A} \Lambda_1 B^{\sigma_1^B} |\sigma_1^A\rangle |\sigma_1^B\rangle$. Now we can insert two more site

$$|\Psi_1\rangle = \sum_{\{\sigma\}} A^{\sigma_1^A} \Psi^{\sigma_2^A,\sigma_2^B} B^{\sigma_1^B} |\sigma_1^A\rangle |\sigma_2^A\rangle |\sigma_2^B\rangle |\sigma_1^B\rangle , \tag{5.7.1}$$

where now the matrix $\Psi^{\sigma_2^A,\sigma_2^B}_{a_1^A,a_1^B}$ is optimized and decomposed to

$$|\Psi_1\rangle = \sum_{\{\sigma\}} A^{\sigma_1^A} A^{\sigma_2^A} \Lambda_2 B^{\sigma_2^B} B^{\sigma_1^B} |\sigma_1^A\rangle |\sigma_1^B\rangle . \tag{5.7.2}$$

At this point the procedure can be iterated. Two things can be achieved with this algorithm. On the one hand, we can stop at finite size L of the chain and use the grown MPS as an initial guess offered to a finite size iterative ground state algorithm. This will dramatically decrease the number of sweeps needed to converge and also helps protect the algorithm from getting stuck in non-global energy minima. This is the constructive prediction procedure promised in section 5.5. On the other hand, we can continue to grow a bigger and bigger chain, until the information of the boundaries (pushed further and further away from the central unit under optimization) is sufficiently unimportant. As a measure for this one can use the fidelity [McC08]

$$F(\rho_1, \rho_2) = \mathrm{Tr}\left[\sqrt{\sqrt{\rho_1}\rho_2\sqrt{\rho_1}}\right] , \tag{5.7.3}$$

which should approach 1 (for more implementation details on this see [Sch11b]). Afterwards, taking the last optimized cell as the unit cell of an infinite chain, properties in the thermodynamic limit can be addressed. We can also proceed similarly with a ground state unit cell found via an imaginary time evolution.

5.7.2 Real and Imaginary Time Evolutions

Putting the unit cell into Γ-Λ notation, either by exact means [Sch11b] or approximately by successively applying unities to the MPS, allows to treat (thermo)dynamics of infinite systems. Imagine an infinite chain of repeating unit cells, e.g. $\ldots(\Lambda\Gamma\Lambda\Gamma)(\Lambda\Gamma\Lambda\Gamma)\ldots$. After a Trotter decomposition of the full time evolution operator into elementary ones, the entire chain can be propagated forward in time by only treating the unit cell explicitly. Whenever elements are needed which would lie outside of the unit cell, copies of their counterpart inside the unit cell are used. This is depicted schematically in Fig. 5.9. The first two steps of the Trotter decomposition require one copy of a Λ matrix and one copy of a $\Gamma\Lambda$ matrix pair. Updates of the copies also affect the matrices inside the unit cell[22]. When one uses Abelian symmetries one needs to be careful with the quantum numbers. After the copying process of certain elements from the unit cell to the boundaries of it, all the quantum numbers belonging to these copied matrices for all sectors should be interpreted as shifted by the global quantum number of the entire unit cell. Thus when copying the Λ matrix in step (1) in Fig. 5.9 the corresponding quantum numbers should be reduced by the global quantum number of the unit cell. In step (2) it should be added instead.

5.8 DMRG: Success and Failure

In this concluding part of the chapter we want to shed some more light on why and when DMRG works particularly good or bad. We have already hinted at appropriate places what renders a DMRG approach better or worse, but we have not at all thoroughly devoted a lot of thought to this. At the bottom of the explanation rests the insight, that the physical entropy dictates the bond dimension one needs to use to achieve a certain accuracy of the MPS. The bond dimension in turn is restricted by numerical resources and thus when the spreading of entropy through the system is to ugly, DMRG is doomed to fail. We already argued that due to area laws thus the one-dimensional case is

[22] Using circular lists implementing this is a trivial extension to the finite size time evolution code.

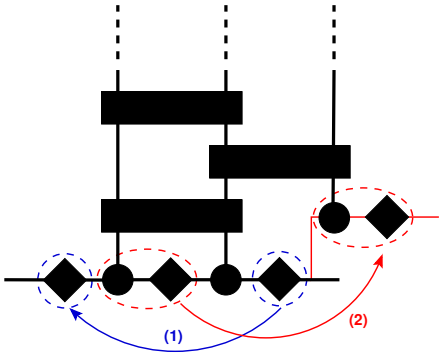


Figure 5.9.: Time evolving a MPS in the thermodynamic limit can be done by treating only some finite unit cell explicitly. Whenever matrices from outside the unit cell are needed, they are periodically copied to the right place.

particularly well suited for DMRG[23]. But we can be more precise. Let us revisit the MPS in mixed canonical form given in Eq. (5.1.12). The bipartition of the system at the position where A- turn to B-matrices, directly gives $|\Psi\rangle = \sum_a S_{a,a} |a\rangle_A |a\rangle_B$, where $|a\rangle_A$ ($|a\rangle_B$) contains all $A(B)$ matrices. From this the reduced density matrices of the two subsystems, divided by the bipartition,

$$\tilde{\rho}_{A/B} = \sum_a S_{a,a}^2 |a\rangle_{A/B} \langle a|_{A/B} \tag{5.8.1}$$

can be read off due to normalization. Both reduced density matrices share a spectrum $w_a = S_{a,a}^2$, which is nothing but the squared singular values. The von Neumann entropy reduces to

$$S_{A|B}(|\Psi\rangle) = -\mathrm{Tr}\left[\tilde{\rho}_A \ln \tilde{\rho}_A\right] = -\sum_a S_{a,a}^2 \ln S_{a,a}^2 \,. \tag{5.8.2}$$

This provides the quantitative link between entropy and singular values needed. If the entropy is 0, due to $\sum S_{a,a}^2 = 1$, there can be only one entry in the spectrum with weight $w_a = S_{a,a}^2 = 1$. We recover a pure state trivially handled by DMRG. The larger the entropy is the more shallow the spectrum gets. Translated this means that more and more singular values contribute with significant weight and the bond dimension needs to increase. In the worse case (for simplicity we assume a bipartition in the middle now) where the entropy is equal to $S_{A|B}^{\max} = L/2 \ln d$, all weights contribute equally, and none of the singular values can be disregarded. DMRG becomes just as expensive as exact diagonalization. Luckily in usual one-dimensional setups this later case rarely occurs in practice.

We can now also understand the performance difference arising from local vs. global quenches. If we have prepared the system in the ground state (or some thermal state when the new disentangler is used for that matter) belonging to some Hamiltonian H_0, applying subsequent time evolutions with H_0 does not alter the entanglement in the system and the bond dimension remains constant. If we now instead apply a quench which acts globally and thus perform time evolutions with a different Hamiltonian H, the entanglement will rise in an exponential fashion with increasing time at *all* sites. For fixed available numerical resources the algorithm runs into a "wall" in time after which the results will quickly loose their significance. Pushing this "wall" to larger times remains exponentially expensive. If one instead applies only a local quench the Lieb-Robinson bounds [Lie72] provide an upper bound on how fast entanglement can spread around this perturbation. This is often referred to as the physical light cone, in analogy to relativistic theories. Therefore the (still exponential) rise in the bond dimension is restricted to sites centred around the position of the local quench. Since in usual application the light cone travels to much fewer sites than the (large) system under consideration has in total, this leads to an immense speed up in the numerics.

[23] And luckily entails very interesting strong correlation physics.

Acknowledgement

We are grateful for the hospitality of the University of California, Berkeley during the summer 2013.

References

Part of the results discussed in this chapter were published in

D. M. Kennes and C. Karrasch
'Extending the range of real time density matrix renormalization group simulations'
ArXiv 1404.3704 (2014)

Chapter 6

Alternative Methods

Contents

6.1. Perturbation Theory **80**
6.2. Hartree-Fock **80**
6.3. Bosonization **81**
6.3.1. Basics 81
6.3.2. Exact Solution in One Dimension 82
6.3.3. ...Expectation Values including the Fermionic Operators? 83
6.4. Real Time Renormalization Group **84**
6.4.1. Introduction 84
6.4.2. Liouville-Laplace Space 85
6.4.3. Setting up Diagrammatics 85
6.4.4. Upgrading to a Renormalization Group 86
6.5. Numerical Renormalization Group **86**
6.5.1. Introduction 86
6.5.2. Iterative Diagonalization 86
6.5.3. Dynamics? 87

Introduction

In this chapter we want to complement our two approaches of choice (FRG → Chapter 4 and DMRG → Chapter 5) by a non-exhaustive list of alternative methods. Those can be used to (1) benchmark the validity range of the perturbatively motivated FRG, (2) approach limits inaccessible to our main methods and/or (3) extract (additional) analytical insights. Years of research have brought forth a zoo of different powerful methods to tackle correlated quantum many-body problems. We concentrate exclusively on those relevant for the remainder of this thesis.

Outline

In the following we want to first relate the FRG to a plain perturbation theory in the Coulomb interaction. Then we advance to the so called Hartree-Fock approach, which treats interactions on the mean field level. For strongly correlated systems both frequently break down in low dimensions and the need for non-perturbative methods arises. Linearizing the dispersion of the one-dimensional Fermi gas around the Fermi points leads to a simplified model. One can find an exact solution of the latter using bosonization. Furthermore, the so called real time renormalization group has proven very useful to tackle quantum impurity problems. Finally, we present some non-formal and very brief introduction to the ideas of the numerical renormalization group, which applied to impurity setups yields numerically exact results in equilibrium.

6.1 Perturbation Theory

To first order in the Coulomb interaction it is straightforward to relate FRG to perturbation theory. We consider a Hamiltonian

$$H = \sum_{k_1 k_2} \epsilon_{k_1 k_2} c^\dagger_{k_1} c_{k_2} + U \frac{1}{4} \sum_{k_1 k_2 k_3 k_4} \bar{v}_{k_1 k_2 k_3 k_4} c^\dagger_{k_1} c^\dagger_{k_2} c_{k_4} c_{k_3} \ , \tag{6.1.1}$$

where we have written explicitly the (supposedly small) parameter U. First, we expand all vertex functions γ^Λ_m in terms of U

$$\gamma^\Lambda_m = \sum_{n=1}^{\infty} \gamma^\Lambda_{m,n} U^n \ . \tag{6.1.2}$$

To $\mathcal{O}(U)$, the flow equations [compare (4.3.17) and (4.3.19)] then read (sums implied)

$$\begin{aligned} \partial_\Lambda \gamma^\Lambda_{1,1} &= \mathrm{Tr}\left(G^\Lambda_0 \left(\partial_\Lambda [G^\Lambda_0]^{-1} \right) G^\Lambda_0 \gamma^\Lambda_{2,1} \right) \ , \\ \partial_\Lambda \gamma^\Lambda_{m,1} &= 0 \ , \quad m \geq 2 \ . \end{aligned} \tag{6.1.3}$$

Therefore, first-order perturbation theory in U is reproduced by the FRG by simply neglecting the feedback of the self-energy to its own flow equation and keeping all further vertex functions constant. There is also a simple diagrammatic argument to why the FRG scheme truncated to first order reproduces first order perturbation theory if the self-energy feed back is neglected. On the right hand side of the single flow equation of a first order truncation scheme an explicit prefactor U due to the two-particle vertex shows up (compare Fig. 4.3). With this all further dependencies on U can be neglected. Especially setting the full Green's function in Eq. (4.3.18) to the non-interacting one, one can replace the star differential operator ∂^*_Λ, acting only on the explicit cut-off dependence, by a full one ∂_Λ as the self-energy was disregarded. Subsequently the flow equation can be integrated trivially leading to the first order diagram (in U) of plain perturbation theory.

6.2 Hartree-Fock

We concentrate for a moment on equilibrium. An upper bound for the ground state energy of a system can be given by minimizing some ansatz for its ground state with respect to energy. If we generalize this to finite temperatures we arrive at the so called Hartree-Fock approach[1]. Considering two arbitrary statistical operators $\hat{\rho}$ and $\tilde{\rho}$ the following inequality holds:

$$\mathrm{Tr}\left[\tilde{\rho}\left(\ln\hat{\rho} - \ln\tilde{\rho}\right)\right] \leq 0 \ . \tag{6.2.1}$$

Plugging in the grand canonical density matrix for $\hat{\rho} = \exp(-\beta H)/Z$ (where a possibly present chemical potential has been shifted to the Hamiltonian) gives

$$\Omega = -T \ln Z \ \leq \ \mathrm{Tr}\left(H\tilde{\rho}\right) + T\,\mathrm{Tr}\left(\tilde{\rho}\ln\tilde{\rho}\right) = \langle H \rangle_{\tilde{\rho}} - T\tilde{S} = \Omega_{\mathrm{var}} \ , \tag{6.2.2}$$

for the free energy. Next, we assume that the Hamiltonian can be written as

$$H = \sum_{ij} \lambda_{ij} A_{ij} + U \ , \tag{6.2.3}$$

such that for $U = 0$ the problem can be solved (e.g. defines a non-interacting theory). Because we aim at an optimal set λ_{ij} we introduce

$$\tilde{\rho} = \frac{\exp\left(-\beta\tilde{H}_0\right)}{\mathrm{Tr}\,\exp\left(-\beta\tilde{H}_0\right)} \ , \quad \tilde{H}_0 = \sum_{ij} \tilde{\lambda}_{ij} A_{ij} = \sum_{ij} \left(\lambda_{ij} + \lambda^{\mathrm{MF}}_{ij}\right) A_{ij} \ . \tag{6.2.4}$$

[1] In the presentation we follow [Kar10a].

to obtain the upper bound of the free energy

$$\Omega_{\text{var}} = \langle \tilde{H}_0 \rangle_{\tilde{\rho}} - T\tilde{S} + \langle U \rangle_{\tilde{\rho}} - \sum_{ij} \lambda_{ij}^{\text{MF}} \langle A_{ij} \rangle_{\tilde{\rho}} = \Omega_0(\lambda \to \tilde{\lambda}) + U(\langle A \rangle_{\tilde{\rho}}) - \sum_{ij} \lambda_{ij}^{\text{MF}} \langle A_{ij} \rangle_{\tilde{\rho}} \ . \tag{6.2.5}$$

For the deviation it was assumed that the expectation value of U depends on $\langle A \rangle$ only, which in practice is always fulfilled. Here the index MF indicates that we treat quantum fluctuations effectively on the mean field level for the part we cannot solve denoted by U. Performing the minimization we find

$$\frac{\partial \Omega_{\text{var}}}{\partial \lambda_{ij}^{\text{MF}}} = \langle A_{ij} \rangle_{\tilde{\rho}} + \sum_{kl} \frac{\partial U(\langle A \rangle_{\tilde{\rho}})}{\partial \langle A_{kl} \rangle_{\tilde{\rho}}} \frac{\partial \langle A_{kl} \rangle_{\tilde{\rho}}}{\partial \lambda_{ij}^{\text{MF}}} - \langle A_{ij} \rangle_{\tilde{\rho}} - \sum_{kl} \lambda_{kl}^{\text{MF}} \frac{\partial \langle A_{kl} \rangle_{\tilde{\rho}}}{\partial \lambda_{ij}^{\text{MF}}} \stackrel{!}{=} 0 \ , \tag{6.2.6}$$

and the ansatz for the free energy becomes minimal if

$$\lambda_{ij}^{\text{MF}} = \frac{\partial U(\langle A \rangle_{\text{MF}})}{\partial \langle A_{ij} \rangle_{\text{MF}}} \quad \Leftrightarrow \quad \langle A_{ij} \rangle_{\text{MF}} = \frac{\partial \Omega_0 \left(\lambda_{ij} \to \lambda_{ij} + \frac{\partial U(\langle A \rangle_{\text{MF}})}{\partial \langle A_{ij} \rangle_{\text{MF}}} \right)}{\partial \lambda_{ij}} \ . \tag{6.2.7}$$

This yields the upper bound of the free energy

$$\Omega_{\text{MF}} = \Omega_0 \left(\lambda_{ij} \to \lambda_{ij} + \frac{\partial U(\langle A \rangle_{\text{MF}})}{\partial \langle A_{ij} \rangle_{\text{MF}}} \right) + U(\langle A \rangle_{\text{MF}}) - \sum_{ij} \frac{\partial U(\langle A \rangle_{\text{MF}})}{\partial \langle A_{ij} \rangle_{\text{MF}}} \langle A_{ij} \rangle_{\text{MF}} \ . \tag{6.2.8}$$

The ideas outlined above can be readily applied to a quantum many-body problem. Here we aim at a set of single-particle states which incorporate the effects of the two-particle interaction in the "optimal mean field way". For our standard Hamiltonian,

$$H = H_0 + U = \sum_{k_1 k_2} \epsilon_{k_1 k_2} c_{k_1}^\dagger c_{k_2} + \frac{1}{4} \sum_{k_1 k_2 k_3 k_4} \bar{U}_{k_1 k_2 k_3 k_4} c_{k_1}^\dagger c_{k_2}^\dagger c_{k_4} c_{k_3} \ , \tag{6.2.9}$$

we can rewrite the expectation value of the Coulomb interaction with respect to some non-interacting density exploiting Wick's theorem

$$\langle U \rangle_{\text{MF}} = \frac{1}{2} \sum_{k_1 k_2 k_3 k_4} \bar{v}_{k_1 k_2 k_3 k_4} \left\langle c_{k_1}^\dagger c_{k_3} \right\rangle_{\text{MF}} \left\langle c_{k_2}^\dagger c_{k_4} \right\rangle_{\text{MF}} \ . \tag{6.2.10}$$

Using the above outlined reasoning we then obtain the self-consistent Hartree-Fock equations

$$\left\langle c_{k_1}^\dagger c_{k_2} \right\rangle_{\text{MF}} = \frac{\partial \Omega_0 \left(\epsilon \to \epsilon^{\text{MF}} \right)}{\partial \epsilon_{k_1 k_2}^{\text{MF}}} \ , \quad \epsilon_{k_1 k_2}^{\text{MF}} = \epsilon_{k_1 k_2} + \sum_{k_3 k_4} \bar{v}_{k_1 k_3 k_2 k_4} \left\langle c_{k_3}^\dagger c_{k_4} \right\rangle_{\text{MF}} \ . \tag{6.2.11}$$

6.3 Bosonization

This section is devoted to the method of bosonization [Hal81, Bru04, Sch05a]. Bosonization is a analytical method to study correlated one-dimensional systems using only a few (often not very crucial) approximations. Importantly, within bosonization one can demonstrate the failure of Fermi Liquid theory in one dimension and that this concept has to be replaced by the theory of a Luttinger Liquid (compare section 3.2.1). Furthermore, it can be used to map the low energy degrees of freedom of certain models to one another as hinted for the IRLM $\leftrightarrow$ SBM in section 3.6.3. In what follows we concentrate on presenting key results and ideas rather than being concerned with details of mathematical rigour.

6.3.1 Basics

Let us consider the one-dimensional Hamiltonian

$$H_0 = \sum_k \epsilon_k c_k^\dagger c_k . \tag{6.3.1}$$

If we assume H_0 to describe a free gas of spinless electrons in a box of width L with periodic boundary conditions the dispersion is simply $\epsilon_k = k^2/2m$. Due to the finite boundary conditions the values of momentum are restricted to $k_n = \Delta n = 2\pi n/L$, and the ground state is given by a filled Fermi sea between k_F and $-k_F$. If one aims solely at the low-lying excitations, linearizing around the Fermi points appears to be a valid approximation. The energy dispersion around those two Fermi points then reads $\epsilon \sim \pm(k \mp k_F)$. Now, for an equidistant spectrum $\epsilon \sim \Delta n$, shifting a single electron from the Fermi edge m steps upwards costs precisely the same amount of energy as raising it only by $m-1$ levels and simultaneously shifting another one from the second-lowest level by one step. This simple idea motivates that the low energy physics is governed by collective particle-hole excitations, which we want to describe mathematically by operators

$$b_n = \frac{1}{\sqrt{n}} \sum_{m=m_0}^{\infty} c_m^\dagger c_{m+n} \ , \tag{6.3.2}$$

where $c_n = c_{k_n}$, $n > 0$, and $m_0 \leq 0$ is the lower boundary of (the right branch of) our linear spectrum. For these one can show [Sch05a] the *Kronig identity*

$$\sum_{n=1}^{\infty} n b_n^\dagger b_n = \sum_{m=m_0}^{\infty} m c_m^\dagger c_m - (\tilde{N}^2 + \tilde{N} - |m_0|^2 - |m_0|)/2 \ . \tag{6.3.3}$$

as well as the commutation relations $n > n'$

$$\begin{aligned} [b_n, b_{n'}] &= 0 \ , \\ [b_n, b_{n'}^\dagger] &= -\frac{1}{\sqrt{nn'}} \sum_{m=m_0}^{m_0+n'-1} c_{m+n-n'}^\dagger c_m \overset{(*)}{=} \delta_{nn'} \ , \end{aligned} \tag{6.3.4}$$

where $(*)$ holds only in the subspace of states in which all single-particle levels $n < N$ are occupied. Surprisingly, all non-quadratic terms on the right hand site of Eq. (6.3.3) vanish except in $\tilde{N} = N - |m_0| - 1$, with N being the particle number operator. The fact that all further non-quadratic terms vanish lies at heart of the exact solution of an interacting quantum many-body problem via bosonization: (1) mapping the quadratic part does not give any non-quadratic contributions (besides the trivial one in $\tilde{N}$) as shown above, (2) interactions (four field operators in the fermionic language) map (less surprisingly) to quadratic contributions in the bosonic bs. In total the interacting fermionic theory is mapped to a non-interacting bosonic one. We will put this in a more formal framework in the next part.

6.3.2 Exact Solution in One Dimension

Following the ideas presented above we now assume that

1. the operators b_n generally fulfil bosonic commutation relations.
2. both branches of the linear spectrum represent different independent Fermi species called "left- and right-movers".
3. the independent branches extend over all values of m, meaning $m_0 \to -\infty$. This adds a filled infinite Fermi sea for each branch.

We can then rewrite

$$H_0 = v_F \sum_{n \neq 0} k_n b_n^\dagger b_n + H_{\mathrm{N}} \ , \tag{6.3.5}$$

where H_{N} contains only the terms depending on N. The operators $b_{n>0}$ and $b_{n<0}$ are associated with the left and right branch, respectively. As hinted above the two-particle interaction $v(x-x')$

can be written in a quadratic bosonic form

$$\begin{aligned} U &= \frac{1}{2L}\sum_{k_1 k_2 q} g(q) c^\dagger_{k_1} c^\dagger_{k_2} c_{k_1-q} c_{k_2+q} = \frac{1}{L}\sum_{q>0} g(q) \sum_{k_1} c^\dagger_{k_1} c_{k_1+q} \sum_{k_2} c^\dagger_{k_2} c_{k_2-q} + H'_{\mathrm{N}} \\ &\overset{(A)}{=} \sum_{n>0} q_n \frac{g(q_n)}{2\pi}\left(b_n + b^\dagger_{-n}\right)\left(b^\dagger_n + b_{-n}\right) + H'_{\mathrm{N}} \ , \end{aligned} \tag{6.3.6}$$

where crucially the Fourier transform $g(q) = \int_{-L/2}^{L/2} e^{-iqx} v(x) dx$ needs to be restricted in a last assumption to

4. be non-vanishing only for small momenta $|q| \ll k_F$

to justify (A). The total Hamiltonian can readily be diagonalized by a Bogoliubov transform

$$a_n = \cosh(u_n) b_n - \sinh(u_n) b^\dagger_{-n} \ , \quad e^{2u_n} = K_n = \sqrt{\frac{1}{1 + g(q_n)/\pi v_F}} \ , \tag{6.3.7}$$

which yields the Tomonaga-Luttinger model

$$\begin{aligned} H - H_{\mathrm{N}} - H'_{\mathrm{N}} &= \sum_{n>0} \left\{ k_n \left(v_F + \frac{g(k_n)}{2\pi} \right) \left(b^\dagger_n b_n + b^\dagger_{-n} b_{-n} \right) + k_n \frac{g(k_n)}{2\pi} \left(b^\dagger_{-n} b^\dagger_n + b_{-n} b_n \right) \right\} \\ &= \sum_{n\neq 0} |k_n| v_F \sqrt{1 + \frac{g(k_n)}{\pi v_F}} a^\dagger_n a_n \ . \end{aligned} \tag{6.3.8}$$

To describe the low-energy physics of models out of the Luttinger Liquid universality class one needs to generalize the above expressions by introducing different interactions g_2 and g_4 in the two terms above (compare section 3.2.1). This is not done here for simplicity. The bosonic excitations feature a linear dispersion in the low energy sector with a velocity $v = v_F/K_0$. Astonishingly, the mapping connects a one-dimensional system of interacting fermions to free boson. The parameters K_n completely characterize the excitation spectrum and the time evolution of the operators $a_n(t) = \exp(-it|k_n|v_F/\sqrt{K_n}) a_n$ determine trivially the time evolution of an arbitrary state. However, a single task remains: how can we deduce ...

6.3.3 ...Expectation Values including the Fermionic Operators?

We aim at a representation of the fermionic operators c_n in terms of the bosonic ones b_n. We consider the Fourier transform

$$\psi(v) = \sum_{m=-\infty}^{\infty} e^{imv} c_m \quad \Rightarrow \quad [\psi(v), \psi(v')]_+ = 0 \ , \ [\psi^\dagger(v), \psi(v')]_+ = 2\pi \delta_{2\pi}(v - v') \ . \tag{6.3.9}$$

and introduce

$$i\varphi(v) = \sum_{n>0} \frac{1}{\sqrt{|n|}} e^{inv} b_n \quad \Rightarrow \quad [\varphi^\dagger(v), \varphi(v')] = \ln\left(1 - e^{i(v'-v)}\right) = -\sum_{m>0} \frac{e^{im(v'-v)}}{m} \ , \tag{6.3.10}$$

as well as

$$\Phi(v) = \varphi(v) + \varphi^\dagger(v) \quad \Rightarrow \quad [\Phi(v), \Phi(v')] = 2i \sum_{m>0} \frac{\sin[m(v-v')]}{m} = \sum_m \frac{e^{im(v-v')}}{m} - 1 \ . \tag{6.3.11}$$

For what follows we will aim at real-space Fourier transform and thus set $v \to 2\pi x/L$ yielding

$$[\partial_x \Phi(x), \Phi(x')] = i\frac{2\pi}{L}\left[2\pi \delta_{2\pi}\left(\frac{2\pi(x-x')}{L} \right) - 1 \right] = 2\pi i \left[\delta_L(x - x') - \frac{1}{L} \right] \ . \tag{6.3.12}$$

Next, we bosonize the fermionic annihilation operator $\psi(v)$. By looking at the commutation relation

$$[b_n^{(\dagger)}, \psi(v)] = -\frac{1}{\sqrt{n}} e^{\mp inv} \psi(v) \ , \tag{6.3.13}$$

one can motivate the ansatz (with $[b_n, \exp(\lambda b_n^\dagger)] = \lambda \exp(\lambda b_n^\dagger)$ for bosons)

$$\psi(v) = O(v) e^{i\varphi^\dagger(v)} e^{i\varphi(v)} \quad \Rightarrow \quad [b_n, \psi(v)] = [b_n, O(v)] e^{i\varphi^\dagger(v)} e^{i\varphi(v)} - \frac{1}{\sqrt{n}} e^{-inv} \psi(v) \ . \tag{6.3.14}$$

Therefore, we choose the so called *Klein factors* $O(v)$ such that $[b_n, O(v)] = 0$. Additionally, the Klein factors need to lower the particle number by one and enforce the fermionic commutation relations. Combining these properties we get

$$\psi(v) = K e^{iNv} e^{i\varphi^\dagger(v)} e^{i\varphi(v)} = K e^{iNv} e^{i\Phi(v)} \ , \quad K = \sum_N |N\rangle\langle N-1| \ . \tag{6.3.15}$$

Finally, we are now able to calculate expectation values involving the fermionic operators such as correlation functions by the operator identity

$$\begin{aligned} \psi_+(x,t) = O_+ \left(\frac{2\pi x}{L}\right) \times \exp\left\{ -\sum_{n>0} \frac{\exp(-ik_n x)}{\sqrt{n}} \Big[\cosh(u_n) a_n^\dagger(t) + \sinh(u_n) a_{-n}(t) \Big] \right\} \\ \times \exp\left\{ \sum_{n>0} \frac{\exp(\ ik_n x)}{\sqrt{n}} \Big[\cosh(u_n) a_n(t) + \sinh(u_n) a_{-n}^\dagger(t) \Big] \right\} \ . \end{aligned} \tag{6.3.16}$$

This concludes our brief overview of the idea of bosonization. Much more details, such as how to include spin-degree of freedoms, treat impurities in a real space and many other interesting issues, can be found in [Sch05a].

6.4 Real Time Renormalization Group

6.4.1 Introduction

The real time renormalization group (RTRG) was developed to describe correlated quantum dots in non-equilibrium [Sch09]. It is based on a diagrammatic approach, and includes a systematic renormalization procedure. The differences in the construction of the RTRG compared to the FRG, renders the two methods complementary to each other (see below).

We will only outline the basic ideas of the RTRG, which are needed to understand some aspect of chapter 7. We demonstrate them on the example of the Kondo quantum dot

$$H = \sum_\alpha \sum_{\omega,\sigma} \epsilon_{\alpha,\omega,\sigma} c_{\alpha,\omega,\sigma}^\dagger c_{\alpha,\omega,\sigma} + \text{H.c.} + h_0 S_z + H_{\text{tun}} \ , \tag{6.4.1}$$

$$H_{\text{tun}} = \sum_{\alpha\alpha'} \sum_{\omega\omega',\sigma\sigma'} J_{\alpha,\alpha'} \vec{S} \cdot \vec{\sigma}_{\sigma\sigma'} c_{\alpha,\omega,\sigma}^\dagger c_{\alpha',\omega',\sigma'} . \tag{6.4.2}$$

This model describes electrons (index ω, σ) in different reservoirs (index α) with dispersion $\epsilon_{\alpha,\omega,\sigma}$, which are coupled by $J_{\alpha,\alpha'}$ to an impurity spin $\vec{S}$. The density of states in the reservoirs is modelled by a Lorentzian shape of width $\sim D$. The initial density matrix at t_0 is supposed to be given by a product $\rho(t_0) = \rho_S(t_0) \prod_\alpha \rho_{\text{res},\alpha}$ of the grand canonical density matrices $\rho_{\text{res},\alpha}$ of the reservoirs times the dot density matrix $\rho_S(t_0)$. At low temperature T the model described above cannot be treated within a perturbative expansion in the tunnel coupling $J_{\alpha,\alpha'}$ as it suffers from logarithmic divergences. Therefore, it is an ideal candidate to demonstrate a strength of the RTRG.

6.4.2 Liouville-Laplace Space

As a first step we consider the von Neumann equation

$$\dot{\rho}(t) = -i[H, \rho(t)]_-, \tag{6.4.3}$$

which describes the time evolution of a full density matrix $\rho(t)$ under the action of H. We define the superoperator L called the *Liouvillian* with adjoint action on any operator $L \bullet = [H, \bullet]_-$ defined by a commutation with H. The von Neumann equation is then formally integrated to

$$\rho(t) = e^{-iL(t-t_0)}\rho(t_0)\,, \tag{6.4.4}$$

with the superoperator in the exponential. We finally aim at the description of the reduced system and therefore trace out the reservoir degrees of freedom. Furthermore, the form of Eq. (6.4.4) renders it possible to transform to the more convenient energy representation via Laplace transformation

$$\rho_S(E) = \int_{t_0}^{\infty} dt\; e^{iE(t-t_0)}\rho_S(t) = \mathrm{Tr}_{\mathrm{res}}\left[\frac{i}{E-L}\rho_S(t_0)\prod_\alpha \rho_{\mathrm{res},\alpha}\right], \tag{6.4.5}$$

where the Laplace (energy) variable can be analytically continued in the complex plane. From now on the RTRG will be set up exclusively employing this Laplace space. The dynamics are in turn determined by the inverse Laplace transformation

$$\rho_S(t) = \frac{i}{2\pi}\int_{-\infty+i0^+}^{\infty+i0^+} dE\; e^{-iEt}\,\rho_S(E), \tag{6.4.6}$$

This signals a distinct advantage of the RTRG: as the integration contour in Eq. (6.4.6) can be deformed to the lower half of the complex E-plane, different contributions to the dynamics can be identified by the different non-analyticities embraced by the deformed contour. This often allows us to deduce analytic expressions describing the dynamics. We note that the (non-equilibrium) steady-state can be extracted by considering the limit $E \to 0$.

6.4.3 Setting up Diagrammatics

In analogy with the Hamiltonian the Liouvillian can be separated into three different contribution $L = L_S^0 + L_{\mathrm{res}} + L_{\mathrm{tun}}$ yielding the reduced density matrix

$$\rho_S(E) = \mathrm{Tr}_{\mathrm{res}}\left[\frac{i}{E - L_0 - L_{\mathrm{res}} - L_{\mathrm{tun}}}\rho_S(t_0)\prod_\alpha \rho_{\mathrm{res},\alpha}\right]. \tag{6.4.7}$$

It can be in turn *expanded in the tunnel vertices*

$$\rho_S(E) = i\mathrm{Tr}_{\mathrm{res}}\left[\sum_n \left(\frac{1}{E - L_S^0 - L_{\mathrm{res}}}L_{\mathrm{tun}}\right)^n \frac{1}{E - L_S^0 - L_{\mathrm{res}}}\rho_S(t_0)\prod_\alpha \rho_{\mathrm{res},\alpha}\right]. \tag{6.4.8}$$

The trace over the reservoir degrees of freedom can now be evaluated using (a superoperator extension of) Wick's theorem and a diagrammatic language for this purpose is set up. Similarly to the diagrammatic approach in Matsubara or Keldysh space the analogue of the Dyson equation Eq. (6.4.8) can be derived

$$\rho_S(E) = \frac{i}{E - L_S^0}\sum_n \left(\Sigma(E)\frac{1}{E - L_S^0}\right)^n \rho_S(t_0) = \frac{i}{E - L_S^0 - \Sigma(E)}\,, \tag{6.4.9}$$

which relates the irreducible kernel $\Sigma(E)$ (analogue of the self-energy) to the reducible object $\rho_S(t)$ (analogue of the Green's function). The problem is now reduced to an evaluation of $\Sigma(E)$ given by a set of irreducible diagrams. However, the terms of perturbation theory feature logarithmic divergences at low T making it ill-defined. Therefore, a theory going beyond perturbation theory is desired.

6.4.4 Upgrading to a Renormalization Group

At this point the idea of a renormalization group regularization can be included. It was realized [Ple12] that with the Laplace variable at hand one can find a very elegant way of introducing the cut-off, which regularizes the frequency integrals: namely the Laplace variable E itself. The resulting regularization scheme was consequently dubbed *E-flow scheme*. Taking one derivative with respect to E for each logarithmically divergent frequency integral in the corresponding diagrams of the flowing quantities under scrutiny renders their evaluation convergent. In addition the relaxation rate which is naturally incorporated into the renormalization group flow equations cuts off infrared divergences. Starting at very high energy $E = i\Lambda_0$ one can fix the initial conditions by the perturbation theory results and re-integrate the flow equations with respect to E to approach the low energy limit. We note that very convincing results for the model outlined here even in the regime of strong coupling have been obtained for the full-fledged non-equilibrium setup [Ple10, Ple12].

Now the above mentioned complementary character of the FRG and the RTRG applied to quantum dots becomes apparent: while in FRG the influence of the reservoirs is integrated out exactly and the interaction on the dot is incorporated via a perturbatively motivated renormalization group procedure (compare chapter 4), this is the other way around in RTRG. In the latter the tunneling to the reservoirs is treated in a renormalization group enhanced perturbative approach, while the interaction on the dot is included exactly in the local many-body basis.

6.5 Numerical Renormalization Group

6.5.1 Introduction

The numerical renormalization group (NRG) is an implementation of Wilson's general renormalization group idea [Wil75], on a numerically exact level. Originally used to tackle the Kondo model (compare section 6.4) it was found to give reliable results in the low energy regime [Hew93]. Soon it was extended to a variety of strongly correlated quantum impurity models (quantum dots) [Bul08] and since has developed to (one of) the state-of-the-art methods to describe equilibrium properties of quantum impurities. However, due to the drastic (exponential) scaling of the numerical resources needed in the local impurity's quantum degrees of freedom it can in practice be applied only to rather small impurity systems with a few correlated degrees of freedom.

6.5.2 Iterative Diagonalization

As a first step within NRG applied to quantum dots one discretizes the structureless conduction band of the reservoir (given by H_{res}) by a set of logarithmically distributed energies $\{\pm(D/2)\Lambda^{-n}, n \geq 0\}$. Here D is the bandwidth and $\Lambda > 1$ a numerical discretization parameter. Then the resulting discrete model is mapped onto a semi-infinite tight-binding chain with the impurity at the first site. Using exact diagonalization the Hamiltonian of the semi-infinite chain is then treated iteratively, adding one site at a time, starting with the isolated impurity. Due to the logarithmic discretization, the hopping matrix elements of the corresponding tight-binding chain t_n between successive sites $t_n \sim \Lambda^{-n/2}$ fall off exponentially with the distance n from the impurity. Including more and more sites of the chain iteratively therefore allows to resolve smaller and smaller energy scales. As the Hilbert space of the chain to be diagonalized grows exponentially in the iteration process the need for a truncation procedure arises: this can be obtained by simply retaining only the N_c lowest-lying many-particle states at each iterative step. This is reasonable as due to the logarithmic discretization the states of the shorter chain (at iteration step $i-1$) affect those of the longer one (at iteration step i) only in a small energy regime $\sim \Lambda^{-1/2}$.

Two essential approximation govern the error in the results of the NRG approach: (1) the logarithmic discretization of the reservoirs via Λ and (2) the truncation of the Hilbert space by N_c. Controlling both parameters (Λ and N_c) one finds that actually numerically exact results can often be reached, which can be check by comparing, e.g., to the Bethe ansatz or to the analytically treatable limit of vanishing correlations.

6.5.3 Dynamics?

In this thesis we concentrate on non-equilibrium dynamics. The huge success of the NRG for equilibrium problems has motivated its extension to the non-equilibrium regime dubbed time dependent NRG [And05, And06]. However, due to the essential approximation of logarithmically discretizing the reservoirs additional complications show up. It was shown that using Wilson chains, which are reservoirs with respect to particles, but not with respect to energy [Ros12], leads to multiple reflections throughout the chain (we will discuss this very briefly also in section 7.1.2). Circumventing this problem is subject of current research [And05, And06, Ngh14].

Questions

Chapter 7

Dynamics in Open Quantum Systems

Contents

7.1.	**Thermodynamic Limit and Pitfalls**	**92**
7.1.1.	Recurrence in Finite Systems	92
7.1.2.	Wilson Chains as Reservoirs?	94
7.1.3.	$N \to \infty$	94
7.2.	**Transient Dynamics of the IRLM**	**96**
7.2.1.	Warm-up: Single-Level ($U = 0$)	96
7.2.2.	FRG Treatment at Finite U	99
7.2.3.	Transport at Finite Temperature	106
7.3.	**Dynamics of Dissipative Quantum Systems**	**110**
7.3.1.	Dynamics at $T = 0$	111
7.3.2.	Dynamics at $T > 0$	120
7.3.3.	Quenches and the Role of Non-Markovian Memory	125
7.4.	**Biased ($V \neq 0$) IRLM $\leftrightarrow$ Spin-Boson Model**	**128**
7.5.	**Conclusion**	**129**

Introduction

Within recent years the preparation and manipulation of quantum systems has excelled in aspects of control as well as reproducibility. Different routes to coherent quantum systems include (among others) the fascinating field of ultra-cold gases [Blo08], atoms in electromagnetic traps [Bie09] as well as more "solid-state" based approaches such as atoms in silicon structures [Pla12]. Earlier, the manipulation of charge- [Pet04] and spin-degrees [Cra04, Pet05] of freedom were already demonstrated in other semiconductor setups. Of course, from a long term perspective, those aim at the controlled manipulation within quantum information processing – thus quantum computing. The quest for quantum computing has triggered a cascade of theoretical as well as experimental investigations. The elementary unit needed for quantum computing is a quantum-bit (qubit), which is often modelled by a single spin. For a more realistic description this single spin is usually coupled to an infinite environment. These open quantum systems are prototypes for more complicated nano-structures envisaged to enable quantum processing [Los98, Eng05] and are thus more than of academic interest. Within these questions the dynamics of open quantum systems, such as a single fermionic energy level coupled to and interacting with some infinite environment [IRLM ($\to$ Section 3.5)] is particularly intriguing.

From a slightly different perspective another promising candidate for a qubit might be a superconducting circuit based on tunnel junctions. Those could have the advantage of easier inter-qubit coupling, more precise electrical control as well as enhanced scalability [Wei12]. One of the simplest of such systems is realized by an rf SQUID and can be described by a single spin plus bosonic environment [SBM ($\to$ Section 3.6)] as shown in [Wei12].

Yet another interesting aspect of investigation of open quantum systems aims at understanding the transport properties of quantum dots, as they could feature particularly interesting strongly correlated physics (e.g. in the context of thermotransport [Mah95] – compare also chapter 8). Furthermore, transport through quantum dot structures are intriguing as those structures describe nano-electronic devices. A field which has attracted a lot of interest in recent years.

Finally, the open systems studied in the following (SBM and IRLM) pose basic prototype models of quantum many-body theory. Understanding their highly non-trivial emergent behavior is thus, apart from the above mentioned reasons, also of fundamental *academic* interest.

Outline

As motivated in the introduction, both the IRLM and SBM will be of central interest in the following, with a clear focus on the transient dynamics encountered within these systems. As we focus on the thermodynamic limit (infinite environment) we will use the developed FRG approach as well as a complementary renormalization group procedure (RTRG → Section 6.4) to describe their dynamics. But before doing so we will first dwell some more on the rather subtle implications of the thermodynamic limit. Within this we start with an investigation of how this limit is realized by increasing system size and motivate the need of a method tackling infinite reservoirs, when an emergent low energy scale (Kondo temperature) is involved. In the first section we present arguments in favour of our choice of method by pointing out possible pitfalls of other approaches and showing explicitly that the FRG produces well controlled results. Section two is then devoted to the transient dynamics of the IRLM, where we also extend the $T = 0$ approach given in [Ken11] to finite T. Next, we focus on the SBM describing the relaxation dynamics of the single spin. We find surprisingly that 'coherence' (measured by the non-monotonicity in the dynamics) can be greatly increased by elevating the temperature. As coherence is the main goal of any setup studied in the context of quantum computing, this has rather counter-intuitive implications to the optimal operating point of such devices, if the description by the SBM is sufficiently accurate. In a final section we establish a link between the transport driven IRLM and the SBM, which goes beyond the formal mapping introduced in Section 3.6. We close this chapter by concluding our findings.

7.1 Thermodynamic Limit and Pitfalls

In this section we want to first rewind to a rather subtle point that – so far – was swept under the rug. It concerns the thermodynamic limit which is properly implemented as $\lim_{N\to\infty}$ with $n/N = \text{const.}$ *before* calculating any observable, where n is the total particle number and N the size of the system. In particular, when addressing the asymptotic long-time regime $t_0 \to -\infty$ this is important as otherwise this limit would certainly be ill-defined, due to recurrence phenomena. DMRG on the one hand is implemented for finite size when considering inhomogeneous systems such that the question remains, whether the systems are sufficiently large to describe the infinite reservoir. Remarkably, it is a distinct advantage of the FRG on the other hand that infinite, i.e. open, systems can be addressed directly. In the derivation however (→ Chapter 4) first finite N is addressed, because statistical operators might otherwise be ill-defined. Then a *steady-state* is assumed and flow equations are derived. Only afterwards the limit of $N \to \infty$ is realized. Thus giving rise to the reasonable question: does the FRG properly encode the physics of the thermodynamic limit? Setting up a FRG framework that can treat transient times (finite $t_0 = 0$) helps to answer this questions. But before doing so we want to dwell some more on the issue of recurrence.

7.1.1 Recurrence in Finite Systems

It is a fundamental assumption of statistical mechanics, that each point in phase space compatible with the values of possible integrals of motion is sampled. Condensed in the statement of (quasi)ergodicity [Sch06] this means that every trajectory[1] comes arbitrarily close to each point in phase space. For any finite dimensional system Poincaré recurrence theorem [Poi90, Bar06] then

[1] besides a set of zero measure

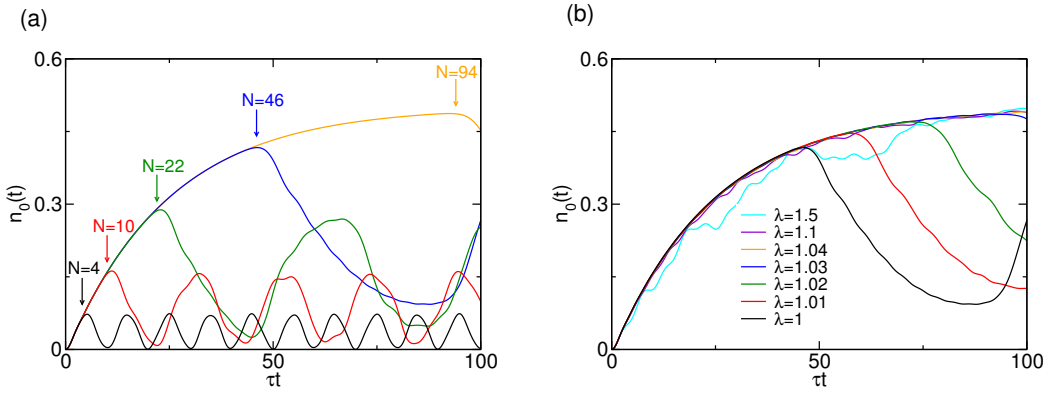


Figure 7.1.: Left: Time evolution of the occupancy $n_0(t)$ residing on a central level tunnel coupled to two tight-binding reservoirs at $t = 0$ (compare the Hamiltonian given in Eq. (7.1.3) with $z_i = 1$) for different size of the reservoir N (initially in equilibrium and at half-filling). The other parameters are $\tau = 1$, $\epsilon = 0$ and $t_{\text{imp}} = 0.1$. The time at which the information about the central level travelled through the chain and back is indicated by vertical arrows. Clearly, this is the relevant time scale where the observable "feels" the influence of the boundary as finite size deviations show up. It scales linearly in N. Right: The same now by usage of a Wilson chain. As λ (with $z_i = \lambda^{-(i-1)}$) is increased the recurrence time can be pushed to larger values. However, artificial oscillations steaming internal reflections induced by $z_i \neq 1$ appear. This renders simple Wilson chains problematic for general non-equilibrium studies.

states that for each quantum system with volume preserving[2] flow in phase space for every $\epsilon > 0$ and $T_0 > 0$ there exists a time $t_r > T_0$ such that

$$||\psi(t_r)\rangle - |\psi(0)\rangle| < \epsilon \,, \tag{7.1.1}$$

with the state vector at t given by $|\psi(t)\rangle$. For a general interacting quantum system this highly non-trivial statement is difficult to scrutinize, but it is known that details (such as the value of t_r) are strongly dependent on the initial state $|\psi(0)\rangle$ as well as the Hamiltonian determining the dynamics. Loosely speaking this means that for a finite quantum system the state vector $|\psi(t)\rangle$ returns arbitrarily close to its initial state vector $|\psi(0)\rangle$ infinitely often. This defines a recurrence time t_r which is expected [Sch06] to scale exponentially in the number of quantum degrees of freedom. But for the usual low-dimensional finite size systems studied here this exponentially large time is not the quantity of interest, determining when finite size effects become prominent. This latter time rather scales linearly in system size. Put more quantitative, if the finite size effects in the initial state are neglected, information about any perturbation travels with a typical speed c through the chain. c is linked to the Lieb-Robinson bound [Lie72] which dictates, that correlators $C_{ij} = \langle A_i B_j(t)\rangle$ are suppressed exponentially[3] outside a "light-cone" of width $2ct$ around site i ($|i-j| < ct$). To illustrate this point we consider a non-interacting finite size model

$$H = H_0 + H_{\text{res}} + H_{\text{tun}} \,, \tag{7.1.2}$$

$$H_0 = \epsilon c_0^\dagger c_0 \,, \quad H_{\text{res}} = \tau \sum_{\alpha=\text{L,R}} \sum_{i=1}^{N} z_i c_{\alpha,i}^\dagger c_{\alpha,i+1} + \text{H.c.} \,, \quad H_{\text{tun}} = t_{\text{imp}} \Theta(t) \sum_{\alpha=\text{L,R}} c_{\alpha,0}^\dagger c_{\alpha,1} + \text{H.c.} \tag{7.1.3}$$

via exact diagonalization. This model describes a single level (denoted by 0) at energy ϵ, which is coupled by reduced hopping $t_{\text{imp}} < |\tau|$ to two nearest neighbor hopping tight-binding reservoirs of size N. For now we choose $\epsilon = 0$ and $z_i = 1$. We prepare the reservoirs in their decoupled

[2] being fulfilled for any physical system due to Liouville's theorem [Sch06].
[3] Note that this is astonishing as we are dealing with non-relativistic theories.

ground states and consider an initially empty single-level. At $t = 0$ the coupling of single-level and reservoirs is switched on. The subsequent non-equilibrium dynamics of the occupancy of the single-level $n_0 = \left\langle c_0^\dagger c_0 \right\rangle$ is shown in Fig. 7.1(a). The velocity c in this non-interacting model is given by the Fermi velocity $c = v_f = 2\tau$. Thus the information of the coupling at site 0 travels through the chain and back to site zero in time $T_0 = 2N/(2\tau) = N/\tau$. These times are marked for different system sizes N by vertical arrows in Fig. 7.1(a). At T_0 the finite size effects are striking[4]. Clearly this "recurrence" time of the perturbation at $t = 0$ around the site denoted by 0 scales linearly in N (and proportionality factor $\sim 1/c$).

7.1.2 Wilson Chains as Reservoirs?

In equilibrium, when aiming at impurity physics (such as the Kondo effect) it is well known that one can modify the reservoirs to model infinite reservoirs very efficiently. In impurity systems where very low energy scales need to be resolved, using a Wilson chain improves the low energy resolution exponentially. This formulation lies at heart of any NRG ($\rightarrow$ Section 6.5) implementation and the corresponding reservoirs are referred to as *Wilson chains*. We can model Wilson chains within the Hamiltonian defined in Eq. (7.1.3) by setting

$$z_i = \lambda^{-(i-1)} , \qquad \lambda > 1 . \tag{7.1.4}$$

This decouples the end of the chain in an exponential fashion. In the context of non-equilibrium, however, it was shown, that modelling the reservoirs this way leads to severe artefacts. This is basically a consequence of the Wilson chains being reservoirs with respect to particles, but not with respect to energy [Ros12]. In setups like considered above, this most prominently leads to the build up of *Wilson Tsunamis* [Sch10, DdS08], which is the piling up of charge in the leads and in multiple reflections throughout the chain. In Fig. 7.1(b) the same is shown as in Fig. 7.1(a), but for constant $N = 46$ and different λ. As λ is increased the time at which the reflection from the boundary becomes prominent can be pushed to large values, but at the costs of artificial oscillations. These oscillations are the consequences of small reflections in the Wilson chain due to the reduced hopping from one site to the next. Thus, despite the usefulness of Wilson chains in equilibrium in non-equilibrium additional complications are encountered.

7.1.3 $N \rightarrow \infty$

No matter how one rephrases the problem, whenever quantum impurity physics involve an emergent low energy scale T_K (e.g. exponentially small for Kondo physics) calculations get quite difficult to handle with finite size algorithms. In a steady-state or equilibrium setup this manifests, e.g., in a long-ranged screening cloud of length $1/T_K$. For the dynamics, on the other hand, it reduces to the fact that very large time scales $t \sim T_K^{-1}$ ought to be reached. As the limit where T_K is much smaller than the "bare" energy scales is usually the interesting one[5] it is a distinct advantage of FRG that the limit $N \rightarrow \infty$ can be addressed readily. As already explained earlier in this section this comes at the price that one might wonder whether the order of limits in the method's derivation properly implements the physics of the thermodynamic limit. Here we will shortly demonstrate explicitly that the long time asymptotes indeed recover the results obtained in a steady-state formulation.

We consider an open system similar to the one defined in Eq. (7.1.3) with $z_i = 1$ and $N \rightarrow \infty$. Additionally, we add the non-trivial interaction term

$$U = \sum_{\alpha=\mathrm{L,R}} U_\alpha \left(n_{\alpha,1} - \frac{1}{2} \right) \left(n_0 - \frac{1}{2} \right) , \tag{7.1.5}$$

to the Hamiltonian to recover the IRLM ($\rightarrow$ Section 3.5). Furthermore, we consider the scaling limit $\tau \rightarrow \infty$ with $t_{\mathrm{imp}}^2/\tau = \Gamma_{\mathrm{1D}}$ finite ($\rightarrow$ Section 3.5) where already in the non-interacting case

[4] fintie size effects steaming from the ground state preparations in the reservoirs are actually irrelevant in this non-interacting model.

[5] because then bandstructure, etc. is irrelevant.

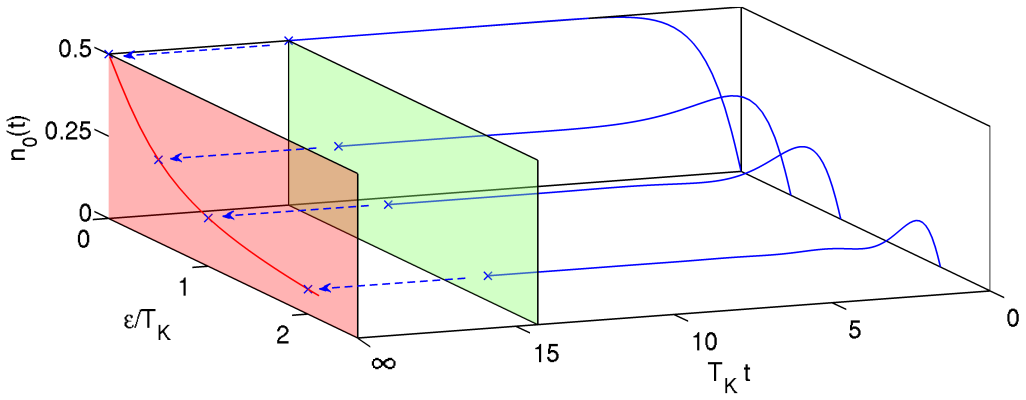


Figure 7.2.: Occupancy n_0 of the IRLM in the scaling limit $t_{\text{imp}}/\Gamma = 0.0025$. The interaction strength is $U_\alpha/\Gamma = 0.1$ and we consider vanishing temperature $T = 0$ and chemical potential $\mu = 0$ in both reservoirs. We solve for the occupancy in the steady-state formulation of the FRG ($\rightarrow$ Section 8.2) as well as resolving its transient dynamics ($\rightarrow$ Section 7.2) and then compare the long time asymptotes of the latter to the values obtained in the former. The slide at $T_K t \rightarrow \infty$ shows the last value obtained for the time evolution (symbols) compared to the values obtained from the steady-state analysis. They are in excellent agreement.

$U_\alpha = 0$ the relevant low energy scale $\Gamma_{1\text{D}} \ll \tau$, rendering this limit difficult to access with finite size algorithms. For more details, e.g., why this limit is particularly interesting we again refer to Section 3.5, for the time being only the results are relevant. We can tackle this model in the steady-state formulation of the FRG ($\rightarrow$ Section 8.2) as well as solve for its transient dynamics ($\rightarrow$ Section 7.2) and then compare the long time asymptotes of the latter to the values obtained in the former. This is depicted in Fig. 7.2. The value obtained for very large times (on the scale $\sim 1/T_K$) compares perfectly to the long-time asymptote obtained from a steady-state code. For the IRLM this was already hinted by comparing to other methods[6] (see [Kar10d, Kar10b] compared to [Doy06, Doy07, Bor07, Bou08, And11b] in various limits). Generally, one can argue that within the first order truncation scheme[7] used to tackle the time evolution one will always recover the steady-state FRG results for asymptotically large times if only one condition is met. If we interpret the combination of physical Hamiltonian and contributions to the self-energy from both the bath and the finite interaction as an effective time dependent non-hermitian Hamiltonian $H^{\text{eff}}(t)$ this becomes particularly easy to see. We consider the matrix $\underline{H}^{\text{eff}}_{i,j}(t)$, with elements $\underline{H}^{\text{eff}}_{i,j}(t) = \langle i| H^{\text{eff}}(t) |j\rangle = U(t)D(t)U^{-1}(t)$ in the single-particle states which can be diagonalized[8] using U with diagonal matrix D. If $\lim_{t\rightarrow\infty} \text{Im}[D_{ii}(t)] < 0$ for all i at large times there exists a decay channel to every quantum level and a steady state is reached which corresponds to the same one as gained by taking $t_0 \rightarrow -\infty$ before hand. Actually, this is a very mild condition, as one usually considers a finite quantum system (e.g. multi-level dot), coupled to an environment introducing some characteristic decay channel Γ. This gives $\lim_{t\rightarrow\infty} \text{Im}[D_{ii}(t)] < 0$ without interaction. Finite interaction, of course, leads to a non-trivial renormalization of those values, but does usually not alter their sign[9], keeping in mind that the interaction is kept small.

[6] such as DMRG, field-theory approaches and RTRG.
[7] Higher order truncation schemes are impractical at the moment [Ken11].
[8] We assume that the matrix is not defective.
[9] $\lim_{t\rightarrow\infty} \text{Im}[D_{ii}(t)] = 0$ would lead to a perfect decoupling of certain levels from their decay channel, $\lim_{t\rightarrow\infty} \text{Im}[D_{ii}(t)] > 0$ is even worse as it would violate the Pauli-principle.

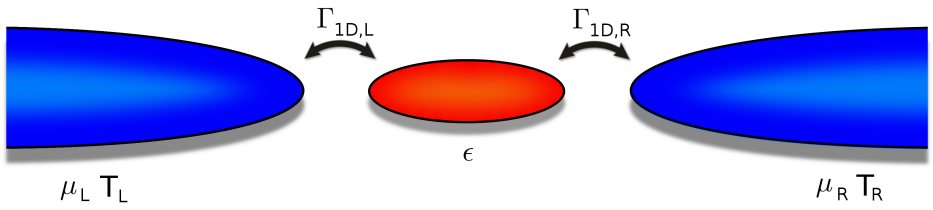


Figure 7.3.: Sketch of the single-level quantum dot studied in this section. It consists of a single site subjected to an onsite energy ϵ and coupled to two structureless reservoirs (index $\alpha = \mathrm{L}, \mathrm{R}$) held at in general different temperatures T_α and chemical potential μ_α.

7.2 Transient Dynamics of the IRLM

In this section we explain in detail how one can solve for the transient time evolution within the FRG scheme outlined in chapter 4. As an example we will study the IRLM ($\rightarrow$ Section 3.5), but extensions to other kinds of systems (fermionic or bosonic, open or closed, ...) are straight forward. For the FRG it is vital to restrict the interaction to the region, which is treated explicitly (in contrast to the reservoirs, which can be integrated out). Thus, we take into account the first site of what is conventionally called the reservoir explicitly and follow the argument outlined in Section 3.5. We always assume a product form $\rho(0) = \rho_0^{\mathrm{dot}} \prod_{\alpha=\mathrm{L},\mathrm{R}} \rho_{\mathrm{res},\alpha}$ for the initial density matrix in the following. Here $\rho_{\mathrm{res},\alpha}$ is the grand canonical density matrix (characterized by temperature T_α and chemical potential μ_α) of reservoir α and ρ_0^{dot} the initial (uncorrelated) density matrix of the dot.

7.2.1 Warm-up: Single-Level ($U = 0$)

As a warm-up and for benchmarking reasons we first consider the non-interacting case $U_\alpha = 0$. Here we can aim right away at a single-level coupled to reservoirs in the wide-band limit, as no interaction needs to be included. The decoupled, non-interacting Green's functions read

$$g^{\mathrm{R/A}}(t,t') = \mp i e^{-i\epsilon(t-t')}\Theta(\pm(t-t')) \,, \tag{7.2.1}$$

$$g^{\mathrm{K}}(t,t') = -i(1-2\bar{n}_0)e^{-i\epsilon(t-t')} \,, \tag{7.2.2}$$

where $\bar{n}_0$ is the initial occupancy of the central level. Those must be dressed by the self-energies

$$\Sigma^{\mathrm{R/A}}_{\mathrm{res},\alpha}(t,t') = \mp i \sum_{\alpha=L,R} \Gamma_{1\mathrm{D},\alpha}\delta(t-t') \,, \tag{7.2.3}$$

$$\Sigma^{\mathrm{K}}_{\mathrm{res},\alpha}(t,t') = \sum_{\alpha=L,R} -T_\alpha e^{-i\mu_\alpha(t'-t)}\Gamma_{1\mathrm{D},\alpha} \sum_{\pm} \frac{1}{\sinh[\pi T_\alpha(t'-t\pm i\delta)]} . \tag{7.2.4}$$

For simplicity, we choose $\Gamma_{1\mathrm{D},\alpha} = \Gamma_{1\mathrm{D}}$ in the following. Using Eq. (4.1.32) and employing a transformation to relative and 'center of time' variables $\Delta t = t_2 - t_1$ and $T = t_1 + t_2$ inside the

double integral one can find closed form expressions for the reservoir dressed Green's functions

$$G^{\mathrm{R/A}}(t,t') = \mp i e^{-i\epsilon(t-t')} e^{\mp 2\Gamma_{1\mathrm{D}}(t-t')} \Theta(\pm(t-t')). \tag{7.2.5}$$

$$\begin{aligned} G^{\mathrm{K}}(t,t) = \; & (1-2\bar{n}_0) e^{-4\Gamma_{1\mathrm{D}} t} \\ & + \lim_{\delta\to 0^+} i\mathrm{Im}\Bigg[\sum_\alpha \left\{ \frac{e^{-2\pi T_\alpha b_1\, \delta}}{-\pi b_1} \, {}_2\mathcal{F}_1\left(1, b_1, b_1+1, e^{-2\pi T_\alpha\, \delta}\right) \right\} \\ & + \sum_\alpha \left\{ \frac{e^{-2\pi T_\alpha b_1\, t}}{-\pi b_1} \, {}_2\mathcal{F}_1\left(1, b_1, b_1+1, e^{-2\pi T_\alpha\, t}\right) \right\} \\ & - e^{-4\Gamma_{1\mathrm{D}} t} \sum_\alpha \left\{ \frac{e^{-2\pi T_\alpha b_2\, \delta}}{-\pi b_2} \, {}_2\mathcal{F}_1\left(1, b_2, b_2+1, e^{-2\pi T_\alpha\, \delta}\right) \right\} \\ & - e^{-4\Gamma_{1\mathrm{D}} t} \sum_\alpha \left\{ \frac{e^{-2\pi T_\alpha b_2\, t}}{-\pi b_2} \, {}_2\mathcal{F}_1\left(1, b_2, b_2+1, e^{-2\pi T_\alpha\, t}\right) \right\} \Bigg], \end{aligned} \tag{7.2.6}$$

where

$$b_1 = \frac{-[i(\epsilon-\mu_\alpha) - 2\Gamma_{1\mathrm{D}} - \pi T_\alpha]}{2\pi T_\alpha}, \tag{7.2.7}$$

$$b_2 = \frac{-[i(\epsilon-\mu_\alpha) + 2\Gamma_{1\mathrm{D}} - \pi T_\alpha]}{2\pi T_\alpha}. \tag{7.2.8}$$

In $b_{1/2}$ we have suppressed the index α. For the observables of interest here, only the equal-time Keldysh Green's function $G^{\mathrm{K}}(t,t)$ is relevant. We used the *Gauss hypergeometric function*

$${}_2\mathcal{F}_1(a,b,c,z) = \sum_{k=0}^{\infty} \frac{(a)_k (b)_k z^k}{(c)_k k!}, \qquad |z|<1 \;\vee\; \left(|z|=1 \;\wedge\; \mathrm{Re}[c-a-b]>0\right), \tag{7.2.9}$$

with the *Pochhammer symbol*

$$(a)_n = \prod_{i=0}^{n-1} (a+i) = \Gamma(a+n)/\Gamma(a). \tag{7.2.10}$$

The special case ${}_2\mathcal{F}_1(1,b,b+1,z)$ can be reduced to the *Hurwitz-Lerch zeta-function* $\phi(z,s,a)$

$${}_2\mathcal{F}_1(1,b,b+1,z) = b\phi(z,1,b), \tag{7.2.11}$$

$$\phi(z,s,a) = \sum_{k=0}^{\infty} \frac{z^k}{(a+k)^s}, \qquad |z|<1 \;\vee\; \left(|z|=1 \;\wedge\; \mathrm{Re}[s]>1\right). \tag{7.2.12}$$

As the Hurwitz-Lerch zeta-function is not part of our standard reference [Abr70] we define it as in [Bat53]. Either special function, Gauss hypergeometric function or Hurwitz-Lerch zeta-function, has to be implemented for complex arguments b, c or a, respectively. This can be done by different representations via Taylor or asymptotic serious expansions in the different limits [Abr70]. The, in principle, problematic limit $\lim_{\delta\to 0^+}$ in (7.2.6) can be evaluated using

$$\lim_{\delta\to 0^+} \mathrm{Im}\left[e^{-2\pi T_\alpha b_1\, \delta} \sum_{i=1,2} \frac{(-1)^i}{\pi b_i} \, {}_2\mathcal{F}_1\left(1, b_i, b_i+1, e^{-2\pi T_\alpha\, \delta}\right) \right] = \frac{1}{\pi} \mathrm{Im}\left[\Psi(0,b_1) - e^{-4\Gamma_{1\mathrm{D}} t} \Psi(0,b_2) \right], \tag{7.2.13}$$

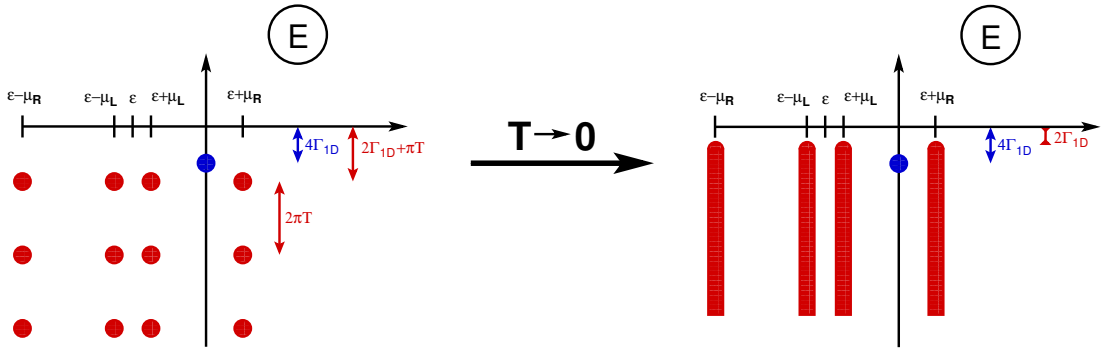


Figure 7.4.: Laplace transform $\bar{n}(E)$ [see (7.2.16)] of the occupancy $\bar{n}(t) - \bar{n}_{\text{stat}}$. In "complex energy" space and at finite temperature four infinite sums of poles giving rise to damped oscillatory behavior can be found. Additionally, there is a single pole situated at the imaginary axis, describing a simple exponential relaxation term. As $T \to 0$ the sums of poles turn to branch-cut contributions and the results of [Ken11] are recovered.

where $\Psi(0.x)$ is the *digamma function*. Using Eqs. (4.1.65) and (4.1.69) one can calculate occupancy and current

$$\begin{aligned}\bar{n}(t) =& \frac{1}{2} - \frac{1}{2} e^{-4\Gamma_{1D} t}(1 - 2\bar{n}_0) + \frac{1}{2}\sum_\alpha \text{Im}\left[\frac{1}{\pi}\Psi(0, b_1) - e^{-4\Gamma_{1D} t}\frac{1}{\pi}\Psi(0, b_2)\right. \\ &\left. - \frac{e^{-2\pi T_\alpha b_1\, t}}{-\pi b_1} {}_2\mathcal{F}_1\left(1, b_1, b_1 + 1, e^{-2\pi T_\alpha t}\right) + \frac{e^{-2\pi T_\alpha b_1\, t}}{-\pi b_2} {}_2\mathcal{F}_1\left(1, b_2, b_2 + 1, e^{-2\pi T_\alpha t}\right)\right] ,\end{aligned} \tag{7.2.14}$$

$$\frac{J_L(t)}{\Gamma_{1D}} = 1 - 2\bar{n}(t) + 2\frac{\text{Im}\left[\Psi(0, b_1)\right]}{\pi} - 2\text{Re}\left[i\frac{e^{-2\pi T_\alpha b_1 t}}{\pi b_1} {}_2\mathcal{F}_1\left(1, b_1, b_1 + 1, e^{-2\pi T_\alpha t}\right)\right] . \tag{7.2.15}$$

From Eq. (7.2.11) and (7.2.12) it is obvious that the time evolution of occupancy and current are governed by a sum of exponential terms in t with prefactors in the exponents given by $-4\Gamma_{1D}$ and $[i(\epsilon - \mu_\alpha) - 2\Gamma_{1D} - \pi T_\alpha] - 2\pi k T_\alpha$ with $k \in \mathbb{N}_0$. It proves instructive to introduce the Laplace transform

$$O(E) = \int_0^\infty dt\; e^{iEt} O(t) , \tag{7.2.16}$$

of the real-time dependent expressions given above. The non-analyticities in the lower[10] half-plane in the complex Laplace variable E ("energy"), determine the real-time dynamics completely. Non-analyticities at positions $(\text{Re}[E], \text{Im}[E])$ lead to oscillatory terms with frequency $\text{Re}[E]$ and exponential damping with rate $\text{Im}[E]$. In the case of branch-cuts (contrary to poles) the damping is supplemented additionally by $1/t^g$ corrections for large t with some exponent g depending on the structure of the branch-cut. Thus the non-analyticity closest to the real axis determines the asymptotic long-time behavior. Generally, a pole at $E = 0$ determines the steady-state value reached for $t \to \infty$ (labelled by an index stat in the following). As this constant is of minor interest we will subtract it from $O(t)$ before taking the Laplace transform, when necessary.

Transforming the above expressions (7.2.14) and (7.2.15) to Laplace ("energy") space we obtain the following picture. The terms belonging to sums of exponentials with prefactors $[i(\epsilon - \mu_\alpha) - 2\Gamma_{1D} - \pi T_\alpha] - 2\pi k T_\alpha$ in the exponents correspond to sums of poles at E with real part (frequencies) $(\epsilon - \mu_\alpha)$ and imaginary part (decay strengths) $-2\Gamma_{1D} - (2k+1)\pi T_\alpha$, where naturally the fermionic Matsubara frequencies $\omega_k = (2k+1)\pi T_\alpha$ enter. Additionally, we find a single pole with real part of E being zero and imaginary part being $-4\Gamma_{1D}$.

[10] In the upper half-plane no non-analyticities show up due to causality.

In the limit $T \to 0$ the infinite sums of poles turn to branch-cut contributions in Laplace space. One can recover explicitly the expressions at vanishing temperature [Ken11] by

$$\begin{aligned}
&\lim_{T_\alpha \to 0} \frac{1}{b_{1/2}} {}_2\mathcal{F}_1(1, b_{1/2}, b_{1/2}+1, e^{-2\pi T_\alpha t}) \\
&\qquad = \lim_{T_\alpha \to 0} \sum_{k=0}^{\infty} \frac{e^{-2\pi T_\alpha k t}}{[-i(\epsilon-\mu_\alpha) \pm 2\Gamma_{1D} + \pi T_\alpha]/(2\pi T_\alpha) + k} \\
&\qquad = \lim_{T_\alpha \to 0} \sum_{k=0}^{\infty} 2\pi T_\alpha \frac{e^{-2\pi T_\alpha k t}}{[-i(\epsilon-\mu_\alpha) \pm 2\Gamma_{1D} + \pi T_\alpha] + 2\pi T_\alpha k} \\
&\qquad \overset{T=2\pi T_\alpha k}{=} \int_0^\infty dT \, \frac{e^{-Tt}}{T + [-i(\epsilon-\mu_\alpha) \pm 2\Gamma_{1D}]} \\
&\qquad = e^{[-i(\epsilon-\mu_\alpha)\pm 2\Gamma_{1D}]t} \mathrm{E}(1, [-i(\epsilon-\mu_\alpha) \pm 2\Gamma_{1D}]t),
\end{aligned} \tag{7.2.17}$$

with the *exponential integrals* $\mathrm{E}(s,z)$ and furthermore,

$$\lim_{T_\alpha \to 0} \mathrm{Im}[\Psi(0, b_{1/2})] = \log(b_{1/2}). \tag{7.2.18}$$

Of course, when working at $T = 0$ these limits have to be taken analytically before doing any numerics. Also, at finite but very small temperature one can use an "expansion" around these $T = 0$ expressions. For visualization the analytic structure of $n(E)$ for finite T and $T = 0$ is summarized in Fig. 7.4.

It is important to realize, also for our study at finite interaction ($\to$ Section 7.2.3), that obviously the reservoir temperatures play a significantly different role than the hybridization. The latter enters in every relaxation rate of Eqs. (7.2.14) and (7.2.15), the temperature in contrast allows to tune the influence of the different terms with respect to each other, because the induced rates depend solely on either T_L or on T_R. Furthermore, even by generalizing to asymmetric couplings, that is generalizing Eqs. (7.2.14) and (7.2.15), this effect cannot be mimicked by the hybridizations, because only the sum of the hybridizations enters the decay rates (for explicit expressions in the case of asymmetric coupling see [Ken12a, Ken13b]).

7.2.2 FRG Treatment at Finite U

Finally, we turn to finite interaction strength U. As discussed in Section 3.5 and hinted above we consider a three-site dot (see Fig. 7.5) with

$$\begin{aligned}
H_{\mathrm{dot}} =& \epsilon d_2^\dagger d_2 + (t_{\mathrm{imp,L}} d_1^\dagger d_2 + t_{\mathrm{imp,R}} d_2^\dagger d_3 + \mathrm{H.c.}) \\
&+ U_{\mathrm{L}} \left(d_2^\dagger d_2 - \frac{1}{2}\right)\left(d_1^\dagger d_1 - \frac{1}{2}\right) + U_{\mathrm{R}} \left(d_2^\dagger d_2 - \frac{1}{2}\right)\left(d_3^\dagger d_3 - \frac{1}{2}\right),
\end{aligned} \tag{7.2.19}$$

coupled to structureless reservoirs (described by $\Gamma_{11,\mathrm{L}}$ and $\Gamma_{33,\mathrm{R}}$). Later, we employ the limits outlined in section 3.5 to describe the IRLM in the scaling limit. We focus here on the symmetric case

$$t_{\mathrm{imp,L}} = t_{\mathrm{imp,R}} = t_{\mathrm{imp}}, \tag{7.2.20}$$
$$\Gamma_{11,\mathrm{L}} = \Gamma_{33,\mathrm{R}} = \Gamma, \tag{7.2.21}$$
$$U_{\mathrm{L}} = U_{\mathrm{R}} = U\,, \tag{7.2.22}$$

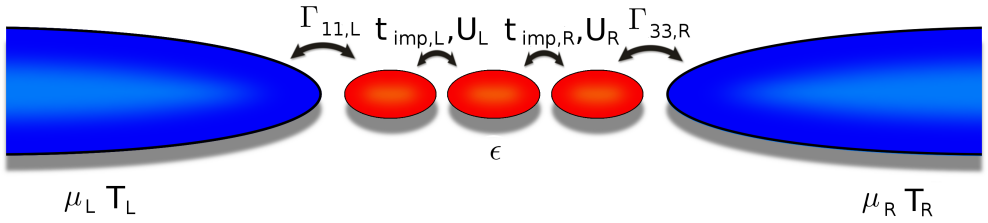


Figure 7.5.: Sketch of the three-level quantum dot studied in this section. It consists of three sites, where the central one is subjected to an onsite energy ϵ and all three are coupled by a nearest neighbor tunnel coupling $t_{\mathrm{imp},\alpha}$ ($\alpha = \mathrm{L}$ for coupling between first and second and $\alpha = \mathrm{R}$ for coupling between second and third site). First and third site are coupled to two structureless reservoirs (index $\alpha = \mathrm{L}$ and $\alpha = \mathrm{R}$, respectively) held at, in general, different temperatures T_α and chemical potential μ_α. A density-density type of interaction U_α is included between neighboring sites of the central region. In the limit described in Section 3.5 this setup corresponds to the field-theoretical IRLM.

while extensions are self-explanatory. Thus we need to dress the non-interacting Green's function of the dot by (1) the reservoir self-energy

$$\Sigma^{\mathrm{R/A}}_{\mathrm{res}}(t,t') = \mp i\hat{\Gamma}\delta(t-t') = \mp i \begin{pmatrix} \Gamma & 0 & 0 \\ 0 & 0 & 0 \\ 0 & 0 & \Gamma \end{pmatrix} \delta(t-t') \,, \tag{7.2.23}$$

$$\begin{aligned} \Sigma^{\mathrm{K}}_{\mathrm{res}}(t,t') &= -T_\alpha \sum_{\pm} \frac{1}{\sinh[\pi T_\alpha (t'-t \pm i\delta)]} \hat{\Gamma}^\mu (t-t') \\ &= -T_\alpha \sum_{\pm} \frac{1}{\sinh[\pi T_\alpha (t'-t \pm i\delta)]} \begin{pmatrix} \Gamma e^{-i\mu_L(t-t')} & 0 & 0 \\ 0 & 0 & 0 \\ 0 & 0 & \Gamma e^{-i\mu_R(t-t')} \end{pmatrix}, \end{aligned} \tag{7.2.24}$$

by (2) the self-energy of the cut-off (during the flow)

$$\Sigma^{\mathrm{R/A}}_{\mathrm{cut}}(t,t') = \mp i\hat{\Lambda}\delta(t-t') = \mp i \begin{pmatrix} \Lambda & 0 & 0 \\ 0 & \Lambda & 0 \\ 0 & 0 & \Lambda \end{pmatrix} \delta(t-t') \,, \tag{7.2.25}$$

$$\Sigma^{\mathrm{K}}_{\mathrm{cut}}(t,t') = 0, \tag{7.2.26}$$

as well as by (3) the self-energy generated by the flow

$$\Sigma^{\mathrm{R/A},\Lambda}(t,t') = \Sigma^{\mathrm{R/A},\Lambda}(t)\delta(t-t') \,, \tag{7.2.27}$$

$$\Sigma^{\mathrm{K},\Lambda}(t,t') = 0 \,. \tag{7.2.28}$$

Because we use a first order truncation scheme no Keldysh self-energy is generated during the flow and the retarded and advanced self-energy stay local in time [compare [Ken11] Eqs. (6.80) and (6.82)]. This also allows for an interpretation of the self-energy generated throughout the flow as a contribution to some effective (time dependent) single-particle Hamiltonian. We proceed as in [Ken11] now for general T. We need to solve the Dyson equations (4.1.24)-(4.1.26) as well as determine S^{K} by Eq. (4.3.18). Vital to the calculation is the "group property" of the retarded Green's function derived in section 7.2 of [Ken11]

$$-iG^{\mathrm{R},\Lambda}(t,t') = G^{\mathrm{R},\Lambda}(t,t_1)G^{\mathrm{R},\Lambda}(t_1,t') \qquad \forall t > t_1 > t' \,. \tag{7.2.29}$$

$\mathrm{Res}_{ij,n}$		ij 11	22	12	13
n	1	$1+\frac{\lvert t_{12}^{\Lambda}\rvert^2}{(\omega_1-\omega_2)(\omega_1-\omega_3)}$	0	0	$\frac{t_{12}^{\Lambda}t_{23}^{\Lambda}}{(\omega_1-\omega_2)(\omega_1-\omega_3)}$
	2	$\frac{\lvert t_{12}^{\Lambda}\rvert^2}{(\omega_2-\omega_1)(\omega_2-\omega_3)}$	$\frac{\omega_2-\omega_1}{\omega_2-\omega_3}$	$\frac{t_{12}^{\Lambda}}{\omega_2-\omega_3}$	$\frac{t_{12}^{\Lambda}t_{23}^{\Lambda}}{(\omega_2-\omega_1)(\omega_2-\omega_3)}$
	3	$\frac{\lvert t_{12}^{\Lambda}\rvert^2}{(\omega_3-\omega_1)(\omega_3-\omega_2)}$	$\frac{\omega_3-\omega_1}{\omega_3-\omega_2}$	$\frac{t_{12}^{\Lambda}}{\omega_3-\omega_2}$	$\frac{t_{12}^{\Lambda}t_{23}^{\Lambda}}{(\omega_3-\omega_1)(\omega_3-\omega_2)}$
33		$\mathrm{Res}_{11,n}(t_{12}^{\Lambda}\to t_{23}^{\Lambda})$			
21		$\mathrm{Res}_{12,n}(t_{12}^{\Lambda}\to (t_{12}^{\Lambda})^*)$			
31		$\mathrm{Res}_{13,n}(t_{12}^{\Lambda}, t_{23}^{\Lambda}\to (t_{12}^{\Lambda})^*, (t_{23}^{\Lambda})^*)$			
23		$\mathrm{Res}_{12,n}(t_{12}^{\Lambda}\to t_{23}^{\Lambda})$			
32		$\mathrm{Res}_{23,n}(t_{23}^{\Lambda}\to (t_{23}^{\Lambda})^*)$			

TABLE 7.1.: Residues of $1/\left\{\omega-\left[\hat{\epsilon}_{\mathrm{dot},0}-i(\hat{\Gamma}+\hat{\Lambda})+\Sigma^{\mathrm{R},\Lambda}(\tilde{\tau})\right]\right\}$ for the labelling introduced in Eq. (7.2.35).

This identity is a consequence of $\Sigma^{\mathrm{R}}(t,t')\sim\delta(t-t')$ (locality in time), which is true only for *structureless reservoirs* and if a *first order truncation* of the FRG flow equations is employed.

Retarded Green's Function

In turn the retarded Green's function can be calculated right away by discretizing time into fine[11] steps $t\to t_n$, so that the total retarded self-energy can be set stepwise constant. Then the retarded Green's function reads

$$G^{\mathrm{R},\Lambda}(t_m,t_n)=\Theta(t_m-t_n)\left(-i\prod_{i=n}^{m-1}iG^{\mathrm{R},\Lambda}(t_{i+1},t_i)\right). \tag{7.2.30}$$

Retarded Green's functions whose time arguments do not span more than a single time step and whose self-energy can be set constant will be called *elementary*. As shown in section 7.3 of [Ken11] such elementary retarded Green's functions can be found by[12]

$$iG^{\mathrm{R},\Lambda}(t_{i+1},t_i)\approx\exp\left\{-i\left[\hat{\epsilon}_{\mathrm{dot},0}-i(\hat{\Gamma}+\hat{\Lambda})+\Sigma^{\mathrm{R},\Lambda}(\tilde{\tau})\right](t_{i+1}-t_i)\right\}, \tag{7.2.31}$$

where $\hat{\epsilon}_{\mathrm{dot},0}$ is the matrix with entries given by the dot part of the single-particle Hamiltonian. Finally, the stepwise constant self-energy contribution is just the average

$$\Sigma^{\mathrm{R},\Lambda}(\tilde{\tau})=\frac{\Sigma^{\mathrm{R},\Lambda}(t_{i+1})+\Sigma^{\mathrm{R},\Lambda}(t_i)}{2}. \tag{7.2.32}$$

For the example discussed here one has

$$\hat{\epsilon}_{\mathrm{dot},0}=\begin{pmatrix}0 & t_{\mathrm{imp}} & 0\\ t_{\mathrm{imp}} & \epsilon & t_{\mathrm{imp}}\\ 0 & t_{\mathrm{imp}} & 0\end{pmatrix}. \tag{7.2.33}$$

The equations for the matrix exponential of a 3×3 matrix can be implemented explicitly (using some computer algebra system as they are rather lengthy). This allows for evaluating Eq. (7.2.31)

[11] The meaning of "fine" being that the total retarded self-energy can be set constant within one time step to a very good approximation.

[12] An arbitrary explicit time dependence on the dot can be included, by replacing $\epsilon\to\epsilon(\tau)$ and using a time grid small enough so that also this contribution can be treated stepwise constant.

very efficiently. Furthermore, one can rewrite the retarded Green's function analytically via

$$G^{\mathrm{R},\Lambda}(t_{i+1},t_i)=\frac{1}{2\pi}\int_{-\infty}^{\infty}e^{-i(\omega+i\eta)(t_{i+1}-t_i)}\frac{1}{\omega-\left[\hat{\epsilon}_{\mathrm{dot},0}-i(\hat{\Gamma}+\hat{\Lambda})+\Sigma^{\mathrm{R},\Lambda}(\tilde{\tau})\right]}; \tag{7.2.34}$$

the key ingredient to find the Keldysh components analytically[13]. Closing the integral in the lower half-plane and using complex analysis we rewrite this as a sum of poles

$$G^{\mathrm{R},\Lambda}(t_{i+1},t_i)\big|_{kl}=-i\sum_{n=1}^{3}\mathrm{Res}_{kl,n}e^{-i\omega_n(t_{i+1}-t_i)}\,, \tag{7.2.35}$$

Defining the effective single-particle parameters

$$\epsilon'^{\Lambda}\equiv\Sigma^{\mathrm{R},\Lambda}_{\tilde{\tau},11}\,, \tag{7.2.36}$$
$$\epsilon^{\Lambda}\equiv\epsilon+\Sigma^{\mathrm{R},\Lambda}_{\tilde{\tau},22}\,, \tag{7.2.37}$$
$$t^{\Lambda}_{12}\equiv t_{\mathrm{imp}}+\Sigma^{\mathrm{R},\Lambda}_{\tilde{\tau},12}\,, \tag{7.2.38}$$
$$t^{\Lambda}_{23}\equiv t_{\mathrm{imp}}+\Sigma^{\mathrm{R},\Lambda}_{\tilde{\tau},23}\,, \tag{7.2.39}$$

the poles can be expressed as

$$\omega_1=\epsilon'^{\Lambda}-i(\Gamma+\Lambda)\,, \tag{7.2.40}$$
$$\omega_{2/3}=\frac{1}{2}\left(\epsilon^{\Lambda}+\epsilon'^{\Lambda}-i\Gamma-2i\Lambda\mp\sqrt{-(\Gamma-i\epsilon^{\Lambda}+i\epsilon'^{,\Lambda})^2+4|t^{\Lambda}_{12}|^2+4|t^{\Lambda}_{23}|^2}\right). \tag{7.2.41}$$

The corresponding residues are given in table 7.1.

Keldysh Green's Function

Again employing Eq. (7.2.29) we can re-express the solution of the Dyson equation Eq. (4.1.25) as a sum of integrals involving only *elementary* retarded Green's functions in the integrand

$$\begin{aligned}G^{\mathrm{K},\Lambda}(t,t)=&-iG^{\mathrm{R},\Lambda}(t,t_0)(1-2\bar{n}_0)G^{\mathrm{A},\Lambda}(t_0,t)\\&-T_\alpha\int_{t_0}^{t}dt_1\int_{t_0}^{t}dt_2\,G^{\mathrm{R},\Lambda}(t,t_1)\Gamma^{\mu}(t_1-t_2)\left(\sum_{\pm}\frac{1}{\sinh[\pi T_\alpha(t'-t\pm i\delta)]}\right)G^{\mathrm{A},\Lambda}(t_2,t)\\=&-iG^{\mathrm{R},\Lambda}(t,t_0)(1-2\bar{n}_0)G^{\mathrm{A},\Lambda}(t_0,t)\\&-T_\alpha\sum_{n,m=0}^{k_{\max}-1}\int_{t_n}^{t_{n+1}}dt_1\int_{t_m}^{t_{m+1}}dt_2\,G^{\mathrm{R},\Lambda}(t,t_{n+1})G^{\mathrm{R},\Lambda}(t_{n+1},t_1)\\&\times\Gamma^{\mu}(t_1-t_2)\left(\sum_{\pm}\frac{1}{\sinh[\pi T_\alpha(t'-t\pm i\delta)]}\right)G^{\mathrm{A},\Lambda}(t_2,t_{m+1})G^{\mathrm{A},\Lambda}(t_{m+1},t)\,,\end{aligned} \tag{7.2.42}$$

with $t_0=0$ and $t_{k_{\max}}=t$ as well as the matrix $\bar{n}_0$ with entries

$$[\bar{n}_0]_{ii'}=\mathrm{Tr}\,\rho_0^{\mathrm{dot}}d^{\dagger}_{i'}d_i. \tag{7.2.43}$$

We restrict ourselves to the equal-time Keldysh Green's function, the only one of relevance here. The integrals can subsequently be solved *analytically* using Eq. (7.2.35) and the transformation to

[13] Analytic solutions are vital due to the Cauchy principal value meaning of $\Sigma^{\mathrm{K}}_{\mathrm{res}}(t,t')$ at $t=t'$.

relative and 'center of time' variables introduced for the single-level case (→ Section 7.2.1)

$$
\begin{aligned}
&\left[\int_{t_n}^{t_{n+1}} ds_1 \int_{t_n}^{t_{n+1}} ds_2\, G^{\mathrm{R}}(t_{n+1}, s_1)\Sigma^{\mathrm{K}}_{res}(s_1, s_2)G^{\mathrm{A}}(s_2, t_{n+1})\right]_{ij} = \lim_{\delta\to 0}\sum_{\substack{\alpha=L,R\\ k,l=1,2,3}} T_\alpha \mathrm{Res}_{i\alpha,k}\mathrm{Res}^*_{j\alpha,l} e^{-i\Delta\omega_{kl}t_{n+1}}\\
&\times\left[\int_{t_n-t_{n+1}}^{-\delta} d\Delta t \int_{2t_n-\Delta t}^{2t_{n+1}+\Delta t} dT + \int_{\delta}^{t_{n+1}-t_n} d\Delta t \int_{2t_n+\Delta t}^{2t_{n+1}-\Delta t} dT\right]\frac{\Gamma}{\sinh(\pi T_\alpha \Delta t)} e^{i\mu_\alpha \Delta t} e^{\frac{1}{2}iT\Delta\omega_{kl}} e^{-i\frac{1}{2}\Delta t(\omega_k+\omega_l^*)}\\
&= \sum_{\substack{\alpha=L,R\\ k,l=1,2,3}} \mathrm{Res}_{i\alpha,k}\mathrm{Res}^*_{j\alpha,l} e^{-i(\omega_k t_{n+1}-\omega_l^* t_{n+1})}\frac{4T_\alpha\Gamma}{i\Delta\omega_{kl}}\Bigg(\\
&\quad e^{i\Delta\omega_{kl}t_{n+1}}\left[\frac{1}{2\pi T_\alpha}\left\{-\psi\left(\frac{-i\mu_\alpha+i\omega_k+\pi T_\alpha}{2\pi T_\alpha}\right)+\psi\left(\frac{i\mu_\alpha-i\omega_l^*+\pi T_\alpha}{2\pi T_\alpha}\right)\right\}\right.\\
&\quad -\frac{e^{(-i\mu_\alpha+i\omega_k+\pi T_\alpha)(t_n-t_{n+1})}}{-i\mu_\alpha+i\omega_k+\pi T_\alpha}{}_2\mathcal{F}_1\left(1,\frac{-i\mu_\alpha+i\omega_k+\pi T_\alpha}{2\pi T_\alpha},\frac{-i\mu_\alpha+i\omega_k+\pi T_\alpha}{2\pi T_\alpha}+1,e^{2\pi T_\alpha(t_n-t_{n+1})}\right)\\
&\quad \left.+\frac{e^{(i\mu_\alpha-i\omega_l^*+\pi T_\alpha)(t_n-t_{n+1})}}{i\mu_\alpha-i\omega_l^*+\pi T_\alpha}{}_2\mathcal{F}_1\left(1,\frac{i\mu_\alpha-i\omega_l^*+\pi T_\alpha}{2\pi T_\alpha},\frac{i\mu_\alpha-i\omega_l^*+\pi T_\alpha}{2\pi T_\alpha}+1,e^{2\pi T_\alpha(t_n-t_{n+1})}\right)\right]\\
&\quad -e^{i\Delta\omega_{kl}t_n}\left[\frac{1}{2\pi T_\alpha}\left\{-\psi\left(\frac{-i\mu_\alpha+i\omega_l^*+\pi T_\alpha}{2\pi T_\alpha}\right)+\psi\left(\frac{i\mu_\alpha-i\omega_k+\pi T_\alpha}{2\pi T_\alpha}\right)\right\}\right.\\
&\quad -\frac{e^{(-i\mu_\alpha+i\omega_l^*+\pi T_\alpha)(t_n-t_{n+1})}}{-i\mu_\alpha+i\omega_l^*+\pi T_\alpha}{}_2\mathcal{F}_1\left(1,\frac{-i\mu_\alpha+i\omega_l^*+\pi T_\alpha}{2\pi T_\alpha},\frac{-i\mu_\alpha+i\omega_l^*+\pi T_\alpha}{2\pi T_\alpha}+1,e^{2\pi T_\alpha(t_n-t_{n+1})}\right)\\
&\quad \left.\left.+\frac{e^{(i\mu_\alpha-i\omega_k+\pi T_\alpha)(t_n-t_{n+1})}}{i\mu_\alpha-i\omega_k+\pi T_\alpha}{}_2\mathcal{F}_1\left(1,\frac{i\mu_\alpha-i\omega_k+\pi T_\alpha}{2\pi T_\alpha},\frac{i\mu_\alpha-i\omega_k+\pi T_\alpha}{2\pi T_\alpha}+1,e^{2\pi T_\alpha(t_n-t_{n+1})}\right)\right]\right),
\end{aligned}
\tag{7.2.44}
$$

for $m = n$ where one has exploited that for $b > 0$

$$
\begin{aligned}
\lim_{x\to 0^+}&\frac{e^{(a+b)x}}{a+b}{}_2\mathcal{F}_1\left(1,\frac{a+b}{2b},\frac{a+b}{2b}+1,e^{2bx}\right)-\frac{e^{(c+b)x}}{c+b}{}_2\mathcal{F}_1\left(1,\frac{c+b}{2b},\frac{c+b}{2b}+1,e^{2bx}\right)\\
&=\frac{1}{2b}\left\{-\psi\left(\frac{a+b}{2b}\right)+\psi\left(\frac{c+b}{2b}\right)\right\},
\end{aligned}
\tag{7.2.45}
$$

and defined

$$
\Delta\omega_{kl} = \omega_k - \omega_l^*. \tag{7.2.46}
$$

In the indices of the residues in Eq. (7.2.44) one has to replace $\alpha = L$ by 1 and $\alpha = R$ by 3. For the case $m \neq n$ one analogously finds

$$\begin{aligned}
&\left[\int_{t_n}^{t_{n+1}} ds_1 \int_{t_m}^{t_{m+1}} ds_2\, G^{\mathrm{R}}(t_{n+1}, s_1)\Sigma^{\mathrm{K}}_{res}(s_1, s_2)G^{\mathrm{A}}(s_2, t_{m+1})\right]_{ij} = \frac{1}{\pi}\sum_{\substack{\alpha=L,R\\k,l=1,2,3}} \mathrm{Res}_{i\alpha,k}\mathrm{Res}^*_{j\alpha,l} e^{-i(\omega_k t_{n+1} - \omega_l^* t_{m+1})} \\
&\times\left[\int_{t_m - t_{n+1}}^{t_{m+1}-t_{n+1}} d\Delta t \int_{2t_m-\Delta t}^{2t_{n+1}+\Delta t} dT + \int_{t_{m+1}-t_{n+1}}^{t_m - t_n} d\Delta t \int_{2t_m-\Delta t}^{2t_{m+1}-\Delta t} dT + \int_{t_m - t_n}^{t_{m+1}-t_n} d\Delta t \int_{2t_n+\Delta t}^{2t_{m+1}-\Delta t} dT\right] \\
&\qquad \frac{\Gamma e^{i\mu_\alpha \Delta t} e^{\frac{1}{2}iT\Delta\omega_{kl}}}{\sinh(\pi T_\alpha \Delta t)} e^{-i\frac{1}{2}\Delta t(\omega_k + \omega_l^*)} \\
&= \sum_{\substack{\alpha=L,R\\k,l=1,2,3}} T_\alpha \mathrm{Res}_{i\alpha,k}\mathrm{Res}^*_{j\alpha,l} e^{-i(\omega_k t_{n+1} - \omega_l^* t_{m+1})} \frac{4T_\alpha\Gamma}{i\Delta\omega_{kl}} \\
&\quad\times\Bigg[- e^{i\Delta\omega_{kl}t_{n+1}} \frac{e^{(i\mu_\alpha - i\omega_l^* + \pi T_\alpha)(t_{m+1}-t_{n+1})}}{i\mu_\alpha - i\omega_l^* + \pi T_\alpha} {}_2\mathcal{F}_1\left(1, \frac{i\mu_\alpha - i\omega_l^* + \pi T_\alpha}{2\pi T_\alpha}, \cdots + 1, e^{2\pi T_\alpha(t_{m+1}-t_{n+1})}\right) \\
&\quad + e^{i\Delta\omega_{kl}t_{n+1}} \frac{e^{(i\mu_\alpha - i\omega_l^* + \pi T_\alpha)(t_m-t_{n+1})}}{i\mu_\alpha - i\omega_l^* + \pi T_\alpha} {}_2\mathcal{F}_1\left(1, \frac{i\mu_\alpha - i\omega_l^* + \pi T_\alpha}{2\pi T_\alpha}, \cdots + 1, e^{2\pi T_\alpha(t_m-t_{n+1})}\right) \\
&\quad - e^{i\Delta\omega_{kl}t_m} \frac{e^{(i\mu_\alpha - i\omega_k + \pi T_\alpha)(t_m-t_{n+1})}}{i\mu_\alpha - i\omega_k + \pi T_\alpha} {}_2\mathcal{F}_1\left(1, \frac{i\mu_\alpha - i\omega_k + \pi T_\alpha}{2\pi T_\alpha}, \cdots + 1, e^{2\pi T_\alpha(t_m-t_{n+1})}\right) \\
&\quad + e^{i\Delta\omega_{kl}t_{m+1}} \frac{e^{(i\mu_\alpha - i\omega_k + \pi T_\alpha)(t_{m+1}-t_{n+1})}}{i\mu_\alpha - i\omega_k + \pi T_\alpha} {}_2\mathcal{F}_1\left(1, \frac{i\mu_\alpha - i\omega_k + \pi T_\alpha}{2\pi T_\alpha}, \cdots + 1, e^{2\pi T_\alpha(t_{m+1}-t_{n+1})}\right) \\
&\quad + e^{i\Delta\omega_{kl}t_m} \frac{e^{(i\mu_\alpha - i\omega_k + \pi T_\alpha)(t_m-t_n)}}{i\mu_\alpha - i\omega_k + \pi T_\alpha} {}_2\mathcal{F}_1\left(1, \frac{i\mu_\alpha - i\omega_k + \pi T_\alpha}{2\pi T_\alpha}, \cdots + 1, e^{2\pi T_\alpha(t_m-t_n)}\right) \\
&\quad - e^{i\Delta\omega_{kl}t_{m+1}} \frac{e^{(i\mu_\alpha - i\omega_k + \pi T_\alpha)(t_{m+1}-t_n)}}{i\mu_\alpha - i\omega_k + \pi T_\alpha} {}_2\mathcal{F}_1\left(1, \frac{i\mu_\alpha - i\omega_k + \pi T_\alpha}{2\pi T_\alpha}, \cdots + 1, e^{2\pi T_\alpha(t_{m+1}-t_n)}\right) \\
&\quad - e^{i\Delta\omega_{kl}t_n} \frac{e^{(i\mu_\alpha - i\omega_l^* + \pi T_\alpha)(t_{m+1}-t_n)}}{i\mu_\alpha - i\omega_l^* + \pi T_\alpha} {}_2\mathcal{F}_1\left(1, \frac{i\mu_\alpha - i\omega_l^* + \pi T_\alpha}{2\pi T_\alpha}, \cdots + 1, e^{2\pi T_\alpha(t_{m+1}-t_n)}\right) \\
&\quad - e^{i\Delta\omega_{kl}t_n} \frac{e^{(i\mu_\alpha - i\omega_l^* + \pi T_\alpha)(t_m-t_n)}}{i\mu_\alpha - i\omega_l^* + \pi T_\alpha} {}_2\mathcal{F}_1\left(1, \frac{i\mu_\alpha - i\omega_l^* + \pi T_\alpha}{2\pi T_\alpha}, \cdots + 1, e^{2\pi T_\alpha(t_m-t_n)}\right)\Bigg].
\end{aligned} \tag{7.2.47}$$

The ... in the third argument of the Gauss hypergeometric functions of Eq. (7.2.47) are shorthand notation for the fact that the second argument has to be repeated. They are introduced only for typographic reasons. We can restore the $T \to 0$ limit [given in (C.17) of [Ken11]] by using Eqs. (7.2.17) and (7.2.18).

Single-Scale Propagator

At heart of the calculation of the single-scale propagator, introduced in Eq. (4.3.18) determining the flow of the self-energy, lies again Eq. (7.2.29). First of all due to Eq. (7.2.29) the retarded single-scale propagator simply fulfils

$$S^{\mathrm{R},\Lambda}(t,t') = \left[S^{\mathrm{A},\Lambda}(t',t)\right]^\dagger = i\int_{t'}^{t} dt_1\, G^{\mathrm{R},\Lambda}(t,t_1)G^{\mathrm{R},\Lambda}(t_1,t') = (t-t')G^{\mathrm{R},\Lambda}(t,t'), \tag{7.2.48}$$

and thus $S^{\mathrm{R},\Lambda}(t,t) = 0$. A consequence of this is that indeed $\Sigma^{\mathrm{K},\Lambda} = 0$ to our truncation order (see [Ken11] sections 6.5.4 and 7.2.2 for more information). For the Keldysh single-scale propagator

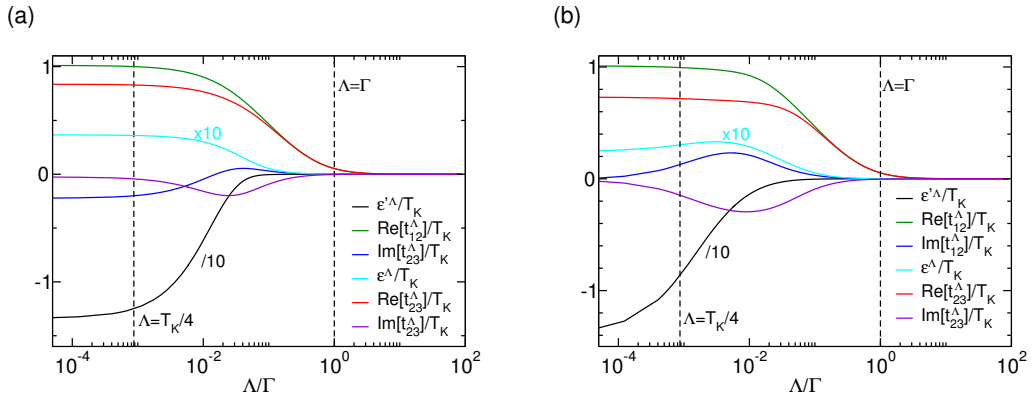


Figure 7.6.: Renormalization of the dot-quantities during the flow for two different times (a) $t_a\Gamma = 40$ and (b) $t_b\Gamma = 2300$. Renormalization is determined by a universal regime given roughly by $\Lambda \in (T_K/4, \Gamma)$. This signals a non-stiff behavior of the differential equations. The parameter choice is not relevant, and exemplary chosen as $t_{\text{imp}}/\Gamma = 0.025$, $U/\Gamma = 0.1$, $T_\alpha/T_K = 0$ and $\epsilon/T_K = V/T_K = 10$ with $V/2 = \mu_L = -\mu_R$. Note that only the renormalization, meaning the change with respect to the bare values is shown.

we find

$$\begin{aligned} S^{K,\Lambda}(t,t) = -\partial_\Lambda^* G^{K,\Lambda}(t,t) \quad &= \quad -iS^{R,\Lambda}(t,0)(1-2\bar{n}_0)G^{A,\Lambda}(0,t) \\ &\quad -iG^{R,\Lambda}(t,0)(1-2\bar{n}_0)S^{A,\Lambda}(0,t) \\ &\quad -\partial_\Lambda^*\left[G^{R,\Lambda}\Sigma^K G^{A,\Lambda}\right](t,t) \qquad (7.2.49) \\ &\overset{(7.2.48)}{=} -2i(t-t_0)G^{R,\Lambda}(t,0)(1-2\bar{n}_0)G^{A,\Lambda}(0,t) \\ &\quad -\partial_\Lambda^*\left[G^{R,\Lambda}\Sigma^K G^{A,\Lambda}\right](t,t)\,, \end{aligned}$$

where again the Green's functions' "group property" was used. The second term can further be evaluated employing Eq. (7.2.48)

$$\begin{aligned} S^{K,\Lambda}(t,t) = &-2itG^{R,\Lambda}(t,0)(1-2\bar{n}_0)G^{A,\Lambda}(0,t) + \int_0^\infty dt_1 \int_0^\infty dt_2 G^{R,\Lambda}(t,t_1) \\ &\times (2t-t_1-t_2)\sum_\alpha \Sigma^K_{\text{res},\alpha}(t_1,t_2)G^{A,\Lambda}(t_2,t). \qquad (7.2.50) \end{aligned}$$

To sum up the main result: One succeeds in recasting the calculation of the Keldysh single-scale propagator into the form known from the Green's functions. This reduces the number of integrals to be performed by one (a huge advantage when discretization in time is fine). Eq. (7.2.50) can be recast into sums of elementary retarded Green's function just like the Keldysh Green's function in Eq. (7.2.42). The subsequent calculation works precisely analogue, the only relevant change with respect to the expression of Eqs. (7.2.44) and (7.2.47) being that additionally the Hurwitz-Lerch zeta-function $\phi(z,2,a)$ shows up. In contrast to the Gauss hypergeometric function [or equivalently $\phi(z,1,a)$] the limit $\lim_{z\to 1}$ which has to be performed at $t_m = t_n$ is completely unproblematic for $\phi(z,2,a)$ as

$$\lim_{z\to 1}\phi(z,2,a) = \Psi(1,z), \qquad (7.2.51)$$

with the *trigamma function* $\Psi(1,z)$.

One Word on Numerics

First, note that to reach the physically relevant time scales of the outlined problem one needs to employ the 'tricks' explained in section 7.5 of [Ken11]. The maximal reuse of the calculation's result

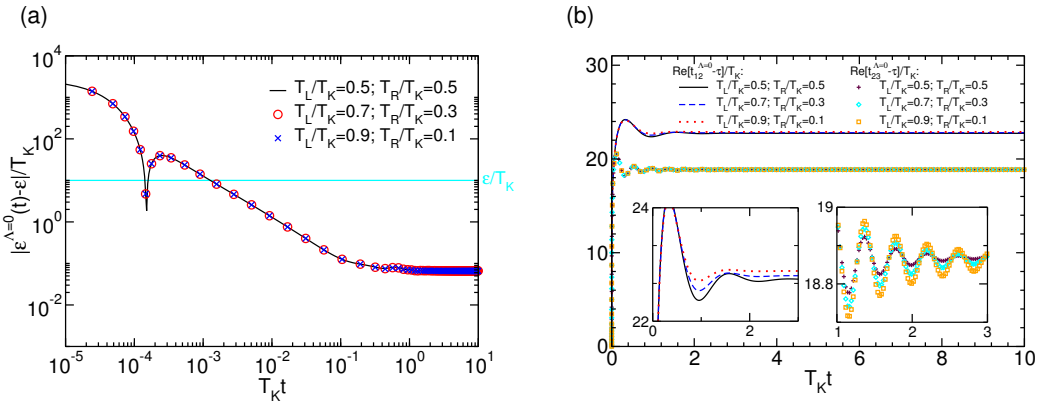


Figure 7.7.: Left: Time dependence of the renormalized onsite energy $\epsilon^{\Lambda=0}(t) - \epsilon \in \mathbb{R}$ (of the central site 2). The parameters are: $t_{\text{imp}}/\Gamma = 0.0025$, $\epsilon/T_K = V/T_K = 10$ with $V/2 = \mu_L = -\mu_R$, and $U/\Gamma = 0.2$. Note the double logarithmic scale and that the dip corresponds to a zero crossing. It occurs in the non-universal regime $t \sim 1/\Gamma$. Right: Time dependence of the renormalized hoppings $t_{12}^{\Lambda=0} - t_{\text{imp}} = \Sigma_{12}^{R,\Lambda=0} \in \mathbb{C}$ between sites 1 and 2, and $t_{23}^{\Lambda=0} - t_{\text{imp}} = \Sigma_{23}^{R,\Lambda=0} \in \mathbb{C}$ between sites 2 and 3. The parameters are: $t_{\text{imp}}/\Gamma = 0.0025$, $\epsilon/T_K = V/T_K = 10$, and $U/\Gamma = 0.2$. The insets show a zoom into the regime where one can most clearly distinguish the temperature's effect on the oscillations' amplitude.

for t_i at t_{i+1} basically reduces the complexity of the algorithm by one order.

Furthermore, one might wonder about the integration procedure used to solve the coupled set of flow equations. We always used the adaptive step-size explicit embedded Runge-Kutta-Fehlberg (4,5) method, which is a good general purpose solver for non-stiff differential equations. We want to substantiate this choice by some exemplary plots. The (real valued) renormalization of the on-site energies of the three sites and (complex valued) renormalization of the hopping amplitudes is shown for $t_{\text{imp}}/\Gamma = 0.025$, $U/\Gamma = 0.1$, $T_\alpha/T_K = 0$ and $\epsilon/T_K = V/T_K = 10$ with $V/2 = \mu_L = -\mu_R$ in Fig. 7.6 for two times (a) $t_a\Gamma = 40$ and (b) $t_b\Gamma = 2300$. Due to the truncation used site one and three renormalize equally, while the hoppings renormalize asymmetrically (due to V). All quantities vary with Λ in the same regime [roughly given by $\Lambda \in (T_K/4, \Gamma)$], which is reasonably determined by the smallest T_k and largest Γ physical scale of the system.

7.2.3 Transport at Finite Temperature

The transient dynamics in the transport setup ($V \neq 0$) of the IRLM was studied for vanishing temperature in [And11b, Ken12a, Ken11], which we can now supplement by a similar study at finite T. The correlation physics at finite U is particularly transparent for $|\epsilon \pm V/2| \gg T_K$. In [Ken12a] it was shown that for $T_\alpha = 0$ the relaxation dynamics in this regime at sufficiently large times can be described by replacing the time independent bare single-particle parameters in the analytical $U = 0$ expressions by the time-averaged renormalized ones. Actually, the same holds at finite T [Ken13b].

Renormalization Effects at $|\epsilon \pm V/2| \gg T_K$

For arbitrary T_α and all relevant times $T_K t \gtrapprox t_{\text{imp}}/\Gamma$ the renormalization of the onsite energy $\epsilon^{\Lambda=0}(t) - \epsilon = \Sigma_{22}^{R,\Lambda=0}(t)$ is of order U^2 and can safely be neglected. This is exemplified for a few temperatures in Fig. 7.7(a). On the other hand the time dependence of the renormalized hopping amplitudes is shown in Fig. 7.7(b). It depends only weakly on the temperature for the case $|\epsilon \pm V/2| \gg T_K$. Similar to $T = 0$ [Ken12a] the effective hopping amplitudes quickly (on a scale $T_K t \sim t_{\text{imp}}/\Gamma$) start to oscillate around their steady-state values with frequencies $|\epsilon - V/2|$ and $|\epsilon + V/2|$ for $t_{12}^{\Lambda=0}$ and $t_{23}^{\Lambda=0}$, respectively. Again due to the left-right asymmetry induced by the voltage and different reservoir temperatures the renormalized level-lead couplings generically flow to

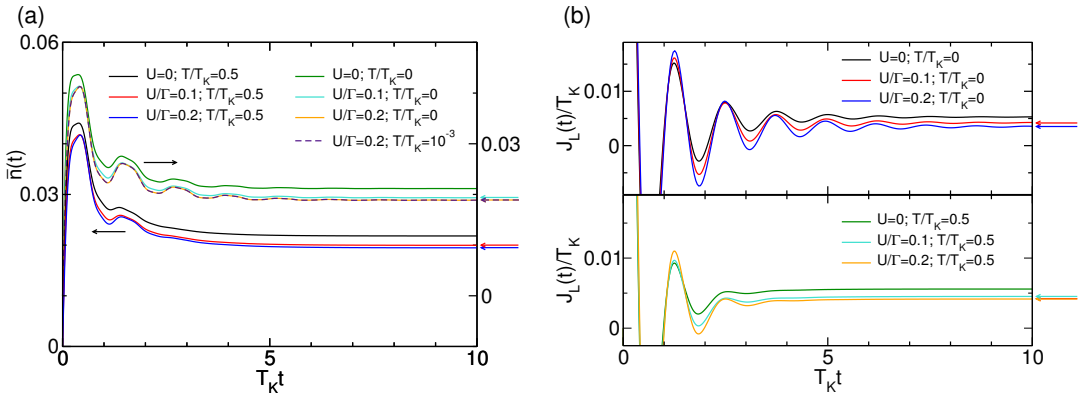


Figure 7.8.: Left: FRG data for the time evolution of the central site occupancy $\bar{n}(t)$. The parameters are the same as in Fig. 7.7 and symmetric temperatures $T_\alpha = T$. The arrows right to the graph indicate the steady-state values obtained by a non-equilibrium steady-state FRG ($\rightarrow$ Section 8.2). Merely as a consistency check we include one graph with very small temperature $T/T_K = 10^{-3}$ (essentially zero) which reproduces the $T = 0$ result. Right: The same as left but for the particle current leaving the left reservoir.

asymmetric values. Increasing the temperature of the left (right) reservoir suppresses the oscillations in the renormalized $t_{12}^{\Lambda=0}$ ($t_{23}^{\Lambda=0}$). Later we will use this to tune observables (see Fig. 7.10). We have restricted the depiction to the real part of the hopping amplitudes at this point, but the same holds for the (much smaller) imaginary one as well.

This analysis of the time dependence of the renormalized single-particle parameters shows that in the limit $|\epsilon \pm V/2| \gg T_K$ the results obtained by the numerical solution of the FRG flow equations and subsequent numerical computation of the observables, for $T_K t \gtrapprox t_{\text{imp}}/\Gamma$ can be interpreted by considering Eqs. (7.2.14) and (7.2.15). One just has to replace the bare parameters by the time-averaged renormalized ones[14]

Observables

Next we discuss our numerical FRG results for the occupancy of the central level $\bar{n}(t)$ and the particle current $J_L(t)$ leaving the right reservoir. We can understand their behavior by using the just established relation to the non-interacting case. Figure 7.8 shows the time evolution of the occupancy and the current for $|\epsilon \pm V/2| \gg T_K$ and different U. For consistency only we also show that in the limit $T \to 0$ the finite T code recovers the $T = 0$ results. This is merely a check for the numerics as it is a physically trivial statement. Increasing the temperature drastically suppresses the amplitude of the oscillatory terms. The quality factor of the oscillations is decreased by the increasing decay rate at finite T. The quality factor belonging to the two frequencies $|\epsilon \pm V/2|$ can be tuned independently by the individual temperatures T_L and T_R, which is not possible via the hybridization.

To see this effect more clearly we introduce the numerical Laplace transform (instead of a Fourier transform) similar to Eq. 7.2.16. Although it can be used to enhance the visibility of, as well as separate the, different contributions to the transient dynamics, it is of course numerically difficult to approach non-analyticities, to learn about their analytic form[15]. The numerical procedure then runs as follows:

1. Subtract the steady-state value of the signal (the signal under consideration has to be "approximately" fully relaxed).

[14] More precisely one would have to generalize these expressions to the case of left-right asymmetric hybridzations. We have pursued this, but the only notable change is that the ratio of the hybridizations enters as prefactors of the different terms, while the relaxation rates remain the sums of left and right hybridization. For explicit expressions consult [Ken13b].

[15] ... and thus their precise influence on the dynamics

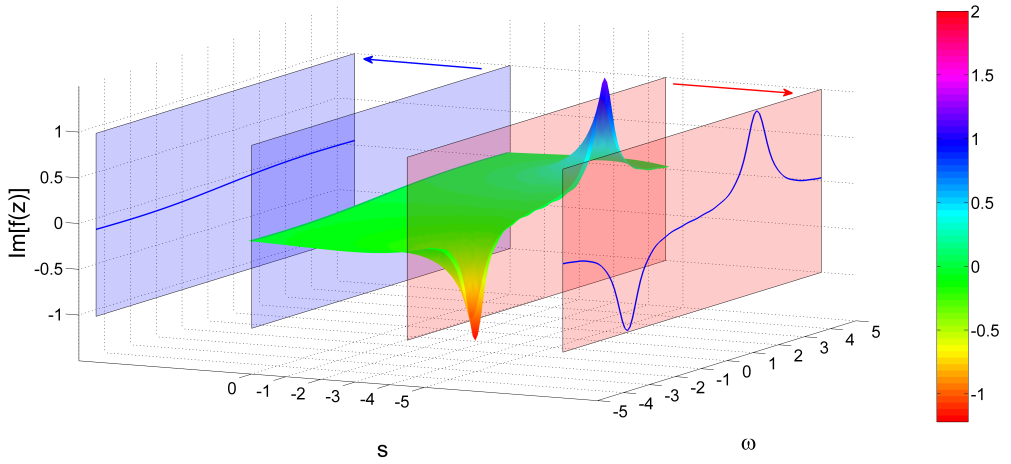


Figure 7.9.: Numerical Laplace transformation of an exemplary function $O(t) = \sin(2.5t)\exp(-5t)$ sampled form $t_0 = 0$ to $t_{\max} = 10$ in steps of $\delta t = 0.1$. It is easy to read off the frequency $\omega = 2.5$ from the Laplace transformed signal (red shaded plane $s = -4.5$), while the Fourier transform (blue shaded plane $s = 0$) barely shows any features.

2. Numerically perform the Laplace integral for different values of $E = is + \omega$ (such that $s = 0$ corresponds to the Fourier transformation). The integral can be cut off at the maximum time of the signal $t_{\max}$, because of 1. .

3. If s was chosen too small ($|s|$ too large), the integral should diverge and strong fluctuations become visible in the numerically transformed signal. Start over at 2.

4. Peaks in the imaginary part of the transformed signal correspond to sine and peaks in the real part to cosine terms.

With the numerical Laplace transform at hand we can largely circumvent any problems calling for more elaborate signal processing techniques[16]. We demonstrate the procedure in figure 7.9 for an exemplary function $O(t) = \sin(2.5t)\exp(-5t)$ sampled form $t_0 = 0$ to $t_{\max} = 10$ in steps of $\delta t = 0.1$. One can clearly determine the frequency ($\omega = 2.5$) from the Laplace transformed signal (red shaded plane $s = -4.5$), while this is not possible for the Fourier transform (blue shaded plane $s = 0$).

Now we return to the issue of tuning the different frequencies against each other. Figure 7.10(a) illustrates this point for the time dependence of the occupancy. For vanishing temperature gradient $\Delta T = 0$ a superposition of the two frequencies $|\epsilon \pm V/2|$ [bottom curve in Fig. 7.10(a)] is visible. With increasing temperature gradient the contribution of the frequency $|\epsilon + V/2|$ belonging to the colder reservoir is pronounced until the signal appears almost sinusoidal (overlayed by an exponential decay) at maximum temperature gradient [top curve in Fig. 7.10(a)]. Figure. 7.10(b) shows the imaginary part of the numerical Laplace transform (normalized to its largest value) of the occupany for the smallest and largest temperature gradient shown in Fig. 7.10(a). The positions of the frequencies $|\epsilon \pm V/2|$ are indicated by the vertical arrows. Increasing ΔT clearly suppresses the feature at $|\epsilon - V/2|$, while the one at $|\epsilon + V/2|$ is pronounced.

Next, we study the far-from-equilibrium case $V \gg T_K, \epsilon = 0$. More precisely, we consider the limit $V \gg T_K, T$ with $T_L = T_R = T$ and $\epsilon = 0$. At $\epsilon = 0$ the expressions for the time evolution are particularly simple and for sufficiently large times $\pi T t \gg 1$ and small interactions we obtain

$$J_L(t) = J_{\text{stat}} + e^{-4\Theta^{\Lambda=0}t} - 2T\text{Im}\left[\frac{4e^{(-iV/2-2\Theta^{\Lambda=0}-\pi T)t}}{iV + 4\Theta^{\Lambda=0} + 2\pi T}\right], \tag{7.2.52}$$

[16] as in the Fourier transform: different window functions, sampling theorem and aliasing

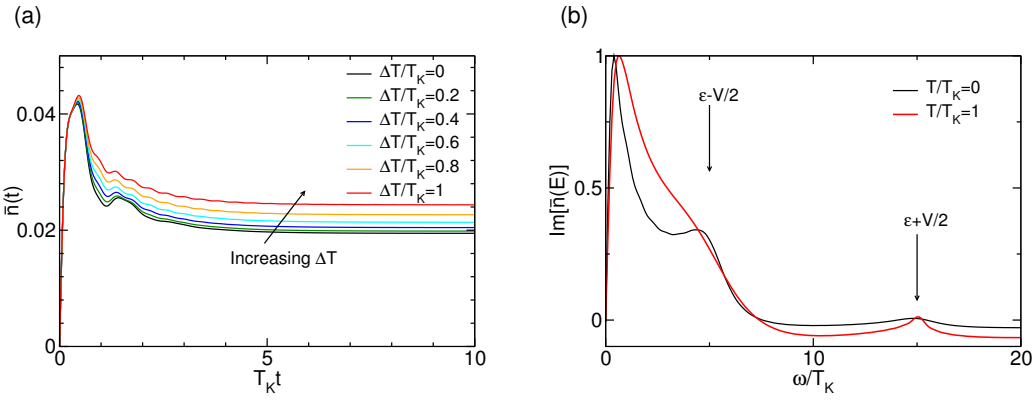


Figure 7.10.: Left: The same as Fig. 7.8(a) with $U/\Gamma = 0.2$, but featuring a temperature gradient across the two reservoirs: $T_L = T + \Delta T/2$ and $T_R = T - \Delta T/2$ for $T = 0.5\,T_K$. Right: The temperature gradient pronounces the frequency $|\epsilon + V/2|$ belonging to the colder reservoir. Shown is the numerical Laplace transform of $\bar{n}(t)$ with the positions of the frequencies $|\epsilon \pm V/2|$ indicated by vertical arrows. Clearly the frequency associated with the colder reservoir $\omega = (\epsilon + V/2)$ is pronounced compared to the second one at $\omega = (\epsilon - V/2)$ with increasing ΔT. The largest value of the Laplace transform is normalized to one for convenience.

with the renormalized steady-state values $\Theta^{\Lambda=0} = \Theta_{12}^{\Lambda=0} = \Theta_{23}^{\Lambda=0} = \left|t_{12}^{\Lambda=0}\right|^2/\Gamma$ and the stationary current J_{stat}. We note that for initially equal Θ_{ij} and $\epsilon = 0$ also the renormalized hybridizations remain equal[17] even for $V \neq 0$. From Eq. (7.2.52) we can read off a coherent-to-incoherent transition in the long-time dynamics at temperature

$$\pi T_c = 2\Theta^{\Lambda=0}. \tag{7.2.53}$$

The long time dynamics switches from being exponential with an overlayed oscillation (second term of Eq. (7.2.52) being the dominant one at large times) for $T < T_c$ to purely (monotonic) exponential relaxation (first term of Eq. (7.2.52) being the dominant one at large times) for $T > T_c$. To determine T_c we need the renormalized expression for $\Theta^{\Lambda=0}$ corresponding to the considered parameter regime $V \gg T_K, T$. We will derive those in section 8.2. Using Eq. (8.2.11) of this section we find

$$\Theta^{\Lambda=0} \sim \frac{t_{\text{imp}}^2}{\Gamma}\left(\frac{\Gamma}{V}\right)^{2U/\pi/\Gamma}. \tag{7.2.54}$$

With this we obtain

$$T_c = \frac{2t_{\text{imp}}^2}{\pi\Gamma}\left(\frac{\Gamma}{V}\right)^{2U/\pi/\Gamma}, \tag{7.2.55}$$

for the critical temperature at which the crossover from coherent to incoherent behavior occurs. Relaxing the condition of equal temperatures in the left and right reservoirs but keeping $V \gg T_K, T_L, T_R$ the transition is found at $\min(T_L, T_R) = T_c$ with the same T_c as defined above. The two-particle interaction thus plays a crucial role for the critical temperature at which the transition occurs as it enters in the exponent of Eq. (7.2.55). The transition from oscillatory damped to monotonic dynamics is illustrated in Fig. 7.11(a) for $U/\Gamma = 0.05$.

Finally, we discuss the time dependence of a current which is not induced by a finite bias voltage but by a finite temperature gradient across the quantum dot. To obtain a non-vanishing steady-state value of the current one needs to choose $\epsilon \neq 0$. Figure 7.11(b) shows the current for this parameter regime. The only frequency in the time evolution is given by ϵ as $V = 0$. Interestingly, the interaction strength enhances the amplitude of the oscillations, but decreases the steady-state current (if measured with respect to T_K). This investigation opens the road to thermal and thermoelectric transport studies which will be pursued for the simpler case of the steady-state in chapter 8.

[17] This is of course a consequence of $\epsilon = 0$ and does not hold generally at finite V and ϵ.

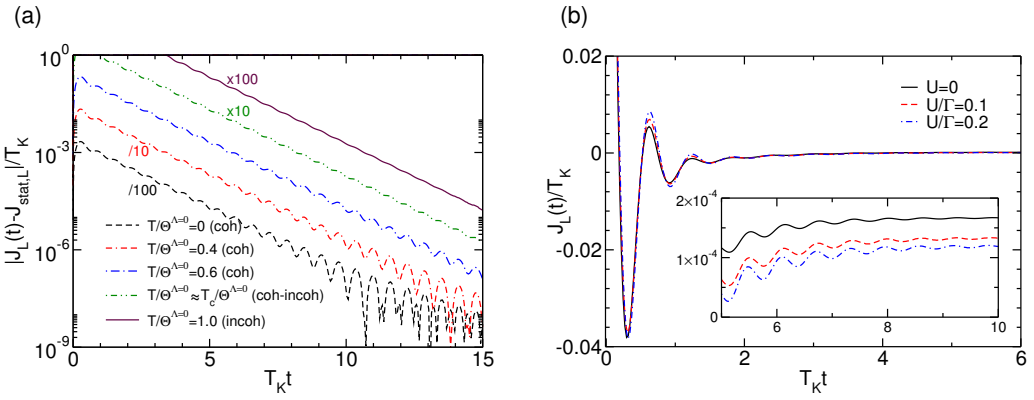


Figure 7.11.: Left: The coherent-incoherent transition described by (7.2.53). The parameters read $t_{\text{imp}}/\Gamma = 0.0025$, $\epsilon/T_K = 0$, $V/T_K = 20$ with $V/2 = \mu_L = -\mu_R$, and $U/\Gamma = 0.05$. We choose $T_\alpha = T$ and thus one finds the transition at $T/\Theta^{\Lambda=0} \approx 0.8028$. Right: Time evolution for the temperature gradient induced current leaving the left reservoir $J_L(t)$. The parameters read $t_{\text{imp}}/\Gamma = 0.0025$, $\epsilon/T_K = 10$ and $V/T_K = 0$. We choose $T_L = T_K$ and $T_R = 0$ (choosing $0 < T_R \ll T_L$ does not alter the qualitative behavior).

7.3 Dynamics of Dissipative Quantum Systems

How classical behavior precisely emerges from the deep quantum limit by the introduction of dissipation remains a puzzle even nowadays, although some major progress has been reported on the issue [Zur03]. For this reason the subtle interplay – or usually competition – of quantum coherence and the dissipation introduced by the presence of a nearby environment is of fundamental interest. The prototype model of such a (small) quantum system coupled to a (large) environment, and therefore of the behavior of dissipative quantum systems, is the ohmic SBM introduced in section 3.6. This extensively studied model [Leg87, Egg97, Les98, Alv09, Ort10, Wei12, Ort13] will be our model of interest for the remainder of this chapter.

We will concentrate always on a parameter regime close to $\alpha = 1/2$, because at this point the dynamics is supposed to turn from coherent to incoherent in the unbiased ($\epsilon = 0$) and vanishing temperature ($T = 0$) case (compare Fig. 3.5) [Leg87, Wei12]. The initial preparation is given by the spin pointing in z-direction and the boson-vacuum for the bosonic environment. In the vicinity of $\alpha = 1/2$ we use the mapping of section 3.6.3, which brings us back to the IRLM studied above (now with $t_{\text{imp,R}} = 0$). We will complement the result found within the FRG approach by those calculated within RTRG ($\rightarrow$ Section 6.4).

Studying the literature one finds that within the *non-interacting blib approximation* (NIBA) [Leg87, Wei12] the dynamics of the spin expectation value $\langle \sigma_z \rangle (t)$ are given by the inverse Laplace transform of

$$\langle \sigma_z \rangle (E) = \frac{1}{-iE + g(E)}, \tag{7.3.1}$$

with

$$g(E) = T_K \left(\frac{\beta T_K}{2\pi} \right)^{1-2\alpha} \frac{h(E)}{\alpha - i\beta E/2\pi}, \quad \text{and:} \quad h(E) = \frac{\Gamma(1+\alpha - i\beta E/2\pi)}{\Gamma(1-\alpha - i\beta E/2\pi)}. \tag{7.3.2}$$

Comparing to results from FRG and RTRG, we will show in the following that such an approximate treatment captures some of the relevant physics in the ohmic SBM, while others are missed.

7.3.1 Dynamics at $T = 0$

Let us start with the most clear cut case of vanishing temperature $T = 0$. The inverse Laplace transform of (7.3.1) at $T = 0$

$$\langle \sigma_z \rangle (t) = \frac{1}{-iE + T_K (iT_K/E)^{1-2\alpha}} , \tag{7.3.3}$$

can be expressed by the *generalized Mittag-Leffler function* [Erd55]

$$E_{a,b}(z) = \sum_{k=0}^{\infty} \frac{z^k}{\Gamma(ak + b)} , \tag{7.3.4}$$

as[18] [Gra85]

$$\langle \sigma_z \rangle (t) = E_{2-2\alpha,1}(-[T_K t]^{2-2\alpha}). \tag{7.3.5}$$

Figure 7.12(a) shows the spin dynamics predicted by Eq. (7.3.5) for different α. NIBA thus describes correctly the relaxation dynamics of (a) the decoupled system ($\alpha = 0$) $\langle \sigma_z \rangle (t) = \cos(\Delta t)$ (persistent oscillations) as well as (b) the Toulouse Limit ($\alpha = 1/2$) $\langle \sigma_z \rangle (t) = \exp(-T_K t)$.

Additionally, as it accounts for all terms in Δ^2 the correct behavior at *short times* is

$$\langle \sigma_z \rangle (t) = 1 - (T_K t)^{2-2\alpha}/\Gamma(3 - 2\alpha) + \mathcal{O}\left([T_K t]^{4-4\alpha}\right) . \tag{7.3.6}$$

Note the power-law $\sim t^{2-2\alpha}$ with interaction dependent exponent in the dynamics, which has to be resummed by our perturbatively motivated renormalization group procedures. For general α analyzing Eq. (7.3.1) gives rise to two contributions to the relaxation dynamics at $0 < \alpha < 1/2$. There is (1) a pair of poles at $E = -i\gamma \mp \Omega = iT_K \exp\{\pm i\pi/[2(1-\alpha)]\}$ and (2) a branch-point at $E = 0$ with attached branch-cut along the imaginary E-axis. This leads to

$$\langle \sigma_z \rangle (t) = P(t) = P_{\rm coh}(t) + P_{\rm inc}(t), \tag{7.3.7}$$

where the different contributions can be calculated [Wei12]

$$P_{\rm coh}(t) = \frac{1}{1-\alpha} \cos(\Omega t) e^{-\gamma t} , \quad \text{and:} \quad P_{\rm inc}(t) \overset{t\to\infty}{=} \sum_{n=1}^{\infty} \frac{(-1)^{n-1}}{\Gamma[1-(2-2\alpha)n]} \frac{1}{(T_K t)^{(2-2\alpha)n}} . \tag{7.3.8}$$

At $\alpha = 0$ and $\alpha = 1/2$ the branch-cut is absent[19] and thus $P_{\rm inc}(t) = 0$. For $\alpha > 1/2$ the poles are not on the principle-sheet any longer and the dynamics are completely described by the branch-cut contribution $P(t) = P_{\rm inc}(t)$. The dynamics thus turn completely incoherent exactly at $\alpha = 1/2$. In Fig. 7.12(b) the analytical behavior is analyzed by showing a contour plot of the strength of the violation of the *Cauchy-Riemann* relation

$$A(E) = \left| \partial_{{\rm Im}E} {\rm Re}\left[\langle \sigma_z \rangle (E)\right] + \partial_{{\rm Re}E} {\rm Im}\left[\langle \sigma_z \rangle (E)\right] \right| , \tag{7.3.9}$$

evaluated numerical. If the function is analytic around z, this expression vanishes in an exact treatment, while all non-zero values signal non-analytic behavior. In a numerical analysis it nicely selects non-analyticities.

As the branch-cut contributing to $P_{\rm inc}$ always starts at $E = 0$ NIBA predicts an unphysical sluggish power-law decay at asymptotic times $P(t) \sim 1/(T_K t)^{2-2\alpha}$ for all $\alpha \neq 0$ and $\alpha \neq 1/2$. This is qualitatively wrong as the asymptotic decay should be exponential instead of algebraic, a behavior correctly restored when applying the more sophisticated *improved NIBA* [Egg97]. Within this approach one finds (remember $g = 1 - 2\alpha$)

$$P(t) = -g[1 + 3\Theta(-g)] \frac{e^{-T_K t/2}}{(T_K t)^{1+|g|}} , \tag{7.3.10}$$

[18] We note in passing that this is only true for $\alpha < 1$.
[19] At $\alpha = 1/2$ also the residue of the pole changes to give $P(t) = \exp(-T_K t)$.

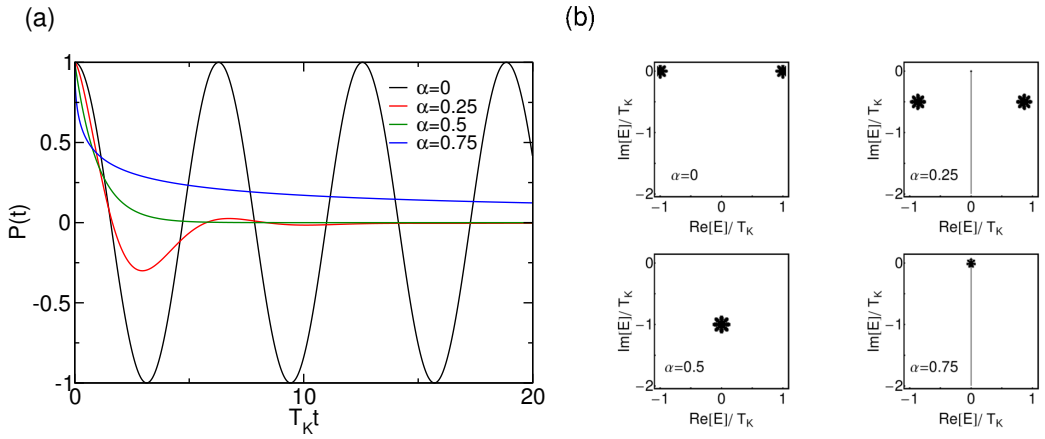


Figure 7.12.: Left: Time evolution of the spin expectation value $\langle\sigma_z\rangle(t) = P(t)$ as predicted from NIBA [see Eq. (7.3.5). Exact results are found for the parameter points $\alpha = 0$ (persistent oscillations) as well as $\alpha) = 1/2$ (exponential decay), where the problem can be posed within a non-interacting theory. For all other values of α only the short times $\mathcal{O}\left([\Delta t]^2\right)$ are described correctly, while the large time limit features an unphysical slow algebraic decay. Right: Non-analyticities of the Laplace transform $P(E)$ [see Eq. (7.3.3)] highlighted by expression (7.3.9) for the same α as in (a). Clearly at $\alpha = 0$ and $\alpha = 1/2$ only pole contributions at $E = \pm\Omega$ and $E = -i\gamma$, respectively are found. Those give rise to the correct time dependence of $\langle\sigma_z\rangle(t) = P(t)$. For all other α a branch-cut starting at $E = 0$ leads to the wrong slow algebraic decay found at large times.

for $g \ll 1$.

Additionally, using *conformal field theory* (CFT) the exact ratio of oscillation frequency Ω and relaxation rate γ in the coherent regime $\alpha < 1/2$ was predicted [Les98]. The ratio is nothing but the quality factor

$$Q = \Omega/\gamma = \cot\left[\frac{\pi\alpha}{2(1-\alpha)}\right]. \tag{7.3.11}$$

NIBA reproduces this quality factor to leading order in α (g) for $\alpha = 0$ ($\alpha = 1/2$). For arbitrary values of α it shows derivation to this scale only in the percent regime. The branch-cut (positioned wrongly) within NIBA is not included in the CFT result. However, we demonstrate in the following that for $\alpha < 1/2$ but close to $\alpha = 1/2$ the predicted CFT behavior (damped oscillations) is *not* the dominant behavior for large times! Actually it is given by another branch-cut contribution[20].

Analytics: Short Times $T_K t \ll 1$

Within both the FRG and RTRG approach one can aim at analytic expressions for short times $T_K t \ll 1$. The expressions found agree to leading order in g with Eq. (7.3.6). We show the detailed calculation of the short time dynamics within FRG here only[21]. As we are working at vanishing $\epsilon = 0$, $\mu_\alpha = 0$ and $\Gamma \gg T_K$ we conclude[22] that the only relevant flow equation is the one for $t_{12}^\Lambda = t_{\text{imp}}^\Lambda$. It reads

$$\partial_\Lambda t_{\text{imp}}^\Lambda(t) = \frac{U}{2} i\partial_\Lambda^* G_{12}^{\text{K},\Lambda}(t,t)\,, \tag{7.3.12}$$

with the interacting Green's function $G_{12}^{\text{K},\Lambda}(t,t)$. Now we interpret the interacting problem as a non-interacting one with renormalized time dependent parameters in the Hamiltonian. In a first

[20] The resulting long-time behavior for *exponentially large times* $(T_K t)^g \gg 1$ is in agreement with improved NIBA [Eq. (7.3.10)].

[21] We note that in general it is much easier to derive analytical expressions from the RTRG equations as they are set up in the more convenient Laplace space.

[22] Renormalization of ϵ^Λ is of order $\mathcal{O}(U^2)$ and ϵ'^Λ appears in sums with Γ only and can thus be neglected.

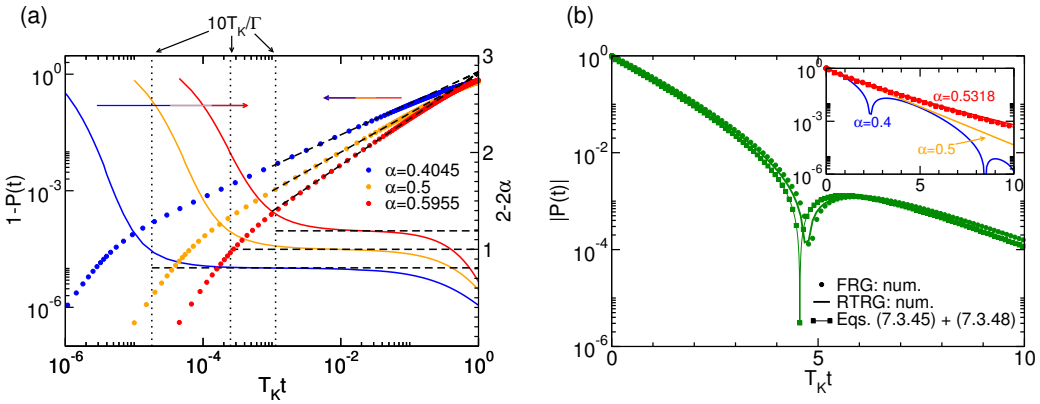


Figure 7.13.: Left: The short time behavior of the spin expectation value $P(t)$ found analytically in Eq. (7.3.21) is compared to the full numerical solution of the flow equations. The symbols show FRG results on a log-log scale and the power-law prediction $2-2\alpha = 1+g$ as a dashed black line. Additionally, vertical dotted lines indicate $T_K t = 10\,T_K/\Gamma$ for which non-universal (finite $\Gamma \sim \omega_c$) features appear. Here the power-law prediction begins to deviate. Furthermore, solid lines show the log derivative of the numerical data. Prediction and the numerical data are in excellent agreement. Right: Comparison of our complementary FRG and RTRG approaches. For the entire time regime the two agree nicely, which strengthens our believe in the accuracy of the two methods. Additionally, the analytic expression for $P(t)$ following from Eqs. (7.3.45) plus (7.3.48), agrees with the full solution for all $T_K t \gtrapprox 1$. The main panel depicts $\alpha = 0.4682$. The inset shows the partially coherent to incoherent transition around $\alpha = 1/2$.

step we rewrite the flow equation into the more convenient form

$$\partial_\Lambda t^\Lambda_{\text{imp}}(t) = Ui\partial^*_\Lambda \int dt'\; t_{\text{imp}}(t') \left[g^>_{\text{res}}(t,t')\tilde{G}^{<,\Lambda}(t',t) - g^<_{\text{res}}(t,t')\tilde{G}^{>,\Lambda}(t',t) \right], \tag{7.3.13}$$

where $g^{</>}_{\text{res}}(t,t')$ are lesser and larger Green's functions of a reservoir in the wide-band limit (bandwidth Γ) and Green's function $\tilde{G}$ are calculated with respect to a single-dot set up ($\rightarrow$ Section 7.2.1). By doing so we have only kept the leading order in $\mathcal{O}(1/\Gamma)$. The reservoir lesser Green's function can be obtained [analogue to Eqs. (4.1.60) and (4.1.61)] by solving the corresponding non-interacting problem

$$g^<_{\text{res}}(t,t') = -\frac{1}{\Gamma}\frac{1}{\pi(t-t')} + \frac{i}{2\Gamma}\,\delta(t-t'). \tag{7.3.14}$$

The larger Green's function can be obtained from particle-hole symmetry $g^<(t,t') = -g^>(t',t)$ in the leads. To order $\mathcal{O}(U)$ we can (1) put $t^\Lambda_{\text{imp}}(t') = t^\Lambda_{\text{imp}}(t)$ in the integrand and divide it to the l.h.s. of the flow equation and (2) subsequently approximate all renormalized quantities by their bare value which allows to replace $\partial^*_\Lambda \rightarrow \partial_\Lambda$. This yields

$$\frac{\partial_\Lambda t^\Lambda_{\text{imp}}(t)}{t^\Lambda_{\text{imp}}(t)} = Ui\partial_\Lambda \int dt' \left[g^>_{\text{res}}(t,t')\tilde{G}^{<,\Lambda}_0(t',t) - g^<_{\text{res}}(t,t')\tilde{G}^{>,\Lambda}_0(t',t) \right] \tag{7.3.15}$$

$$= Ui\partial_\Lambda \left[\frac{i}{2\Gamma}\tilde{G}^{\text{K},\Lambda}_0(t,t) - \int dt' \frac{1}{\pi\Gamma(t'-t)}\tilde{G}^{\text{A},\Lambda}_0(t',t) \right]. \tag{7.3.16}$$

A subindex 0 indicates that the bare (time independent) value t_{imp} is used in the calculation of the corresponding Green's function. So far we have been sloppy with the boundary of the integral which in principle runs from 0 to ∞, but is cut off from above at t due to the advanced Green's function in the integrand. The lower bound has to be set to $1/\Gamma$ ($\Gamma \sim \omega_c$), which corresponds to introducing a high energy (small times) cut-off of the renormalization flow by hand. This replacement

by hand is only necessary because we neglected higher order terms in $\mathcal{O}([1/\Gamma]^2)$ and naturally shows up in any numerical study of the full flow equations[23]. The integral on the r.h.s. of Eq. (7.3.16) can be integrated by use of exponential integrals, because $\tilde{G}_0^{A,\Lambda}$ takes the simple form $\tilde{G}_0^{A,\Lambda}(t',t) = i\Theta(t-t')\exp[(-\Gamma_{1D}-\Lambda)(t-t')]$. We can then trivially integrate the flow equation (7.3.16) to find

$$\begin{aligned} t_{\text{imp}}^{\Lambda=0}(t) =& t_{\text{imp}} \exp\left\{-\frac{U}{\Gamma} i\left[\frac{1}{2}\left(G_0^R(t,0)G_0^A(0,t)-1\right) - \frac{1}{\pi} i\mathrm{E}(1,\Gamma_{1D}t) - \frac{1}{\pi} i \log\left(\frac{\Gamma_{1D}}{\Gamma}\right)\right]\right\} \\ =& t_{\text{imp}} \left(\frac{\Gamma_{1D}}{\Gamma}\right)^{-\frac{U}{\pi\Gamma}} e^{-\frac{iU}{2\Gamma}\exp(-2\Gamma_{1D}t)} e^{-\frac{U}{\pi\Gamma}\mathrm{E}(1,\Gamma_{1D}t)}, \end{aligned} \tag{7.3.17}$$

for an initially unoccupied dot [$P(0) = 1$]. To derive Eq. (7.3.17) we have neglected the second term of the Keldysh Green's function in Eq. (7.2.42) as the double integral is $\sim t^2$. The quantity of relevance in the following will be the renormalized linewidth of the central level at time t

$$\Gamma_{1D}^{\Lambda=0}(t) = \frac{t_{\text{imp}}^{\Lambda=0}(t) t_{\text{imp}}^{\Lambda=0*}(t)}{\Gamma}. \tag{7.3.18}$$

Taking into account only the leading terms in $\Gamma_{1D}t \ll 1$ and U we find

$$\Gamma_{1D}^{\Lambda=0}(t) \approx e^{\frac{2U}{\pi\Gamma}\gamma}(\Gamma_{1D}t)^{\frac{2U}{\pi\Gamma}} \approx e^{g\gamma}\frac{1}{2}\underbrace{T_K^0\left(\frac{\Gamma}{T_K}\right)^g}_{T_K}(T_K t)^g, \tag{7.3.19}$$

where we have used the Euler-Mascheroni constant γ. With this time dependent renormalized linewidth, observables like the occupancy can be evaluated next. Again the double integral term in the Keldysh Green's function evaluated for the occupancy can be neglected as it is $\sim t^2$, which gives

$$\bar{n}(t) = \frac{1}{2} - \frac{1}{2}\mathcal{T}\left[e^{\int_0^t d\tau\ \Gamma_{1D}(\tau)}\right]^2 \approx \frac{1}{2} - \frac{1}{2}e^{-\frac{1}{g+1}(T_K t)^{g+1}\exp(g\gamma)} \approx \frac{e^{g\gamma}}{2(g+1)}(T_K t)^{g+1}. \tag{7.3.20}$$

In turn the spin expectation value is given by

$$P(t) = 1 - 2\bar{n}(t) = 1 - \frac{e^{g\gamma}}{g+1}(T_K t)^{g+1} = 1 - \frac{e^{(1-2\alpha)\gamma}}{2-2\alpha}(T_K t)^{2-2\alpha}. \tag{7.3.21}$$

The prefactor of the power-law decay agrees to the one of Eq. (7.3.6) to leading order in g, since $\frac{e^{g\gamma}}{g+1} \approx (1+g\gamma)(1-g) \approx 1+g(\gamma-1)$ just as well as $1/\Gamma(3-2\alpha) = 1/\Gamma(2+g) \approx 1/[(1-g\gamma)(1+g)] \approx 1+g(\gamma-1)$.

The short time behavior found analytically above is compared to the full numerical solution of the flow equation in Fig. 7.13(a). The symbols show FRG results on a log-log scale and the power-law prediction as a dashed black line. The numerical data clearly shows a power-law behavior with the correct exponent for small times $T_K t \ll 1$. Additionally, vertical dotted lines indicate $T_K t = 10 T_K/\Gamma$ for which non-universal (finite Γ) features are expected. Here the power-law prediction begins to deviate. Furthermore, solid lines show the log derivative of the numerical data, which is a very sensitive measure for power-laws. In the universal small-time regime the plateau of height given by the correct exponent clearly shows the predicted power-law $\sim t^{2-2\alpha}$.

Numerics: Full Solution of Flow Equations for general $T_K t$

Before proceeding the analytical analysis of the large time behavior and thus complementing the short times result of the previous section, we shortly compare our complementary FRG and RTRG results

[23] This is in perfect analogy to the steady-state case (compare section 8.2).

in the full time regime. We begin by recapitulating shortly in which sense the two renormalization group approaches are complementary. First of all, they are both formally set up very differently. As explained in chapter 4 FRG aims at the (time dependent) irreducible vertex functions, while RTRG ($\rightarrow$ Section 6.4) directly aims at the reduced density matrix of the local system under consideration (in this case the single central level). Furthermore, FRG implements an auxiliary reservoir cut-off scheme ($\rightarrow$ Section 4.4.2), oppose to RTRG, which being set up in Laplace space, can utilize the Laplace variable E itself as a convenient way of defining the flow variable. In general, the methods are complementary in the way the approximations are applied. While in FRG the influence of the reservoirs is treated exactly, but one keeps only the lowest order in U on the right hand side of the flow equations, in RTRG in general the local system is treated exactly, but one incorporates the coupling to the environment only to a given order in the flow equations. As we are using the lowest order truncation scheme within RTRG for the IRLM this means that while all terms in $\mathcal{O}(g\Delta^2/\omega_c E)$ are kept, we do not control $\mathcal{O}(g[\Delta^2/\omega_c E]^2)$. On the other hand, it is a distinct advantage of the RTRG that the representation in Laplace space allows for analytical predictions. Within FRG finding analytical expressions is much more difficult and in fact only possible in certain limits (compare to the previous section).

In the context of the SBM, mapped to the IRLM, the relevant RTRG flow equations to leading order read

$$\Pi_1(E) = \frac{1}{E + i\Gamma_1(E)}\ , \tag{7.3.22}$$

$$\frac{d\Gamma_{1/2}(E)}{dE} = -\,(1-2\alpha)\,\Gamma_1(E)\,\Pi_{2/1}(E),\ , \tag{7.3.23}$$

$$\Pi_2(E) = \frac{1}{E + i\Gamma_2(E)/2}\ , \tag{7.3.24}$$

and initially $\Gamma_n(i\omega_c) = \Delta^2/\omega_c$. These can be trivially integrated numerically and subsequently the spin expectation value can be deduced by performing the inverse Laplace transform

$$P(t) = \frac{i}{2\pi}\int_{-\infty+i0^+}^{\infty+i0^+} dE\, e^{-iEt}\,\Pi_1(E). \tag{7.3.25}$$

To numerically perform this integral efficiently one can shift the line of integration by a small amount into the lower half of the complex E-plane, but keeping in mind that none of the non-analyticities should be crossed.

In Fig. 7.13(b) we compare the dynamics found for the spin expectation value within a full solution of the FRG flow equations to those obtained from a RTRG treatment via solving Eqs. (7.3.22)-(7.3.24) numerically. For all time scales the dynamics found in both approaches agree very nicely for $\alpha < 1/2$ (main panel) as well as $\alpha > 1/2$ (inset). This greatly strengthens our faith in the approximative renormalization group approaches used. Especially higher order terms in the coupling to the reservoir, which are not captured in the RTRG framework, do not spoil the applicability of the method. Additionally, one can clearly see that the qualitative behavior of the dynamics changes from non-monotonic[24] to monotonic at $\alpha = 1/2$ as predicted by NIBA and CFT. Importantly, as one approaches smaller values of α (deeper in the coherent regime) more dips signalling a higher frequency appear [compare main panel to blue line of inset in Fig. 7.13(b)]. We note, that only a *finite number of dips* show up in the time evolution for the values of α shown in Fig. 7.13(b). This means that the entire signature of the coherent regime (non-monotonic decay dynamics of the spin expectation value) is restricted to some finite times. We can quantify this statement by looking at the spin expectation value in Laplace space $P(E)$. In Fig. 7.14 we show Eq. (7.3.9) for the numerically determined quantity $P(E)$ from RTRG, which highlights the different contributions to the time evolution in Laplace space. We find that there is no artificial branch-cut starting at $E = 0$, like in NIBA. Rather the branch-cut contribution starts at some finite value of E, leading asymptotically to an exponential decay superimposed by subleading power-law corrections in t. One

[24] Note that crossings of zeros in the expectation value manifest as dips in a log plot of its absolute value.

can also see that for $\alpha > \alpha_c$ the dominant behavior in the long time limit (given by the non-analyticity closest to real axis) is not determined by the poles at finite frequency, but actually by the branch-cut contribution on the imaginary axis. It is thus wrong to think about the asymptotic behavior close to $\alpha = 1/2$ as damped oscillatory dynamics even in the coherent regime! The RTRG procedure used here finds $\alpha_c \approx 0.3$ for the coupling strength when the dominant long time behavior switches from damped oscillatory to asymptotically monotonic. Therefore we propose to refine the way we classify the dynamical regimes in the SBM by differentiating between

1. *asymptotically coherent* for $0 \leq \alpha < \alpha_c$: non-monotonic on all time scales (poles dominant feature).
2. *partially coherent* for $\alpha_c < \alpha < 1/2$: non-monotonic on intermediate time scales (central branch-cut dominant feature with subleading pole contributions).
3. *incoherent* for $\alpha \geq 1/2$: monotonic on all time scales (only central branch-cut contribution).

Values as $\alpha_c \approx 0.3$ are strictly speaking beyond the regime $|1/2 - \alpha| \ll 1$ in which our approximate RTRG and FRG equations (derived for the IRLM) are controlled. One can, however, numerically solve for the *SBM at weak coupling* $\alpha \ll 1$ within the RTRG [Kas13b] which is complementary to the presented approach. This approach confirms the asymptotically to partially coherent transition and puts α_c at $\alpha_c \approx 0.36$. This hints that our results can be trusted even down to $\alpha \approx 0.3$, with the exact value of α_c being located close to these values.

Analytics: Intermediate to Large Times $T_K t \gtrapprox 1$

For intermediate to large time scales $T_K t \gtrapprox 1$ the RTRG can be used to derive analytic expressions for the relaxation dynamics. Within RTRG, the dynamics is fully determined via Eq. (7.3.25), by the non-analyticities of the resolvent $\Pi_1(E) = 1/[E + i\Gamma_1(E)]$ in the lower half of the complex plane. As shown in Fig. 7.14 we find three singularities, which we parametrize by

$$z_0 = -i\frac{1}{2}\Gamma_2^*, \qquad \text{and} \qquad z_\pm = \pm\Omega - i\Gamma_1^*, \tag{7.3.26}$$

and where the decay rates (distance to real axis) $\Gamma_i > 0$ are of the order of T_K, whereas the oscillation frequency (distance to imaginary axis) is $0 < \Omega \sim gT_K$. The singularity z_0 is a branching point followed by a branch-cut with a jump of $\mathcal{O}(g)$. Furthermore, $z_\pm$ denote the positions of two poles which are followed by branch-cuts with a jump of $\mathcal{O}(g^2)$. These are not controlled by our approach and will thus be neglected. As in NIBA we aim at the separate pole and branch-cut contributions to the time evolution

$$P(t) = P_{\text{coh}}(t) + P_{\text{inc}}(t). \tag{7.3.27}$$

Next, we study the non-analyticities of $\Pi_1(E)$ by analyzing the renormalization group equations (7.3.22)-(7.3.24). From the renormalization group equation for $\Gamma_2(E)$ we find that if E approaches a pole $z_\pm = -i\Gamma_1(z_\pm)$ of $\Pi_1(E)$, $\Gamma_2(E)$ obtains a branch-cut with jump of $\mathcal{O}(g)$ starting at $z_\pm$, which, subsequently inserted into the renormalization group equation for $\Gamma_1(E)$ leads to a branch-cut for $\Gamma_1(E)$ with jump of $\mathcal{O}(g^2)$. Additionally, as E approaches the pole $z_0 = -i\Gamma_2(z_0)/2$ of $\Pi_2(E)$, similarly $\Gamma_1(E)$ obtains a branch-cut starting at z_0 with jump of $\mathcal{O}(g)$. Now, we calculate the positions of the singularities up to $\mathcal{O}(g)$ by solving the renormalization group equations within a systematic weak coupling expansion in $g \ll 1$. For $|E - z_i| \sim \mathcal{O}(T_K)$ as well as $g|\ln(|E - z_i|/T_K)| \ll 1$ we expand the solution of Eqs. (7.3.22)-(7.3.24) in g and fix the integration constants by comparing to the solution at very high energies:

$$\Gamma_{1/2}(E) = \Gamma_0\left(\frac{\omega_c}{-iE}\right)^g = T_K\left(\frac{T_K}{-iE}\right)^g, \tag{7.3.28}$$

where

$$T_K = \Gamma_0\left(\frac{\omega_c}{T_K}\right)^g = \Gamma_0\left(\frac{\omega_c}{\Gamma_0}\right)^{g/(1+g)}. \tag{7.3.29}$$

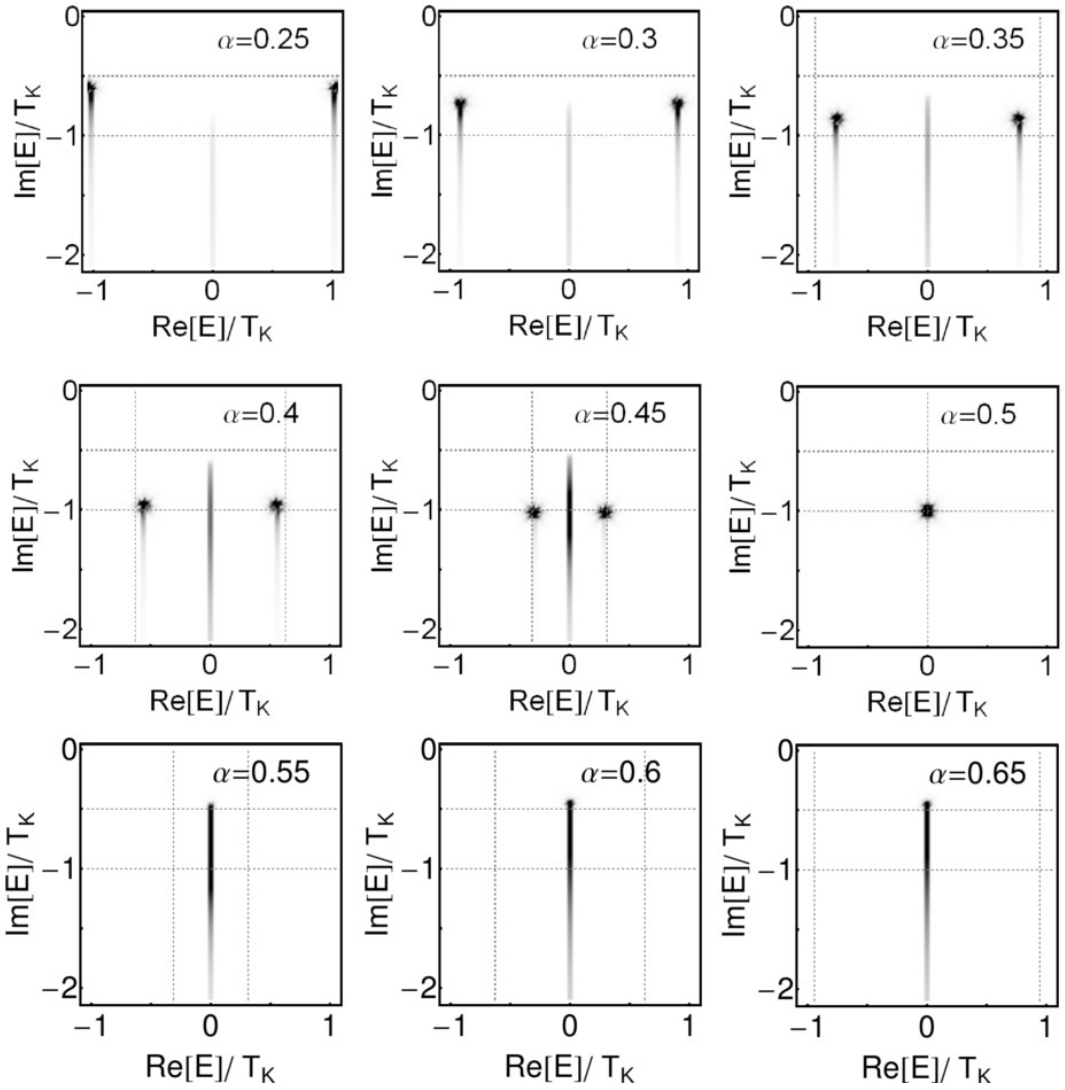


Figure 7.14.: The non-analyticities found in the Laplace transform of the spin expectation value $P(E)$ from RTRG. Using Eq. (7.3.9) highlights the different contributions to the time evolution in Laplace space. There is no artificial branch-cut starting at $E = 0$, like in NIBA, which removes the unphysical asymptotic algebraic decay found in this method. Instead, the branch-cut contribution starts at some finite imaginary value of E, leading asymptotically to an exponential decay superposed by subleading power-law corrections in t. For $1/2 > \alpha > \alpha_c \approx 0.3$ the dominant behavior in the long time limit (given by the non-analyticity closest to real axis) is not determined by the poles at finite frequency, but actually by the branch-cut contribution on the imaginary axis. This gives rise to the emergence of the partially coherent regime in between the expected asymptotically coherent ($\alpha < \alpha_c$) and incoherent ($\alpha \geq 1/2$) regimes.

Up to $\mathcal{O}(g)$ we then obtain

$$\Gamma_1(E)/T_K \approx 1 - g \ln \frac{-iE + \Gamma_2(E)/2}{T_K}, \tag{7.3.30}$$

$$\Gamma_2(E)/T_K \approx 1 - g \ln \frac{-iE + \Gamma_1(E)}{T_K}. \tag{7.3.31}$$

Since $g|\ln g| \ll 1$ for $g \ll 1$, we can trust these equations as long as $g^2 \lesssim |E - z_i|/T_K \sim \mathcal{O}(1)$. So far we cannot replace $\Gamma_{1/2}(E)$ by T_K in the argument of the logarithm since the argument could still be a negative real number of $\mathcal{O}(1)$. In this case the $\mathcal{O}(g)$-correction of the imaginary part of $\Gamma_i(E)$ might be important as it could be the leading contribution. As long as we consider energies E close to one of the pole positions $iz_\pm = \Gamma_1(z_\pm)$ or $iz_0 = \frac{1}{2}\Gamma_2(z_0)$, we can safely disregard this subtlety for the corresponding decay rate since we can expand around the pole position and use $\partial_E \Gamma_i \sim \mathcal{O}(g)$

$$\ln[-iE + \Gamma_2(E)/2] \approx \ln\{-i(E - z_0)[1 + i\partial_E \Gamma_2(z_0)/2]\} \approx \ln[-i(E - z_0)], \tag{7.3.32}$$

$$\ln[-iE + \Gamma_1(E)] \approx \ln\{-i(E - z_\pm)[1 + i\partial_E \Gamma_1(z_\pm)]\} \approx \ln[-i(E - z_\pm)]. \tag{7.3.33}$$

With Eqs. (7.3.30) and (7.3.31) we find $\Gamma_n(E)/T_K \approx 1 - g\ln(\Lambda/T_K)$ with $E = z_0 + i\Lambda$ for $n = 1$ and $E = z_\pm + i\Lambda$ for $n = 2$. Now, we can set $\Gamma_1(E) = T_K$ in Eq. (7.3.31) and $\Gamma_2(E) = T_K$ in Eq. (7.3.30), respectively, and obtain for the $\mathcal{O}(g)$ correction

$$2iz_0/T_K = \Gamma_2(z_0)/T_K \approx 1 - g\ln(-iz_0/T_K + 1) \approx 1 - g\ln\left(-\frac{1}{2} + 1\right) \approx 1 + g\ln 2 \approx 2^g, \tag{7.3.34}$$

$$\begin{aligned} iz_\pm/T_K = \Gamma_1(z_\pm)/T_K &\approx 1 - g\ln\left(-iz_\pm/T_K + \frac{1}{2}\right) \approx 1 - g\ln\left(-1 \mp i\Omega/T_K + \frac{1}{2}\right) \\ &\approx 1 + g\ln 2 \pm i\pi g \approx 2^g \pm i\pi g. \end{aligned} \tag{7.3.35}$$

where we have used $-iz_0/T_K = -\frac{1}{2} + \mathcal{O}(g)$ and $-iz_\pm/T_K = -1 + \mathcal{O}(g)$. Assuming $\Omega > 0$ the equation $E + i\Gamma_1(E) = 0$ has only a solution for positive $g > 0$. Thus, we find finite frequency poles for $g > 0$ only. To sum up, we obtain from Eqs. (7.3.34) and (7.3.35) the following result for the decay rates and the oscillation frequency up to $\mathcal{O}(g)$

$$\Gamma^*_{1/2} \approx 2^g\, T_K, \quad \Omega \approx \pi\, g\, T_K, \tag{7.3.36}$$

where the poles at $z_\pm$ exist only for $g > 0$.

For E exponentially close to one of the poles, i.e. $g\ln(|E - z_i|/T_K) \gg \mathcal{O}(1)$ [which probes the regime of exponentially large times $g\ln(T_K t) \gg \mathcal{O}(1)$] we can safely replace $\Gamma_i(E) \to \Gamma_i(z_i)$ on the r.h.s. of the renormalization group equations (7.3.23). By fixing the integration constants by comparing with the solutions Eqs. (7.3.30) and (7.3.31) at intermediate energies, we obtain

$$\Gamma_1(E) \approx T_K \left[\frac{T_K}{-i(E - z_0)}\right]^g, \quad \Gamma_2(E) \approx 2iz_0, \tag{7.3.37}$$

$$\tag{7.3.38}$$

for $E \approx z_0$ and

$$\Gamma_1(E) \approx iz_\pm, \quad \Gamma_2(E) \approx T_K \left[1 - g\ln\frac{-i(E - z_\pm)}{T_K}\right]. \tag{7.3.39}$$

for $E \approx z_\pm$. It was found [Ken13a, Kas13a] that the solutions Eqs. (7.3.28), (7.3.30), (7.3.37), and (7.3.39) for $\Gamma_1(E)$ at high, intermediate, and exponentially small energy difference from z_i can be interpolated by the expression

$$\Gamma_1(E) \approx T_K \left[\frac{T_K}{-i(E - z_0)}\right]^g \tag{7.3.40}$$

to leading order in g. We have checked numerically that, for the special points $E = z_0 + i\Lambda \pm 0^+$, with $\Lambda \in \mathbb{R}$, this formula holds even for larger values of g, which will be important later where we use this result also for the evaluation of the branch-cut contribution to obtain $P_{\rm inc}(t)$. On the other hand, for E exponentially close to the poles $z_\pm$ a numerical analysis shows that Eq. (7.3.40) is correct for small values of g. For larger couplings it turns out numerically that one can significantly improve on this result by using

$$\Gamma_1(E) \approx T_K \left[\frac{T_K}{-i(E-\Gamma_1(E)/2)}\right]^g . \tag{7.3.41}$$

for $E \approx z_\pm$. In turn, this equation can be employed for an improved evaluation of the poles' positions and the residuum of the resolvent $\Pi_1(E)$. This yields

$$\Gamma_1^*/T_K = 2^{\frac{g}{1+g}} \left[1 + \tan^2\left(\frac{\pi g}{1+g}\right)\right]^{-1/2} , \tag{7.3.42}$$

$$\Omega = \Gamma_1^* \tan\left(\frac{\pi g}{1+g}\right) = \Gamma_1^* \cot\left(\frac{\pi}{2}\frac{1-g}{1+g}\right) , \tag{7.3.43}$$

$$\frac{1}{1+\partial_E \Gamma_1(z_\pm)} = \frac{1-g}{1+g} . \tag{7.3.44}$$

The calculated quality factor Ω/Γ_1^* is in agreement with NIBA [Wei12] and the CFT [Les98] result of Eq. (7.3.11). From Eqs. (7.3.25), (7.3.42) and (7.3.44) we then obtain

$$P_{\rm coh}(t) = 2\frac{1-g}{1+g}\cos(\Omega t)\, e^{-\Gamma_1^* t}\, \Theta(g) \tag{7.3.45}$$

for the coherent contribution to the dynamics. A similar – albeit much more complicated – analysis can be pursued for $\Gamma_2(E)$ which is not needed here.

Rather, we want to determine the position of $z_0 = -i\Gamma_2^*/2$ for larger values of g next. Replacing $\Gamma_{1/2}(E) \to \Gamma_2^*$ on the r.h.s. of the renormalization group equations (7.3.23) provides a very good approximation which can be verified numerically. For $E = z_0 + i\Lambda$, with $\Lambda > 0$, a rather lengthy calculation [Kas13a] leads to the improved formula

$$\frac{\Gamma_2^*}{2} \approx T_K \left[\frac{\pi g}{2\sin(\pi g)}\right]^{\frac{1}{1+g}} . \tag{7.3.46}$$

Note that in the analysis of the positions of the non-analyticities we have taken higher order terms in g into account although the RTRG flow equations (7.3.23) were derived by concentrating only on the leading order in g. The confidence that this procedure is actually meaningful is drawn from the fact that this way we reproduce non-perturbative results from CFT exactly.

Finally, we give $P_{\rm inc}(t)$ steaming from the branch-cut, by setting $E = z_0 - ix \pm 0^+$ with $0 < x < \infty$ and using $\Gamma_1(E)^* = \Gamma_1(-E^*)$

$$P_{\rm inc}(t) = \frac{1}{\pi} e^{-\frac{\Gamma_2^*}{2}t} \mathrm{Im} \int_0^\infty \frac{e^{-xt}}{\Gamma_2^*/2 + x - \Gamma_1(z_0 - ix - 0^+)} dx, \tag{7.3.47}$$

where $\Gamma_1(z_0 - ix - 0^+) \approx T_K (T_K/x)^g e^{-i\pi g}$ is taken from Eq. (7.3.40). For intermediate to long times $T_K t \gtrapprox 1$ we can replace the slowly varying function $x^g \to t^{-g}$ since the exponential function e^{-xt} in the integrand of Eq. (7.3.47) restricts the integration range to the regime $x \sim \mathcal{O}(1/t)$. This leads to

$$P_{\rm inc}(t) \approx \frac{1}{\pi} \mathrm{Im}\Big\{ e^{-\gamma_t t} \mathrm{E}\Big(1, \big[\tfrac{1}{2}\Gamma_2^* - \gamma_t\big]\, t\Big)\Big\} , \tag{7.3.48}$$

with $\gamma_t = T_K (T_K t)^g e^{-i\pi g}$. For exponentially large times $(T_K t)^{|g|} \gg 1$ the branch-cut contribution Eq. (7.3.48) leads to the result from improved NIBA given in Eq. (7.3.10) by the asymptotic expansion

$$\mathrm{E}(1, z) \sim \frac{e^{-z}}{z} , \quad \text{for:} \quad |z| \to \infty, \tag{7.3.49}$$

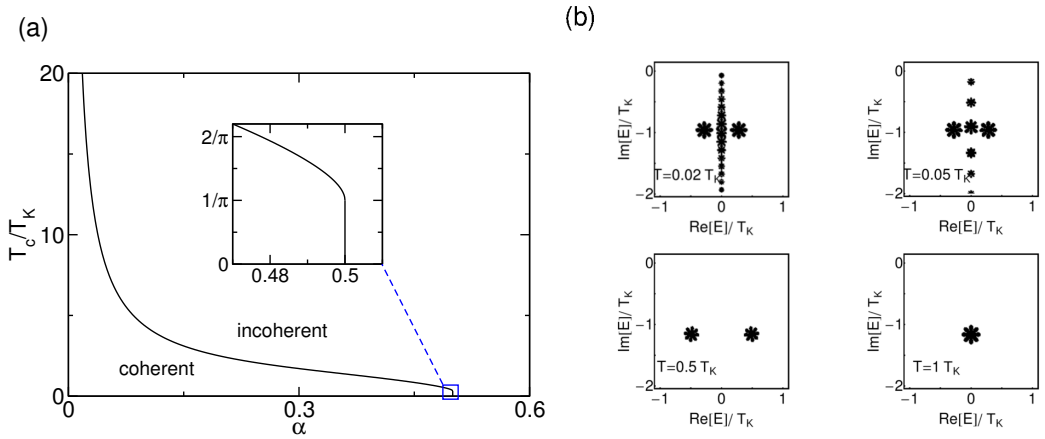


Figure 7.15.: Left: Transition line separating coherent and incoherent dynamics as found by NIBA in Eq. (7.3.50) [Wei12]. Approaching $\alpha \to 1/2$ from below one finds the finite value $\lim_{\alpha\to 1/2-0^+} T_c(\alpha) = T_K/\pi$. We have already discussed in the previous part of this section that the expectation of where coherent and incoherent dynamics are expected at long times needs to be refined. In the following, we derive a new transition diagram of dynamical phases summarized in Fig. 7.18. Right: Analytic structure of the Laplace transform of the spin expectation value $P(E)$ determined with NIBA. We employ Eq. (7.3.9) to highlight the non-analyticities. Shown is $\alpha = 0.45$ for different temperatures T. For finite T the branch-cut found at $T = 0$ is resolved into an infinite series of non-analyticities, which are still located on the imaginary axis. Their mutual distance is $\sim 2\pi T/T_K$, and the distance of the pole closest to the real axis is $\approx \pi T/T_K$. The finite frequency poles start moving away from the real axis when T is increased. At some temperature this movement is inverted and they finally collapse on the real axis for some $T = T_c$. Afterwards two poles move up and down on the real axis (not shown).

of the exponential integral. Close to $\alpha = 1/2$ meaning $g \to 0$ exponentially large time scales are needed to meaningfully use the latter approximation. It is important to note that thus Eq. (7.3.10) is only useful for times so large that $P_{\rm coh}(t)$ can safely be neglected compared to the dominating term $P_{\rm inc}(t)$. It is thus meaningless to combine the results for the coherent part obtained with CFT [given in Eq. (7.3.11) [Les98]] and the predictions from improved NIBA [given in Eq. (7.3.10) [Egg97]]. On the other hand, a comparison of the improved expression for $P(t)$ found analytically from Eqs. (7.3.45) and (7.3.48) to the full numerics is included in the main panel of Fig. 7.13. The analytical solution is in excellent agreement with the numerical solution of the flow equations[25]. To sum up: the interesting competition of the branch-cut and pole contributions under scrutiny here can only be studied by keeping Eq. (7.3.48). In fact, it is this competition which leads to the interesting asymptotically coherent→partially coherent→incoherent transition as α is swept from 0 through $1/2$.

7.3.2 Dynamics at $T > 0$

Next, we turn our attention to the influence of finite temperature on the system's dynamics. We begin again by a treatment within the NIBA. We can right away analyze Eq. (7.3.1) at finite T and find that the branch-cut originating at $E = 0$ for $T = 0$ is resolved into an infinite series of non-analyticities, which are still located on the imaginary axis. Their mutual distance is $\sim 2\pi T/T_K$, and the distance of the non-analyticity closest to the real axis is $\approx \pi T/T_K$. For $T \to 0$ this contribution leads to the unphysical sluggish decay mentioned above. Therefore, within NIBA one should analyze the behavior of these non-analyticities only for $T \gg T_K$, where one can hope that the missing indent at $T \to 0$ is negligible compared to the one $\sim T$. Therefore, we concentrate

[25] The meaningless combination of the expression Eq. (7.3.10) for the incoherent part $P_{\rm inc}(t)$ and the CFT results of Eq. (7.3.11) for the coherent one is not shown, as it strongly deviates for times $T_K t \gtrapprox 1$.

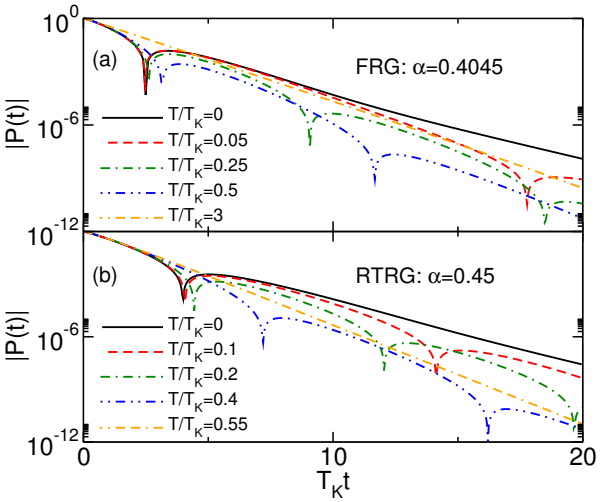


Figure 7.16.: Dynamics of the spin expectation value P(t) for a FRG (a) and RTRG (b) treatment and different temperatures T. The dynamics found in both approaches features a very interesting behavior in the partially coherent regime at elevated temperature. First the coherence of the system (measured by the non-monotonicity in the dynamics) is elevated (more dips appear). Only for larger T the transition towards the monotonic (incoherent) regime shows up.

on the finite frequency poles. From a numerical analysis it is obvious [compare Fig. 7.15(b)] that these poles start moving away from the real axis when T is increased. At some temperature this movement is inverted until they collapse on the imaginary axis for some $T = T_c$. Afterwards two poles move up and down on the imaginary axis. From an analytic treatment [Wei86, Wei87, Wei12] one finds that the temperature T_c, at which the poles collapse, reads[26]

$$T_c = \frac{T_K}{2\pi}\left\{\frac{\Gamma(\alpha)}{\alpha\Gamma(1-\alpha)}\left[1+\pi\alpha\cot(\pi\alpha)+2\sqrt{W(\alpha)}\right]\right\}^{1/2(1-\alpha)}, \tag{7.3.50}$$

with

$$W(\alpha) = \pi\alpha\cot(\pi\alpha) - \alpha^2 g(\alpha) \tag{7.3.51}$$

and

$$g(\alpha) = \frac{1}{2}\left\{\Psi(1,1-\alpha) - \Psi(1,1+\alpha) - [\alpha^{-1} - \pi\cot(\pi\alpha)]^2\right\}. \tag{7.3.52}$$

Within NIBA these expressions determine the coherent-incoherent transition line [Gar85, Wei12]. This transition line was already referenced in Fig. 3.5 of section 3.6. For the reader's convenience it is again shown in Fig. 7.15(a).

FRG and RTRG analysis

First, we have to extend the RTRG approach to $T > 0$. Integrating out the reservoirs' degrees of freedom at $T > 0$ (keep in mind that RTRG aims at the reduced density matrix of the central level directly) leads to a summation over Matsubara frequencies $\omega_m = \pi T(2m+1)$ on the right hand side of the renormalization group equations. The renormalization group equations (7.3.22)-(7.3.24) thus change to

$$\frac{d\Gamma_{1/2}(E)}{dE} = ig\Gamma_1(E)\,2\pi T\sum_{m=0}^{\infty}\left[\Pi_{2/1}(E+i\omega_m)\right]^2, \tag{7.3.53}$$

$$\Pi_n(E) = i\left[E + i\Gamma_n(E)/n\right]^{-1}, \quad n = 1,2, \tag{7.3.54}$$

[26] Note that apparently there is a typographic error of a missing factor $1/2\pi$ in [Wei12], as one can see by comparing to [Wei86].

while the initial conditions still read $\Gamma_{1/2}(i\omega_c) = \Delta^2/\omega_c$. To perform the Matsubara sum to order g we neglect the E-dependence of $\Gamma_{1/2}$ in $\Pi_{2/1}$, which yields

$$\frac{d\Gamma_{1/2}(E)}{dE} = ig\frac{\Gamma_1(E)}{2\pi T}\Psi\left(1, \frac{1}{2} + \frac{1}{2\pi T\Pi_{2/1}(E)}\right), \tag{7.3.55}$$

where $\Psi(1,z)$ again is the trigamma function (see above). This set of equations can be solved numerically to obtain Π_n in Laplace or (after an inverse Laplace transform) $P(t)$ in real-time space. The dynamics of the spin expectation value shown in Fig. 7.16 for both our FRG (a) and RTRG (b) approaches feature a very interesting behavior in the partially coherent regime at elevated temperature: the coherence of the system, measured by the non-monotonicity in the dynamics appears to be elevated at elevated temperature at first and only later the transition towards the monotonic (incoherent) regime shows up. This is a rather counter-intuitive finding, but actually using the RTRG in Laplace space we will show next that one can in fact drive the partially coherent to the asymptotic coherent regime raising temperature.

To achieve this we first analyze the RTRG flow equation (7.3.55) in more detail. The right hand side of the differential equation (7.3.55) contains a series of second order poles, which after integration turn into essential singularities of the propagator Π_1 at z_n. They result from the disintegration of the branch-cut of $\Gamma_1(E)$ found at $T = 0$ and are located on the imaginary axis [see Fig. 7.17 ($T = 0.01\,T_K$)]; their mutual distance is $2\pi T[1 + \mathcal{O}(g)]$. Close to those singularities we have $\Pi_1 \propto e^{-g/(E-z_n)}$. The finite frequency branch-cuts (black circles with gray tails) of Figs. 7.17 ($T = 0.05\,T_K$) and ($T = 0.12\,T_K$) are artefacts of the lowest order truncation. In the full diagrammatic series underlying the RTRG approach [Sch00, Sch09] there are no integrals over the reservoirs excitation frequencies for $T > 0$, but only summations over ω_m; branch-cuts are excluded. However, the artificial non-analyticities contribute to $P(t)$ in order $\mathcal{O}\left(g^2\right)$. Furthermore, as they are always located below the leading order singularities they do not affect the long-time behavior of $P(t)$.

Coherence by Elevated Temperature

The non-analyticities of the propagator $\Pi_1(E)$ determining the dynamics of $P(t)$ generically behave as shown in Fig. 7.17 for $1/2 > \alpha > \alpha_c$ as T is increased. Initially, $\Pi_1(E)$ shows a pair of poles with non-vanishing real parts of equal absolute value [damped oscillations of $P(t)$] as well as a branch-cut on the imaginary axis [monotonic decay of $P(t)$] at $T = 0$ (see previous section). The distance of the start of the branch-cut to the real axis is smaller than the distance between the latter and the poles giving rise to the partially coherent behavior found at $T = 0$. As indicated above, indeed, for $T > 0$ the branch-cut disintegrates into singularities [Wei12] as can be seen in Fig. 7.17 ($T = 0.01\,T_K$). With increasing T these move down while the imaginary part of the finite frequency poles barely changes, see Fig. 7.17 ($T = 0.05\,T_K$). At a certain temperature [$T_{c1}(\alpha)$] the top zero frequency singularity passes the level of the pole pair and the system undergoes a transition from the partially coherent into the asymptotically coherent regime [compare Fig. 7.17 ($T = 0.12\,T_K$)]. The additional finite frequency features (black circles with gray tails) visible in Figs. 7.17 ($T = 0.01\,T_K$) and ($T = 0.12\,T_K$) are the above mentioned artefacts of $\mathcal{O}(g^2)$. Further increasing T the pair of poles starts to move inwards resulting in a decreasing oscillation frequency, while the singularities on the imaginary axis continue to move down and finally leave the frame shown in Fig. 7.17, [see Fig. 7.17 ($T = 0.49\,T_K$)] . The frequency vanishes when the pole pair hits the imaginary axis at $T_{c2}(\alpha)$. This indicates the transition from the asymptotically coherent to the incoherent regime [shown in Fig. 7.17 ($T = 0.51$)]. If T is increased further two singularities move in opposite directions along the imaginary axis such that the one moving up approaches the decay rate of $\alpha = 1/2$ for $T \to \infty$, [see Fig. 7.17 ($T = 0.59\,T_K$-$T = 1000\,T_K$)]. This is due to the fact that as $T > \omega_c$ (leaving the scaling limit) the renormalization flow is directly cut by T resulting in the unrenormalized decay rate. For our choice of parameters ($\Delta^2/\omega_c^2 = 2.5 \cdot 10^{-5}$) this results in $\Delta^2/\omega_c \approx 0.59\,T_K$. The corresponding distance from the real axis, indicated by a red line in Fig. 7.17 ($T = 1000\,T_K$), is in excellent agreement with our numerics.

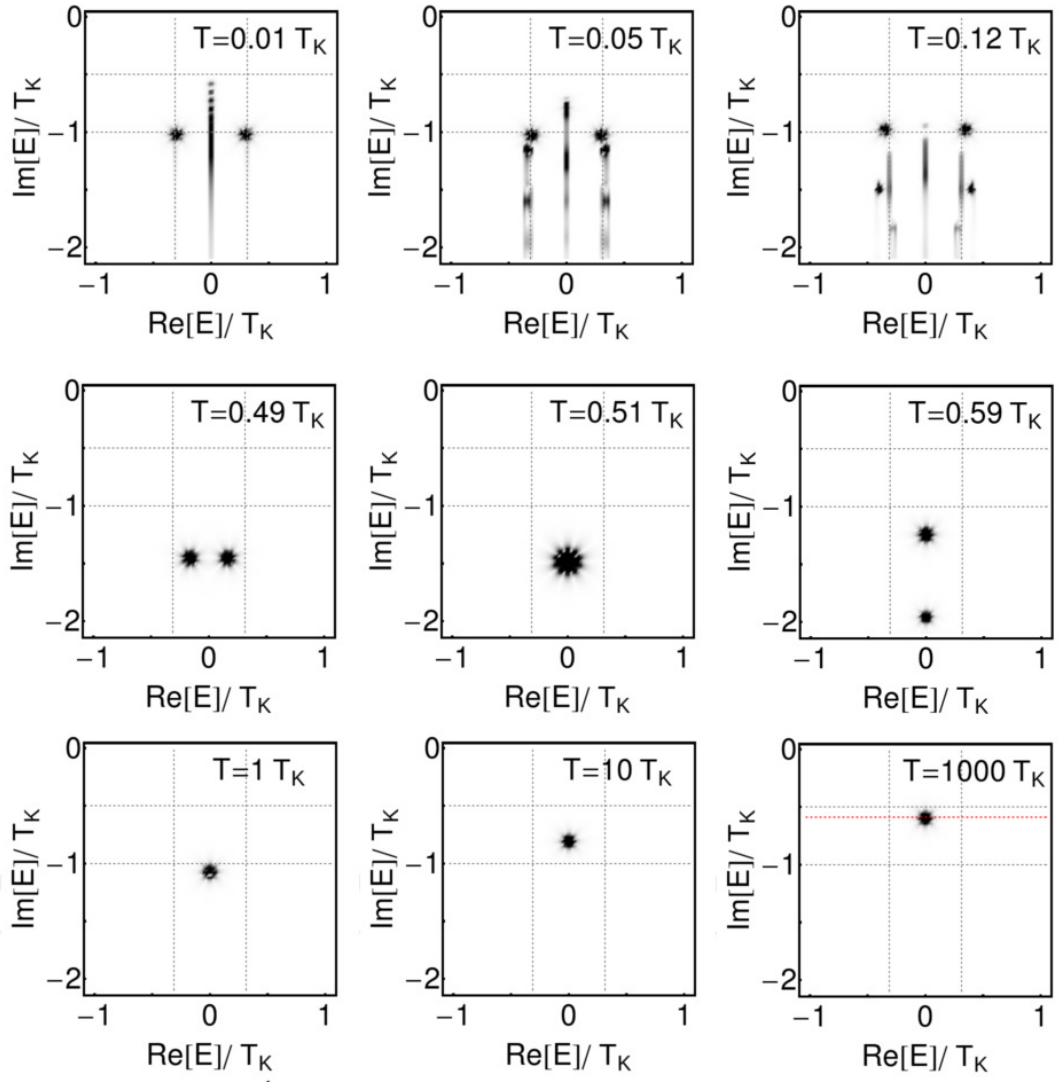


Figure 7.17.: The non-analyticities found in the Laplace transform of the spin expectation value $P(E)$ from RTRG for $\alpha = 0.45$ (partially coherent regime). Using Eq. (7.3.9) highlights the different contributions to the time evolution in Laplace space. The branch-cut found on the imaginary axes at $T = 0$ (compare Fig. 7.14) is dissolved into an infinite series of poles for $T > 0$. Two transitions can be identified: (a) from partially coherent to asymptotically coherent at $T/T_K \approx 0.12$ and (b) from asymptotically coherent to incoherent at $T/T_K \approx 0.51$. For very large temperature $T > \omega_c$ the pole relaxes to the unrenormalized decay rate corresponding to $\alpha = 1/2$ (indicated by red dotted line for $T/T_K = 1000$).

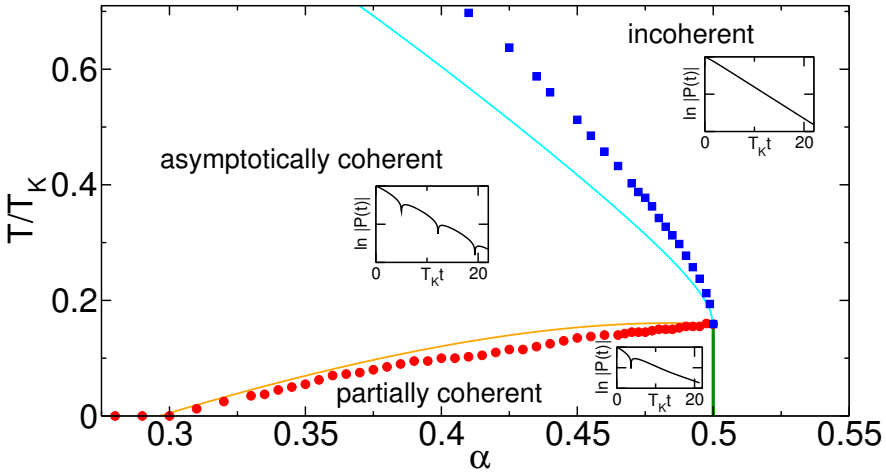


Figure 7.18.: Diagram showing the extend of the incoherent, asymptotically, and partially coherent sectors. The critical temperatures T_{c1} (lower branch) and T_{c2} (upper branch) obtained from the numerical solution of the RTRG equations (7.3.55) are shown as circles; solid lines correspond to the approximatations Eqs. (7.3.60) (lower) and (7.3.61) (upper). The insets exemplify the time evolution of the spin expectation value $P(t)$ in the different regimes for $\alpha = 0.45$ and $T/T_K = 0.01$ (partially coherent), 0.3 (asymptotically coherent), 0.59 (incoherent).

Finally, we (additionally to T) vary over α. With this we numerically determine $T_{c1/2}(\alpha)$, which is summarized by the symbols shown in Fig. 7.18. To sum up the diagram of different dynamical regimes in the ohmic SBM we note that the above outlined more complicated picture of an asymptotic to partially coherent transition at α_c for $T = 0$ is furthermore complemented by a transition from partially coherent to asymptotic coherent dynamics for $1/2 > \alpha > \alpha_c$ as the temperature is elevated. This can be understood as *elevated coherence at elevated temperature*. Only for even larger T the transition to the incoherent regime occurs.

In passing we note that our numerics also lead to a value of the temperature $T_{c1} = T_{c2} = 1/2\pi$ at which the 'triple point' at $\alpha = 1/2$ is found which differs from the NIBA result[27] $T_{c2} = 1/\pi$. This is attributed to the interplay of branch-cut and poles at $\alpha \to 1/2 - 0^+$, which is missed by NIBA. We will come back to this issue later and prove this results also analytically.

Analytic treatment

We complement our findings by analytical approximations for $T_{c1/2}(\alpha)$ (curved lines in Fig. 7.18). As in the $T = 0$ case we solve Eq. (7.3.55) for Γ_1 to leading order in g, where we neglect the weak E-dependence of Γ_2 and finds

$$\Gamma_1(E) = \widetilde{T}_K e^{-g\Psi\left(0,\frac{1}{2}+\frac{-iE+\Gamma_2(E)/2}{2\pi T}\right)}, \tag{7.3.56}$$

with $\widetilde{T}_K = T_K (2\pi T/T_K)^{-g}$ resulting from the high energy integration limit and where $\Psi(0,x)$ denotes the digamma function. Now we determine the positions of the non-analyticities of $\Pi_1(E)$ approximately using Eq. (7.3.56). The finite frequency poles $z_\pm = \pm\Omega - i\Gamma_1^*$ are the solutions of $iz_\pm = \Gamma_1(z_\pm)$, where we can additionally set $\Gamma_2(E) \approx \Gamma_1(E)$, which was found to be a reasonable approximation at $T = 0$ (see above). This yields the self-consistency equation $\Gamma_2^* = \Gamma_2(z_0)$ with $z_0 = -i\pi T - i\Gamma_2^*/2$. Setting $\Gamma_2(E)$ to Γ_2^* in Eq. (7.3.56) and using Eq. (7.3.55) we obtain $\Gamma_2^* = 2\pi T g \int_0^\infty u(x)\psi'(x + u(x) - \Gamma_2^*/4\pi T)dx$, where $u(x) = (T_K/2\pi T)^{1-g} e^{-g\Psi(0,x)}$.

The *first transition* occurs at $\Gamma_1^* = \Gamma_2^*/2 + \pi T_{c1}$. For decreasing α, $T_{c1}(\alpha)$ decreases and we furthermore approximate the digamma function in Eq. (7.3.56) by its low temperature ($2\pi T \ll T_K$) expansion

$$\Psi(0,x) \approx \log x\,, \quad \text{for:} \quad |x| \gg 1. \tag{7.3.57}$$

[27] U. Weiss informed us that using improved NIBA [Egg97] at finite T gives $T_{c2}(1/2)$ in agreement with our result [Wei].

This simplifies Eq. (7.3.56) to

$$\Gamma_1(E) = \frac{T_K}{[(-iE + \pi T + \Gamma_2(E)/2)/T_K]^g}, \tag{7.3.58}$$

which is just the same as the $T = 0$ result with a πT shift on the right hand side. Thus the rates $\Gamma^*_{1/2}$ are just given by their $T = 0$ counterparts [see Eqs. (7.3.42) and (7.3.46)].

The *second transition* takes place when the finite frequency poles collapse. This means that $\Gamma^*_1 = \Gamma_1(-i\Gamma^*_1)$ has only a single real valued solution Γ^*_1. For decreasing α, $T_{c2}(\alpha)$ increases, and we apply

$$\psi(x) \approx -\gamma - 1/x\,, \quad \text{for:} \quad |x| \ll 1\,, \tag{7.3.59}$$

for $2\pi T \gg T_K$ in Eq. (7.3.56).

In sum, we find

$$T_{c1}(\alpha) = \frac{1}{\pi}\left(\Gamma^{*(0)}_1 - \Gamma^{*(0)}_2/2\right), \tag{7.3.60}$$

with $\Gamma^{*(0)}_{1/2}$ of Eqs. (7.3.42) and (7.3.46) and $g = 1 - 2\alpha$ (lower curved line in Fig. 7.18) for the first transition line. It yields a very good approximation to the numerically obtained T_{c1} (circles in Fig. 7.18) for $0.3 < \alpha < 1/2$. For the second transition temperature (upper curved line in Fig. 7.18) we approximate

$$T_{c2}(\alpha) = \frac{T_K}{2\pi} e^{\frac{g(1+\gamma)+\sqrt{2g+g^2}}{1+g}} \left(1+g+\sqrt{2g+g^2}\right)^{\frac{1}{1+g}}. \tag{7.3.61}$$

For α close to $1/2$ ($g \ll 1$) this further simplifies to

$$T_{c2}(\alpha) \approx \frac{T_K}{2\pi}\left(1 + 4\sqrt{\frac{1}{2} - \alpha}\right), \tag{7.3.62}$$

with a leading square root behavior around $\alpha \to 1/2 - 0^+$.

For $\alpha \to 1/2 - 0^+$, where $\Gamma^*_{1/2} = T_K$, the $T_{c1/2}$ can be calculated without approximating the digamma function in Eq. (7.3.56). With

$$\Gamma^*_1 = \Gamma^*_2/2 + \pi T_{c1}, \tag{7.3.63}$$

we find

$$T_{c1}(1/2) = T_K/(2\pi). \tag{7.3.64}$$

For $T_{c2}(1/2)$ we again aim at a single real valued solution of $\Gamma_1(-i\Gamma^*_1) = \Gamma^*_1$, which implies $d\Gamma_1(-i\Gamma^*_1)/d\Gamma^*_1 = 1$. Using Eq. (7.3.56) with $\Gamma_1(E) \approx \Gamma_2(E)$ this can be written as

$$d\Gamma_1(-i\Gamma^*_1)/d\Gamma^*_1 = g\Gamma^*_1\psi'([\pi T - \Gamma^*_1/2]/[2\pi T]) = 4\pi T. \tag{7.3.65}$$

For $g \to 0$ this equation can only be fulfilled for vanishing argument of the trigamma function, which readily yields

$$T_{c2}(1/2) = T_K/(2\pi). \tag{7.3.66}$$

7.3.3 Quenches and the Role of Non-Markovian Memory

We next investigate the role of non-Markovian memory in dissipative systems. As the FRG is set up in real time incorporating quench scenarios is straight forward. The time dependent self-energy is simply dressed with the time dependent part of the Hamiltonian and thus the above outlined framework can be adopted right away (for more details see [Ken12b]). For time dependent two-particle interactions (as is the case here) the right hand site of the flow equations (to our truncation order) is simply dressed with the bare time dependent two-particle vertex. For the RTRG tackling quenches requires some extension which the interested reader can find in [Kas13a]. We concentrate on $T = 0$ where we find the above mentioned transition between partially coherent and incoherent dynamics at $\alpha = 1/2$ and always quench from one to the other. This means that at time t_q we abruptly change the value of $\alpha = \alpha_i$ to $\alpha = \alpha_f$. To reduce the number of free parameters we keep the distance of $\alpha_{i/f}$ from $\alpha = 1/2$ constant, such that $2\alpha_f - 1 = 1 - 2\alpha_i$.

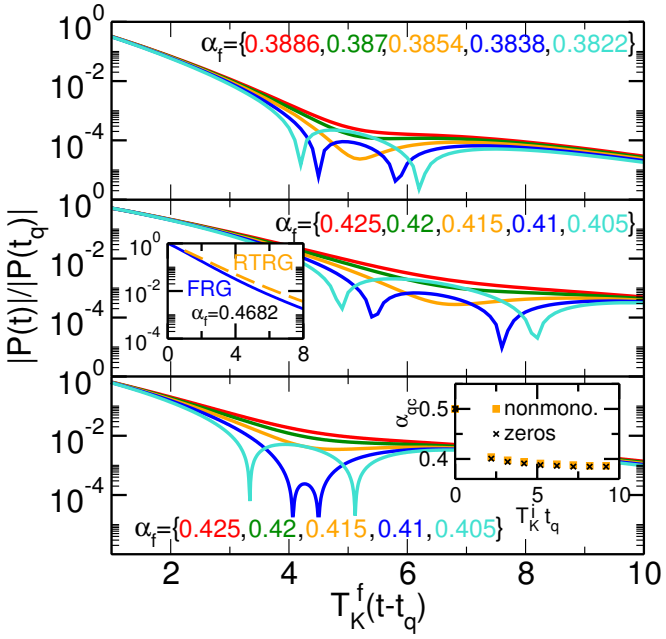


Figure 7.19.: Spin expectation value $P(t)$ with the initial time evolution determined by a coupling from the incoherent regime $\alpha_i > 1/2$. At $t = t_q$ it is switched to $\alpha_f < 1/2$ from the partially coherent one. The scaling limit is realized by $\Delta/\omega_c = 1/200$. Times are restricted to $t > t_q$; for $0 < t < t_q$, see Fig. 7.13(b). Left inset: comparison of numerical FRG and RTRG data; the non-Markovian memory completely suppresses the partially coherent 'oscillatory' behavior. It only survives for α_f smaller than a critical coupling α_{qc}; see the upper [numerical solution of FRG equations], central [numerical solution of RTRG equations], and lower [analytical result Eq. (7.3.69)] panels. Right inset: dependence of α_{qc} on the time $T_K^i t_q$ the evolution was performed in the incoherent regime (FRG data). Two different definitions of α_{qc} are compared. In the first α_{qc} is defined as the α_f at which the first zero of $P(t)$ can be observed, in the second as the α_f at which the curve first shows a non-monotonicity. The two values barely differ.

Quench from incoherent to coherent

In Fig. 7.19 we show $P(t)$ when quenching at t_q from the incoherent to the partially coherent regime. Since we have two couplings α_i and α_f we also encounter two characteristic scales T_K^i and T_K^f, which in the scaling limit differ by orders of magnitude. With this Δ and ω_c cannot be scaled out as efficiently as before (by taking T_K as the unit of energy). We consider times t_q before the quench between $T_K^i t_q = 5$ and $T_K^i t_q = 10$ to minimize the influence of the initial transient dynamics. In the left inset we compare the data obtained by the numerical solution of the FRG and RTRG equations. The agreement for $\alpha_{i/f}$ close to $1/2$ is excellent. Note that we use the same coupling $\alpha_f = 0.4682$ as in the main panel of Fig. 7.13(b). The data for the quench dynamics in the left inset of Fig. 7.19 are monotonic. There is no indication of coherent behavior. Thus we conclude that the incoherent dynamics before the quench heavily affects the one afterwards, to the extend that the coherence signature can be suppressed completely. In the upper (FRG) and central (RTRG) panel results for smaller α_f are shown. Nonmonotonic ('oscillatory') behavior can only be found for α_f being smaller than some critical coupling α_{qc}. As $|1 - 2\alpha_{qc}| \ll 1$ is not strictly fulfilled our two approximate renormalization group methods give values for α_{qc} which differ by a few percent. Its precise value can only be obtained using a non-perturbative method.

Within the RTRG the memory of the spin state is preserved in the excitations of the bath. Classifying the memory contributions by the number of bath excitations that have gone through the quench one can show [Kas13a] that the terms with n excitations are proportional to $A^n = (T_K^i/T_K^f)^{n/2} \approx (\Delta/\omega_c)^{2n|g_f|}$, with $A \ll 1$. If we concentrate on the case of a single excitation with

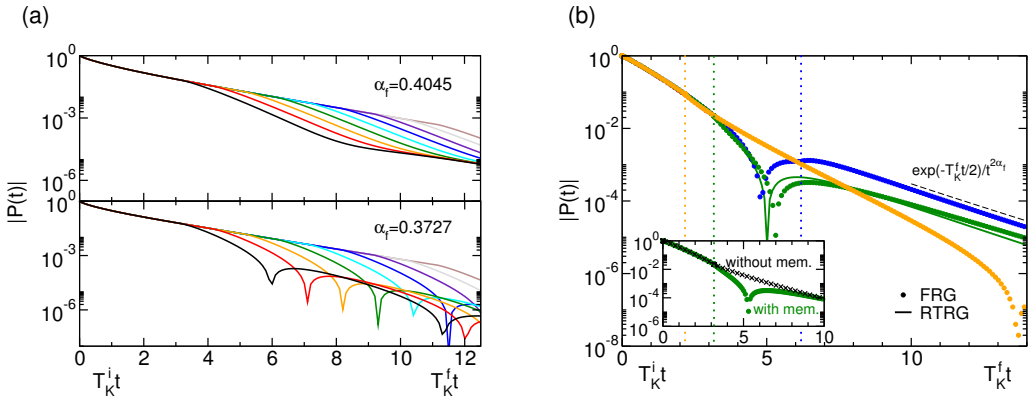


Figure 7.20.: Left: Time evolution of the spin expectation value $P(t)$ obtained from the numerical solution of the FRG flow equations. The quench protocol is the same as in Fig. 7.19. Note that the time axis is chosen to be $T_K^i t$ before the quench and $T_K^f t$ after it. Different lines correspond to different quench times t_q increasing from left to right. Upper panel: $\alpha_f > \alpha_{qc}$, that is the time evolution even after the quench is monotonic even though it is performed with a positive coupling constant. The non-Markovian memory heavily affects the dynamics after the quench. The qualitative behavior is independent of t_q. Lower panel: $\alpha_f < \alpha_{qc}$; nonmonotonic behavior is found after the quench. This is again independent of t_q. Right: The same as in Fig. 7.19 but for quenches from the coherent to the incoherent regime. The spin expectation value $|P(t)|$ for $\alpha_i = 0.4682$ and different quench times t_q (indicated by the vertical dotted lines) is shown. At the respective t_q the x-axis scale is switched from $T_K^i t$ to $T_K^f t$. Main panel: data of the numerical solutions of the FRG and RTRG flow equations. The thin dashed line is an exponential term with rate $T_K^f/2$ and a subleading power-law correction. Inset: FRG data with and without the memory term.

Matsubara frequency Λ we obtain ($t' = t - t_q \geq 0$)

$$P(t') = P^f(t')P^i(t_q) - g_i \int_0^\infty d\Lambda F_\Lambda^f(t') F_\Lambda^i(t_q), \tag{7.3.67}$$

$$F_\Lambda^\kappa(t) = -\int_{-\infty}^{\infty} \frac{dE}{2\pi} e^{-iEt} \Pi_1^\kappa(E + i\Lambda) \sqrt{\Gamma_1^\kappa(E)} \Pi_2^\kappa(E)\,, \tag{7.3.68}$$

with $\kappa = i, f$, P^κ and $\Gamma_{1/2}^\kappa$ computed as above, but with the corresponding $\alpha_{i/f}$ and initial condition $P^\kappa(0) = 1$. The two contributions can be interpreted separately. The first term describes the standard relaxation while the second memory term implies (dissipative) non-Markovian dynamics. There exists no analogue for quenches in closed systems [Pol11].

For varying ω_c the results depend only very weakly on Δ^2/ω_c (via A). E.g. changing $(\Delta/\omega_c)^2$ by an order of magnitude around the average value $2.5 \cdot 10^{-5}$ results in a change of α_c by only a few percent.

Furthermore, we can again obtain analytical insight of the interplay of the relaxation dynamics and the non-Markovian correction by RTRG. This results [Ken13a, Kas13a] in

$$\frac{P(t')}{P(t_q)} \approx 2(1-A) e^{-\Gamma_1^{*f} t'} \cos(\Omega^f t') + A e^{-\Gamma_2^{*f} t'/2}, \tag{7.3.69}$$

which is shown in the lower panel of Fig. 7.19. The memory clearly features a coherent and an incoherent contribution $\propto A$. The first has a negative sign and suppresses the coherent part while the second enhances the incoherent term compared to the one encountered for a simple relaxation. For $g_f \ll 1$ the latter is subdominant compared to the former and is thus omitted in Eq. (7.3.69). With this we can understand the appearance of α_{qc} analytically. We conclude these consideration by revealing the independence of the behavior of $P(t)$ with respect to the time of the quench t_q

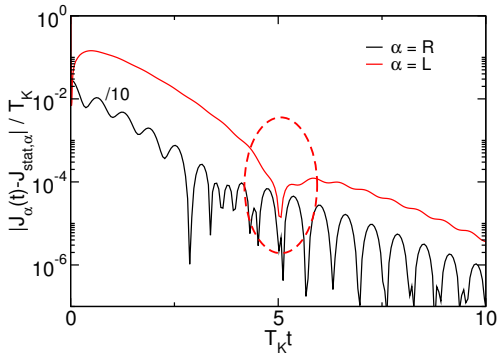


Figure 7.21.: The current leaving the left or right reservoir. We determine the strength of the two-particle interaction by $g = 0.3183$ and choose $V/2 = \epsilon = \mu_L = -\mu_R = 5T_K$. The dynamics of the current leaving the left reservoir features the characteristic oscillation with rather small frequency $\Omega \sim g$ (marked by an ellipse in Fig. 7.21), while only sub-dominantly [to $\mathcal{O}([\epsilon/T_K]^{-1})$] an oscillation with frequency $\sim \epsilon$ shows up (wiggles barely visible at times $T_K t > 5$). For the current leaving the right reservoir (not in resonance with the central level) we clearly find a single dominant oscillation with frequency $\Omega \sim V$ for all t.

(as long as $T_K^i t_q$ not too small). This is shown in Fig. 7.20(a). Many different quenching times for both cases $\alpha > \alpha_{qc}$ (upper panel) and $\alpha < \alpha_{qc}$ (lower panel) are compared. The qualitative behavior remains unaffected.

Quench from coherent to incoherent

As a second example we discuss the dynamics when quenching at t_q in the opposite direction, that is from the partially coherent to the incoherent regime. For simplicity of discussion we focus on α_i's for which only a single zero at time t_0 is found in the relaxation protocol. In Fig. 7.20(b) we show $|P(t)|$ obtained from the numerical solution of the FRG and RTRG equations for $\alpha_i = 0.4682$. Again, the simple relaxation for this coupling can be found for comparison in Fig. 7.13. Now, we sweep through the quenching time t_q. For $t_q > t_0$ the dynamics at times larger than t_q very quickly adapts to the new rate $\approx T_K^f/2$ of the incoherent dynamics [see Eq. (7.3.10) and the dashed line in Fig. 7.20(b)]. The behavior changes significantly for $t_q < t_0$. In this case non-monotonic ('oscillatory') behavior is found for times $t > t_q$ at which the time evolution is performed with $\alpha_f = 0.5318 > 1/2$; thus where the relaxation dynamics is incoherent. The smaller $t_q - t_0$ the further the zero is transfered into the incoherent regime. Just like in the opposite quench the memory persist over several $1/T_k^f$. For turning off the memory terms in the renormalization group equations the inset of Fig. 7.20(b) demonstrates that the zero of $P(t)$ vanishes. This indicates that the appearance of the zero is exclusively coded in the history of the dynamics (opposed to simply in the values of the system's density matrix at a selected time).

7.4 Biased (V ≠ 0) IRLM ↔ Spin-Boson Model

We extensively used the mapping of the SBM to the unbiased IRLM ($V/2 = \mu_L = -\mu_R = 0$) in the preceding part of our analysis. The signature of the partially coherent behavior of the unbiased ohmic SBM $\epsilon = 0$ was found to be given by a finite number of zeros (non-monotonic behavior) at intermediate times only. If we now consider the dynamics of the biased ($V \neq 0$) IRLM, which constitutes an interesting transport setup, one might wonder about the consequences entailed by this finding. To be more precise, if we apply a finite bias $\mu_L = -\mu_R = V/2$ and choose the onsite energy of the central level ϵ such that the level is at resonance with, e.g., the left reservoir ($\epsilon = V/2$), the left reservoir plus the central level can be viewed (besides of a trivial shift in energy) as the same

system as studied above. Without the right reservoir in place we would thus perfectly reproduce all the findings given above in the dynamics, leading to the interesting question about the influence of the presence of the other reservoir. In the following, we concentrate on the particle current, which is the most studied quantity of transport setups. For $t \to \infty$ due to the finite value of V obviously a steady current sets in, describing the continuous transport of particles across the dot junction from the left to the right reservoir. The FRG can be right away applied to study this setup and the results of such an analysis are shown in Fig. 7.21 for the current leaving the left and right reservoir, respectively. We clearly find that the dynamics of the current leaving the left reservoir features the characteristic oscillation with rather small frequency $\Omega \sim g$ (marked by an ellipse in Fig. 7.21), while only sub-dominantly [to $\mathcal{O}([\epsilon/T_K]^{-1})$] an oscillation with frequency $\sim \epsilon$ shows up (wiggles barely visible at times $T_K t > 5$). For the current leaving the right reservoir (not in resonance with the central level) we clearly find a single dominant oscillation with frequency $\Omega \sim V$ for all t.

Interestingly, the non-equilibrium on resonance dynamics of the strongly biased IRLM can thus be understood by the dynamics found in the ohmic SBM ($\to$ Section 7.3) as well as an off resonance setup ($\to$ Section 7.2). Left and right current show the physics of the one or the other (depending on with which the central level is at resonance with) separately, instead of a mixture of both.

7.5 Conclusion

Extending Time Dependent FRG

We have shown how the time dependent FRG approach, introduced for open quantum systems in [Ken11] and outlined in general in chapter 4, can be applied at finite temperature. For this we have focussed on the example of a charge-fluctuating quantum dot (IRLM $\to$ Section 3.5), which can be seen as a proof of principle. Importantly, we have derived analytic expressions for the Green's functions, involving Gauss hypergeometric and Hurwitz-Lerch zeta-functions, pivotal to describing the dynamics within the FRG. Closed form expressions are desirable not only from a viewpoint of numerical efficiency, but rather essential for the scaling limit, where Cauchy principle valued integrals have to be treated ($\to$ Section 4.1.2). With this we can close the gap which arises between the initial preparation of a system and the steady-state reached for $t \to \infty$, which can be aimed at directly by a complementary FRG treatment. We also exemplify that no subtle problem arises from permuting the limits $N \to \infty$ and $t \to \infty$ in the derivation of the latter. All of these statements were derived on the level of a first order truncation scheme, where only the leading order on the right hand side of the flow equations is kept. Thus, we are restricted to rather small two-particle interactions (U in the example of the IRLM).

Results for the Bias Driven IRLM

We showed that analogously to the $T = 0$ case the effect of the two-particle interaction to a very good approximation can be condensed in effective constant Hamiltonian parameters in the transport regime $|\epsilon \pm V/2| \gg T_K$. This facilitates the interpretation of the results to a great deal, as the time evolution of the observables can be understood from the non-interacting case. For finite temperature already this simplified picture gives rise to very rich physics. We have found that different temperature in the left and right reservoir can be used to detune the different contributions found in the dynamics with respect to each other. This cannot be achieved at $T = 0$ and leads to a variety of different dynamical regimes at large times. Where these crossovers from one regime to the other occur are generally described by a power-law in the bare parameters with interaction dependent exponent (renormalization induced). FRG can be used to correctly resum the exponent to leading order in the interaction strength.

Results for Dissipative Systems

Using a formal mapping between the IRLM and the SBM we have shown that the dynamics encountered in the latter at $T = 0$ is significantly different to what one might expect. Although we reproduce the coherent-to-incoherent transition at $\alpha = 1/2$ found in NIBA and CFT, we showed that the large time dynamics for $1/2 > \alpha > \alpha_c$ in this "coherent" dynamical phase are actually

monotonic! Only at intermediate times the signature of the coherent dynamics (non-monotonic behavior) can be found. These results lead us to propose a more refined picture of the dynamical phases found, where one differentiates between the asymptotically coherent $\alpha < \alpha_c$ (non-monotonic for all times) and the partially coherent $1/2 > \alpha > \alpha_c$ regime.

Turning to finite T we even more surprisingly found that starting in the partially coherent regime at $T = 0$ elevating temperature drives the system into a regime of asymptotic coherence. Only for even larger T the dynamics finally turns incoherent. This elevated coherence at elevated temperature is rather counter-intuitive.

The aforementioned results were not obtained using only the FRG, but also the complementary RTRG approach. This further strengthens the reliability of our results.

A second interesting application targets quantum quenches where parameters of the Hamiltonian are switched instantly at some time t_q. We have seen using our complementary renormalization group procedures that the non-Markovian memory of the bosonic bath, storing information about the pre-quench history, greatly affects the dynamics after the quench. Because in this example non-Markovian memory plays a major role for the dynamics found, this could be seen as a motivation to a more systematic study of when and why modelling baths as Markovian ones is justified.

Outlook

For the future it would be interesting to analyze the consequences implied by our finding of elevated coherence at elevated temperature in the ohmic SBM. For quantum computing devising highly coherent systems is crucial, where usually temperature largely reduces this property. As we always operate at finite temperature, understanding the precise dependence of the coherence at different temperature is important. An experiment showing the proposed effect would certainly make a huge contribution to this.

Furthermore, considering different left and right reservoir temperatures raises the question about thermoelectric transport through quantum dots. Therefore the following section will be devoted to this issue – albeit in the steady-state regime.

Acknowledgement

We are grateful to Oleksiy Kashuba, Mikhail Pletyukhov and Herbert Schoeller for the derivation of the RTRG equations. Furthermore we would like to thank Ulrich Weiss for fruitful discussion on the SBM.

References

Part of the results discussed in this chapter were published in

D. M. Kennes and V. Meden
'Interacting resonant level model in nonequilibrium: Finite-temperature effects'
Phys. Rev. B **87**, 075130 (2013)

D. M. Kennes, O. Kashuba, M. Pletyukhov, H. Schoeller and V. Meden
'Oscillatory dynamics and non-Markovian memory in dissipative quantum systems'
Phys. Rev. Lett. **110**, 100405 (2013)

O. Kashuba, D. M. Kennes, M. Pletyukhov, V. Meden and H. Schoeller
'Quench dynamics of a dissipative quantum system: A renormalization group study'
Phys. Rev. B. **88**, 165133 (2013)

D. M. Kennes, O. Kashuba and V. Meden
'Dynamical regimes of dissipative quantum systems'
Phys. Rev. B. **88**, 241110 (2013)

Chapter 8

Thermoelectric Transport

Contents

8.1.	**Basics and Definitions**	**132**
8.1.1.	Linear Response	132
8.1.2.	Non-Equilibrium Beyond Linear Response	134
8.2.	**Thermoelectric Transport in the IRLM**	**135**
8.2.1.	IRLM: Finite Temperature an FRG Analysis	135
8.2.2.	RLM case: $U = 0$	137
8.2.3.	IRLM: $U \neq 0$	141
8.2.4.	Application: Charging	142
8.3.	**Thermoelectric Transport in the AHM**	**144**
8.3.1.	First order perturbation theory	144
8.3.2.	AHM: FRG Analysis	145
8.3.3.	AHM: Thermoelectric Properties in Linear Response	152
8.4.	**Conclusion**	**156**

Introduction

Ever since we are using energy to facilitate our many aspects of modern life, a central question remains the quest for transport, storage and efficient conversion of energy in its various forms. In the context of thermodynamics and statistical mechanics typically two types of engines are studied: (a) refrigerators and (b) power generators. Those of course have opposite functionality, the former uses energy to cool down a system, while the second uses heat to generate an output power. In solid-state physics thermoelectric materials can be used for both of the aforementioned purposes. Those, in contrast to other engines, have no moving parts and thus prove very reliable [Mah95].

For low-dimensional quantum system, such as quantum dots, the natural question arises, whether particularly interesting thermoelectric features can be found. This can be viewed either from a more "microscopic transport" ansatz to quantum impurity systems [Mur08, Oja08, Lei10, Cos10, And11a, Sot12, Aze12, Sán13], as also usually pursued by us, as well as from a more phenomenological viewpoint of thermodynamics [Mah95, Mah97, Esp09, Ben11, Sán11, Yan12a, Yan12b]. In the following we want to focus on engines that generate power, meaning that we investigate how a given temperature gradient can induce a net bias voltage across different impurity structures. We will focus on the IRLM (→ Section 3.5) as a prototype model of charge fluctuations and the AHM (→ Section 3.4) which also incorporates spin as well as phononic degrees of freedom.

Outline

In the following we will motivate that quantum dots are interesting candidates for materials used in thermoelectric applications. They do not follow the Wiedemann-Franz law which strongly limits the efficiency of ordinary bulk systems and thus renders their investigation highly interesting. To

establish a common vocabulary and to review some of the main findings from thermodynamics, we will first give a rough introduction into the matter. In this preliminary section the language used in the following will be introduced under the specific viewpoint of the investigation conducted later. The depiction is far from complete and more details can be found in e.g. [Dom54, Bec85, Sch06]. In the next two sections we will investigate (1) the IRLM and (2) the AHM within the FRG. For the IRLM, FRG has proven before to be a reliable tool to tackle its transport properties. We start by analyzing the renormalization group equation of the IRLM in the steady-state regime at finite temperatures, vital to any further consideration. We will then extract the IRLM's thermoelectric behavior were the main part of the interaction effects can be understood by the renormalization found in the previous part combined with the non-interacting results. Next, we discuss a more "applied" charging scenario. Afterwards, we turn to the AHM and again begin with an analysis of the flow equations. Here we focus on equilibrium. We present different routes to extracting the linear response conductances at finite temperature without the need of possibly ill-defined analytic continuation. We finish this section by recapitulating how the route to the strong correlations limit appears to be blocked by the limitations of the FRG (similarly to the SIAM see below). A final remark, concluding the work done and including prospects of future work, can be found in the last section.

8.1 Basics and Definitions

First, we review the vocabulary that is commonly used in the field of thermoelectric transport. We start out with a very general system that is divided into a left (L) and a right (R) part. Both parts are coupled via some, at this point unspecific, link structure which allows for energy and/or particle exchange between the two. We focus exclusively[1] on the steady-state regime, be it in terms of linear response quantities or full-fledged non-equilibrium setups. The particle/heat current leaving subsystem $\alpha \in \{\mathrm{L}, \mathrm{R}\}$ is then denoted by $I_{\mathrm{c}}^{\alpha}(I_{\mathrm{h}}^{\alpha})$. Usually, it is sufficient to focus on one of the two subsystems for each of the two currents. Because we are interested in power generators we choose $V/2 = \mu_{\mathrm{L}} = -\mu_{\mathrm{R}} > 0$ and $\Delta T = T_{\mathrm{L}} - T_{\mathrm{R}} < 0$ and consider the particle current *leaving* the left subsystem and the heat current *entering* the right one[2]. Then we drop the additional index α to shorten notation. In this context the quantities of interest are the output power

$$P = \dot{W} = (\mu_{\mathrm{L}} - \mu_{\mathrm{R}})\frac{dq}{dt} = -VI_{\mathrm{c}}, \tag{8.1.1}$$

with q the particles in the left subsystem and the efficiency

$$\eta = \frac{P}{-I_{\mathrm{h}}} < \eta_C, \tag{8.1.2}$$

where the upper bound of the efficiency is given by the Carnot efficiency $\eta_C = 1 - \frac{T_L}{T_R}$, a consequence deeply rooted in the second law of thermodynamics [Sch06].

8.1.1 Linear Response

Particularly easy to tackle is the linear response regime, in which bias voltage V and temperature gradient ΔT (with respect to some mean temperature T) between left and right subsystem are chosen to be so small that only the linear order of each must be kept. Thus the heat and charge currents are determined by a first order Taylor expansion

$$\begin{pmatrix} I_{\mathrm{c}} \\ I_{\mathrm{h}} \end{pmatrix} = \begin{pmatrix} G_{\mathrm{c},V} & G_{\mathrm{c},\Delta T} \\ G_{\mathrm{h},V} & G_{\mathrm{h},\Delta T} \end{pmatrix} \begin{pmatrix} V \\ \Delta T \end{pmatrix} = \underline{G} \begin{pmatrix} V \\ \Delta T \end{pmatrix}, \tag{8.1.3}$$

[1] Note that in the framework outlined in the previous chapter (→ Chapter 7) a generalization to the transient behavior is right away possible, but less instructive.

[2] which has to be compensated by a heat current from some super-reservoir to the right subsystem and can thus be used to define efficiency.

with the "conductance"-matrix $\underline{G}_{a,b} = \lim_{b\to 0} I_a/b|_{\bar{b}=0}$, where $a \in \{\mathrm{c},\mathrm{h}\}$ and $b \in \{V\Delta, T\}$ are taken as indices of the matrix and $\overline{V} = \Delta T$ as well as $\overline{\Delta T} = V$. Of those conductances usually only the electrical conductance $G_{\mathrm{c},V}$ bears direct significance for experiments as it can be readily accessed. However, certain combinations including also the other conductances are additionally of very strong experimental relevance. To be more precise, one can access the *thermopower*

$$S = \lim_{\Delta T\to 0} \frac{V}{\Delta T}\bigg|_{I_c=0} = \frac{-G_{\mathrm{c},\Delta T}}{G_{\mathrm{c},V}}\,, \tag{8.1.4}$$

in experiments as well as the *thermal conductance*

$$k_e = -\lim_{\Delta T\to 0} \frac{I_\mathrm{h}}{\Delta T}\bigg|_{I_c=0} = G_{\mathrm{h},\Delta T} - G_{\mathrm{h},V}\frac{G_{\mathrm{c},\Delta T}}{G_{\mathrm{c},V}} = G_{\mathrm{h},\Delta T} - G_{\mathrm{c},V}TS^2. \tag{8.1.5}$$

The last equality is a consequence of the famous *Onsager (reciprocal) relation* [Ons31a, Ons31b]

$$TG_{\mathrm{c},\Delta T} = G_{\mathrm{h},V}, \tag{8.1.6}$$

which holds under the assumption of the time reversibility of microscopic dynamics.

So far we have considered the "transport" notation, a vantage point that we usually take within this thesis. This is clear as $G_{\mathrm{c},v}$ is nothing but the conductance defined in Eq. (4.1.82). Now we want to shift our paradigm to connect to the "thermodynamic's angle". Generally, we define the charge force $F = \mu_\mathrm{L} - \mu_\mathrm{R} = V$ and thermodynamic charge force $X_1 = F/T$. The conjugate of this force is the charge itself, $x = q$ in the left subsystem. Consequently, the current $I_\mathrm{c} = \dot{x}$. For the heat current we analogously define a thermodynamic heat force $X_2 = 1/T_L - 1/T_R$. In this notation the linear response regime is characterized by

$$\begin{pmatrix} I_\mathrm{c} \\ -I_\mathrm{h} \end{pmatrix} = \begin{pmatrix} L_{11} & L_{12} \\ L_{21} & L_{22} \end{pmatrix} \begin{pmatrix} X_1 \\ X_2 \end{pmatrix} = \underline{L}\,\underline{X} = \underline{L} \begin{pmatrix} V/T \\ -\Delta T/T^2 \end{pmatrix} = \begin{pmatrix} G_{\mathrm{c},V}T & -G_{\mathrm{c},\Delta T}T^2 \\ -G_{\mathrm{h},V}T & G_{\mathrm{h},\Delta T}T^2 \end{pmatrix} \begin{pmatrix} V/T \\ -\Delta T/T^2 \end{pmatrix}. \tag{8.1.7}$$

Thus the entries of $\underline{G}$ and $\underline{L}$ are simply related by factors $\pm 1/T$ and $\pm 1/T^2$. The *entropy production*

$$\frac{dS}{dt} = I_\mathrm{c}X_1 - I_\mathrm{h}X_2 = \underline{X}^T\,\underline{L}\,\underline{X} = I_\mathrm{c}\frac{V}{T} - I_\mathrm{h}\frac{\Delta T}{T^2} \geq 0\,, \tag{8.1.8}$$

is positive, as it should from the second law of thermodynamics. Considering the limits

$$\Delta T = 0: \quad \frac{dS}{dt} = L_{11}\left(\frac{V}{T}\right)^2 \geq 0 \quad \Rightarrow \quad L_{11} \geq 0\,, \tag{8.1.9}$$

$$V = 0: \quad \frac{dS}{dt} = L_{22}\left(\frac{\Delta T}{T^2}\right)^2 \geq 0 \quad \Rightarrow \quad L_{22} \geq 0\,. \tag{8.1.10}$$

This implies $G_{c,V} \geq 0$ and $G_{h,\Delta T} \geq 0$. Furthermore from the Onsager relation Eq. (8.1.6) follows

$$L_{12} = L_{21} \tag{8.1.11}$$

and thus $\underline{L}$ is symmetric. Additionally, because of Eq. (8.1.8) its determinant then fulfils

$$\det(\underline{L}) = L_{11}L_{22} - L_{12}^2 \geq 0. \tag{8.1.12}$$

Finally, we now turn to output power P and efficiency η in linear response.

Maximum Efficiency

Let us aim at maximum efficiency $\eta^{\mathrm{lin},0}$ at given T, which is advisable if loses are to be minimized. To this end we introduce the *figure of merit*

$$ZT = \frac{L_{12}^2}{\det(\underline{L})} \;\Rightarrow\; 0 \overset{(8.1.12)}{\leq} ZT, \tag{8.1.13}$$

where $ZT \overset{\det(\underline{L})\to 0}{\longrightarrow} \infty$ (as long as $L_{12} \neq 0$). Taking $\eta = I_c X_1 T / I_h$ and maximizing with respect to X_1 yields

$$\eta^{\text{lin},0} = \eta_C^{\text{lin}} \frac{\sqrt{ZT+1}-1}{\sqrt{ZT+1}+1} \leq \eta_C^{\text{lin}}, \tag{8.1.14}$$

where $\eta_C^{\text{lin}} = \frac{-\Delta T}{T}$ is the linearised part of the Carnot efficiency and $\eta^{\text{lin},0} = \eta_C^{\text{lin}}$ only if $ZT \overset{\det(\underline{L})\to 0}{\longrightarrow} \infty$. Thus the magnitude of the figure of merit is a measure for the efficiency of the thermoelectric process. At $ZT \to \infty$, even though the efficiency reaches Carnot value, this value is still very small as $\eta_C^{\text{lin}} \sim \Delta T$ is very small. The corresponding power output at maximum efficiency is then given by

$$P^{\text{lin},0} = \frac{\eta_C^{\text{lin}}}{T} \frac{L_{22}}{\sqrt{1+ZT}} \eta^{\text{lin},0}. \tag{8.1.15}$$

Unfortunately, the power output thus vanishes when maximum efficiency is reached ($ZT \to \infty$). Due to this reason it might be more important to consider...

Maximum Power Output

Technical application usually require a certain power output. Therefore, next we consider maximum power output $P^{\text{lin,max}}$ rather than efficiency. Maximizing $P = -I_c X_1 T$ again with resepect to X_1 [VdB05, Ben11] yields

$$\eta^{\text{lin,max}} = \eta_{CA}^{\text{lin}} \frac{ZT}{ZT+2}, \tag{8.1.16}$$

$$P^{\text{lin,max}} = \frac{\eta_{CA}^{\text{lin}}}{T} \frac{ZT+2}{ZT+1} L_{22} \eta^{\text{lin,max}}. \tag{8.1.17}$$

Here the role of the Carnot efficiency is taken by the so called Curzon-Ahlborn efficiency $\eta_{CA}^{\text{lin}} = \eta_C^{\text{lin}}/2$, which limits the efficiency of systems operated at maximum power [Cur74].

Lorenz number

Again the determining factor is the figure of merit ZT. In many (bulk) materials the *Wiedemann-Franz law* dictates that the *Lorenz number*

$$Ln = \frac{k_e}{G_{c,V} T} \quad \Rightarrow \quad ZT = \frac{S^2}{Ln} \tag{8.1.18}$$

is a *system independent constant*. This limits the figure of merit drastically. But in systems where an energy-dependent transmission amplitude occurs (such as the quantum-dot systems considered here), the Wiedemann-Franz law is violated and higher figure of merits are possible.

8.1.2 Non-Equilibrium Beyond Linear Response

For the full-fledged non-equilibrium less is known about the thermoelectric properties of different systems, as it is usually much more difficult to handle. For interacting quantum dots however the Meir-Wingreen formula can be used to derive the charge and heat currents though the quantum-dot region (charge [Mei92] and heat [Wan06, Oja08]). The corresponding expressions are given in Eqs. (4.1.72) and (4.1.79). The efficiency that can be achieved with an engine operating in non-equilibrium is of course still bounded from above by the Carnot efficiency η_C defined above. For maximum power output optimization it was shown that the Curzon-Ahlborn efficiency $\eta_{CA} = 1 - \sqrt{1-\eta_C}$ describes correctly the efficiency of "a large number of systems" [VdB05] if one stays in the vicinity of linear irreversible thermodynamics. Schmiedl and Seifert introduce an upper bound $\eta_{SS} = \eta_C/(2-\eta_C)$ for the entire non-equilibrium regime [Sch08b]. Importantly, the FRG can be used to tackle a microscopic model in non-equilibrium, where given its speed vast parameter spaces can be sampled efficiently. Analogue to linear response, in non-equilibrium maximum efficiency η^0 and corresponding power P^0 and maximum power output $P^{\max}$ and corresponding efficiency $\eta^{\max}$ are defined [via Eqs. (8.1.1) and (8.1.2)].

In the following we will investigate the IRLM and AHM with the FRG in the light of the above raised criteria.

8.2 Thermoelectric Transport in the IRLM

The (non-interacting) resonant level model (RLM) in the limit of vanishing hybridization was studied in [Esp09]. Adding finite hybridization as well as interaction to the quantum dot system (leading to the IRLM) is one step to a more realistic description of charge-fluctuating quantum dots. The steady-state of the IRLM was studied so far only at vanishing temperature where renormalization effects are expected to be most prominent. Thus as a first step we extend the analysis to include finite temperatures.

8.2.1 IRLM: Finite Temperature an FRG Analysis

The IRLM was studied in detail in the previous chapter (→ Chapter 7). we will employ the same framework (truncation order, cut-off scheme, etc.), but focusing on the steady-state. Then the flow equations read

$$\partial_\Lambda t_{12}^\Lambda = \frac{iU}{4\pi}\int S_{12}^{\mathrm{K},\Lambda}(\omega)d\omega, \quad t_{12}^{\Lambda\to\infty} = t_{12} = t_{\mathrm{imp,L}}\ , \tag{8.2.1}$$

$$\partial_\Lambda t_{23}^\Lambda = \frac{iU}{4\pi}\int S_{23}^{\mathrm{K},\Lambda}(\omega)d\omega, \quad t_{23}^{\Lambda\to\infty} = t_{23} = t_{\mathrm{imp,R}}\ , \tag{8.2.2}$$

$$\partial_\Lambda \epsilon^\Lambda = -\frac{iU}{4\pi}\int \left[S_{11}^{\mathrm{K},\Lambda} + S_{33}^{\mathrm{K},\Lambda}\right](\omega)d\omega, \quad \epsilon^{\Lambda\to\infty} = \epsilon\ , \tag{8.2.3}$$

$$\partial_\Lambda \epsilon'^\Lambda = -\frac{iU}{4\pi}\int S_{22}^{\mathrm{K},\Lambda}(\omega)d\omega, \quad \epsilon'^{\Lambda\to\infty} = 0\ , \tag{8.2.4}$$

where at this point the Keldysh components nicely incorporates any changes steaming from finite temperature. The single-scale propagator is calculated by Eq. (4.3.18). Eqs. (8.2.1)-(8.2.4) can be implemented straightforwardly on a computer and the numerical effort executing this implementation is negligible. However, we postpone this, because one even succeeds in obtaining analytical results. Similar to [Kar10d, Kar10a][3] first, we suppress the renormalization of the central onsite energy ϵ^Λ which is $\mathcal{O}(U^2)$ as well as ϵ'^Λ, which always appears in combination with the much larger scale Γ. This yields

$$\begin{aligned}\partial_\Lambda t_{12}^\Lambda = &-\frac{U\Gamma}{\pi}\int_{-\infty}^{\infty}\partial_\Lambda^*\left[G_{11}^{\mathrm{R},\Lambda}(\omega)(f_L(\omega)-1/2)G_{12}^{\mathrm{A},\Lambda}(\omega)\right]d\omega\\ &-\frac{U\Gamma}{\pi}\int_{-\infty}^{\infty}\partial_\Lambda^*\left[G_{13}^{\mathrm{R},\Lambda}(\omega)(f_R(\omega)-1/2)G_{32}^{\mathrm{A},\Lambda}(\omega)\right]d\omega\ ,\end{aligned} \tag{8.2.5}$$

$$\begin{aligned}\partial_\Lambda t_{23}^\Lambda = &-\frac{U\Gamma}{\pi}\int_{-\infty}^{\infty}\partial_\Lambda^*\left[G_{21}^{\mathrm{R},\Lambda}(\omega)(f_L(\omega)-1/2)G_{13}^{\mathrm{A},\Lambda}(\omega)\right]d\omega\\ &-\frac{U\Gamma}{\pi}\int_{-\infty}^{\infty}\partial_\Lambda^*\left[G_{23}^{\mathrm{R},\Lambda}(\omega)(f_R(\omega)-1/2)G_{33}^{\mathrm{A},\Lambda}(\omega)\right]d\omega\ ,\end{aligned} \tag{8.2.6}$$

as the only remaining flow equations. The star differential operator ∂_Λ^* was introduced in Section 4.3.2 as to act only on the non-interacting Green's function of a Dyson expansion of the full Green's function. The flow equations of the level-lead hybridization $\Theta_{ij} = |t_{ij}|^2/\Gamma$ can be extracted

[3] Also compare to section 7.3.1.

analytically by suppressing all terms $\mathcal{O}(1/\Gamma^2)$

$$\partial_\Lambda \Theta_{12}^\Lambda = \frac{U}{2\pi\Gamma}\partial_\Lambda^* \int_{-\infty}^{\infty} \left[\tanh\left(\frac{\beta_L(\omega-\mu_L)}{2}\right)\frac{\Theta_{12}^\Lambda}{\omega-\epsilon-i(\Lambda+\Theta_{12}^\Lambda+\Theta_{23}^\Lambda)}+\text{c.c.}\right]d\omega\,, \tag{8.2.7}$$

$$\partial_\Lambda \Theta_{23}^\Lambda = \partial_\Lambda \Theta_{12}^\Lambda (1\leftrightarrow 3, L\leftrightarrow R)\,. \tag{8.2.8}$$

Furthermore, in a good approximation one can neglect the renormalization of Θ_{12} and Θ_{23} in the denominator. This is denoted as approximation 1 in the following. Integrating Eq. (8.2.7) yields

$$\partial_\Lambda \Theta_{12}^\Lambda = -\frac{U}{\pi\Gamma}\Theta_{12}^\Lambda \text{Re}\left\{\frac{\beta_L}{\pi}\Psi\left(1,\frac{1}{2}-\frac{i}{\pi}\frac{\beta_L}{2}\left[\epsilon-\mu_L+i(\Lambda+\Theta_{12}+\Theta_{23})\right]\right)\right\}, \tag{8.2.9}$$

with $\Psi(1,x)$ being the trigamma function. Additionally, setting $\Psi(1,1/2+x)\approx 1/(2/\pi^2+x)$ for all $\text{Re}[x]>0$[4] on the right hand site of the flow equation, which is referred to as approximation 2 in the following, finally gives

$$\partial_\Lambda \Theta_{12}^\Lambda \approx -\frac{U}{\pi\Gamma}\Theta_{12}\frac{2(2T_L/\pi+\Lambda+\Theta_{12}+\Theta_{23})}{(2T_L/\pi+\Lambda+\Theta_{12}+\Theta_{23})^2+[(\epsilon-\mu_L)/2]^2}. \tag{8.2.10}$$

Now we have to reintroducing the ultraviolet cutoff[5] Γ before we integrate this equation analytically leading to

$$\frac{\Theta_{12}^{\Lambda=0}}{t_{12}^2} \sim \begin{cases} \left(2t_{12}^2\right)^{-2U/(\pi\Gamma)+\mathcal{O}(U^2)} & |\epsilon-\mu_L|,\, T_L \ll T_K \ll \Gamma \\ V^{-2U/(\pi\Gamma)+\mathcal{O}(U^2)} & |\epsilon|,\, T_K,\, T_L \ll V \ll \Gamma \\ |\epsilon|^{-2U/(\pi\Gamma)+\mathcal{O}(U^2)} & V,\, T_K,\, T_L \ll |\epsilon| \ll \Gamma \\ T_L^{-2U/(\pi\Gamma)+\mathcal{O}(U^2)} & |\epsilon-\mu_L|,\, T_K \ll T_L \ll \Gamma \end{cases} \tag{8.2.11}$$

where we concentrated on $t_{12}=t_{23}$ and introduced T_K being the universal equilibrium low energy scale of the model [Sch80a, Sch82a, Fil81, Doy07, Bor07, Bor08, Bou08, Meh06, Kas09] defined in Eq. (3.5.6).

The renormalization of $\Theta_{23}^{\Lambda=0}$ can be obtained by replacing $(1\to 3, L\to R)$ in Eqs. (8.2.9)-(8.2.11). Explicitly, the reservoir temperatures provide infrared cutoffs [see Eq. (8.2.11)]. The Eq. (8.2.10) indicates a subtle interplay of the different cutoff scales $\epsilon-\mu_\alpha$, $\Theta_{12}+\Theta_{23}$, T_α in the denominator. Importantly, the left (right) hybridization is cut off by the temperature of the left (right) reservoir only. Different cutoff scales for the left and right hybridization have been observed before (at $T_\alpha=0$); it is $|\epsilon-\mu_L|$ ($|\epsilon-\mu_R|$) and not $V=\mu_L-\mu_R$ which enters as a cutoff for Θ_{12} (Θ_{23}) [Kar10b].

We next shortly clarify the quality of the approximations 1 and 2 used to find this analytical result. Fortunately we can take the full numerical solution of the flow equations (the only approximation being the truncation) and step by step apply approximations 1 and 2. A comparison for the renormalized line width $\Theta^{\Lambda=0}$ as a function of temperature is shown in Fig. 8.1. For the entire temperature range ($T_L=T_R=T$ and $t_{12}=t_{23}$ for simplicity) the results of approximations 1 and 2 agree well with the full numerical solution. Clearly, for $T\gtrapprox T_K$, the power-law Eq. (8.2.11) with the correct exponent is reproduced on each level of approximation. It is important to note that although the temperatures cut off the renormalization of the line width in a very intuitive way, the power-laws induced by this in different observables are quite subtle. For the question of thermoelectric transport this is secondary, and for a detailed analysis we refer to [Kar10b] ($T=0$) and [Ken13b] ($T>0$).

[4] ensuring the correct value at $x=0$ as well as asymptotic behavior

[5] Without any approximations the high energy cutoff Γ appears naturally, e.g. in any numerical study. In the derivation of the analytical Eq. (8.2.10) however, we disregarded terms $\mathcal{O}(1/\Gamma^2)$ which now renders it obligatory to introduce the high energy cutoff as an upper bound of integration by hand.

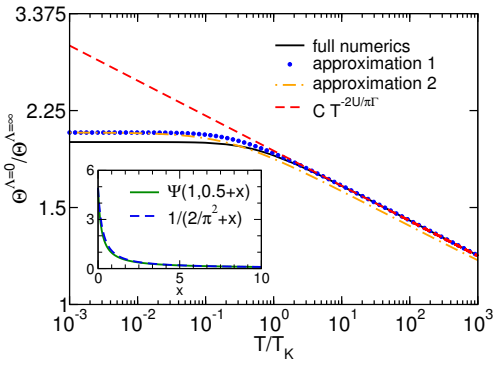


Figure 8.1.: Renormalized line width $\Theta^{\Lambda=0}$ as a function of temperature T. The parameters are $\epsilon/T_K = V/T_K = 0$, $t_{\rm imp}/\Gamma = 0.0025$, $T = T_L = T_R$ and $U/\Gamma = 0.1$. Since left and right lead are chosen symmetrically ($V = \Delta T = 0$) $\Theta_{12} = \Theta_{23} = \Theta$. Notice the double logarithmic scale, which indicates the power-law behavior for large T. The inset shows the replacement of the trigamma function used in approximation 2.

8.2.2 RLM case: $U = 0$

Before we focus on the IRLM we review some expressions for the $U = 0$, RLM case. As this limit is exactly solvable one can gain valuable insights into the problem at hand. Importantly, the $U = 0$ considerations will be important to interpret the results for the IRLM as well. As in the used truncation scheme (first order) interaction effects are incorporated in effective Hamiltonian parameters, it will allow us to draw some analytic conclusions, by plugging the renormalized parameters into the expressions for the non-interacting case.

Non-equilibrium Analysis

Since we do not need to incorporate interactions we can focus on the single-level description of the RLM ($\rightarrow$ Sections 3.5 and 7.2.1). Steady-state transport through this non-interacting dot ($\Gamma_{1\rm D} = 2\Gamma_{1\rm D,L} = 2\Gamma_{1\rm D,R}$) is fully characterized by the Breit-Wigner transmission resonance

$$\tau_{\rm BW}(\omega) = \Gamma_{1\rm D}^2 |G^{\rm R}(\omega)_{11}|^2 = \frac{\Gamma_{1\rm D}^2}{(\omega-\epsilon)^2 + \Gamma_{1\rm D}^2} \tag{8.2.12}$$

of width $\Gamma_{1D} = 2\pi\rho_{1\rm D}\tau^2 (= \Theta_{\rm L} + \Theta_{\rm R})$. The steady-state currents $I_{\rm c}$ and $I_{\rm h}$ are given in the Landauer-Büttiker formalism

$$I_{\rm c} = \frac{1}{2\pi}\int d\omega\, \tau_{\rm BW}(\omega)\left[f_L(\omega) - f_R(\omega)\right], \tag{8.2.13}$$

$$I_{\rm h} = \frac{1}{2\pi}\int d\omega\, (\omega-\mu_R)\tau_{\rm BW}(\omega)\left[f_L(\omega) - f_R(\omega)\right]. \tag{8.2.14}$$

Furthermore, we can recast the ω-integral in $I_{\rm c}$ in terms of the digamma function $\Psi(0,z)$ as

$$I_{\rm c}(\epsilon) = \frac{\Gamma_{1\rm D}}{2\pi}\,{\rm Im}\left[\Psi\left(0, \frac{1}{2} + \frac{i}{2\pi T_R}[\epsilon - \mu_R - i\Gamma_{1\rm D}]\right) - \Psi\left(0, \frac{1}{2} + \frac{i}{2\pi T_L}[\epsilon - \mu_L - i\Gamma_{1\rm D}]\right)\right]. \tag{8.2.15}$$

In the limit of vanishing hybridization [Esp09] charge and heat currents are perfectly coupled $I_h = (\epsilon - \mu_{\rm R})I_c$, this perfect coupling is broken by finite hybridization, but replaced by a Hilbert transform (Kramers-Kronig relation) [Ken13d]

$$I_{\rm h}(\epsilon) = (\epsilon - \mu_R)I_{\rm c}(\epsilon) - \frac{\Gamma_{1\rm D}}{\pi}\,\mathcal{P}\!\int d\epsilon' \frac{I_{\rm c}(\epsilon')}{\epsilon - \epsilon'}, \tag{8.2.16}$$

which links the one to the other.

This relation can be understood as follows. As long as the particle current can be cast into the general form

$$I_c(\epsilon) = \int_{-\infty}^{\infty} d\omega F(\omega, T_L, T_R, \mu_L, \mu_R) \frac{1}{(\omega-\epsilon)^2 + \Gamma_{1D}^2}, \tag{8.2.17}$$

with some arbitrary real function $F(\omega, T_L, T_R, \mu_L, \mu_R)$, we can introduce a new complex function

$$M(z) = \frac{1}{\Gamma_{1D}} \int_{-\infty}^{\infty} d\omega F(\omega, T_L, T_R, \mu_L, \mu_R) \frac{1}{i(\omega - z) - \Gamma_{1D}}, \tag{8.2.18}$$

to write $I_c(\epsilon) = \mathrm{Re}[M(\epsilon)]$. Considering $M(z) = \int dz' M(z')\delta(z-z')$ and using

$$i\pi\delta(x) \longrightarrow \mathcal{P}\left(\frac{1}{x}\right) - \frac{1}{x + i\eta}, \tag{8.2.19}$$

with $\eta \to 0^+$ to be evaluated in a distributive sense, we find

$$M(z) = \underbrace{-\frac{i}{\pi} \int dz' \frac{M(z')}{z' - z - i\eta}}_{=0,\ \text{close below}} + \frac{i}{\pi} \oint\!\!\!\!\!\!- \, dz' \frac{M(z')}{z' - z}. \tag{8.2.20}$$

From this the Kramers-Kronig relation

$$\mathrm{Im}[M(\epsilon)] = -\frac{1}{\pi} \oint\!\!\!\!\!\!- \, d\epsilon' \frac{\mathrm{Re}[M(\epsilon')]}{\epsilon - \epsilon'} \tag{8.2.21}$$

follows. Therefore, the heat current is related to the charge current[6] as given in Eq. (8.2.16), as it follows $I_h(\epsilon) = \mathrm{Im}[M(\epsilon)] + (\epsilon - \mu_L) I_c(\epsilon)$.

Thus to our truncation order, if interactions effects are incorporated on the level of renormalized Hamitonian parameters, this highly non-trivial coupling also carries over to the $U \neq 0$ case. In Eqs. (8.2.15) and (8.2.16) Γ_{1D} can be scaled out (taken as the unit of energy) rendering η and P functions of the parameters ϵ/Γ_{1D}, V/Γ_{1D}, and $T_{L/R}/\Gamma_{1D}$ alone. Experimentally the temperatures are difficult to control and thus we assume that $T_{L/R}$ are fixed by the environment. Figure 8.2(a) shows $P = V|I_c|$ in the ϵ-V-plane for $T_L/\Gamma_{1D} = 1$ and $T_R/\Gamma_{1D} = 20$. It has a unique maximum, which can be found iteratively. This way we determine maximum power and analogously maximum efficiency in the following.

To connect to existing results we first consider the limit $\Gamma_{1D} \to 0$ [Esp09]. The second term in Eq. (8.2.16) is of higher order in Γ_{1D} as compared to the first one and can be neglected[7]. As for applications the maximum power output is of particular interest, we perform such an optimization with respect to the level energy ϵ and the externally applied voltage V. In experiments on quantum dots both parameters can routinely be varied with high precision. As shown analytically in [Esp09] for $\Gamma_{1D} \to 0$, $\eta^{\max}$ and $P^{\max}$ are functions of T_L/T_R only. This allows to express them in terms of the Carnot efficiency η_C.

We now turn to $\Gamma_{1D} > 0$ and numerically maximize the output power with respect to ϵ and V using Eqs. (8.2.15) and (8.2.16). Both, $\eta^{\max}$ and $P^{\max}$ are no longer functions of η_C alone. This is demonstrated in Fig. 8.3 which depicts $\eta^{\max}$ and $P^{\max}$ as functions of T_L/Γ_{1D} and η_C. Importantly, for small T_L/Γ_{1D} rather large $\eta_C = |\Delta T|/T_R$ (close to 1) are required to obtain a sizable efficiency at maximum power, compared to the case of vanishing hybridization considered above.

To sum up how the RLM compares to bounds of thermoelectric efficiency derived in the literature from a more "phenomenological" point of view we present additionally Fig. 8.2(b). We show the

[6] Obviously in the end the relation is a consequence of the fact that retarded and advanced Green's functions fulfil similar Kramers-Kronig relations.

[7] As a consequence the aforementioned perfect coupling of charge and heat current is restored, because for $\Gamma_{1D} \to 0$ the energy of every particle coming from the dot level becomes "sharp" with fixed value ϵ

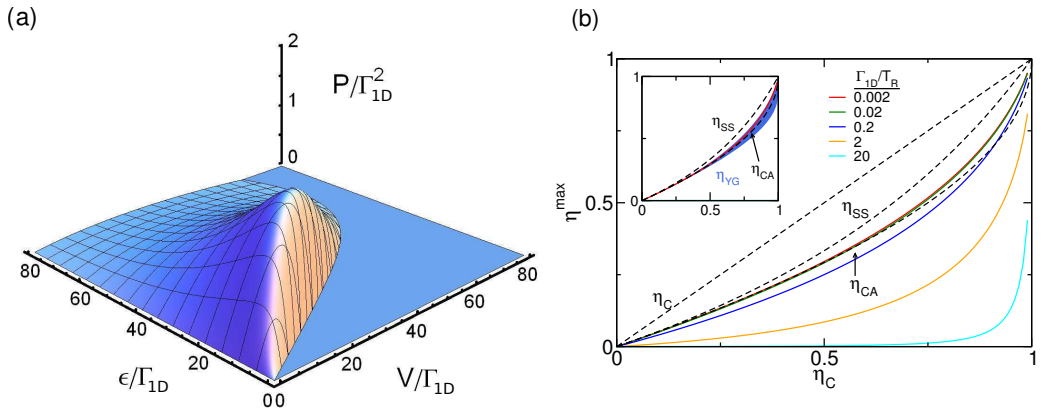


Figure 8.2.: Left: Output power P of the RLM for vanishing two-particle interaction $U = 0$ as a function of ϵ/Γ_{1D} and V/Γ_{1D} for $T_L/\Gamma_{1D} = 1$ and $T_R/\Gamma_{1D} = 20$. Data points are only shown in the regime in which the device acts as a power engine (curved surface with lines). Right: The efficiency η^{max} at maximum power in dependence of η_C for different Γ_{1D}. Up to intermediate values of $\eta_C \approx 0.5$, η_{CA} can be used to describe the efficiency of the RLM with $\Gamma_{1D} \to 0$. For all values of Γ_{1D} the efficiency found in the RLM remains below the upper bound η_{SS} of [Sch08b]. Inset: Comparison for $\Gamma_{1D} \to 0$ to the upper and lower bound (η_{YG}) proposed in [Yan12b]. Within these bounds the RLM operates nearly optimal for all η_C

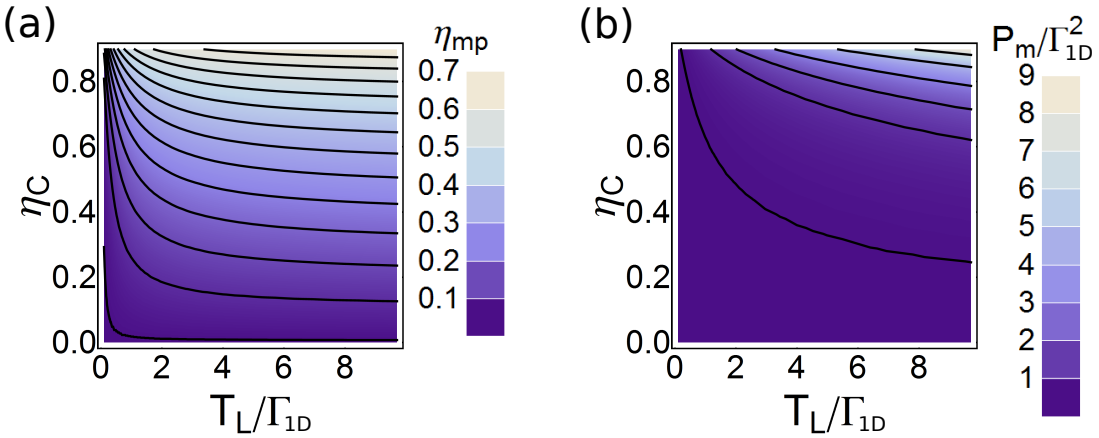


Figure 8.3.: Left: the efficiency at maximum power for vanishing interaction $U = 0$ as a function of T_L/Γ_{1D} and η_C. Right: the same for maximum power. Contour lines are shown.

efficiency η^{max} at maximum power in dependence of η_C for different Γ_{1D}. Up to intermediate values of $\eta_C \approx 0.5$ the Curzon-Ahlborn efficiency (η_{CA}) describes the efficiency of the RLM with $\Gamma_{1D} \to 0$ very accurately. For all values of Γ_{1D} the efficiency found in the RLM remains below the upper bound η_{SS} found in [Sch08b]. The inset shows a comparison for $\Gamma_{1D} \to 0$ to the upper and lower bound (η_{YG}) proposed in [Yan12b] for such a setup. Within these bounds the RLM operates nearly optimal for all η_C.

Linear Response

We can reproduce the linear response results of [Mur08] by expanding Eqs. (8.2.15) and (8.2.16) to lowest order in $\Delta T/\Gamma_{1D}$ and V/Γ_{1D}. The currents in turn are given by the conductances with

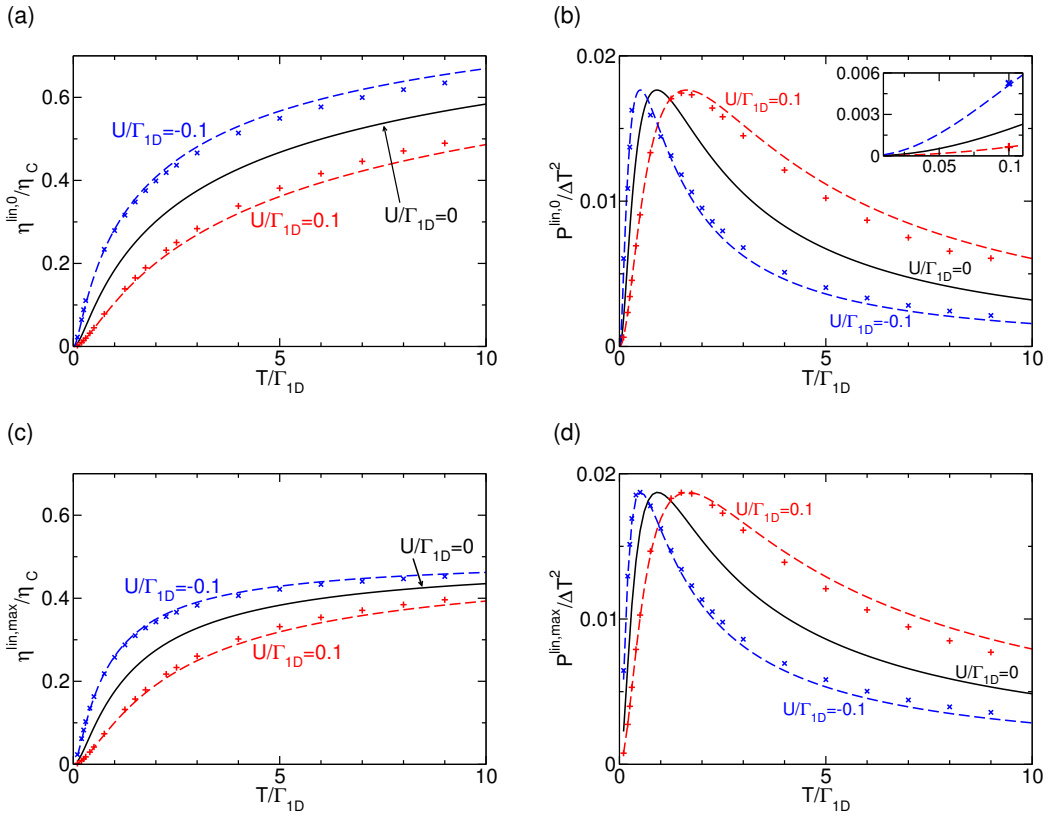


Figure 8.4.: Top: Linear response maximum efficiency (left) and the corresponding output power (right) for different interactions U as functions of T/Γ_{1D}. The lines follow from Eqs. (8.2.22)-(8.2.24) and (8.2.26) (for $U \neq 0$) while the symbols are numerical data obtained from the full flow equations. Inset: zoom-in of the regime $T/\Gamma_{1D} \ll 1$. Bottom: the same for the linear response maximum power output.

$T = T_L = T_R$, and the independent matrix elements ($G_{h,V} = TG_{c,\Delta T}$) can be written as

$$G_{c,V} = \frac{\Gamma_{1D}}{8\pi^2 T}\left[\psi\left(1, \frac{\pi + w}{2\pi}\right) + \text{c.c.}\right], \tag{8.2.22}$$

$$G_{c,\Delta T} = -\frac{i\Gamma_{1D}}{8\pi^2 T}\left[w\,\psi\left(1, \frac{\pi + w}{2\pi}\right) - \text{c.c.}\right], \tag{8.2.23}$$

$$G_{h,\Delta T} = \frac{\Gamma_{1D}}{2\pi}\left(\frac{\Gamma_{1D}}{T} - \frac{1}{4\pi}\left[w^2\,\psi\left(1, \frac{\pi + w}{2\pi}\right) + \text{c.c.}\right]\right), \tag{8.2.24}$$

with the trigamma function $\psi(1, z)$ and $w = (\Gamma_{1D} + i\epsilon)/T$. Considering the limit $\Gamma_{1D} \to 0$, independent of $\epsilon \neq 0$, one finds $ZT \sim 1/\Gamma_{1D}$ [Mur08] and thus with Eq. (8.1.14) finally $\eta^{\text{lin},0} \to \eta_C$ [Esp09]. Furthermore, $G_{h,\Delta T} \sim \Gamma_{1D}$ and $P^{\text{lin},0} \to 0$. For maximum power output from $ZT \sim 1/\Gamma_{1D}$ and Eq. (8.1.17) follows that in the limit $\Gamma_{1D} \to 0$, $\eta^{\text{lin},max} \to \eta_{CA}$ [Esp09].

For $\Gamma_{1D} > 0$ we numerically maximize η (in addition) with respect to ϵ using Eqs. (8.2.22)-(8.2.24) [Mur08]. The resulting efficiency $\eta^{\text{lin},0}$ and power at maximum efficiency $P^{\text{lin},0}$ as functions of T/Γ_{1D} are shown in the top panel of Fig. 8.4. As shown above $\Gamma_{1D} \to 0$, that is large T/Γ_{1D}, implies $\eta^{\text{lin},0} \to \eta_C$ and $P^{\text{lin},0}/\Delta T^2$ vanishes. The latter also vanishes for $T/\Gamma_{1D} \to 0$ and is thus a non-monotonic function with a maximum at $T \approx \Gamma_{1D}$. Our calculations show that for small T the level energy at which optimal efficiency is reached approaches a constant. Expanding Eqs. (8.2.22)-(8.2.24) we then obtain $TG_{h,\Delta T} \sim T^2$ and $ZT \sim T^2$. Therefore, $P^{\text{lin},0}/\Delta T^2 \sim T^2$ (see the inset

of Fig. 8.4). The same can be done for optimizing the power output $P^{\mathrm{lin,max}}$ and the resulting efficiency $\eta^{\mathrm{lin,max}}$. This is depicted in the lower panel of Fig. 8.4.

8.2.3 IRLM: $U \neq 0$

As discussed ($\rightarrow$ Section 8.2) the main effect of the two-particle interaction can be condensed in a renormalization of the hybridization $\Gamma_{1D}/2$ to the individual reservoirs. For the left reservoir the renormalization flow is cut off by the largest of the energy scales $|\epsilon - \mu_L|$, T_L, and the total hybridization Γ_{1D}; for the right one can simply replace the index $L \rightarrow R$ [Kar10d, Kar10b, Ken12a]. This entails a power-law scaling

$$\Gamma_{1D}^{\mathrm{ren}}/\Gamma_{1D} \sim (s/\Gamma)^{-\nu(U)}, \tag{8.2.25}$$

with the corresponding largest scale s (still much smaller than Γ) and the U-dependent exponent ν. To leading order[8] one finds $\nu(U) = 2U/(\pi\Gamma)$ [Sch80a, Bor07, Doy07, Kar10d, And11b, Kar10b, Ken12a]. This interaction induced effect cannot be treated by perturbative means (in either U or Γ_{1D}). In a general non-equilibrium setup $\Gamma_{1D,L}^{\mathrm{ren}} \neq \Gamma_{1D,R}^{\mathrm{ren}}$ even in the case of equal bare hybridizations, because of the temperature bias and voltage applied across the junction. From the knowledge of the renormalization one can derive very good approximations to the observables. We consider the linear response ($V, \Delta T \rightarrow 0$) charge conductance G_c as a function of ϵ close to the resonance (at $\epsilon = 0$) and $T = 0$ [Boh07, Kar10d, And11b]. The largest scale cutting off the renormalization group flow of the hybridizations is then Γ_{1D} itself. Plugging this into Eq. (8.2.25) one finds that G_c has the width

$$\Gamma_{1D}^{\mathrm{ren}} = W = \Gamma_{1D} \left(\frac{\Gamma_{1D}}{\Gamma}\right)^{-2U/(\pi\Gamma)}, \tag{8.2.26}$$

which defines the emergent energy scale W. The resonance becomes wider for weak (to intermediate [Boh07]) repulsive interactions while it narrows for attractive ones. To illustrate how $\Gamma_{1D}^{\mathrm{ren}}$ changes when two or more of the energy scales are of the same order [Kar10d, Kar10b, Ken12a] we consider $T \gtrapprox W$. Then, $\Gamma_{1D}^{\mathrm{ren}} \approx W(T/W)^{-2U/(\pi\Gamma)}$; see Fig. 8.1. Since $|U|/\Gamma \ll 1$ the correction to W is of order one as long as T does not exceed W by several orders of magnitude. In the following part this will become crucial.

Linear Response

We begin with the discussion of the linear response results of correlation effects on the efficiency and power. The symbols in the top panels of Fig. 8.4 show the maximum efficiency $\eta_{\mathrm{lin},0}$ (maximized with respect to V and ϵ) as well as the power at maximum efficiency $P^{\mathrm{lin},0}$ for $U/\Gamma = \pm 0.1$ obtained by numerically integrating the renormalization group equations and computing the charge and thermal currents [9]. For weak repulsive interactions $\eta^{\mathrm{lin},0}$ is reduced compared to the non-interacting result, while it is increased for weak attractive ones. Depending on the temperature regime considered the interaction enhances or reduces $P^{\mathrm{lin},0}$. These results can be understood analytically by employing the above discussed energy scale dependent renormalization of the resonance width. For $U = 0$ the level energy ϵ at which the maximum efficiency is reached is of the order of a few T at large T [Mur08] while it saturates at a constant of order Γ_{1D} for small T. This remains true for small $|U|$. Thus Eq. (8.2.26) gives a very good estimate of the renormalized hybridization for all temperatures shown in Fig. 8.4. This motivates the approximation of replacing Γ_{1D} in the non-interacting expressions Eqs. (8.2.22)-(8.2.24) for the charge and heat currents by the renormalized one W Eq. (8.2.26). The corresponding results for $\eta^{\mathrm{lin},0}$ and $P^{\mathrm{lin},0}$ are depicted as dashed lines in Fig. 8.4. As expected they show excellent agreement with the numerical data. The deviations at $T/\Gamma_{1D} \gtrapprox 1$ are consistent with the finite T correction to W discussed above. Very similar results are obtained for operating at maximum power [bottom panels of Fig. 8.4].

[8] Higher orders are not controlled by out current approach.

[9] For $U \neq 0$ the Landauer-Büttiker formulas for the currents can in general not be used anymore. One has to resort to the more general approach of Ref. [Mei92, Wan06, Oja08] given in Eqs. (4.1.72) and (4.1.79) . However, in the lowest order truncation scheme used here the expressions for the currents within the latter can simply be dressed with the renormalized single-particle parameters [Kar10a, Ken12a]

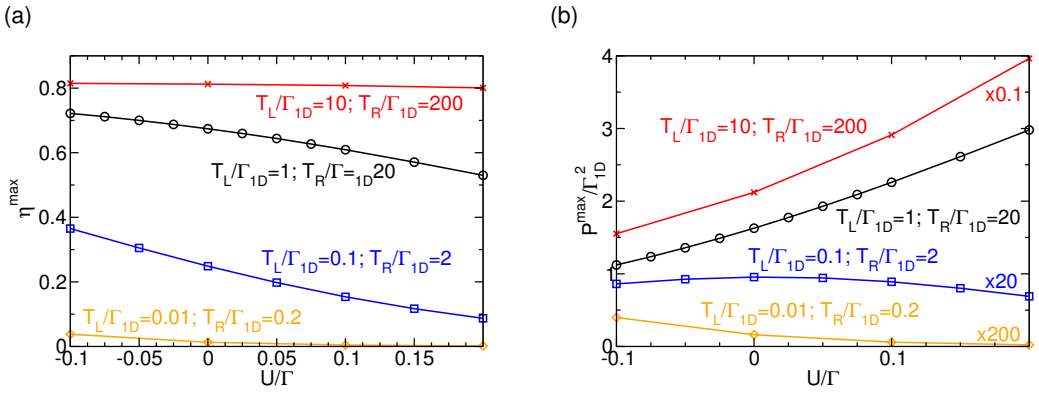


Figure 8.5.: Efficiency at maximum power (a) and the maximum power (b) for different sets of $T_{L/R}$ as functions of U. The lines are guide to the eyes. The data are scaled by the given factors.

Within the FRG approach we are restricted to $|U| \ll 1$ we cannot access the regime of large interactions, but it is known that Γ_{1D}^{ren} is a nonmonotonic function of $U > 0$ and for large repulsive interactions one finds $\Gamma_{1D}^{ren} < \Gamma_{1D}$ [Boh07, Bor07]. This follows from a second order term $\sim -U^2$ which dominates for $U > 1$ and changes the sign of the exponent ν [Bor07]. Based on our above results it is thus reasonable to assume that for large repulsive interactions η will be larger than in the non-interacting case. It would be very interesting to explicitly verify this using a method complementary to the FRG.

Non-Equilibrium

We next turn to the non-equilibrium case. Figure 8.5 depicts the U dependence of the maximum power P^{max} and the efficiency at maximum power η^{max} for different combinations of $T_{L/R}$. In analogy to the maximum efficiency in linear response η^{max} is a decreasing function of U. A similar analogy to the linear response results for $P^{lin,max}$ (Fig. 8.4) holds for the maximum power P^{max}. It is a decreasing function of U for temperatures $T_{L/R}$ smaller than Γ_{1D} and an increasing one for $T_{L/R}/\Gamma_{1D} \gg 1$. For intermediate temperatures it is a nonmonotonic function. One can also consider the U dependences of the maximum efficiency (with respect to V and ϵ) and the corresponding output power beyond the linear response regime. They are, however, qualitatively similar to the results for η^{max} and P^{max} shown in Fig. 8.5.

8.2.4 Application: Charging

We have demonstrated that the renormalization of the linewidth leads to a very rich behavior of the power output. Generally, one can trade power output for efficiency or vice versa, but what happens if we are interested in neither maximizing the one or the other, but rather call for a certain minimum output power, e.g. to charge a battery, but leave the engine otherwise unconstrained? Can one utilize the two-particle interaction U in such a – more applied – scenario to increase efficiency? We can actually show that under this constrain the decrease of the efficiency for repulsive interactions, generally found above, can be overcome. We exploit an appropriate temperatures regime $T_{L/R}$ where the maximum power increases with U, which in turn can be traded for efficiency in this charging scenario. For fixed $T_{L/R}$ we proceed as follows: (1) as our lower bound of the power P_b we for simplicity take the maximum power at $U = 0$, $P_b = P^{max}(U = 0)$. (2) Varying ϵ and V we then search for the largest efficiency $\eta^{>}$ at fixed $U > 0$ with $P \geq P_b$. This is demonstrated in the top panel of Fig. 8.6. We show the output power P as a function of ϵ and V for $U/\Gamma = 0.1$ as well as the constrain $P = P_b$ as a transparent blue plane. Optimizing for P would yield the point P^{max} indicated by a red dot. But now we are actually not interested in this point any more, but rather in the maximum efficiency which can be achieved, under the condition that the output power does not drop below the transparent blue plane. This gives the optimal operating point $P^{>}$ indicated by

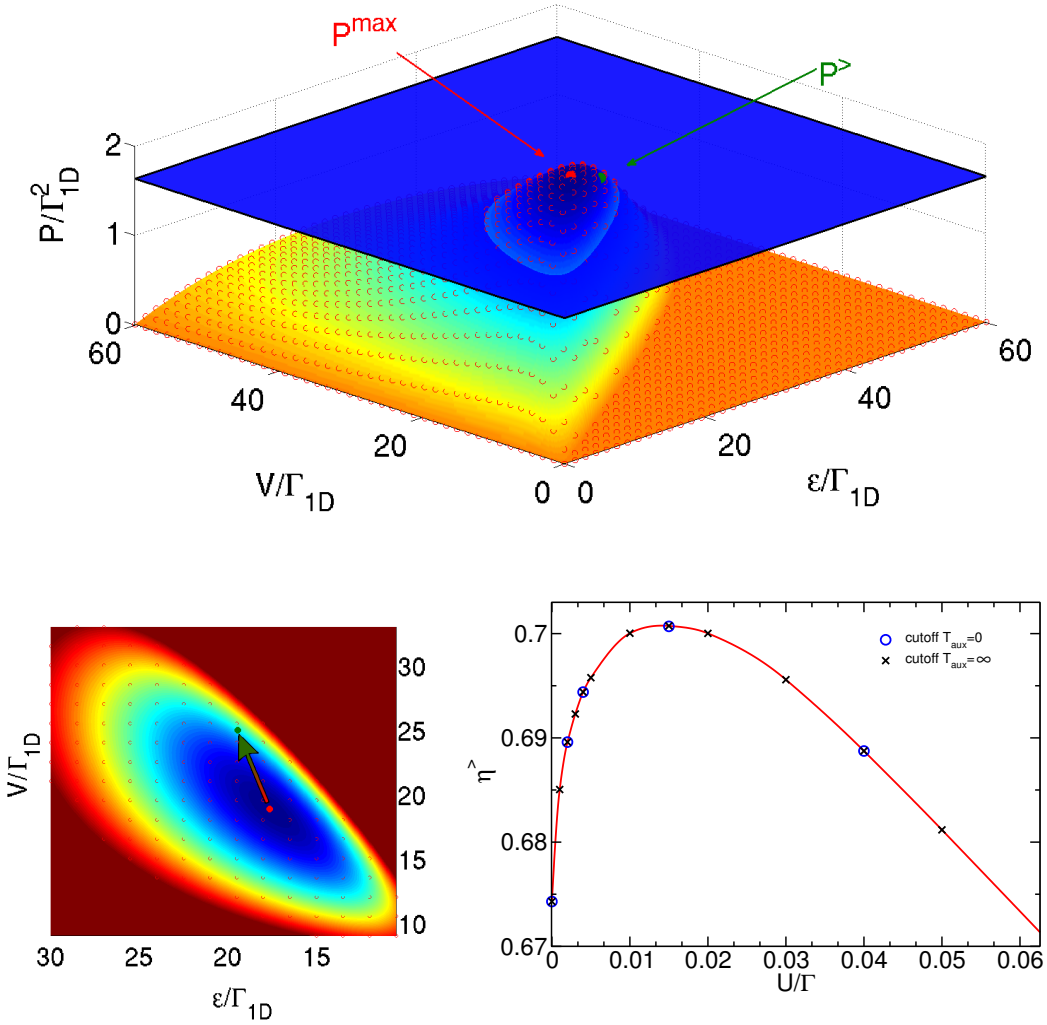


Figure 8.6.: (Color online) Interaction U dependence of the largest efficiency obtainable with $P \geq P_b$ for $T_L/\Gamma_{1D} = 1$ and $T_R/\Gamma_{1D} = 20$ (for details see the text). The line is an Akima spline interpolating between the computed data points (crosses: $T_{aux} = \infty$; circles: $T_{aux} = 0$). The efficiency can be raised by a few percent by turning on a small repulsive interaction.

a green dot. A contour plot of this is depicted in the lower left of Fig. 8.6. In this plot all points below the constrain are coloured deep red. Under the given constrain the optimal operating point shifts from P^{max} to $P^{>}$ indicated by an arrow. Note that $P^{>}$ does however not lie at an intersection point with the plane $P = P_b$. As this is a numerically demanding procedure – remind that for every parameter set the currents $I_{c/h}$ have to be computed numerically solving coupled differential flow equations – we restrict ourselves to one of the temperature sets of Fig. 8.5 namely $T_L/\Gamma_{1D} = 1$ and $T_R/\Gamma_{1D} = 20$. The U dependence of $\eta^{>}$ is shown in the lower right of Fig. 8.6. Within this setup the efficiency first increases with increasing interaction at small U until at larger U the generic decrease of the efficiency with increasing U takes over leading to a maximum at $U/\Gamma \approx 0.005$. It is known [Kar10d, Kar10b] that the FRG approached employed here is quantitatively reliable up to significantly larger U. To demonstrate the robustness of the subtle efficiency gain, which in addition to the cases studied before involves heat transport we considered two different cutoff procedures: the reservoir cutoff with temperature $T_{aux} = \infty$ in the auxiliary leads, used also for the other results presented here, as well as with $T_{aux} = 0$ [Kar10d] (for technical details → Section 4.4). Due to the

excellent agreement, we expect that the precise value of the few percent optimal efficiency gain and its position are only very weakly affected by higher order terms not captured by us.

8.3 Thermoelectric Transport in the AHM

As a next step to a more realistic model of electronic transport in solid-state physics we include the spin as well as phononic degree of freedom within the AHM (→ Section 3.4). We concentrate on the case where the details of the band structure of the electronic reservoirs are unimportant (wideband limit → Section 4.1.2). The induced hybridization is denoted by $\Gamma = \sum_\alpha \pi|\gamma_\alpha|^2\rho$. The AHM as posed in Section 3.4 displays a wealth of different parameters (taking Γ as the unit of energy those are ϵ, B, U, λ and ω). This renders the AHM a natural candidate for a FRG treatment, which is very fast and thus parameter spaces can be scanned rather quickly. The downside being however that already the large U-limit (Kondo-limit) of the simpler SIAM is difficult to access. We will focus on an equilibrium analysis and reference non-equilibrium results from [Laa14, Laa] only.

Other approaches to the AHM under the assumption of a bias voltage driven non-equilibrium steady-state, include studies using real-time diagrammatics [Kön96], rate equations [Bra03, Mit04, Koc05], and slave-boson techniques with the non-crossing approximation [Rou13]. In all these cases the double occupation of the dot was forbidden explicitly by considering the limit of an infinitely strong Coulomb repulsion. Recently, the case of finite Coulomb repulsion was also addressed using the imaginary-time non-equilibrium formalism [Han06, Han10].

8.3.1 First order perturbation theory

To gain first insights into the problem we start with a simple perturbative approach. This helps also to judge the quality of the more sophisticated FRG approach introduced later. We concentrate on $U = B = 0$ and small $U_{\text{epe}}/\Gamma = 2\lambda^2/(\omega_0\Gamma)$ as this is the case we want to compare to the FRG results. The two contributions (Hartree and Fock) yield two separable contributions to the retarded self-energy in first order perturbation theory. The Hartree part is frequency independent,

$$\Sigma^{\text{R}}_{\text{H}\,\sigma'\sigma} = -\delta_{\sigma'\sigma} U_{\text{epe}}(\bar{n}_\uparrow + \bar{n}_\downarrow), \tag{8.3.1}$$

where $\bar{n}_\sigma$ denotes the average occupation of the spin level σ in the non-interacting dot. It appears to be reasonable to evaluate this contribution self-consistently as motivated strictly for equilibrium in section 6.2 in order to maintain particle-hole symmetry. The self-consistency equation reads

$$\Sigma^{\text{R}}_{\text{H},\sigma'\sigma} = \Sigma^{\text{R}}_{\text{H}}\delta_{\sigma'\sigma} = -U_{\text{epe}}\delta_{\sigma'\sigma}\frac{2}{\pi}\int d\omega\, n_{\text{eff}}(\omega)\frac{\Gamma}{\left(\omega - \tilde{\epsilon} - \Sigma^{\text{R}}_{\text{H}}\right)^2 + \Gamma^2}, \tag{8.3.2}$$

where we used

$$n_{\text{eff}}(\omega) = \frac{1}{2}\left[f_{\text{L}}(\omega) + f_{\text{R}}(\omega)\right]. \tag{8.3.3}$$

For $T_{\text{L}} = T_{\text{R}} = 0$ follows

$$\Sigma^{\text{R}}_{\text{H}} = U_{\text{epe}}\left(-1 + \frac{2}{\pi\Gamma}\sum_r \Gamma_r \arctan\frac{\tilde{\epsilon} + \Sigma^{\text{R}}_{\text{H}} - \mu_r}{\Gamma}\right). \tag{8.3.4}$$

For $\mu_{\text{L}} = \mu_{\text{R}} = \mu$ this equation has an unique solution for $U_{\text{epe}}/\Gamma \leq \pi/2$. At $\tilde{\epsilon} = \mu$ one finds $\Sigma^{\text{R}}_{\text{H}}(\tilde{\epsilon} = \mu) = -U_{\text{epe}}$. For $U_{\text{epe}}/\Gamma > \pi/2$ and $\tilde{\epsilon}$ sufficiently close to μ the equation has three solutions, which leads to a hysteresis of $\Sigma^{\text{R}}_{\text{H}}(\tilde{\epsilon})$. We can thus only treat $U_{\text{epe}}/\Gamma \leq \pi/2$.

For calculating the Fock term we choose the free propagation to include the self-consistent Hartree contribution determined above. For $T_{\text{L}} = T_{\text{R}} = 0$ the resulting can be evaluated analytically, yielding

$$\begin{aligned}\Sigma^{\text{R}}_{\text{F},\sigma'\sigma} = \Sigma^{\text{R}}_{\text{F}}\delta_{\sigma'\sigma} = \frac{\lambda^2}{2}\Bigg\{&\sum_{s=\pm1}\frac{1}{\omega + s\omega_0 - \bar{\epsilon} + \text{i}\Gamma} - \frac{1}{2}\sum_\alpha\sum_{s,s'=\pm1}\frac{s}{\omega + s\omega_0 - \bar{\epsilon} + \text{i}s'\Gamma}\\ &\times\left[\frac{1}{\pi}\arctan\frac{\bar{\epsilon} - \mu_\alpha}{\Gamma} + \frac{s'}{2}\text{sign}(\omega + s\omega_0 - \mu_\alpha) + \frac{\text{i}s'}{\pi}\ln\left|\frac{\omega + s\omega_0 - \mu_\alpha + \text{i}\eta}{\bar{\epsilon} - \mu_\alpha - \text{i}s'\Gamma}\right|\right]\Bigg\},\end{aligned} \tag{8.3.5}$$

and

$$\bar{\epsilon} = \tilde{\epsilon} + \Sigma_{\mathrm{H}}^{\mathrm{R}}. \tag{8.3.6}$$

The total retarded self-energy is thus

$$\Sigma_{1\mathrm{PT}}^{\mathrm{R}}(\omega) = \Sigma_{\mathrm{H}}^{\mathrm{R}} + \Sigma_{\mathrm{F}}^{\mathrm{R}}(\omega). \tag{8.3.7}$$

Note that $\Sigma_{\mathrm{F}}^{\mathrm{R}}(\omega)$ diverges logarithmically at $\omega = \pm\omega_0 + \mu_\alpha = \pm\omega_0 \pm \epsilon/2$. Consequently, the spectral density $\rho(\omega) = -1/\pi \mathrm{Im}[G^{\mathrm{R}}(\omega)]$ in first order perturbation theory vanishes at these frequencies. An exception is the particle-hole symmetric situation with $\epsilon = 2\omega_0$ where this is not the case due to a cancellation of these logarithmic divergencies.

8.3.2 AHM: FRG Analysis

It turns out that including the phonons within a FRG treatment is in no way more complicated than tackling the simpler SIAM if a second order truncation scheme is employed. The latter was done in [Kar08]. From there we also borrow the parametrization of the two-particle vertex

$$\begin{aligned}\gamma_2^{\Lambda}(\omega_1'\sigma_1\omega_2'\sigma_2';\omega_1\sigma_1\omega_2\sigma_2) &= \delta(\omega_1' + \omega_2' - \omega_1 - \omega_2) \\ &\times\Big[\quad U_{\uparrow}^{\Lambda}\,(\omega_1'\omega_2';\omega_1\omega_2)\delta_{\sigma_1'\uparrow}\delta_{\sigma_2'\uparrow}\delta_{\sigma_1\uparrow}\delta_{\sigma_2\uparrow} \;+\; U_{\downarrow}^{\Lambda}\,(\omega_1'\omega_2';\omega_1\omega_2)\delta_{\sigma_1'\downarrow}\delta_{\sigma_2'\downarrow}\delta_{\sigma_1\downarrow}\delta_{\sigma_2\downarrow} \\ &\quad + U_{\uparrow\downarrow}^{\Lambda}(\omega_1'\omega_2';\omega_1\omega_2)\delta_{\sigma_1'\uparrow}\delta_{\sigma_2'\downarrow}\delta_{\sigma_1\uparrow}\delta_{\sigma_2\downarrow} \;-\; U_{\uparrow\downarrow}^{\Lambda}(\omega_2'\omega_1';\omega_1\omega_2)\delta_{\sigma_1'\downarrow}\delta_{\sigma_2'\uparrow}\delta_{\sigma_1\uparrow}\delta_{\sigma_2\downarrow} \\ &\quad - U_{\uparrow\downarrow}^{\Lambda}(\omega_1'\omega_2';\omega_2\omega_1)\delta_{\sigma_1'\uparrow}\delta_{\sigma_2'\downarrow}\delta_{\sigma_1\downarrow}\delta_{\sigma_2\uparrow} \;+\; U_{\uparrow\downarrow}^{\Lambda}(\omega_2'\omega_1';\omega_2\omega_1)\delta_{\sigma_1'\downarrow}\delta_{\sigma_2'\uparrow}\delta_{\sigma_1\downarrow}\delta_{\sigma_2\uparrow}\quad\Big],\end{aligned} \tag{8.3.8}$$

which accounts explicitly for conserved energy and spin. It has proven very useful [Kar08] to rewrite the three coupling functions in terms of the three bosonic frequencies

$$\nu_1 = \omega_1' + \omega_2', \qquad \nu_2 = \omega_1' - \omega_1, \qquad \nu_3 = \omega_2' - \omega_1. \tag{8.3.9}$$

Now it is easy to see, that integrating out the phonons exactly [Tsa05], leads to a shift in the initial conditions compared to the SIAM ($\lambda \to 0 \Rightarrow U_{\mathrm{epe}} \to 0$)

$$\Sigma(i\omega)_{\sigma}^{\Lambda\to\infty} = \frac{U}{2} - U_{\mathrm{epe}}, \tag{8.3.10}$$

$$U_{\sigma}^{\Lambda\to\infty}(\nu_1,\nu_2,\nu_3) = 2U_{\mathrm{epe}}\left(\frac{1}{1+(\nu_3/\omega_0)^2} - \frac{1}{1+(\nu_2/\omega_0)^2}\right), \tag{8.3.11}$$

$$U_{\uparrow\downarrow}^{\Lambda\to\infty}(\nu_1,\nu_2,\nu_3) = U - \frac{U_{\mathrm{epe}}}{1+(\nu_2/\omega_0)^2}, \tag{8.3.12}$$

$$\tag{8.3.13}$$

while the FRG flow equations remain unchanged. To keep this thesis self-contained they are reiterated[10] from [Kar08]:

$$\partial_\Lambda \Sigma_{\sigma}^{\Lambda}(i\omega) = -T\sum_{i\Omega} e^{i\Omega\eta}\left[S_{\sigma}^{\Lambda}(i\Omega)U_{\sigma}^{\Lambda}(\Omega+\omega,0,\Omega-\omega) + S_{\bar{\sigma}}^{\Lambda}(i\Omega)U_{\uparrow\downarrow}^{\Lambda}(\Omega+\omega,0,\pm\Omega\mp\omega)\right], \tag{8.3.14}$$

$$\begin{aligned}\partial_\Lambda U_{\sigma}^{\Lambda}(\nu_1,\nu_2,\nu_3) = -T\sum_{i\omega}\Big[&\\ &P_{\sigma\sigma}^{\Lambda}(\omega,\nu_1-\omega)U_{\sigma}^{\Lambda}(\nu_1,\omega+\nu_{-++},\nu_{+++}-\omega)U_{\sigma}^{\Lambda}(\nu_1,\omega+\nu_{-+-},\omega+\nu_{--+}) \\ +\Big\{ &P_{\sigma\sigma}^{\Lambda}(\omega,\nu_2+\omega)U_{\sigma}^{\Lambda}(\omega+\nu_{++-},\nu_2,\omega+\nu_{-++})U_{\sigma}^{\Lambda}(\omega+\nu_{+++},-\nu_2,\omega+\nu_{-+-}) \\ &+P_{\bar{\sigma}\bar{\sigma}}^{\Lambda}(\omega,\nu_2+\omega)U_{\uparrow\downarrow}^{\Lambda}(\omega+\nu_{++-},\pm\nu_2,\pm\omega\pm\nu_{-++})U_{\uparrow\downarrow}^{\Lambda}(\omega+\nu_{+++},\mp\nu_2,\pm\omega\pm\nu_{-+-}) \\ &+(\nu_2\to-\nu_2,\nu_3\to-\nu_3) - \left[(\nu_2\leftrightarrow\nu_3)+(\nu_2\to-\nu_2,\nu_3\to-\nu_3)\right]\Big\}\Big],\end{aligned} \tag{8.3.15}$$

[10] we correct some very minor typographic errors.

and

$$\begin{aligned}
&\partial_\Lambda U^\Lambda_{\uparrow\downarrow}(\nu_1,\nu_2,\nu_3)\\
&= -T\sum_{i\omega}\Big[-P^\Lambda_{\uparrow\downarrow}(\omega,\nu_1-\omega)\quad U^\Lambda_{\uparrow\downarrow}(\nu_1,\omega+\nu_{-++},\nu_{+++}-\omega)\quad U^\Lambda_{\uparrow\downarrow}(\nu_1,\nu_{++-}-\omega,\nu_{+-+}-\omega)\\
&\qquad -P^\Lambda_{\downarrow\uparrow}(\omega,\nu_1-\omega)\quad U^\Lambda_{\uparrow\downarrow}(\nu_1,\nu_{+++}-\omega,\omega+\nu_{-++})\quad U^\Lambda_{\uparrow\downarrow}(\nu_1,\omega+\nu_{-+-},\omega+\nu_{--+})\\
&\qquad +P^\Lambda_{\uparrow\uparrow}(\omega,\nu_2+\omega)\quad U^\Lambda_{\uparrow}(\omega+\nu_{++-},\nu_2,\omega+\nu_{-++})\quad U^\Lambda_{\uparrow\downarrow}(\omega+\nu_{+++},\nu_2,\nu_{+-+}-\omega)\\
&\qquad +P^\Lambda_{\downarrow\downarrow}(\omega,\nu_2+\omega)\quad U^\Lambda_{\downarrow}(\omega+\nu_{+++},-\nu_2,\omega+\nu_{-+-})\quad U^\Lambda_{\uparrow\downarrow}(\omega+\nu_{++-},\nu_2,\omega+\nu_{-++})\\
&\qquad +P^\Lambda_{\uparrow\uparrow}(\omega,-\nu_2+\omega)\quad U^\Lambda_{\uparrow}(\omega+\nu_{+--},\nu_2,\omega+\nu_{---})\quad U^\Lambda_{\uparrow\downarrow}(\omega+\nu_{+-+},\nu_2,\nu_{+++}-\omega)\\
&\qquad +P^\Lambda_{\downarrow\downarrow}(\omega,-\nu_2+\omega)\quad U^\Lambda_{\downarrow}(\omega+\nu_{+-+},-\nu_2,\omega+\nu_{---})\quad U^\Lambda_{\uparrow\downarrow}(\omega+\nu_{+--},\nu_2,\omega+\nu_{--+})\\
&\qquad -P^\Lambda_{\uparrow\downarrow}(\omega,\nu_3+\omega)\quad U^\Lambda_{\uparrow\downarrow}(\omega+\nu_{+-+},\omega+\nu_{-++},\nu_3)\quad U^\Lambda_{\uparrow\downarrow}(\omega+\nu_{+++},\nu_{++-}-\omega,\nu_3)\\
&\qquad -P^\Lambda_{\downarrow\uparrow}(\omega,-\nu_3+\omega)\quad U^\Lambda_{\uparrow\downarrow}(\omega+\nu_{++-},\nu_{+++}-\omega,\nu_3)\quad U^\Lambda_{\uparrow\downarrow}(\omega+\nu_{+--},\omega+\nu_{-+-},\nu_3)\Big],
\end{aligned}\tag{8.3.16}$$

with

$$\bar{\uparrow}=\downarrow,\quad \bar{\downarrow}=\uparrow,\quad \nu_{\pm\pm\pm}=\frac{\pm\nu_1\pm\nu_2\pm\nu_3}{2},\quad P^\Lambda_{\sigma_1\sigma_2}(\omega_1,\omega_2)=S^\Lambda_{\sigma_1}(i\omega_1)G^\Lambda_{\sigma_2}(i\omega_2)\,. \tag{8.3.17}$$

and, as we are using the same sharp cut-off scheme in equilibrium

$$G^\Lambda_{\sigma,0}(i\omega)=G_{\sigma,0}(i\omega)\Theta_\Lambda(|\omega|-\Lambda),\ \Theta_\Lambda(|\omega|-\Lambda)=\begin{cases}0 & -\pi T>|\omega|-\Lambda\\ 1/2+\frac{|\omega|-\Lambda}{2\pi T} & -\pi T\le|\omega|-\Lambda\le\pi T\\ 1 & |\omega|-\Lambda>\pi T\,.\end{cases} \tag{8.3.18}$$

Because only the initial conditions change with respect to the SIAM at this point we note two important consequences. (a) It is now trivial to see, that for $U_{\text{epe}}=\text{const}$ and $\omega_0\to\infty$ we reproduce the negative-U SIAM with $U=-U_{\text{epe}}$. (b) The initial conditions still obey all symmetries found in the SIAM and thus those symmetries are still fulfilled throughout the entire flow. Explicitly those are [Kar08, Kar10a]

- anti-symmetry:

$$U^\Lambda_\sigma(\nu_1,\nu_2,\nu_3)=U^\Lambda_\sigma(\nu_1,-\nu_2,-\nu_3)=-U^\Lambda_\sigma(\nu_1,\nu_3,\nu_2). \tag{8.3.19}$$

- time-reversal symmetry:

$$U^\Lambda_\sigma(\nu_1,\nu_2,\nu_3)=U^\Lambda_\sigma(\nu_1,-\nu_2,\nu_3)\,,\qquad U^\Lambda_{\uparrow\downarrow}(\nu_1,\nu_2,\nu_3)=U^\Lambda_{\uparrow\downarrow}(\nu_1,-\nu_2,\nu_3). \tag{8.3.20}$$

- symmetry under complex conjugation:

$$G_\sigma(-i\omega)=[G_\sigma(i\omega)]^*\,,\qquad \Sigma_\sigma(-i\omega)=[\Sigma_\sigma(i\omega)]^*\,, \tag{8.3.21}$$

$$U^\Lambda_\sigma(\nu_1,\nu_2,\nu_3)=\left[U^\Lambda_\sigma(-\nu_1,\nu_2,\nu_3)\right]^*\,,\qquad U^\Lambda_{\uparrow\downarrow}(\nu_1,\nu_2,\nu_3)=\left[U^\Lambda_{\uparrow\downarrow}(-\nu_1,\nu_2,-\nu_3)\right]^*\,. \tag{8.3.22}$$

and depending on the parameters

- particle-hole symmetry ($\epsilon=0$; with associated spin flip)

$$-[G_\uparrow(i\omega)]^*=G_\downarrow(i\omega)\,,\qquad -[\Sigma_\uparrow(i\omega)]^*=\Sigma_\downarrow(i\omega)\,, \tag{8.3.23}$$

$$\left[U^\Lambda_\uparrow(\nu_1,\nu_2,\nu_3)\right]^*=U^\Lambda_\downarrow(\nu_1,\nu_2,\nu_3)\,,\qquad \left[U^\Lambda_{\uparrow\downarrow}(\nu_1,\nu_2,\nu_3)\right]^*=U^\Lambda_{\uparrow\downarrow}(\nu_1,-\nu_2,-\nu_3)\,, \tag{8.3.24}$$

- spin symmetry ($B = 0$)

$$G_\uparrow(i\omega) = G_\downarrow(i\omega)\,, \qquad \Sigma_\uparrow(i\omega) = \Sigma_\downarrow(i\omega)\,, \tag{8.3.25}$$

$$U^\Lambda_\uparrow(\nu_1,\nu_2,\nu_3) = U^\Lambda_\downarrow(\nu_1,\nu_2,\nu_3) = U^\Lambda_{\uparrow\downarrow}(\nu_1,\nu_2,\nu_3) - U^\Lambda_{\uparrow\downarrow}(\nu_1,\nu_3,\nu_2)\,, \tag{8.3.26}$$

$$U^\Lambda_{\uparrow\downarrow}(\nu_1,\nu_2,\nu_3) = U^\Lambda_{\uparrow\downarrow}(\nu_1,\nu_2,-\nu_3)\,. \tag{8.3.27}$$

- spin- and particle-hole symmetry ($\epsilon = B = 0$):

$$U^\Lambda_{\uparrow\downarrow}(\nu_1,\nu_2,\nu_3) \in \mathbb{R}\,, \qquad \Sigma_\sigma(i\omega) \in i\mathbb{R}\,. \tag{8.3.28}$$

In the following we will always use the perturbatively motivated approximate channel decomposition introduced in [Kar08], which consists in putting

$$\nu_{i\neq j} = 0 \tag{8.3.29}$$

in the terms proportional to $P^\Lambda(\omega, \pm\nu_j \pm \omega)$ on the right hand side of Eqs. (8.3.15) and (8.3.16). From this results an immense speed up in the numerics, because the two-particle vertex U^Λ is then no longer a function of three independent arguments but rather a sum of functions each depending on one variable ν_j only:[11]

$$U^\Lambda_{\uparrow\downarrow}(\nu_1,\nu_2,\nu_3) = U + U^\Lambda_1(\nu_1) + U^\Lambda_2(\nu_2) + U^\Lambda_3(\nu_3)\,, \tag{8.3.30}$$

and likewise for U^Λ_σ. Furthermore, we also implement the simple improvement to the flow equations of the two-particle vertex functions

$$S^\Lambda \to -\frac{dG^\Lambda}{d\Lambda} = S^\Lambda - G^\Lambda \frac{d\Sigma^\Lambda}{d\Lambda} G^\Lambda\,, \tag{8.3.31}$$

which helps obeying certain Ward identities [War50, Kat04].

Quick Reminder: The SIAM dilemma

Let us for a second retreat to the SIAM $\lambda = 0$ and review the dilemma that is encountered when a FRG ansatz is employed. In a very simple approximation where only the static part of the flow is kept [And08, Kar10a] one can already find an emergent exponentially small low energy scale for large-U in static quantities such as the spin susceptibility. For $T = \epsilon = B = 0$, within this simple treatment the large-U Kondo temperature is then found to be $T_K \propto \exp(-U/(\pi\Gamma))$, which exhibits exponential behavior, albeit with slightly wrong exponent[12]. In this approach "frequency independent" quantities (e.g. occupancies, conductances, ...) agree nicely to the exact results from Bethe ansatz [Ger00], which exhibit strong correlation physics. However, of course "frequency dependent observables" cannot be managed in an appropriate way (e.g. the dot spectral function $\rho(\omega)$ at $T = \epsilon = B = 0$ always is a Lorentzian of width 2Γ as for $U = 0$). It was thus reasonable to believe that including the frequency dependency of the flow, could lead to (a) and improvement of the Kondo temperature found and (b) that also "frequency dependent observables" can be addressed reasonably. It turned out that including the frequency dependency in the flow *destroys* the exponential behavior found in the simpler treatment[13]. Nonetheless, comparison to numerically exact NRG data showed that the FRG treatment (also employed in this thesis), although it does not exhibit the exponential behavior as discussed above, gives very accurate results upto intermediate U (e.g. upto values of $U/\Gamma \leqslant 5$ for $T = \epsilon = B = 0$) [Kar08, Kar10a]. This warning of course has to be kept in mind, when treating the AHM, which is expected to face similar difficulties. For the values of the interaction strength, where the FRG treatment remains valid, within this frequency dependent approach, "frequency dependent observables" can be calculated rather reliably. This is of course crucial for any thermoelectric transport study, where frequency dependency is key, because the conductances are determined by this dependency explicitly (as shown in the following section).

[11] This approximation maintains all symmetries outlined above.
[12] The exact value being $\pi/8 \approx 0.3927$ [compare Eq. (3.3.7)] instead of $1/\pi \approx 0.3183$.
[13] This behavior: power-law entailed in simpler approximation, but destroyed in the more sophisticated frequency dependent approach, actually also shows up in the IRLM discussed above [Kar10a].

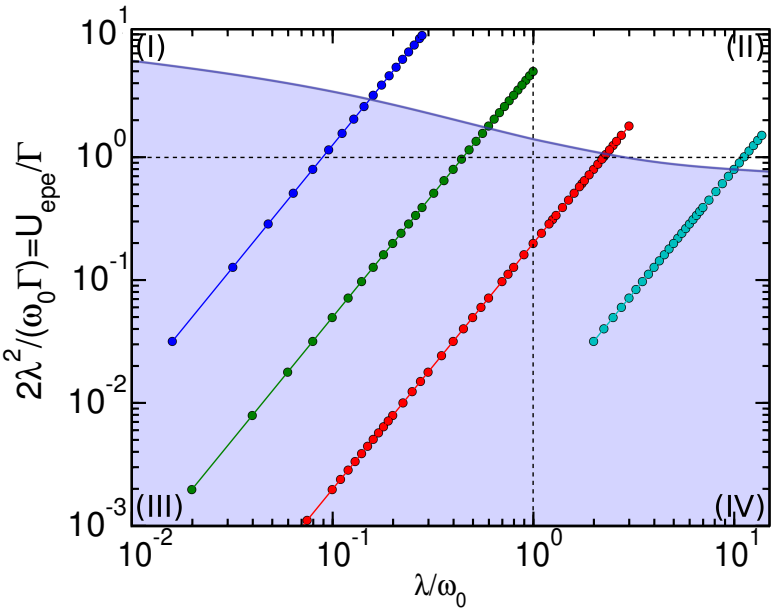


Figure 8.7.: Illustration of the division into four different parameter regimes: attractive single impurity Anderson model (I), extended anti-adiabatic (II), perturbative (III), and adiabatic (IV). The colored lines and data points correspond to those of Fig. 8.8. The shaded light-blue area roughly corresponds to the regime, where FRG renders reliable results.

Effective Mass

The effective mass

$$m^* = 1 - \left.\frac{d\Sigma(i\omega)}{d\omega}\right|_{i\omega=0} = \left.\frac{d\mathrm{Im}[G(i\omega)]}{d\omega}\right|_{i\omega=0} \propto \frac{1}{T_K} \in \mathbb{R}. \tag{8.3.32}$$

provides first insights into strongly correlated systems. At $\epsilon = B = 0$ in the context of our quantum dot it describes the inverse of the effective width of the spectral function if approximated by a Lorentzian around zero frequency

$$\begin{aligned}\rho_\sigma(\omega)\pi\Gamma = -\Gamma\ \mathrm{Im}\left[G^{\mathrm{R}}_\sigma(\omega)\right] &= -\Gamma\ \mathrm{Im}\left[\frac{1}{\omega + i\Gamma - \Sigma^{\mathrm{R}}(\omega)}\right] \\ &= -\Gamma\ \mathrm{Im}\left[\frac{1}{\omega + i\Gamma - (\Sigma^{\mathrm{R}}_\sigma(0) + \partial_\omega \Sigma^{\mathrm{R}}_\sigma(\omega)|_{\omega=0}\omega + \dots)}\right] \\ &\approx -\Gamma\ \mathrm{Im}\left[\frac{1}{m^*}\frac{1}{\omega + i\Gamma/m^*}\right] = \frac{(\Gamma/m^*)^2}{\omega^2 + (\Gamma/m^*)^2},\end{aligned} \tag{8.3.33}$$

where in the last step we have exploited the analytic structure of G^{R} around $\omega = 0$. As the effective mass is determined by the frequency dependency of the self-energy (being unity in any static treatment) and is particularly easy to access within the equilibrium Green's functions approach[14] we utilize it to benchmark our FRG results. Since the AHM is rather difficult to treat (besides of the limits addressed analytically → Section 3.4.2) we will check for consistency with our simple first order perturbation theory results as well as another FRG ansatz set up in Keldysh space [Laa14, Laa].

We will focus on the case $U = 0$ first where the effects of the coupling to the phonon is perfectly isolated from the "bare" electron–electron part. To identify the different parameter regimes we first borrow a classification found in the literature for the spinless resonant level model with a local phonon mode, which commonly uses the ratio ω_0/Γ [Eid13]: For the *adiabatic* regime, $\omega_0/\Gamma \ll 1$,

[14] Particularly there is no need for an ill-defined analytic continuation by numerical means.

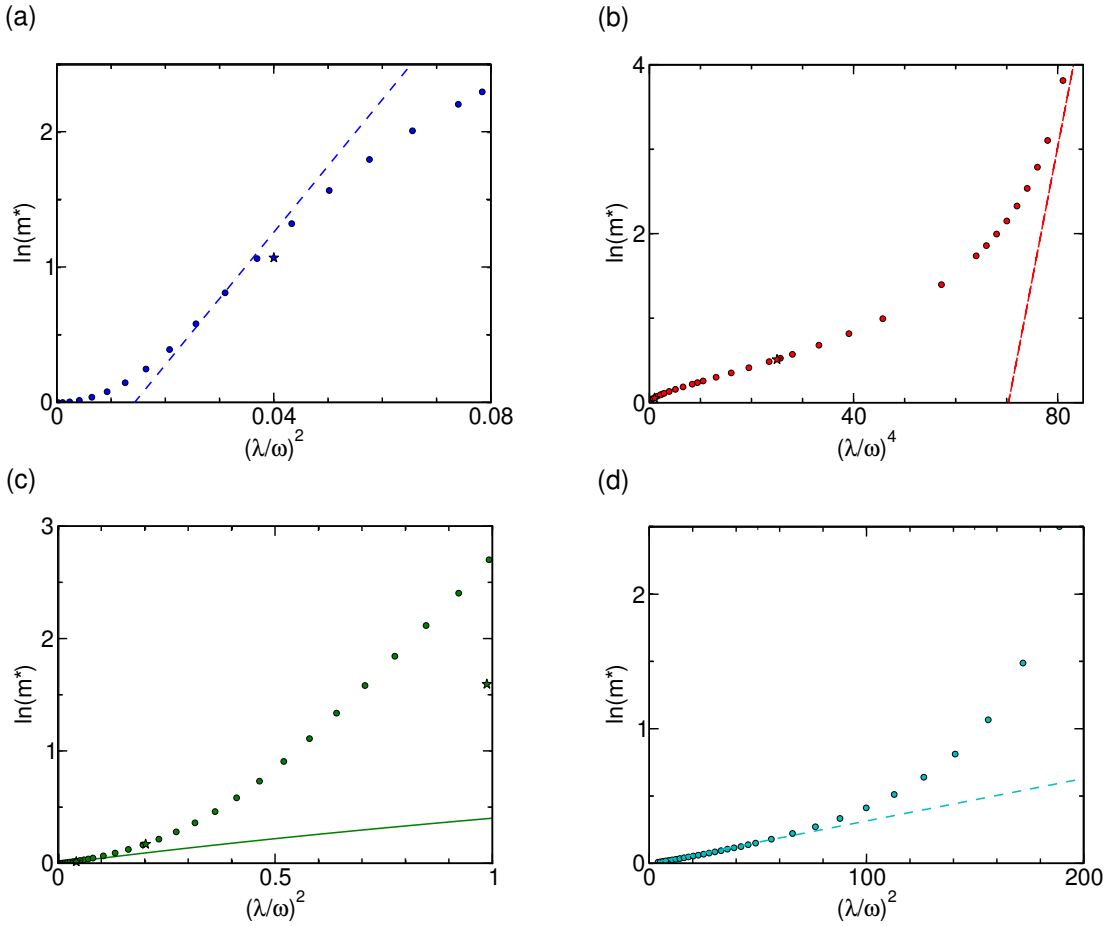


Figure 8.8.: Logarithm of the effective mass as a function of $(\lambda/\omega_0)^2$ or $(\lambda/\omega_0)^4$ for $\omega_0/\Gamma = 62.5$ (a), 0.1 (b), 2.5 (c), and 0.004 (d), calculated with the Matsubara FRG. Stars mark data points calculated with the Keldysh FRG. Dashed lines in (a), (b), and (d) are analytical asymptotic predictions from the Kondo model. Dashed-dotted line in (c) corresponds to first order perturbation theory. See text for details.

the local phonon is too slow to effectively respond to the rapidly tunneling electrons and its presence has little effect on their motion. For the *anti-adiabatic* regime, $\omega_0/\Gamma \gg 1$, an electron on the dot can lower its energy by forming a polaron with the phonon mode, the energy shift being[15] $E_\mathrm{p} = -2\lambda^2/\omega_0 = -U_\mathrm{epe}$. In the limit $\lambda/\omega_0 \gg 1$ the tunneling rate becomes strongly renormalized to $\Gamma_\mathrm{eff} = \Gamma/m^* \ll \Gamma$. The crossover from anti-adiabatic to the adiabatic regime thus is expected at $\omega_0/\Gamma_\mathrm{eff} \approx 1$ instead of $\omega_0/\Gamma \approx 1$. For the resonant level model this has been confirmed using NRG in [Eid13]. Subsequently we thus characterize the parameter space by the two quantities λ/ω_0 and U_epe/Γ shown in Fig. 8.7. For $\lambda/\omega_0 \gg 1$, $\omega_0 \approx \Gamma$, it follows that $U_\mathrm{epe}/\Gamma \gg 1$, which lies in the regime of strong renormalization, regime (II) in Fig. 8.7, and is therefore analogous to the extended anti-adiabatic regime of the resonant level model [Eid13]. Decreasing ω_0/Γ draws a vertical line towards the adiabatic regime (IV), with the crossover happening roughly at $U_\mathrm{epe}/\Gamma \approx 1$ where $\omega_0 \ll \Gamma$. Regime (I) is identified with the negative-U SIAM with $U = -U_\mathrm{epe}$. Finally, in regime (III) the electron–phonon interaction is weak, and the model can be studied perturbatively.

Now we turn to our numerical analysis of the effective mass. Its dependence on λ/ω_0 with ω_0/Γ fixed, obtained numerically (from the equilibrium Matsubara FRG), is shown in Fig. 8.8. We include a few data points from Keldysh FRG for benchmarking. By varying λ/ω_0 we trace a line across the

[15] This way an IRLM with effectively negative interaction, as studied in the previous section, can be realized.

four different regimes described above (see Fig. 8.7). In regime (I), the effective mass should be described by (3.3.7) with $U = -U_{\text{epe}}$, indicated as a dashed line in Fig. 8.8(a). The numerically calculated effective mass for $(\lambda/\omega_0)^2 \in [0.02, 0.05]$ grows with a slightly smaller prefactor in the exponential function than the expected $\pi\omega_0/(4\Gamma)$. This is due to the fact that the asymptotic regime is not realized perfectly for these values of λ/ω_0, which can be seen by comparing to the positive-U SIAM [Kar08, Jak09, Jak10a]. For very large U_{epe}/Γ, $(\lambda/\omega_0)^2 \gtrsim 0.05$, the effective mass bends away from the exponentially increasing trend. This effect is the same as observed for the SIAM and signals the limit of the validity of our FRG method.

In the regime (IV), the effective mass follows Eq. (3.3.7) with $U = -U_{\text{epe}}$ instead of Eq. (3.4.10) as shown in Fig. 8.8(d) for $(\lambda/\omega_0)^2 \in [4, 50]$. As U_{epe}/Γ approaches unity at $(\lambda/\omega_0)^2 = 125$ the effective mass starts to increase rapidly. We are unable to reach far into the regime (II), with m^* described by Eq. (3.4.10), since the renormalized interaction vertex grows too large[16]. This again signals the limit of the validity of our FRG method. This becomes even more clear in Fig 8.8(b) in which $\ln(m^*)$ is plotted against $(\lambda/\omega_0)^4$ instead of $(\lambda/\omega_0)^2$ as in (a), (c), and (d). The behavior described by Eq. (3.4.10), indicated as a dashed line, cannot be observed for the largest values of λ/ω_0 reached. Here, $U_{\text{epe}}/\Gamma = 1$ at $(\lambda/\omega_0)^4 = 25$. Another indicator that the limit of the FRG approach is reached is given by the deviations of the effective masses calculated from Keldysh and Matsubara FRG showing up as we approach regime (II) such that $U_{\text{epe}}/\Gamma \gg 1$. This is exemplified in Fig. 8.8(c) by the rightmost Keldysh data point. Finally, in the regime (III), see Fig. 8.8(c), the effective mass from FRG and first order perturbation theory agree up to $\lambda/\omega_0 \approx 0.3$, or, equivalently, $U_{\text{epe}}/\Gamma \approx 0.45$. To sum up all these considerations, we roughly shaded the area in the parameter range where Matsubara FRG can be trusted in Fig. 8.7.

Finally we turn to finite U. The numerical results are summarized in Fig. 8.9(a). In the limit $\omega_0 \to \infty$ the situation reduces to the simple SIAM with $U \to U - U_{\text{epe}}$. Thus the two terms compete and if $U = U_{\text{epe}}$ the non-interacting problem is recovered ($m^* = 1$). Since there is a $\pm U$ symmetry in the SIAM this point corresponds to a global minimum in m^*. For the limit $U \gg U_{\text{epe}}$ ($U \ll U_{\text{epe}}$) we expect exponential behavior with exponent $-\pi/8(\pi/8)$. Due to the problems mentioned above we cannot reach very far into either regime, but only hint the onset of the exponential behavior [compare Fig. 8.8(a)]. We find that as one gradually leaves the $\omega_0 \to \infty$ limit, the minimum shifts to smaller values of U_{epe} and the perfect cancellation is destroyed (meaning $m^* > 1$). If the frequency ω_0 becomes too small compared to U the strong renormalization found in this regime overcompensates the competition of U and U_{epe} and m^* becomes a monotonic function of U_{epe}.

Spectral Function

To access the spectral function within our Matsubara formalism, we need to analytically continue

$$\rho_\sigma = -\frac{1}{\pi}\text{Im}\left[G_\sigma(i\omega \to \omega + i\eta)\right] \tag{8.3.34}$$

via performing a numerical Padé approximation [Bak75, Vid77]. These are numerically unstable due to the appearance of spurious pole-zero pairs (Froissart doublets) [Gil03], rendering this procedure difficult for certain parameter regimes, in particular $T > 0$. However for $T = B = \epsilon = 0$ rather stable results can be extracted for not too large interaction U and U_{epe}. In Fig. 8.9(b) and (c) we present some spectral functions for small and intermediate U_{epe} and $U = \epsilon = B = T = 0$. The artificial logarithmic suppression around $\omega = \pm\omega_0$ found in first order perturbation theory is smoothed by the renormalization group procedure employed. Clear phonon satellites in the spectral functions are positioned next to this characteristic energy scale $\omega \approx \pm\omega_0$. For larger interaction the precise position as well as the height and width is renormalized. The position tends to shift outwards, while height and width increase with increasing U_{epe}. In (c) we also present the non-interacting spectral function $U_{\text{epe}} = 0$ and the spectral function approximated by the effective mass Eq. (8.3.33) for comparison. Trivially, the low energy part of the spectral function is approximated well by simply using the effective mass, while the phonon satellites (being a non-zero frequency

[16] We abort the FRG calculation if the renormalized value of the vertex function grows to more than ten times its original value at any energy during the flow.

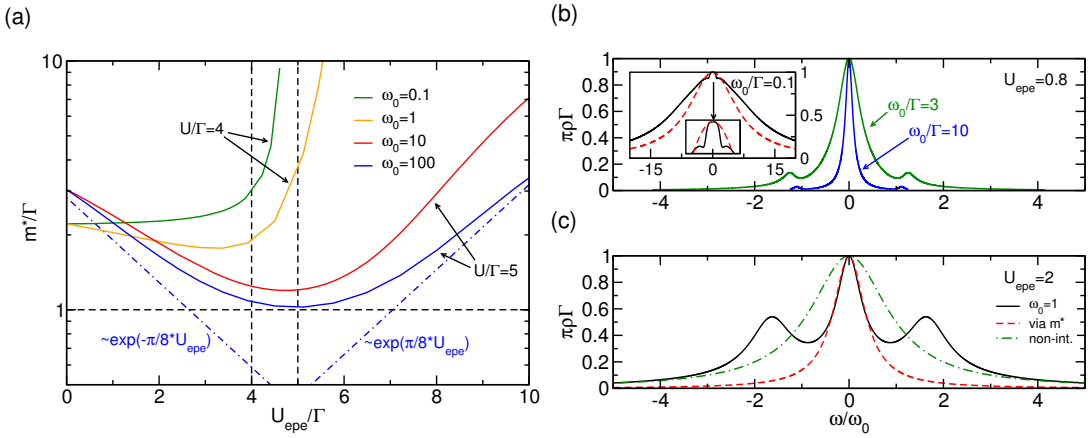


Figure 8.9.: Left: Finite U and U_{epe} results for the effective mass. For $\omega_0 \to \infty$ the setup reduces to the SIAM with $U \to U - U_{\text{epe}}$. The two competing terms lead to the non-interacting problem if $U = U_{\text{epe}}$ ($m^* = 1$). Since there is a $\pm U$ symmetry in the SIAM this point corresponds to a global minimum in m^*. For the limit $U \gg U_{\text{epe}}$ ($U \ll U_{\text{epe}}$) we expect exponential behavior with exponent $-\pi/8(\pi/8)$. We cannot reach very far into either regime, but only hint the onset of the exponential behavior [compare Fig. 8.8(a)]. As one gradually leaves the $\omega_0 \to \infty$ limit, the minimum shifts to smaller values of U_{epe} and the perfectly non-interacting parameter point is destroyed (meaning $m^* > 1$). If the frequency ω_0 becomes too small compared to U the strong renormalization found in this regime overcompensates the competition of U and U_{epe} and m^* becomes a monotonic function of U_{epe}. Right: Spectral functions for small and intermediate U_{epe} and $U = \epsilon = B = T = 0$. Phonon satellites in the spectral functions are positioned next to the characteristic energy scale $\omega \approx \pm\omega_0$, where the precise position as well as the height and width of those is renormalized by the interaction. For comparison we also present the non-interacting spectral function $U_{\text{epe}} = 0$ in (c) as well as the spectral function approximated by the effective mass Eq. (8.3.33). In the inset of (b) we also depict $\omega_0 = 0.1$. In reducing ω_0 the range of validity of the description of the spectral function via an effective mass shrinks until the central peak is smeared out so significantly by the close by phonon satellites that only the very top of it is described correctly.

signature of the phonons) are completely missed. If one further reduces ω_0 the range of validity of this effective mass description of the spectral function shrinks until the central peak is smeared out so significantly by the close by phonon satellites that only the very top of it is described correctly. This is demonstrated in the inset of 8.9(b) for $\omega_0 = 0.1$.

Linear Conductance at $T = 0$: A First Step to Thermotransport

From a technical point of view the linear conductance at $T = 0$ is straightforward to access within the Matsubara formalism as it can be calculated without the need of a possibly ill-behaved numerical Padé approximation and is thus our natural starting point for investigating thermotransport (which by its very definition of course will require finite temperature in the end). The linear conductance itself is of major experimental relevance, as it is a measure for the current's response to an applied small bias voltage. For the AHM and at $T = 0$ it is determined completely by the Green's function at zero frequency with respect to the chemical potential[17] (→ Section 4.1.3). Again we can benchmark against first order perturbation theory or the FRG set up analogous to our method, but in Keldysh space [Laa14]. For the most clear cut case $\omega_0 \to \infty$ we expect that the linear conductance in dependence of ϵ shows a very narrow resonance of width $\sim T_K$. This is due to the fact that when changing from the positive- to the negative-U SIAM, the role of spin and charge interchange with respect to the low-lying excitations. Thus the broad plateau of width $\sim U$ expected for the linear conductance when varying ϵ in the positive-U SIAM is now found when scanning through the magnetic field B, while the narrow resonance seen in a B-sweep of the positive-U SIAM is expected

[17] A fact that does not carry over to finite T.

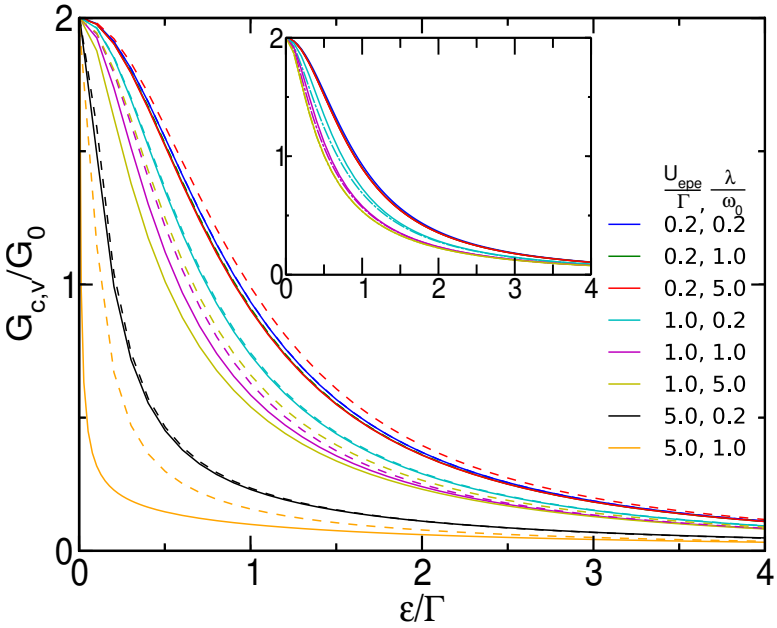


Figure 8.10.: Linear conductance for the AHM as a function of the gate voltage ϵ for different values of U_{epe}/Γ and λ/ω_0. Solid lines are obtained with the equiliubrium Matsubara formalism and dashed lines with the non-equilibrium Keldysh formalism presented elsewhere [Laa14]. The inset shows a comparison to first order perturbation theory (dash-dotted lines).

in ϵ in the negative-U counterpart. The linear conductance as a function of the gate voltage ϵ is shown in Fig. 8.10. In general the linear conductance exhibits a peak at a vanishing gate voltage, i.e., at the particle–hole symmetric point, where perfect conductance is reaches $G = 2G_0$. The inset of Fig. 8.10 shows results from first order perturbation theory. They agree perfectly with the results from Matsubara FRG for $U_{\text{epe}}/\Gamma = 0.2$, whereas for $U_{\text{epe}}/\Gamma = 1$ deviations start to appear. Importantly, the Keldysh formulation of FRG produces markedly different results than the Matsubara FRG when approaching the regime (II). This is consistent with the validity limit of our truncated FRG equations found above.

8.3.3 AHM: Thermoelectric Properties in Linear Response

Finally, we turn to the central question of this chapter: which thermoelectric properties can be found for the AHM? We will concentrate on the linear response regime of the quantum impurity model, as we are using the Matsubara formalism prone to the non-linear non-equilibrium regime. We mentioned briefly that treating finite frequency is key for any study of thermoelectric properties (and thus $T > 0$). We also outlined, that Padé approximation, being numerically stable at $T = 0$, is rather difficult to handle for finite T. Luckily there is a convenient way around Padé approximating the spectral function, when aiming at the finite temperature linear response conductivities $G_{a,b}$ defined in Eq. (8.1.3). For this we have to generalize a procedure introduced to calculate the electrical conductance $G_{c,V}$ in [Kar10c]. In linear response and for the considered quantum-dot geometry the relevant *transport integrals* are defined as

$$I_n = -2\pi\Gamma \int d\omega\, \omega^n \rho(\omega) f'(\omega)\,, \tag{8.3.35}$$

with the dot spectral function $\rho(\omega) = \sum_\sigma \rho_\sigma(\omega)$ and $n \in \mathbb{N}_0$. Only the first three moments $n \in \{0, 1, 2\}$ are needed for the thermotransport analysis as they determine completely all $G_{a,b}$ given in Eqs. (4.1.83)-(4.1.85). All integrals I_n are exponentially convergent with respect to both of the infinite boundaries, because of the derivative of the Fermi function f'.

Evaluating $G_{a,b}$ by Rapidly Convergent Sums

The central idea is now to partially integrate expression (8.3.35) and rewrite the resulting integral with integrand $\sim f$ as a rapidly convergent sum of the poles of f. Explicitly the first three moments after integration by parts read

$$I_0 = 2\pi\Gamma \int d\omega\ \rho'(\omega) f(\omega)\ , \tag{8.3.36}$$

$$I_1 = 2\pi\Gamma \int d\omega\ \rho(\omega) f(\omega) + 2\pi\Gamma \int d\omega\ \omega\rho'(\omega) f(\omega)\ , \tag{8.3.37}$$

$$I_2 = 2\Gamma^2 + 2\pi\Gamma \int d\omega\ \left[\omega^2\rho'(\omega) f(\omega) + 2\omega\rho(\omega) f(\omega)\right]\ . \tag{8.3.38}$$

Since $\rho(|\omega|) \overset{|\omega|\to\infty}{\longrightarrow} 1/|\omega|^2$ Eq. (8.3.36) and (8.3.37) are quite unproblematic, while the integral of Eq. (8.3.38) converges only if the integrand is evaluated as a sum. If one would now rewrite the Fermi function as an infinite sum over the poles at the Matsubara frequency and subsequently uses the residue theorem one faces the problem, that the sum is rather slowly convergent. Different routes to numerically evaluating such slowly convergent sums have been presented [Oza07, Mon10]. The basic idea is similar to Gaußian quadrature rules for integrals. Instead of evaluating the sums at certain points given by the summation index, we shift these positions slightly and weight them according to some (nearly) optimal scheme. We follow [Oza07, Kar10c] and use a representation of the Fermi function as

$$f(x) - \frac{1}{2} = -\sum_{\alpha>0} \frac{R_\alpha}{x - i/b_\alpha} + \frac{R_\alpha}{x + i/b_\alpha}\ , \qquad R_\alpha = \frac{|\langle 1|b_\alpha\rangle|^2}{4b_\alpha^2}\ , \tag{8.3.39}$$

where b_α and $|b_a\rangle$ are eigenvalues and vectors of the single-particle tight-binding Hamiltonian with entries $H_{n,n+1} = H_{n+1,n} = 1/(2\sqrt{4n^2-1})$ and dimension $M \times M$. The vector $|1\rangle$ denotes $(1, 0, 0, \ldots, 0)^T$ in the basis chosen for H. When inserting Eq. (8.3.39) for $f(x)$ due to residue theorem one thus evaluates the sum at positions b_α and with weights R_α instead of at the Matsubara frequencies with weight 1. Only in the limit $M \to \infty$ the original Matsubara sum is recovered, but in fact very small $M < 40$ are sufficient to approximate the Fermi function perfectly for all practical purposes (not too large temperatures). Since we are now in need of the Green's function at frequencies not equal to the Matsubara ones we can use Padé interpolation on the imaginary axis, which is numerically more stable than analytical continuation to the real axis by Padé approximation. Nonetheless, it still suffers from spurious pole-zero pairs, even though stability is enhanced. This restricts the applicability of this method similar to the SIAM case [Kar10c]. For the integrals Eqs. (8.3.36)-(8.3.38) we get in linear response

$$I_0 = \frac{4\pi\Gamma}{\beta} \sum_{\alpha>0} R_\alpha \mathrm{Im}\left[\frac{G(i\tilde{\omega}_\alpha)}{d\omega}\right]\ , \tag{8.3.40}$$

$$I_1 = \frac{4\pi\Gamma}{\beta} \sum_{\alpha>0} R_\alpha \mathrm{Re}\left[G(i\tilde{\omega}_\alpha) - \tilde{\omega}_\alpha \frac{G(i\tilde{\omega}_\alpha)}{d\omega}\right]\ , \tag{8.3.41}$$

$$I_2 = 2\Gamma^2 - \frac{4\pi\Gamma}{\beta} \sum_{\alpha>0} R_\alpha \mathrm{Im}\left[i + 2\tilde{\omega}_\alpha G(i\tilde{\omega}_\alpha) + \tilde{\omega}_\alpha^2 \frac{G(i\tilde{\omega}_\alpha)}{d\omega}\right]. \tag{8.3.42}$$

For convergence reasons it is vital to evaluate the sums in the depicted way. The derived expressions can be used in any diagrammatic approach that aims at the Matsubara self-energy and thus have relevance beyond the FRG approach employed here. Fig. 8.11 shows a proof of principle of the outlined method to avoid analytic continue for the free case $U = \alpha = 0$. The data obtained by Padé interpolating the Green's function for $M = 40$ (symbols) is in perfect agreement with the exact analytical calculation (lines). This shows that if the numerically found Green's function is determined accurately enough, such that spurious pole-zero pairs in the interpolation can be avoided, all entries of the conductance-matrix can be determined.

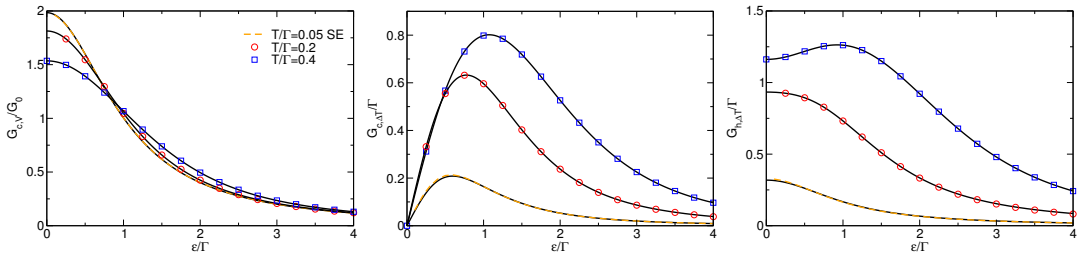


Figure 8.11.: A proof of principle of the outlined methods to avoid analytic continuation. We concentrate on the non-interacting case $U = \alpha = 0$ for all entries of the conductance-matrix defined in Eq. (8.1.3). For the method using rapidly convergent sums the data is obtained by Padé interpolation of the Green's function choosing $M = 40$ (symbols) at all T. Additionally for very small temperature $T/\Gamma = 0.05$ we show the conductances found by a Sommerfeld expansion (dashed lines). Both proposed methods yield results in perfect agreement with the exact analytical calculation (lines).

Evaluating $G_{a,b}$ by Sommerfeld Expansion

Before turning to the thermotransport analysis at finite interaction λ and/or U we discuss yet another method to determine the conductances, For very small temperature $T \ll \Gamma^{eff} \sim 1/m^*$ one can employ a Sommerfeld expansion (making use of the narrowness of f'). The above transport integrals

$$I_n = 2\pi\Gamma \int dx\, \frac{e^x}{(e^x+1)^2}\left[F_n(0) + \frac{x}{\beta}F_n'(0) + \frac{1}{2}\left(\frac{x}{\beta}\right)^2 F_n''(0) + \ldots\right] = 2\pi\Gamma \sum_{j=0}^{\infty} \frac{1}{j!\beta^j} F_n^j(0) S_j$$

$$\text{with: } F_n(\omega) = \omega^n \rho(\omega) \quad \text{and} \quad S_j = \int_{-\infty}^{\infty} dx\, x^j \frac{e^x}{(e^x+1)^2}, \tag{8.3.43}$$

now depend on all derivatives of the auxiliary function F_n at zero frequency. Truncating this expression after the second derivative of $\rho(\omega)$ due to the Sommerfeld expansion we find (using that G is analytic at complex $\omega = 0$)

$$\rho'(\omega)|_{\omega=0} = \frac{1}{\pi}\mathrm{Im}\left[G(0)^2\right]\left(1 - \mathrm{Im}\left[\frac{d\Sigma(i\omega)}{d\omega}\right]_{\omega=0}\right), \tag{8.3.44}$$

$$\rho''(\omega)|_{\omega=0} = -\frac{2}{\pi}\mathrm{Im}\left[G(0)^3\right]\left(1 - \mathrm{Im}\left[\frac{d\Sigma(i\omega)}{d\omega}\right]_{\omega=0}\right)^2 - \frac{1}{\pi}\mathrm{Im}\left[G(0)^2\right]\mathrm{Re}\left[\frac{d^2\Sigma(i\omega)}{d\omega^2}\right]_{\omega=0}, \tag{8.3.45}$$

involving only zero frequency properties, which can be evaluated very stably. In Fig. 8.11 we included one graph for[18] $T/\Gamma = 0.05$ (dashed lines) obtained by the Sommerfeld expansion outlined here.

Thermotransport Analysis: The SIAM Dilemma Reloaded

All this preliminary work was done solely to evaluate the thermotransport properties of the AHM for a parameter regime as wide as possible[19]. As we are using an approximate method again the question of validity arises now at finite T. We have seen in the previous section that this is actually a subtle question, as we can currently only compare to what is known from the SIAM or to the FRG method set up in Keldysh space. The parameter regime of most interest at this point is

[18] $T/\Gamma = 0.05$ is roughly the boundary of the validity range.
[19] Keeping in mind, that such fast methods as the FRG are ideal to scan large parameter regimes efficiently.

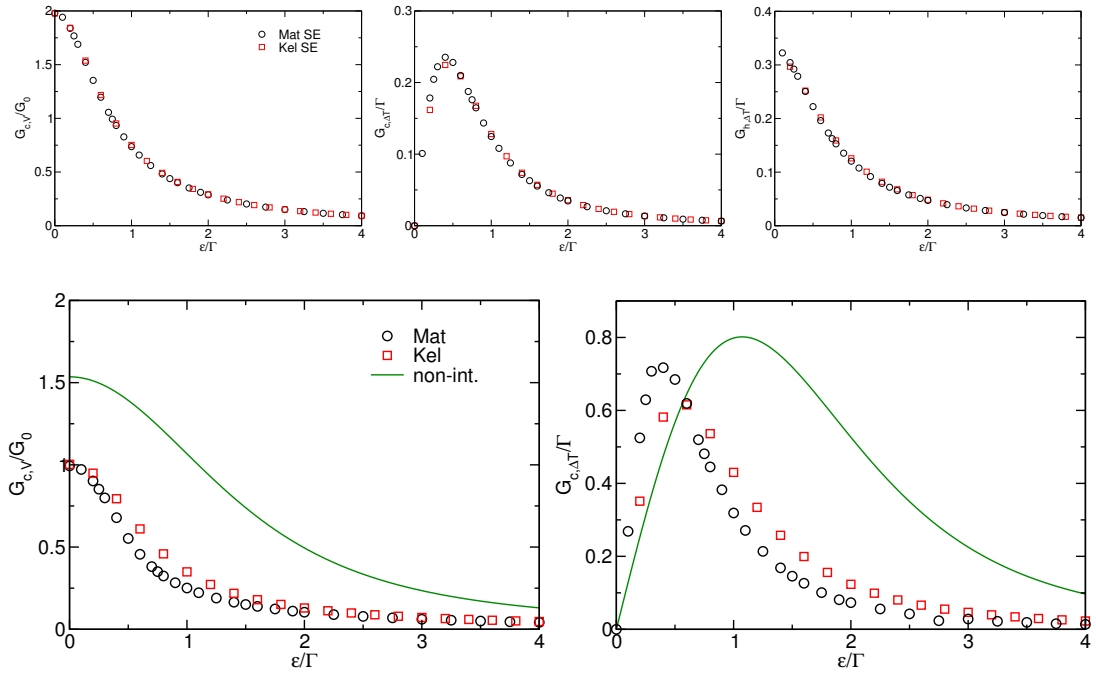


Figure 8.12.: Top: Conductances for $U = 0$ and $T/\Gamma = 0.05$, $\alpha/\Gamma = 1.1, \omega_0/\Gamma = 3$ ($\lambda/\omega_0 \approx 0.37$) obtained by a Sommerfeld expansion. For this smaller interaction ($U_{\text{epe}} \approx 0.81$) Matsubara and Keldysh FRG agree nicely. Bottom: $G_{c,V}$ and $G_{c,\Delta T}$ for $T/\Gamma = 0.4$, $\lambda/\Gamma = 2.8$ and $\omega_0/\Gamma = 4$ ($U_{\text{epe}}/\Gamma = 3.92$, $\lambda/\omega_0 = 0.7$) obtained by rapidly convergent sums [using Eqs. (8.3.40)-(8.3.42)]. We also show the non-interacting curves as a point of reference for the interaction effects.

clearly the one approaching the strong-correlation limit of the AHM, which is not mappable to negative-U SIAM[20]. Therefore, we choose $U = 0$ and $\omega_0/\Gamma \leq 5$. For smaller interaction U_{epe} Matsubara and Keldysh FRG give agreeing results (as they should). This is shown in the top panels of Fig. 8.12. Here we evaluate the conductances by a Sommerfeld expansion[21] (small $T/\Gamma = 0.05$) and choose $\lambda/\Gamma = 1.1$ as well as $\omega_0/\Gamma = 3$ ($U_{\text{epe}}/\Gamma \approx 0.81$, $\lambda/\omega_0 \approx 0.37$). But if we now turn to larger electron-phonon coupling λ and thus approach the limit of stronger renormalization, deviations between Matsubara and Keldysh formalism show up. In the bottom panels of Fig. 8.12 we demonstrate this for $T/\Gamma = 0.4$ [therefore using Eqs. (8.3.40)-(8.3.42)] and $\lambda/\Gamma = 2.8$ as well as $\omega_0/\Gamma = 4$ ($U_{\text{epe}}/\Gamma = 3.92$, $\lambda/\omega_0 = 0.7$). We also show the non-interacting curves as a point of reference for the interaction effects. As we cannot judge whether at least one of the FRG approaches (Keldysh or Matsubara) gives reasonable results, due to a missing independent benchmark, we cannot conclude, whether a further thermotransport study is meaningful in either approach. It appears however, that the AHM is plagued by the same difficulties encountered in the SIAM for each parameter regime featuring strong renormalization (Kondo-) physics (which was clear beforehand only for the limit $\omega_0 \to \infty$). An exact study (for example within the NRG) could resolve this puzzle, which at this point has to be postponed to the future.

[20] Since the negative-U SIAM has been studied already in [And11a] with NRG and a static formulation of the FRG.
[21] Evaluating the expressions (8.3.40)-(8.3.42) for the conductances gives the same results but tends to be less stable.

8.4 Conclusion

Results for the IRLM

The FRG has been successfully applied before to the IRLM studying a variety of different aspects. It is well understood that parametric logarithmic divergences showing up in a perturbative treatment are resummed correctly by FRG, motivating the presented thermoelectric study of this model. The results obtained for the IRLM were interpreted using basically non-interacting expressions dressed with the dominant Kondo-like renormalization of the hybridization induced by the reservoirs. With this we could connect our microscopic ansatz to viewpoints attributed to phenomenological thermodynamics. Interestingly, positive interaction (leading to a broader resonance) generally reduces the efficiency encountered in power-engines, while negative interaction (as achievable effectively by including phonons) renders the opposite effect. The flexibility and speed of the FRG is ideal for the posed problem as huge parameter spaces have to be sampled for thermoelectric questions (since usually multiple parameters are optimized). We have also proposed an alternative more "applied" scenario of interest. Here instead of the usual quest for maximum power or efficiency, we search for the optimal efficiency under the constrain of a certain minimum power output. This scenario appears to be of relevance when, e.g., charging applications are envisaged. For this, even in the regime of positive interactions, the general decrease in maximum efficiency can be overcome by an increase in the power output, yielding a net increase of the achievable efficiency. This part demonstrated some of the impressive key advantages of FRG (flexibility and speed).

Results for the AHM

The AHM features much more complicated physics than the IRLM and thus we applied a second order truncation scheme to handle this problem. This more sophisticated truncation scheme restricts our study to equilibrium, but non-equilibrium FRG results were available from [Laa14]. Similarly to the SIAM studied before in the same framework (truncation scheme, cut-off, channel decomposition, ...) major difficulties show up. It is not possible to reach far into the regime of strong correlations as might be hoped for from an renormalization group approach. For the adiabatic regime this was clear from the beginning as the AHM can then be mapped to the negative-U SIAM. Unfortunately, also for all other cases the range of validity of our FRG approach appears to be limited to small to intermediate interaction strength. For the question of thermoelectric transport we extended an existing approach to compute $G_{c,V}$ from the Matsubara frequency propagator to access all linear response conductances without the need of a possibly ill-posed analytic continuation. Furthermore, we introduced an alternative route based on a Sommefeld expansion. Comparing the conductances obtained by these methods to those from non-equilibrium Keldysh FRG major deviations show up for rather small values of the interaction. As we do not have any non-perturbative benchmark results at hand (e.g. using NRG) at this point it remains an open question, whether either of the FRG approaches yield meaningful results (at least up to intermediate interaction strength). The route to thermoelectric transport at intermediate to large interactions strength is thus blocked. This part demonstrated an unfortunate disadvantage of the FRG. The deep Kondo limit is not accessible; another reminder of the dilemma encountered already for the SIAM.

Outlook

For the future it could be interesting in the context of the IRLM to use a non-perturbative method (e.g. extensions of NRG for linear response, field-theory or DMRG for non-equilibrium) to tackle the thermoelectric properties. The width of the central conductance resonance is a non-monotonic function for positive interactions. Thus the initial broadening is reversed at some point, which could lead to highly efficient thermoelectric devises. Obviously, the renormalized single-particle picture breaks down completely for such large interactions and thus a different effect could take over. Certainly, an interesting open question of strongly correlated physics encountered in charge-fluctuating quantum dots. Furthermore, an extension to truly time dependent problems (compare chapters 7 and 11) pose an intriguing venue of future interest.

On the other hand the AHM could not be analyzed in the broad parameter regime we aimed at. We are restricted to small interaction as deviations between equilibrium or non-equilibrium FRG become prominent at intermediate to large interactions. Thus devising different approaches is vital. If such a reliable approach was found, it could be used to provide the missing benchmark, clarifying whether at least one of the equilibrium or non-equilibrium FRG approaches yields reliable results upto intermediate interaction strength. The FRG could then in turn be used to sample parameter regimes quickly (in its range of validity).

A different route to the highly interesting deep Kondo limit is currently followed by Matti A. Laakso. Starting with the AHM a generalized Schrieffer-Wolff transformation is employed to pose the problem directly in this limit. The procedure is similar to the usually studied transition from the SIAM to the Kondo model (compare chapter 3). Concentrating on the relevant degrees of fluctuations (just like Kondo model versus SIAM) should certainly help to access the fascinating Kondo physics and its consequences for thermoelectric transport [Laa].

Acknowledgement

The presented results greatly benefited from fruitful discussions with a variety of people. For the IRLM part we would like to specifically thank Dirk Schuricht. The AHM section relies on comparisons to results kindly provided by Matti A. Laakso. He and additionally Severin G. Jakobs also shared their helpful thoughts on the AHM with us. Finally, we thank Christoph Karrasch for benchmark result on the frequency dependent FRG.

References

Part of the results discussed in this chapter were published in

D. M. Kennes and V. Meden
'Interacting resonant level model in nonequilibrium: Finite-temperature effects'
Phys. Rev. B **87**, 075130 (2013)

D. M. Kennes, D. Schuricht, and V. Meden
'Efficiency and power of a thermoelectric quantum dot device'
EPL (Europhysics Letters) **102**, 57003 (2013)

M. A. Laakso, D. M. Kennes, S. G. Jakobs, and V. Meden
'Functional renormalization group study of the AndersonHolstein model'
New Journal of Physics **16**, 023007 (2014)

Chapter 9

Dynamics in Closed Quantum Systems

Contents

9.1. Basics and Definitions **160**
- 9.1.1. Thermalization and Non-Thermal Steady-States 160
- 9.1.2. Models 162

9.2. Reminder of Luttinger Liquid Physics **163**

9.3. Real-Time FRG for Closed Quantum Systems **165**
- 9.3.1. Efficiently Evaluating Keldysh Green's Function Using GPU... 167
- 9.3.2. ... or Trotter Decompositions 168
- 9.3.3. Benchmark: Dynamics of Interacting Fermions 168

9.4. Luttinger Liquid properties in Non-Thermal Steady-States **169**
- 9.4.1. The Tomonaga-Luttinger Model 170
- 9.4.2. Lattice Model: Spinless Fermions 175

9.5. Thermalization in One Dimension **179**
- 9.5.1. Models and Method 179
- 9.5.2. Time Evolution of Observables 181
- 9.5.3. A Single Measure of Thermalization 182
- 9.5.4. Chaos Induced Thermalization 183

9.6. Conclusion **184**

Introduction

In this chapter we want to complement the results of the dynamics in open systems (→ Chapter 7) by those found in closed ones. Several interesting questions arise. (1) As the bath is absent one might wonder if a given closed system even equilibrates? (2) If so how can the steady-state reached for asymptotic times be characterized? (3) Under which conditions (if any) does the steady-state resemble known equilibrium ensembles? (4) Does the equilibrium concept of Luttinger Liquid universality carry over to the time evolution *towards* the steady-state and/or to the *steady-state itself*? To name but a few. Recent advances in the field of ultra-cold atoms [Blo08] reignited the interest in the dynamics in closed quantum systems.

Outline

This chapter is structured as follows. The first section is devoted to the basics underlying the following sections. In this part we will outline the general questions and models we will consider. Next, we recapitulate some of the Luttinger Liquid equilibrium physics needed to understand the remainder of this chapter. Then we will describe in more detail how the general FRG formalism of chapter 4 can be used to tackle the time-dependence of closed quantum many-body systems. Next, we apply this method to the time evolution of quenched spinless fermions. Here we will compare in

detail predictions for steady-state expectation values of a continuum model obtained by bosonization with FRG and DMRG results for lattice models. Afterwards, we will try to shed some light on the issue of thermalization and its connection to integrability. Finally, a conclusion sums up the findings.

9.1 Basics and Definitions

9.1.1 Thermalization and Non-Thermal Steady-States

Concrete calculations in equilibrium statistical mechanics rely on the *assumption* of a micro canonical, canonical or grand canonical ensemble. Those describe the equilibrium density matrices of a given system, maximizing the entropy, under different physical constrains:

- the micro canonical ensemble is used if the energy of the system is fixed within a narrow interval $(E, E + \Delta E)$. Equal probability is then assigned to each micro state $\rho \sim C$ within this energy interval.
- the canonical ensemble describes a system in contact with a much larger heat bath, such that the *expectation value of the energy* is constrained. The density matrix then simply reads $\rho = \exp(-\beta H)/Z$, where the inverse temperature β is determined by the energy expectation value.
- the grand canonical ensemble is used if the system is in contact with a heat and particle bath. The corresponding density matrix reads $\rho = \exp[-\beta(H - \mu N)]/Z$, where the inverse temperature β and the chemical potential μ are fixed by the *energy and particle number expectation values*.

Due to the fundamental role of these ensembles, the question arises under which conditions they provide the long time asymptotic description of a closed quantum system prepared in some arbitrary (non-equilibrium) initial state. Put formally one could state the central question as

$$\lim_{t\to\infty} \langle A \rangle_{\rho(t)} \stackrel{?}{=} \langle A \rangle_{\rho^{\text{eq}}}\,, \tag{9.1.1}$$

for (almost) any local observable A, where ρ^{eq} is the appropriate of the three equilibrium ensembles. If the above relation holds the system is said to *thermalize*. We simply assume the relaxation of the observable A towards a steady-state at this point, which implies that we have to take the thermodynamic limit before considering large times[1]. The (also intriguing) question about whether relaxation generically occurs will not be addressed. We rather take a pragmatic point of view: for the models and observables studied in the following it turns out that this is always the case. We can also define the condition for thermalization in the (stronger) sense of

$$\rho^{\text{red,ss}} = \lim_{t\to\infty} \text{Tr}_{\text{B}}\left[\rho(t)\right] \stackrel{?}{=} \text{Tr}_{\text{B}}\left[\rho^{\text{eq}}\right] = \rho^{\text{red,eq}}, \tag{9.1.2}$$

where we have bipartitioned the full system into two parts A and B, with subsystem B being much larger than subsystem A.

Considering the logic of the derivation of the equilibrium ensembles (maximizing entropy under given constrains of fixed energy, fixed energy expectation value or fixed energy and particle number expectation value), it appears rather reasonable to follow that fixing further expectation values $\langle Q_n \rangle$ will surely prohibit thermalization (as these constrains are not included in the equilibrium ensembles mentioned above). For such systems it appears plausible that, if at all, the system relaxes to a generalized version of the typical equilibrium ensembles, maximizing entropy under all these fixed expectation values. The corresponding ensemble was dubbed *generalized Gibbs ensemble* (GGE) [Jay57, Rig07] with $\rho^{\text{GGE}} = \exp(\sum q_n Q_n)/Z$ and $\langle Q_n \rangle = \text{Tr}\left[\rho^{\text{GGE}} Q_n\right]$, which fixes the Lagrange multipliers q_n. Already this simple idea proves to be difficult on second thought.

[1] Otherwise we would find recurrence → Section 7.1.1.

For quantum mechanical models there always exists an exponentially large number of conserved quantities $\langle Q_n \rangle$ with $[H, Q_n] = 0$, namely all the expectation values of the projectors onto the eigenstates of the Hamiltonian. Furthermore, if $\langle Q \rangle$ is conserved, so is $\langle Q^m \rangle$ for all $m \in \mathbb{N}$. Therefore, it appears that not all of the conserved $\langle Q_n \rangle$ restrict the phase space in the same manner. Identifying which conserved quantities constitute constrains of the above mentioned type (thus entering the GGE), and which do not, is highly debated. We note however that for effectively non-interacting models, meaning models that can be brought into the form $H = \sum_n \lambda_n a_n^\dagger a_n$ (e.g. by bosonization), the GGE reproduces the correct steady-state expectation values for local observables (see e.g. [Rig06, Rig07]), if the conserved mode occupancies $a_n^\dagger a_n$ are taken as Q_n.

For generic interacting models (meaning those not of the above mentioned effectively non-interacting type) it was suggested to borrow a concept from classical physics ([Deu91, San10] as well as references therein). For classical systems thermalization occurs via chaos [Gal10], which is excluded for so called *integrable* models. In a classical system integrability is defined as the property of a system to be described by a complete set of integrals of motion. In a quantum system this concept proves to be more complicated and integrability is often used synonymic to Bethe ansatz solvable. We want to follow this convention from now on and consequently focus on one-dimensional models for which in certain cases Bethe ansatz solutions are available. In analogy to classical systems integrability could prevent thermalization in quantum systems, rendering one-dimensional systems especially interesting in this context. Actually, for Bethe ansatz solvable models not only the energy expectation value (canonical) and possibly additionally the particle expectation value (grand canonical) are conserved, but rather an infinite set of (quasi-)local[2] expectation values $\langle Q_n \rangle$. One finds that the steady-states approached asymptotically for non-equilibrium setups in those integrable modes indeed appear to be given by non-thermal steady-states. However, plugging Q_n into the GGE given above does not seem to describe the asymptotically reached states correctly at least for the Heisenberg model and some specific initial states[3] [Poz14, Wou14].

To sum up, so far one finds: (1) the common believe that some large class of generic models thermalize, motivated by the success of equilibrium statistical mechanics. (2) In some special cases (so far shown for effectively non-interacting models) instead of thermalization one finds relaxation towards a GGE. (3) In integrable models a non-thermal steady-state is approached that appears not to be always characterized by the GGE. For us two interesting questions arise, which we want to present separately in the following two paragraphs

Luttinger Liquid properties in Non-Thermal Steady-States

Thermal states have been analyzed and understood in much detail, however non-thermal states appear to be less studied. Characterizing those could open a route to novel and fascinating physics. In the near future it should be possible to realize these states in experiments with ultra-cold atoms [Blo08]. In this chapter we want to, primary, contribute to this by asking the question: do non-thermal steady-states reached in a non-equilibrium setup in one dimension resemble Luttinger Liquid (LL) universality, similar to what is known from equilibrium? To this end, we study the following: a system is initially prepared in a thermal state (including $T = 0$) of some model described by H_{ini}. Then suddenly a parameter of the Hamiltonian is switched, thus constituting a *quantum quench*, leading to non-equilibrium dynamics. The model defined by the final Hamiltonian H_{fin} is chosen to be out of the Luttinger Liquid universality class. We then want to analyze the steady-state reached for asymptotic times with respect to Luttinger Liquid properties. For this in section 9.2 we first recapitulate what is known about Luttinger Liquids in equilibrium relevant to understand the results presented for non-equilibrium later on.

Thermalization in One Dimension

As a secondary question we return to the subject of when and how thermalization occurs. Thermalization was and is the subject of intense research and we will not be able to give a complete

[2] We do not dwell further on the meaning of this. More information can be found in [Fag14].

[3] Explicit calculations where performed for the Néel state and one of the ground states of the Majumdar-Ghosh Hamiltonian.

overview of the literature here, but rather concentrate on what is important from now on.

Although, generally the question about thermalization is interesting for systems in any dimensions (see e.g. [Moe08, Moe09, Eck09]), we want to restrict ourselves to the, to us, most interesting case of one dimension (see above). We want to scrutinize the statement "interacting integrable models do not thermalize, while non-integrable ones do", as has been posed by many authors before [Kol07, Man07, Rig09, Sir14]. Approaches to this problem can be subdivided mainly into exact diagonalization and DMRG treatments for lattice systems. The former has been used e.g. in [Rig09, Sir14]. It is, however, restricted to rather small systems of ≈ 30 lattice sites. Two problems occur. (1) No steady-state (plateaus in the observables of any kind) is reached, before recurrence sets in. Oscillations dominate the time evolution for all times. Therefore in such an approach one frequently averages in time over the strong oscillations. This is not the way we defined thermalization above. (2) Even in an analysis of the time-averaged quantities small difference of thermal and steady-state observables are difficult to separate from the rather large finite size effects. A convincing finite size scaling is prohibited by the severe limitations in size. On the other hand, DMRG calculations can tackle rather large systems, but are restricted in the accessible time scales. Thermalization of non-integrable models was not observed generically by DMRG studies of one-dimensional systems (e.g. [Kol07, Man07]). Later we present a DMRG study in an infinite system. The time evolution of local observables can be pushed into rather steady regimes. As these are only first results of our ongoing research, this is left on the level of an outlook.

9.1.2 Models

Next, we describe the models we want to study for the rest of this chapter. All Hamiltonians under consideration are of the general tight-binding form depicted in Section 3.2.

Luttinger Liquid properties in Non-Thermal Steady-States

For our main inquiry of Luttinger Liquid properties in steady-states reached after a quantum quench presented in section 9.4, we will focus on the lattice Hamiltonian

$$H_{\mathrm{SF}}(U) = \sum_{j=1}^{N-1} \left[-J c_j^\dagger c_{j+1} + \mathrm{H.c.} + U c_j^\dagger c_j \, c_{j+1}^\dagger c_{j+1} \right], \tag{9.1.3}$$

describing spinless fermions with nearest neighbor hopping J as well as interaction U and open boundaries terminating the N-site chain. For $|U/J| < 2$ this model is known to feature Luttinger Liquid properties in equilibrium (see section 9.2), which is important for section 9.4. To describe impurity physics $H_{\mathrm{SF}}(U)$ can additionally be supplemented by a hopping impurity

$$H_{\mathrm{imp}}(h) = h c_{N/2}^\dagger c_{N/2+1} + \mathrm{H.c.} \tag{9.1.4}$$

of strength $h \in [0, J]$ located in the middle of the chain. We note that the Hamiltonian is related to the Heisenberg model via a Jordan-Wigner transformation ($\rightarrow$ Section 3.2.2).

True relaxation of course is only possible in the thermodynamic limit $N \rightarrow \infty$, where $\lim_{t\rightarrow\infty} \rho(t)$ can be taken without recurrence[4]. Our FRG approach to this problem however cannot be performed with a truly infinite system. Thus we will choose the system size to be so large, that recurrence is not yet an issue for the questions under consideration and the system can be considered as infinite for all practical purposes. This strategy is also adopted to our DMRG studies of section 9.4.

The physics encountered in this model will be compared to those of the so called Tomonaga-Luttinger model. An outline of the Tomonaga-Luttinger model is postponed to section 9.2, where we will also recapitulate some of its equilibrium physics.

[4] Obviously otherwise the subsystem would not even approach a steady-state, which is a necessary condition for the following considerations ($\rightarrow$ Section 7.1.1).

Thermalization in One Dimension

For our study of thermalization in one dimension. We will consider (1) variants of the Heisenberg model

$$H_{\text{Heis}}(\Delta, \Delta_2) = \sum_n J(S^x_n S^x_{n+1} + S^y_n S^y_{n+1} + \Delta S^z_n S^z_{n+1} + \Delta_2 S^z_n S^z_{n+2}) \,, \tag{9.1.5}$$

possibly including next-nearest neighbor interactions and (2) a variant of the particle-hole symmetrized extended Hubbard model

$$\begin{aligned} H_{\text{Hub}}(U, V) = \sum_n \sum_{\sigma=\uparrow,\downarrow} \left[\frac{J}{2} c^\dagger_{n,\sigma} c_{n+1,\sigma} + \text{H.c.} + V \left(c^\dagger_{n,\sigma} c_{n,\sigma} - \frac{1}{2} \right) \left(c^\dagger_{n+1,\sigma} c_{n+1,\sigma} - \frac{1}{2} \right) \right] \\ + U \left(c^\dagger_{n,\uparrow} c_{n,\uparrow} - \frac{1}{2} \right) \left(c^\dagger_{n,\downarrow} c_{n,\downarrow} - \frac{1}{2} \right) \quad , \end{aligned} \tag{9.1.6}$$

or equivalently its formulation in terms of spin operators

$$H_{\text{Hub}}(U, V) = \sum_n \sum_{\sigma=\uparrow,\downarrow} \left[J(S^x_{n,\sigma} S^x_{n+1,\sigma} + S^y_{n,\sigma} S^y_{n+1,\sigma}) + V S^z_{n,\sigma} S^z_{n+1,\sigma} \right] + U S^z_{n,\uparrow} S^z_{n,\downarrow} \,. \tag{9.1.7}$$

Both models defined in Eqs. (9.1.5) or (9.1.7) are known to be Bethe ansatz solvable (integrable) for $\Delta_2 = 0$, respectively $V = 0$. Thus, they feature a tunable integrability breaking term important for section 9.5. Exploiting translational invariance of the model we will conveniently employ an infinite DMRG scheme, treating these systems in the thermodynamic limit.

9.2 Reminder of Luttinger Liquid Physics

In equilibrium the exactly solvable Tomonaga-Luttinger (TL) model reads [Gia03, Sch05b]

$$H_{\text{TL}} = \sum_{n>0} \left[k_n \left(v_{\text{F}} + \frac{g(k_n)}{2\pi} \right) \left(b^\dagger_n b_n + b^\dagger_{-n} b_{-n} \right) + k_n \frac{g(k_n)}{2\pi} \left(b^\dagger_{-n} b^\dagger_n + b_{-n} b_n \right) \right] , \tag{9.2.1}$$

where $b^{(\dagger)}_n$ are bosonic ladder operators associated to the densities of left- and right-moving fermions, v_{F} is the Fermi velocity, and $k_n = 2\pi n/L$, with $n \in \mathbb{Z}$. We concentrate on repulsive interactions and periodic boundary conditions for simplicity now. Later we will also reference results from an open boundary bosonization calculation, which is only slightly more complicated. The details of the potential $g(k \neq 0)$, do not affect the low energy results, as long as it decays sufficiently fast at large k (compare section 6.3). It turned out that the TL model is the infrared (low energy) fixed point model under a renormalization group flow of a large class of interacting one-dimensional models in their ungapped metallic phase[5] [Sól79]. This means that the low energy physics of models out of this so called LL *universality class* [Hal80] is the same as that of the TL model. For spinless models the fixed point is characterized by only two independent quantities: the velocity v of the elementary excitations and the LL parameter K entering exponents of algebraically decaying correlation functions, with $0 \leq K < 1$ for repulsive interaction and $K = 1$ for non-interacting theories. Results for the low energy physics of a given microscopic model (falling into the LL universality class) can then be obtained by calculating observables or correlators in the TL model and subsequently inserting v and K of the microscopic model (see below) in these expressions. Therefore, two objectives remain: (1) Solving the TL model including the calculation of fermionic expectation values (correlators) and (2) determining v and K for microscopic models. For (1) one can use bosonization, which has been introduced briefly in section 6.3. For the sake of brevity we do not want to present the full glory bosonization procedure here, but only reference some results below. Regarding (2) we note that both parameters are in general non-trivial functions depending on the details of the microscopic model and its parameters. We can determine K and v of a microscopic

[5] Like for spinless fermions featuring not too large nearest neighbor interactions (compare Fig. 3.1).

model from two independent low energy quantities, employing that the relations between these quantities and v and K are known from the TL model. An example of one of such a low energy quantity is the compressibility

$$\kappa/\kappa_0 = v_0 \frac{K}{v}. \tag{9.2.2}$$

Here we divide by the compressibility of the non-interacting model (index 0), to eliminate unknown prefactors. If the model can be treated by Bethe ansatz, then its eigenenergies can be extracted and from them two independent quantities determining K and v, e.g., the compressibility and the size dependency of the ground state energy [Gia03]. If the model is suited for a DMRG calculation one can numerically determine, e.g., the specific heat and susceptibility [Kar12b] at low T to achieve the same. For our study concerning Luttinger Liquids we will need K and v almost exclusively for the model of spinless fermions with nearest neighbor interaction defined in Eq. (9.1.3) at half-filling. For this case analytic formulae can be derived from the Bethe ansatz expression of the energy, which read

$$K = \frac{\pi}{4\eta}\,, \qquad v = J\frac{\pi \sin(2\eta)}{\pi - 2\eta}\,, \qquad 2\eta = \arccos\left(-\frac{U}{2J}\right). \tag{9.2.3}$$

With K and v at hand we are only left with analyzing the TL model. We only reference the key equilibrium results in the following [Sól79, Hal80, Lut74, Kan92, Egg95, Fab95, Gia03, Sch05b]. An index "eq" is used everywhere to distinguish the result from the later presented non-equilibrium analysis. Each result features the critical power-law behavior characterizing LL physics, which are determined solely by the TL model's $K = [1 + g(0)/(\pi v_F)]^{-1/2}$. At heart of all the results lies the calculation of the equilibrium Green's functions $G_{eq}(x,t)$ in the bulk (translation invariant) and $G_{eq}(x,x',t)$ in the boundary case, which can be done as hinted in section 6.3.

Bulk Properties

The first LL bulk property we consider is the momentum distribution $n(k) = \int dx\; e^{-ikx} i G^<_{eq}(x,0)$, which at $T = 0$ exhibits power-law behavior at low energies [Gia03, Sch05b]

$$|n_{eq}(k) - 1/2| \sim (|k - k_F|)^{(K+K^{-1}-2)/2}\,, \tag{9.2.4}$$

as long as $(K+K^{-1}-2)/2 < 1$. The continuous momentum distribution with a power-law behavior close to the Fermi momentum has to be contrasted to the characteristic jump with quasi-particle weight Z at the Fermi momentum encountered for Fermi Liquids. For $(K+K^{-1}-2)/2 > 1$ [Med99] as well as for $T > 0$ [Sch93, Kar12b] the leading dependence for $k \approx k_F$ turns linear.

The second bulk quantity we consider is the (frequency resolved) bulk local spectral function $\rho_{eq}(\omega) = \int dt' e^{i\omega t'} i[G^<_{eq}(0,t') + G^>_{eq}(0,t')]/(2\pi)$, which at $T = 0$ shows the characteristic suppression [Gia03, Sch05b]

$$\rho_{eq}(\omega) \sim |\omega|^{(K+K^{-1}-2)/2} \tag{9.2.5}$$

in the presence of interactions at low energies, because $(K+K^{-1}-2)/2 > 0$ for $0 \le K < 1$. We also introduce the bulk local spectral function $\rho^<_{eq}(\omega) = \int dt' e^{i\omega t'} i G^<_{eq}(0,t')/(2\pi)$, which is measured in photoemission spectroscopy [Fre09]. In equilibrium and for $T = 0$ it is given by

$$\rho^<_{eq}(\omega) \sim |\omega|^{(K+K^{-1}-2)/2}\Theta(-\omega)\,, \tag{9.2.6}$$

at low energies. This is a consequence of $G^<_{eq}(0,t')$ being analytical in the upper half of the complex t' plane. In section 9.4, we also consider the momentum resolved spectral function $\rho^<_{eq}(k,\omega) = \int dx \int dt' e^{-i(kx-\omega t')} i G^<_{eq}(x,t')/(2\pi)$. Its behavior is more complicated and therefore $\rho^<_{eq}(k,\omega)$ is discussed together with the steady-state results in section 9.4, where we can also refer to graphical representations of this function.

Concluding the bulk results, we present the $T = 0$ zero frequency bulk charge susceptibility $\chi(\omega = 0, q - 2k_F)$ for wave vectors close to the backscattering condition $q = 2k_F$. It diverges as

$$\chi_{eq}(\omega = 0, q - 2k_F) \sim (q - 2k_F)^{2(K-1)}\,, \tag{9.2.7}$$

for $0 \le K < 1$ [Lut74]. This result will be used again in the context of the impurity properties below.

Boundary Properties

Next, we concentrate on the density profile $n(x) = iG^<_{\text{eq}}(x,x,0)$ at $T = 0$. Boundaries[6] induce Friedel oscillations of the local density with a wave vector $2k_F$. For non-interacting systems these oscillations decay proportional to the inverse distance from the boundary $n_{\text{eq}}(x) - \nu \sim 1/x$ with ν being the filling factor. For an interacting LL the Friedel oscillations are found [Egg95] to decay as

$$\Delta n_{\text{eq}}(x) = n_{\text{eq}}(x) - \nu \sim x^{-K} \sin(2k_F x) \tag{9.2.8}$$

at large distances. Thus the decay is slower for a system with repulsive interaction ($0 \leq K < 1$) than for a non-interacting ($K = 1$) model.

Furthermore, we can obtain the (frequency resolved) local spectral function at $T = 0$ near the boundary [Fab95], which behaves as

$$\rho_{\text{eq}}(\omega) \sim |\omega|^{K^{-1}-1}, \tag{9.2.9}$$

and therefore is suppressed at low energies for $0 \leq K < 1$, as in the bulk case – albeit with different exponent.

Impurity Properties

One of the most important hallmarks of LL physics is their sensitivity towards impurities [Kan92]. For repulsive interactions the ground state density response function of a LL diverges with the Fermi momentum k_F [see Eq. (9.2.7)]. This indicates that linear response theory breaks down. In fact in a Luttinger Liquid even a single *weak impurity* acts as a strong perturbation (calling for a non-perturbative approach). For such a single weak impurity the linear conductance is expected to scale as

$$\text{weak impurity:} \qquad G_0 - G_{\text{eq}}(T) \sim T^{2(K-1)}, \tag{9.2.10}$$

with the constant homogenous chain conductance G_0. The power-law, however, holds only as long as the right hand side stays small, that is for not too small T. In terms of the equilibrium renormalization group this indicates that the perfect chain fixed point is unstable.

Fermis Golden Rule-like arguments lead to a tunneling conductance across a *weak link* (strong impurity) connecting two semi-infinite chains, each with a boundary local spectral function as given in Eq. (9.2.9), which scales as

$$\text{strong impurity:} \qquad G_{\text{eq}}(T) \sim T^{2(K^{-1}-1)}. \tag{9.2.11}$$

In contrast to the perfect chain fixed point, the open chain one is stable. With this we could not rule out – a priori – intermediate impurity fixed points. It was shown, however, that those do not exist [Ens05b].

9.3 Real-Time FRG for Closed Quantum Systems

Additionally to open quantum systems FRG can be used to tackle the real-time dynamics of closed quantum systems as well. Simply by decoupling the reservoirs $\Sigma_{\text{res}} \to 0$ we can reuse the equations derived in Chapter 4 (see also [Ken11] for more details). In contrast to open systems, we cannot set up the formalism to describe the steady-state reached for asymptotically large times directly, and thus using a formalism that explicitly handles the time dependence is imperative.

Like always when tackling non-equilibrium we employ the lowest order truncation scheme in the two-particle interaction. As outlined ($\to$ Chapter 4) to this order the self-energy acquires a renormalization group flow, which was shown to be crucial to capture the impurity LL physics in equilibrium [Kan92, And04, Ens05b]: the same truncation correctly describes the characteristic power-law scaling of the equilibrium LL properties in inhomogeneous (impurity or boundary) lattice models ($\to$ section 9.2). In such an approximation the resulting impurity exponents for the model of Eq. (9.1.3),

[6] and actually impurities as well, but this is not analyzed explicitly here.

given by K, agree to the exact ones to order $\mathcal{O}(U)$ [And04, Ens05b]. In contrast, the bulk exponent $(K + K^{-1} - 2)/2$ of $n_{\text{eq}}(k)$ and $\rho_{\text{eq}}(\omega)$ with K taken for the lattice model of Eq. (9.1.3), which is given in Eq. (9.2.3) at half-filling, is of order $\mathcal{O}(U^2)$ and thus impossible to access via our truncated FRG treatment, which captures only $\mathcal{O}(U)$ in the exponent [And04]. This behavior [exponents of bulk $\mathcal{O}(U^2)$, while exponents induced by boundaries and impurities show $\mathcal{O}(U)$] actually caries over to the non-equilibrium analysis.

For the outline of the method, we concentrate on tight-binding Hamiltonians as described in Section 3.2 and write them generally as

$$H = H_0 + H_{\text{int}}, \tag{9.3.1}$$

$$H_0 = \sum_{ij} \epsilon_{ij} c_i^\dagger c_j, \tag{9.3.2}$$

$$H_{\text{int}} = \frac{1}{4} \sum_{ijkl} \bar{u}_{ijkl} c_i^\dagger c_j^\dagger c_l c_k, \tag{9.3.3}$$

where $\bar{u}_{ijkl}$ is the antisymmetrized two-particle interaction. Note that the Hamiltonians Eqs. (9.1.3), (9.1.5) and (9.1.7) trivially fall into this class [after a Jordan-Wigner transformation ($\rightarrow$ Section 3.2.2)]. For the results presented within the FRG approach we always choose the non-interacting canonical statistical operator as the initial density matrix $\rho^0 = \rho_{\text{c}}^0 = \exp(-\beta H_0)/\operatorname{Tr}[\exp(-\beta H_0)]$. The Green's functions then read

$$g^{\text{R},\Lambda}(t,t') = \left[g^{\text{A},\Lambda}(t',t)\right]^\dagger = -i\Theta(t-t')e^{-i\epsilon(t-t')}e^{-i\Lambda(t-t')}, \tag{9.3.4}$$

$$g^{\text{K},\Lambda}(t,t') = -ig^{\text{R},\Lambda}(t,0)(1-2\bar{n})g^{\text{A},\Lambda}(0,t'), \tag{9.3.5}$$

with ϵ being the $N \times N$ matrix with entries ϵ_{ij} and $\bar{n}_{ii'} = \operatorname{Tr}\left[\rho^0 d_{i'}^\dagger d_i\right]$. The self-energy is obtained by solving the flow equation

$$\partial_\Lambda \Sigma^{\text{R},\Lambda}_{i_1 i_{1'}}(t',t) = \partial_\Lambda \Sigma^{\text{A},\Lambda}_{i_1 i_{1'}}(t',t) = -\sum_{i_2,i_2'} S^{\text{K},\Lambda}_{i_2' i_2}(t,t)\left[-i\bar{u}_{i_1 i_2 i_1' i_2'}(t)\right]\delta(t'-t), \tag{9.3.6}$$

$$\partial_\Lambda \Sigma^{\text{K},\Lambda} = 0, \tag{9.3.7}$$

with the initial conditions at $\Lambda = \infty$

$$\Sigma^{\text{R},\Lambda=\infty}_{i'i}(t',t) = \frac{1}{2}\delta(t-t')\sum_j \bar{u}_{i'jij}, \tag{9.3.8}$$

$$\Sigma^{\text{K},\Lambda=\infty}_{i'i}(t',t) = 0. \tag{9.3.9}$$

No Keldysh self-energy is generated throughout the flow. This largely simplifies the calculations. The single-scale propagator Eq. (4.3.18) reads

$$S^{\text{K},\Lambda}(t,t) = \partial_\Lambda^* G^{\text{K},\Lambda}(t,t) = -2tG^{\text{K},\Lambda}(t,t), \tag{9.3.10}$$

with the full Keldysh component of the Green's function

$$G^{\text{K},\Lambda}(t,t') = -iG^{\text{R},\Lambda}(t,0)(1-2\bar{n})G^{\text{A},\Lambda}(0,t'). \tag{9.3.11}$$

Observables can be calculated by using the formula given in Section 4.1.3. However it is well known from equilibrium that certain operators – so called composite operators – should not be evaluated from the Green's function but rather should be implemented by their own flow equation (which trivially does not couple back to the other flow equations) [Ens05a, Zin02]. The occupancy is one of such composite operators and one might wonder whether a similar problem shows up in the approach followed here using the Keldysh framework. To check this we derive the flow equation for

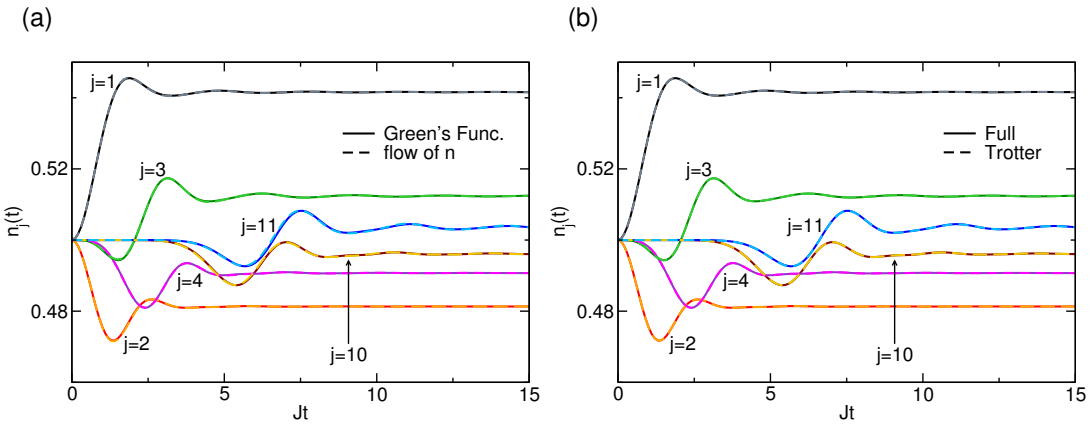


Figure 9.1.: We study the quench dynamics of a system described by the nearest neighbor Hamiltonian of Eq. (9.1.3). The initial preparation is given by the ground state of $H_{\text{ini}} = H_{\text{SF}}(U = 0)$. The time evolution is performed with respect to $H_{\text{fin}} = H_{\text{SF}}(U)$. We focus on $N = 1000$ and $U = 0.2$. Left: Comparison of the occupancy obtained by Eq. (4.1.63) or by its own flow equation (9.3.12). Right: The same but comparing results of the occupancy obtained with and without a Trotter decomposition ($\Delta t = 0.1$). The agreement in either case is excellent.

the occupancy

$$\partial_\Lambda n_j^\Lambda(t) = \frac{1}{2}\left[iS^{\text{K}}(t) - \{\Omega(t) + \text{H.c.}\}\right], \tag{9.3.12}$$

$$\Omega(t) = \int_0^\infty dt_1\; G^{\text{R}}(t,t_1)\left[\partial_\Lambda \Sigma^{\text{R}}(t_1)\right] G^{\text{R}}(t_1,0)(1-2\bar{n})G^{\text{A}}(0,t), \tag{9.3.13}$$

$$\lim_{\Lambda\to\infty} n_j^\Lambda(t) = \frac{1}{2}. \tag{9.3.14}$$

It turns out that for the Keldysh FRG both approaches [(1) calculating the occupancy via the Green's function as in Eq. (4.1.63) and (2) using Eq. (9.3.12)] yield the same results. This is shown in Fig. 9.1(a) for the nearest neighbor Hamiltonian given by Eq. (9.1.3). We show the dynamics resulting out of a quantum quench, where the system is prepared in the ground state of $H_{\text{ini}} = H_0 = H_{\text{SF}}(U = 0)$, and subsequently time evolved with $H_{\text{fin}} = H_{\text{SF}}(U)$. Motivated by this agreement we focus on calculating the occupancy via Green's functions only from now on.

Finally, numerically it proves useful to transform the flow parameter like $x = \exp(-2\Lambda t)$ everywhere.

9.3.1 Efficiently Evaluating Keldysh Green's Function Using GPU...

We can calculate $G^{\text{K},\Lambda}(t,t')$ very efficiently by using an iterative procedure similar to the one outlined in section 7.2. First, we discretize time in steps such that during one small step Δt the time dependent self-energy can be set constant. We always vary Δt such that we can ensure that further reduction of Δt does not lead to any changes visible on the scale of the respective plots. We use

$$G^{\text{R},\Lambda}(t,t')G^{\text{R},\Lambda}(t',t'') = -i\Theta(t-t')\Theta(t'-t'')G^{\text{R},\Lambda}(t,t''). \tag{9.3.15}$$

$$G^{\text{R},\Lambda}(t,t') = \left[G^{\text{A},\Lambda}(t',t)\right]^\dagger, \tag{9.3.16}$$

to write $G^{\text{R}}(t,t')$ as a product of Green's functions [Ken12a]

$$G^{\text{R},\Lambda}(t_1+\Delta t,t_1) = -ie^{-i[\epsilon+\bar{\Sigma}^{\text{R},\Lambda}(t_1)]\Delta t}e^{-i\Lambda(t-t')}, \tag{9.3.17}$$

where $\bar{\Sigma}^{R,\Lambda}(t_1)$ is the time-averaged self-energy over the interval $(t_1, t_1 + \Delta t)$. Iteratively, we calculate the interacting Keldysh Green's function $G^{K,\Lambda}(t,t)$ by employing

$$G^{K,\Lambda}(t+\Delta t, t+\Delta t) = G^{R,\Lambda}(t+\Delta t, t) G^{K,\Lambda}(t,t) G^{R,\Lambda}(t, t+\Delta t), \tag{9.3.18}$$

$$G^{K,\Lambda}(0,0) = -i(1-2\bar{n}). \tag{9.3.19}$$

If we denote the number of sites in the chain by N, for each time step two matrix exponentials of $N \times N$ matrices have to be performed and multiplied with the Keldysh component of the Green's function of the previous one. This renders the problem a natural candidate for graphics processing unit (GPU) supported algorithms, in which these operations can be performed very rapidly. We therefore employ such an GPU assisted algorithm to compute the results shown. The number of time steps N_t needed to obtain sufficient accuracy (and resolution) as well as to reach times which are large enough for the relevant questions (steady-state) enters the number of flow equations to be solved. For a nearest neighbor Hamiltonian like the one of Eq. (9.1.3) one ends up with a set of $(3N-2)N_t$ coupled differential equations. Due to the nearest neighbor structure of the interaction only $3N-2$ components of the self-energy flow for each of the N_t time steps. With this procedure we can therefore easily access $N = 1000$ lattice sites as well as a rather large number of time steps $N_t = 1600$ (usually resulting in times upto 200 in units of the hopping).

9.3.2 ... or Trotter Decompositions

As we are interested in time steps Δt chosen small enough such that the self-energy can be set constant throughout a single time step one can also employ a Suzuki-Trotter decomposition as used in DMRG ($\rightarrow$ Section 5.6.1). One can simply decompose the effective single-particle matrix $\epsilon + \bar{\Sigma}^{R,\Lambda}(t)$ in Eq. (9.3.17) into odd and even bonds and employ a second- or fourth-order decomposition scheme as in Eqs. (5.6.4) or (5.6.5), respectively. The numerical effort of calculating and applying a $N \times N$ matrix exponential reduces to successively applying 2×2 (4×4) matrices for Hamiltonians featuring nearest (and next-nearest) neighbor interaction. Fortunately, we can also test this approximate evaluation of G^R against the full numerics to show explicitly that the decomposition poses an unimportant approximation. We depict this explicitly for the nearest neighbor Hamiltonian used also above in Fig. 9.1(b).

9.3.3 Benchmark: Dynamics of Interacting Fermions

As a first test, we study the dynamics of interacting fermions after a quantum quench. We focus on the setup used for Fig. 9.1 above, where the interaction U is quenched from zero to some final value. Fig. 9.2(a) shows the access density $n_j(t) - \nu$, with the filling ν, for fixed site j starting out of the non-interacting ground state. We concentrate on half-filling $\nu = 0.5$. With FRG we can reach times of the order of a few $10^2/J$. This has to be contrasted to the DMRG approach outlined which becomes unreliable for times of the order of $10/J$ [Kar12c]. The main plot and the left inset shows that a signal originating from the left boundary travels through the system. Obviously, a similar signal is generated at the right end. For a spatial region in which the left signal passed through and the right one did not enter yet the density becomes stationary. For $t \approx 10^2/J$ and sites j up to $\mathcal{O}(10^2)$ the physics is thus dominated by the steady-state and barely suffers from finite size effects[7]. The two signals clearly propagate with the LL velocity v of the elementary excitations ($\rightarrow$ Section 9.2) [Cal07, Lan09, Gan12]. Our method provides an excellent approximation to the exact v [right inset of Fig. 9.2(a)] obtained from Eq. (9.2.3).

In Fig. 9.2(b) we benchmark the validity of the approximate FRG data versus numerically exact DMRG results. We focus on the same quench as described above in which the interaction amplitude U in Eq. (9.1.3) is abruptly changed from $U/J = 0$ to $U/J = 0.2$. Interestingly, on the scale of the plot the two datasets are indistinguishable for all sites j and all times reachable with DMRG [Sch11b, Dal04, Whi04, Dal04]. The numerical parameters of the iterative ground state search ($\rightarrow$

[7] Finite size effects steaming from the ground state preparation for this particular quench ($U = 0$ to U finite) are very small.

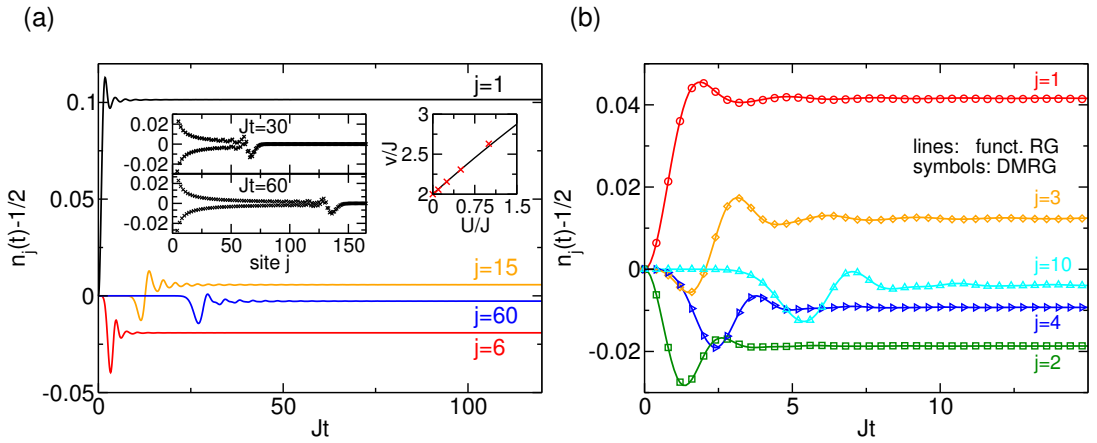


Figure 9.2.: Left: FRG data for the time evolution of $n_j(t) - \nu$ at half filling $\nu = 1/2$ after a quench in the interaction amplitude for the model defined in Eq. (9.1.3) from $U/J = 0$ to $U/J = 0.5$ for $N = 10^3$, and different sites j. The initial preparation is given by the non-interacting ground state. Left inset: Friedel oscillations induced by the boundary and the propagation of a main signal from the boundary to $j \approx vt$ for two values of t. Right inset: Velocity of the main signal for different U (symbols). The exact Bethe ansatz v (line) from Eq. (9.2.3) is in excellent agreement with our data. Right: Comparison of FRG and DMRG data for the time evolution of $n_j(t) - \nu$ at half filling $\nu = 1/2$ after the same quench protocol as in (a) from $U/J = 0$ to $U/J = 0.2$ for $N = 10^2$ and different sites j. FRG and the numerically exact DMRG are in excellent agreement for times reachable by the DMRG calculation

Section 5.5) as well as the time evolution algorithm (→ Section 5.6) were chosen such that the data is converged on the scale of the plot. The excellent agreement of the results obtained by FRG and DMRG (a) strengthens our confidence in the FRG approach for the following analysis and (b) shows that within FRG we correctly incorporate the high energy physics of the underlying lattice model, which is crucial for short times as well as the crossover regime from short to large times. Since the FRG is directly applied to the microscopic model, i.e. without the need of mapping it to an effective low energy field-theory, the information about the high energy modes is not lost. Although the DMRG results might look sufficiently relaxed to accurately describe the steady-state reached asymptotically on first glance (at least for the j shown) in Fig. 9.2(b), this is actually not the case for the sensitive analysis of the steady-state, including a search for power-laws, we have in mind next. We want to extract the exponents of these power-laws, via a logarithmic derivative, a very accurate measure. For this we need to access much larger systems sizes and times than shown in Fig. 9.2(b).

9.4 Luttinger Liquid properties in Non-Thermal Steady-States

With the machinery outlined before we want to address the question how the steady-state of a quantum system reached after an interaction quench can be characterized. Specifically, we are concerned with systems that in equilibrium would be classified as LLs. If a quantum quench is performed for parameters, within the LL regime (in equilibrium) can a signature of Luttinger physics also be found in the steady-state reached?

Some of the most important hallmarks of LLs in equilibrium were recapitulated in section 9.2. As introducing boundaries and impurities proved to bear significant consequences for the low energy properties (and as FRG has proven to correctly describe the corresponding equilibrium physics); such as the vanishing linear conductance $G \sim T^{2K^{-1}-2}$ for temperature $T \to 0$, in the following we will consider such setups as an ideal testing ground for the central question raised.

Furthermore, we will investigate the homogeneous (momentum resolved) spectral function which turns out to provide a sensitive characterization of the non-equilibriium steady-state reached after

a quantum quench. Differences between equilibrium (possibly finite temperature) and steady-state spectral function are so prominent that future experiments should be able to detect them (for a recent of such experiments for a LL – albeit in equilibrium – see [Blu11]).

The logic is analogous to the equilibrium case: in equilibrium one can use the infrared fixed point model, the TL model, to describe the low energy physics of a large class of models including microscopic ones (→ section 9.2). We now derive predictions for the steady-state reached in the TL model after an interaction quench has been performed and compare those to the steady-state reached after a similar quench in the microscopic model of Eq. (9.1.3). We want to concentrate on an often studied scenario where the interaction is suddenly quenched from zero to some final value. For the spectral function we additionally consider the inverse quench, where the interaction is suddenly switched off. Thus, the natural next step is to first derive the corresponding steady-state expressions for an interaction quenched LL. After this we compare those expressions to what we find for the microscopic model of Eq. (9.1.3) within our FRG (for the boundary and the impurity physics) or DMRG (for the bulk spectral function) approach.

9.4.1 The Tomonaga-Luttinger Model

Treating quench dynamics within the Tomonaga-Luttinger model is not more complicated than in equilibrium. This is due to the fact that the time evolution can be found trivially by explicit diagonalization. We re-iterate the result of section 6.3, where we used the Bogoliubov transform

$$a_n = \cosh(u_n) b_n - \sinh(u_n) b_{-n}^\dagger \,, \quad e^{2u_n} = K_n = \sqrt{\frac{1}{1+g(q_n)/\pi v_F}} \,, \tag{9.4.1}$$

to diagonalize the TL model

$$\begin{aligned} H_{\mathrm{TL}} &= \sum_{n>0} \left\{ k_n \left(v_F + \frac{g(k_n)}{2\pi} \right) \left(b_n^\dagger b_n + b_{-n}^\dagger b_{-n} \right) + k_n \frac{g(k_n)}{2\pi} \left(b_n^\dagger b_{-n}^\dagger + b_{-n} b_n \right) \right\} \\ &= \sum_{n\neq 0} |k_n| v_F \sqrt{1 + \frac{g(k_n)}{\pi v_F}} a_n^\dagger a_n \,. \end{aligned} \tag{9.4.2}$$

With this the time evolution can be determined by $a_n(t) = \exp(-it|k_n|v_F/\sqrt{K_n}) a_n$. Again we will not show the full calculation but rather reference the relevant results [Ken13c, Ken14a]. A comparative summary of all the equilibrium and steady-state exponents derived for the TL model in the following is given in table 9.1.

Boundary and Impurity Physics

We study a sudden quench in the interaction from the non-interacting TL model $g_{\mathrm{ini}}(k) = 0$ to some finite $g_{\mathrm{fin}}(k)$. With this, one can derive closed analytical expressions for the time dependent access density $n_t(x) - \nu$ in the presence of a boundary, with x being the distance from it, the boundary spectral function $\rho_t(\omega)$, and the bulk density response $\chi_t(q,\omega)$ (needed to determine impurity physics below) defined analogous to the equilibrium case [Ken13c]. For the TL model one can analytically perform the thermodynamic limit, after which the steady-state can be accessed by $t \to \infty$. We find that the above quantities converge and their steady-state limits are indicated by dropping the index t and replacing it by "ss" to distinguish it from the equilibrium quantities (indexed "eq" of section 9.2).

For the Tomonaga-Luttinger model (being effectively non-interacting) one can verify that the same $t \to \infty$ expectation values can be computed using the statistical operator of a GGE [Rig07, Caz06, Iuc09, Ken10, Ren12, Ess12], with the conserved quantities being the mode occupancies of the diagonal representation (compare section 9.1.1).

The calculation shows that at $T = 0$, with the initial state given by the non-interacting ground state[8], the steady-state reached after the quench is "critical", in the sense that it is characterized by

[8] This holds also for the more general case where the quench is not performed staring from $g(q) = 0$. The results can be found in [Ken13c].

observable/correl. function	variable	eq. exp.	steady-state exp.
momentum distribution $n(k)$	$\lvert k-k_F\rvert$	$(K+K^{-1}-2)/2$	$(K^2+K^{-2}-2)/4$
local bulk spectral function ρ	$\lvert\omega\rvert$	$(K+K^{-1}-2)/2$	$(K^2+K^{-2}-2)/4$
access density Δn	x	$-K$	$-(K^2+1)/2$
local boundary spectral function ρ	$\lvert\omega\rvert$	$K^{-1}-1$	$(K^{-2}-1)/2$
bulk χ at $\omega=0$	$q-2k_F$	$2(K-1)$	K^2-1

impurity strength	stable	eq. exp.	steady-state exp.
weak	no	$2(K-1)$	K^2-1
strong	yes	$2(K^{-1}-1)$	$K^{-2}-1$

TABLE 9.1.: Top: Equilibrium and steady-state scaling exponents of different observables and correlation functions (at $T=0$). Bottom: Equilibrium and steady-state scaling of the conductance $G(T)$ in the presence of a single impurity.

power-law scaling [Caz06, Uhr09, Iuc09, Ren12]. These characteristic power-laws manifest in different observables with exponents which in general are different to the exponents found in equilibrium of section 9.2 [Gia03, Sch05b, Hal80, Sól79, Lut74, Kan92]. It was found that, just as in equilibrium, they are all determined by the parameter $K=[1+g_{\text{fin}}(0)/(\pi v_F)]^{-1/2}$ of the TL model after the quench. Therefore, like in equilibrium, the precise form of the potential is not relevant for the critical power-laws. For our calculations we always assume $g_{\text{fin}}(q)=ge^{-[(q/q_c)^2/2]}$ if not explicitly stated otherwise. We restrict our depiction to the observables/correlation functions of interest from now on, which are the same ones as outlined in the equilibrium section 9.2.

First, we consider the access density $\Delta n_{\text{ss}}(x)=n_{\text{ss}}(x)-\nu$, where ν denotes the filling. For large distances from the boundary x it falls off as

$$\Delta n_{\text{ss}}(x)\sim x^{-(K^2+1)/2}\sin(2k_F x), \tag{9.4.3}$$

at $T=0$. In both the equilibrium and the steady-state case we find decaying Friedel oscillations with frequency $2k_F$. As the (repulsive) interaction strength is increased and thus K becomes smaller (starting at $K=1$ for the non-interacting case), the access density in the presence of an open boundary in either case falls off slower than for vanishing two-particle interaction. However, the equilibrium and steady-state expressions show different exponents for the decay of the Friedel oscillations. This difference between ground- and steady-state exponents in the TL model was examined before considering other observables and correlation functions [Caz06, Uhr09, Iuc09, Ren12].

Next, we analyze the frequency resolved boundary spectral function $\rho(\omega)$ at small $|\omega|$ and $T=0$ near the boundary. In the steady-state it is suppressed as

$$|\rho_{\text{ss}}(\omega)-\rho_{\text{ss}}(0)|\sim|\omega|^{(K^{-2}-1)/2}. \tag{9.4.4}$$

In contrast to the equilibrium case, in the steady-state reached after the interaction quench the spectral function takes a finite value $\rho_{\text{ss}}(0)$ at $\omega=0$. This will be investigated in more detail in the next section [Ken14a]. Again, the exponents of the power-law behavior with which the $\omega=0$ spectral weights are approached differ between the equilibrium and steady-state situation, but both increase with increasing interaction.

Last but not least, we discuss the zero frequency bulk charge susceptibility $\chi(\omega=0)$ for wave vectors close to the backscattering condition $q=2k_F$

$$\chi_{\text{ss}}(\omega=0,q-2k_F)\sim(q-2k_F)^{K^2-1}. \tag{9.4.5}$$

Like in equilibrium this quantity diverges (as $K<1$) in the steady-state reached for asymptotic times, but once more with a different exponent.

The scaling behavior of the bulk static density response $\chi_{ss}(q, \omega = 0)$ allows us to make predictions for how the steady-state reacts to a single impurity. For repulsive interactions $K^2 - 1 < 0$ and χ diverges for $q \to 2k_F$. Therefore, just like in equilibrium, even a weak single impurity strongly disturbs the homogenous system. Next, we apply an infinitesimal bias voltage V across the impurity to access the steady-state linear conductance $G = dI_{ss}/dV$ (with the stationary current I^{ss}). Within this framework it is expected to scale as

$$\text{weak impurity:} \qquad G_0 - G_{ss}(T) \sim T^{K^2-1}, \tag{9.4.6}$$

with the constant homogenous chain conductance G_0. The power-law only holds as long as the right hand side stays small, that is for not too small T. As in equilibrium, this indicates that the perfect chain fixed point is unstable. In contrast, the steady-state analogue of the open chain one is stable as follows from the scaling of the local spectral function. Again, employing Fermis Golden Rule-like arguments (compare section 9.2) leads to

$$\text{strong impurity:} \qquad G_{ss} \sim T^{K^{-2}-1}, \tag{9.4.7}$$

in a temperature regime which (in contrast to equilibrium) at the lower end is cut off by the finite spectral weight at $\omega = 0$ [see Eq. (9.4.4)]. Just like in equilibrium these arguments cannot rule out intermediate impurity fixed points.

Below, we will scrutinize whether the concept of LL universality holds for the steady-state decay of the Friedel oscillations as well as in the context of weak and strong impurity scaling laws of $G_{ss}(T)$ also for microscopic models within FRG. Before doing so we will outline, however, what can be found for the bulk spectral properties in the TL model.

Spectral Properties

We saw above, that the analytical expression for observables and correlation functions of LLs in equilibrium and for the relaxed steady-state reveal different exponents in terms of K. One thus might be tempted to conclude that measuring one of the described quantities allows to distinguish the LL ground and steady-states experimentally. However, for an experimental system K is usually unknown and measuring a single exponent does thus not allow to conclude which of the states is realized. Therefore, K would first have to be determined (within some bounds) from the measurement of another observable. Distinguishing the two states would therefore require a precise determination of two exponents which is hardly achievable. We next show that the *spectral properties* are more suitable to distinguish the two states.

We concentrate on the bulk case now and recall that the lesser Green's function $iG_t^<(x, t') = \langle \psi^\dagger(0,0)\psi(x,t')\rangle_{\rho(t)}$ determines spectral properties by a Fourier transform with respect to t'. We have used t in the subindex and t' as a function argument to distinguish this definition of the lesser Green's function from the two-times Green's functions of chapter 4, which are related by $G_t^<(x, t') = -G^<(x, t, t' + t)$. The definition introduced here, however, is more convenient for what follows. For comparison we consider three different initial conditions for $\rho_{ini} = \rho(0)$:

1. $\rho_{ini} = |gs\rangle\langle gs|$, with the interacting ground state $|gs\rangle$, leading to the t independent ground state Green's function.

2. $\rho_{ini} = |gs_0\rangle\langle gs_0|$, with the non-interacting ground state $|gs_0\rangle$, leading to the t *dependent* Green's function of the quenched system.

3. $\rho_{ini} = \exp(-H/T)/Z$ with the (canonical) partition function Z, leading to the temperature T equilibrium Green's function (t independent).

The subsequent time evolution of these initial density matrices is then again performed with the interacting TL Hamiltonian. The initial conditions labelled by 1. and 3. are the ones known from an equilibrium analysis (for $T = 0$ and finite T, respectively). To obtain the *dynamical* correlation function following from the second initial condition in the limit $iG_{ss}^<(x, t') = \lim_{t\to\infty} iG_t^<(x, t')$ we

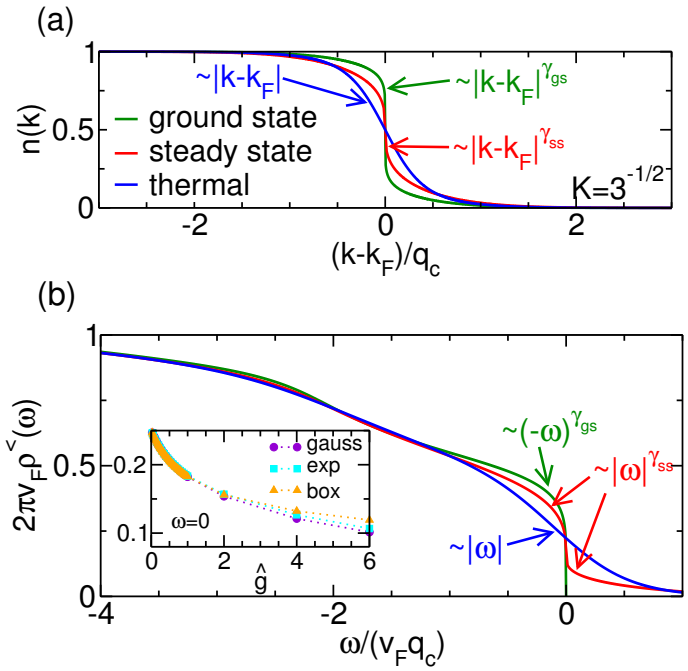


Figure 9.3.: (a) The TL model momentum distribution functions of the ground state, the non-equilibrium steady-state following the interaction quench with $g_{\text{fin}}(0) = g = 2\pi v_F$, and the thermal equilibrium state with temperature $T/(v_F q_c) \approx 0.2804$ for which the average energy is equal to the one quenched into the system. (b) The corresponding momentum integrated spectral functions. The smooth features at $\omega/(v_F q_c)$ of order 1 are non-universal and depend on the chosen potential. The inset of (b) shows the non-universal $2\pi v_F \rho^<_{\text{ss}}(0)$ as a function of the interaction $\hat{g} = g/(\pi v_F)$ for the Gaußian potential, an exponential one $g_{\text{fin}}(q) = g e^{-|q/q_c|}$, and a box potential $g_{\text{fin}}(q) = g\Theta(q_c - |q|)$.

can either perform the thermodynamic limit and afterwards take $t \to \infty$ or we can, as for the impurity study, compute $iG^<_{\text{ss}}(x,t')$ for $L \to \infty$ [Ess12] directly by

$$iG^<_{\text{ss}}(x,t') = \left\langle \psi^\dagger(0,0)\psi(x,t') \right\rangle_{\rho_{\text{GGE}}} , \tag{9.4.8}$$

with the GGE density matrix $\rho_{\text{GGE}} = \exp\left(-\sum_{n\neq 0} \lambda_n a_n^\dagger a_n\right)/Z_{\text{GGE}}$. The Lagrange multipliers λ_n are fixed by the conserved eigenmode occupancies $N_n = a_n^\dagger a_n$ such that $\langle \text{gs}_0 | N_n | \text{gs}_0 \rangle = \langle N_n \rangle_{\rho_{\text{GGE}}}$. Afterwards, the momentum distribution $n(k)$ and the spectral function $\rho^<(\omega)$ can be obtained by numerically performing the momentum integral as well as the corresponding Fourier integral.

We additionally want to consider the momentum resolved spectral function $\rho^<(k,\omega)$. To determine this more complicated function we resort to an often applied ad hoc procedure in which $\omega(k) = |k| v_F \sqrt{1 + \frac{g(k)}{\pi v_F}}$ is replaced by its lowest order expansion vk with the renormalized velocity v and the momentum integral is regularized in the ultraviolet by $e^{-|q/q_c|}$. The consequences of this *approximation* [Med99] are discussed below. Within this ad hoc approximation the q integral can be performed analytically and the remaining Fourier integrals numerically.

In Fig. 9.3(a) we show the ground state, the steady-state as well as the thermal $n(k)$. For the latter T is chosen such that the average energy corresponds to the energy quenched into the system [see also Figs. 9.3(b) and 9.4]. The steady-state is characterized by a power-law

$$|1/2 - n_{\text{ss}}(k)| \sim (|k - k_F|/q_c)^{\gamma_{\text{ss}}} , \tag{9.4.9}$$

with $\gamma_{\text{ss}} = (K^2 + K^{-2} - 2)/4$ [Caz06, Uhr09, Ren12]. This has to be contrasted to the ground state, where the power-law shows the different exponent $\gamma_{\text{gs}} = (K + K^{-1} - 2)/2$ (see section 9.2). This

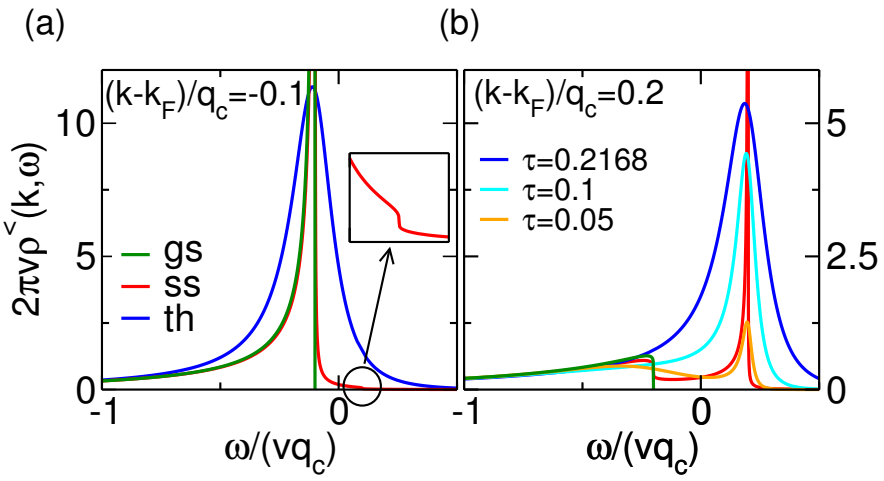


Figure 9.4.: The momentum resolved spectral functions of the TL model in the ground state, the non-equilibrium steady-state following the interaction quench with $g_{\text{fin}}(0) = g = 2\pi v_F$, and the thermal equilibrium state with temperature $\tau = T/(vq_c) \approx 0.2168$ for which the average energy is equal to the one quenched into the system. The steady-state function shows a characteristic peak at positive energies for $k - k_F > 0$. For this case thermal curves with two additional τ are shown for comparison.

holds in both cases for all $\gamma < 1$, while for $\gamma > 1$ [Med99] as well as for $T > 0$ [Sch93, Kar12b] the leading dependence for $k \approx k_F$ turns linear. Still the difference in ground state and steady-state manifest only on the quantitative level in the exponent.

Finally, the spectral function, studied next, will lift this similarity in behavior. To this end we show the three $\rho^<(\omega)$ for ground state, steady-state as well as a thermal one with the same energy as in the quenched system in Fig. 9.3(b). In the ground state $\rho^<_{\text{gs}} \sim [-\omega/(v_F q_c)]^{\gamma_{\text{gs}}}$ for $\omega \leq 0$ [Gia03, Sch05b], while $\rho_{\text{gs}} = 0$ for $\omega > 0$. For fixed T and $|\omega|/T \ll 1$ the corrections to the finite weight at $\omega = 0$ are found to be linear in ω [Sch93]. The vanishing of the weight in the ground state for $\omega \geq 0$ as well as the linear behavior close to $\omega = 0$ in thermal equilibrium can be used to distinguish these states from the steady-state. As shown in Fig. 9.3(b) $\rho^<_{\text{ss}}$ has weight for all ω and is finite at $\omega = 0$. The zero frequency weight is non-universal, meaning that it does not only depend on v and K, but on the details of the q dependence of the potential chosen in the Tomonaga-Luttinger model of Eq. (9.2.1) [see inset of Fig. 9.3(b)]. The zero frequency finite weight of $\rho^<_{\text{th}}(0)$ and $\rho^<_{\text{ss}}(0)$ behave opposite on increasing the interaction. Using asymptotic analysis one gets [Ken14a]

$$|\rho^<_{\text{ss}}(\omega) - \rho^<_{\text{ss}}(0)| \sim |\omega|^{\gamma_{\text{ss}}} \quad \text{for: } \omega \to 0^- \text{ and } \omega \to 0^+, \tag{9.4.10}$$

which holds again only as long as $\gamma_{\text{ss}} < 1$, for the opposite case we find a linear dependence $\rho^<_{\text{ss}}(\omega) - \rho^<_{\text{ss}}(0) \sim -\omega$. Summed up, $\rho^<_{\text{ss}}(0)$ is finite and non-universal, but the corrections to it show universal critical power-law scaling. This rather unusual behavior is unique to the steady-state spectral function.

From an experimental point of view even easier to detect are the hallmarks of the steady-state found in the momentum resolved spectral function $\rho^<_{\text{ss}}(k, \omega)$.

$k - k_F < 0$:

Although, for $k - k_F < 0$ the spectral functions of Fig. 9.4(a) are all *dominated* by a peak located at $\omega = v(k - k_F)$, important changes show up for $\omega > v(k - k_F)$. In sharp contrast to $\rho^<_{\text{gs}}$, which vanishes for $\omega > v(k - k_F)$, $\rho^<_{\text{ss}}$ carries weight also for these larger energies. In fact, a weak second structure is visible at $\omega = -v(k - k_F)$ [inset of Fig. 9.4(a)]. At $\omega = \pm v(k - k_F)$ power-laws show up for the steady-state results, however we expect that without the ad hoc approximation employed here the spectra look very similar but are most likely not characterized by algebraic singularities [Med99]. For a finite T canonical ensemble the dominating peak is broadened.

$k - k_F > 0$:

The most striking difference however between the steady-state spectra and their ground state or thermal counterparts is found for $k - k_F > 0$ [Fig. 9.4(b)]. In this case $\rho^<_{gs}$ only shows a weak bump around $\omega = -v(k - k_F)$ and vanishes for larger energies. The dominating feature of $\rho^<_{ss}$ is a very narrow peak at *positive energies* $\omega = v(k - k_F)$. Again we expect that only within the ad hoc procedure its form is given by a power-law. The peak can be clearly distinguished from the finite T case as it is much more narrow. To show this strong difference we also show the latter for two additional T smaller than the one determined by the energy quenched into the system in Fig. 9.4(b).

9.4.2 Lattice Model: Spinless Fermions

Finally, we compare the non-equilibrium results derived in the previous section for the TL model to those found for lattice models. It is a priori not clear whether the results obtained from the Tomonaga-Luttinger model can be applied to a microscopic lattice model in the non-equilibrium steady-state. Naively, this might actually sound rather counter-intuitive as not only the low energies contribute to the dynamics following a global quench. We will see next however, that indeed the (non-equilibrium) steady-state shows prominent LL properties. A similar result was found for the long-time evolution *towards* the steady-state in [Kar12c]. The Hamiltonian of interest in the following is the one of Eq. (9.1.3) in its Luttinger Liquid regime $|U/J| < 2$. In equilibrium this model can be treated (a) by Bethe ansatz and (b) shows universal LL physics with K and v known [Hal80]. For the case of half-filling mainly studied here those are given in Eq. (9.2.3). For the Luttinger Liquid phase $|U/J| < 2$ it is unclear whether because of (a) the steady-state after an interaction quench is described by a GGE. The results of [Poz14, Wou14], which showed that the GGE does not correctly describe the steady-state of this model can only be applied to the gapped phase $|U/J| > 2$. Even if the GGE is applicable the corresponding statistical operator was so far neither constructed nor was a proof of its existence given. Importantly, our analysis does not rely on any such assumption.

Again, we concentrate first on the situation where a boundary or an impurity [here Eq. (9.1.3) is supplemented by Eq. (9.1.4)] is present. This case can efficiently be tackled with FRG. Afterwards, we will show that similar features as found in the TL model for the spectral function can also be obtained in lattice models. This study will rely on a DMRG calculation.

Boundary and Impurity Physics

We consider a quench protocol analogue to the one used in the TL model. The initial preparation corresponds to the canonical ensemble of the non-interacting Hamiltonian $U = 0$ with temperature T (including $T = 0$). The subsequent time evolution is performed with respect to finite U.

Already from the left inset of Fig. 9.2(a) we see that in analogy to the ground state density [And04] the steady-state one n_j^{ss} shows Friedel oscillations in the presence of a boundary with the same frequency $2k_F$ as in the ground state [see the $j < 80$ region of the lower part of the left inset of Fig. 9.2(a)]. Now we compare their decay to the one predicted from the TL model. Figure 9.5(a) shows the logarithmic derivative of $|n_j^{ss} - 1/2|$, that is an effective exponent. The dashed lines indicate the prediction from the TL model of Table 9.1, where we use the exact lattice model K from Eq. (9.2.3). Using the FRG approach we can reach times large enough that the logarithmic derivative is not spoiled by (small) residual fluctuations. The power-law decay found is consistent with the exponent predicted from the TL model. This finding is the first indication of LL universality of the steady-state. The differences between the exact exponent and our result showing up are of order $(U/J)^2$, which are not captured by the truncate FRG. We are not restricted to the case of half filling and a similar behavior is found away from it. The inset of Fig. 9.2(a) shows $|n_j^{ss} - \nu|$ for $\nu = 0.375$ on a log-log scale and the corresponding TL model prediction as a red line[9].

Next we compute the steady-state linear conductance of the lattice model. We consider the canonical density matrix ρ_c^0 (with $T > 0$) corresponding to $H_{SF}(U = 0) + H_{imp}(h)$ (h determining the impurity strength) as the initial state. The time evolution is then performed with $H_{SF}(U >$

[9] In this case K for the lattice model was determined by a numerical solution of the Bethe Ansatz expression of the energy.

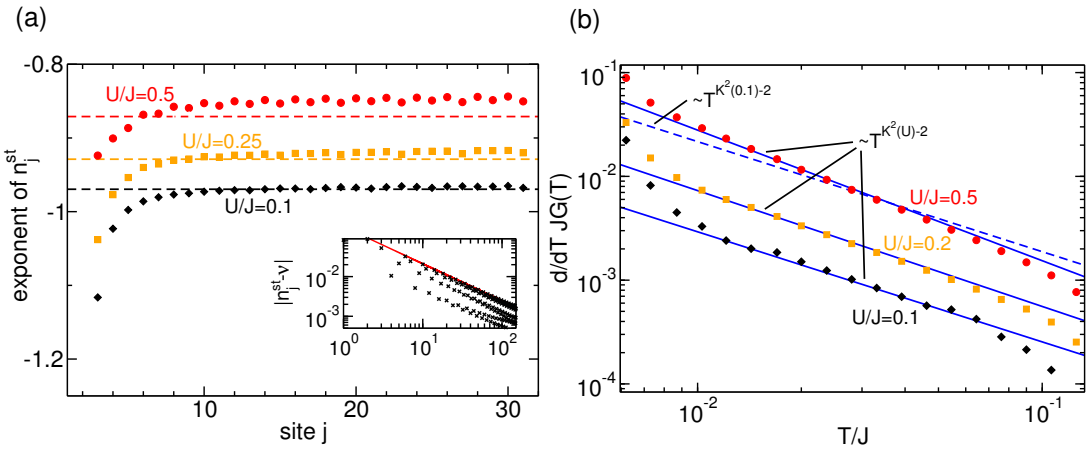


Figure 9.5.: Left: FRG data for the effective exponent of the Friedel oscillations of the steady-state density n_j^{ss} for $\nu = 1/2$, $N = 10^3$, and $T = 0$ determined by taking the logarithmic derivative. The predictions from the TL model with the exact lattice model K (dashed lines) are consistent with our results. The inset shows $|n_j^{ss} - \nu|$ at $\nu = 0.375$ and $U/J = 0.25$ (symbols). The line is the TL model prediction. Right: FRG data for the temperature derivative of the steady-state linear conductance of our lattice model for a weak impurity $h/J = 0.05$, filling $\nu = 1/2$, and $N = 10^3$ (symbols). The prediction from the TL model with the exact lattice model K is shown as the solid lines. To emphasize the sizable differences in the exponents we have added a power-law with the $U/J = 0.1$ exponent as the dashed line to the $U/J = 0.5$ data.

$0) + H_{\text{imp}}(h)$ supplemented by onsite energies $V/2$ $(-V/2)$ for all $j \leq N/2$ $(j > N/2)$. Then we can calculate the current $I(t)$ across the impurity bond via Eq. (4.1.68). Similarly to the occupancy, the current becomes stationary for t of the order of $10^2/J$. We take V to be the smallest energy scale of the problem (typically $V = 10^{-3}J$) to capture the purely linear regime $I^{ss} = GV$. In our lattice model for $T \gtrapprox J$ we find $G(T) \sim T^{-1}$ [Ens05b], which is a band effect [see the inset of Fig. 9.6]. Universal scaling of the conductance predicted by the TL model is only expected for the regime $T \ll J$.

We start with the case of weak impurities. First, we take the derivative of G with respect to T to eliminate the constant G_0. Based on the TL model we expect to find $dG/dT \sim T^{K^2-2}$. Over roughly one order of magnitude the FRG data follow the TL model prediction with the exact K of our lattice model; see Fig. 9.5(b). The deviations for $T/J > 0.1$ indicate the crossover to the non-universal $G(T) \sim T^{-1}$ regime, described above. The reason for the ones for $T/J < 0.01$ is two-fold. As discussed the scaling only holds as long as T does not become too small. Additionally, the finite energy level spacing $\delta_N = v_F/N$ $(= 2 \cdot 10^{-3}J$ for the parameters of the plot) is an energy scale of the problem which cuts off any universal behavior [And04, Ens05b]. The latter is an artefact of our treatment of finite systems. For small h and $T/J \in [0.1, 0.005]$, $G_0 - G(T) \ll 1$. Thus our analysis requires very accurate data. To minimize the error due to small residual oscillations of $I(t)$ present even for t of the order of $10^2/J$ we additionally averaged the data at large t over a small time interval.

For the strong impurity case we present our results for $G(T)$ in the inset of Fig. 9.6. Here no t averaging of our data is necessary to yield very accurate results. The logarithmic derivative gives a smooth curve. The crossover from the non-universal T^{-1} behavior at large T to the TL model prediction $T^{K^{-2}-1}$ at small ones is clearly visible in the data. For $T \to 0$ the scaling is cut off by two different sources: (1) The finite size scale δ_N as well as (2) the finite spectral function at $\omega = 0$ [see Eq. (9.4.4)]. Therefore, for both the limit of strong as well as the limit of weak impurities our results for the linear conductance of the lattice model agree to the TL model prediction: our second indication of the LL universality of the steady-state.

We finally show that in the steady-state of the lattice model – similar to the equilibrium case – no fixed point in between the steady-state analogue of the perfect and the open chain ones exist. To

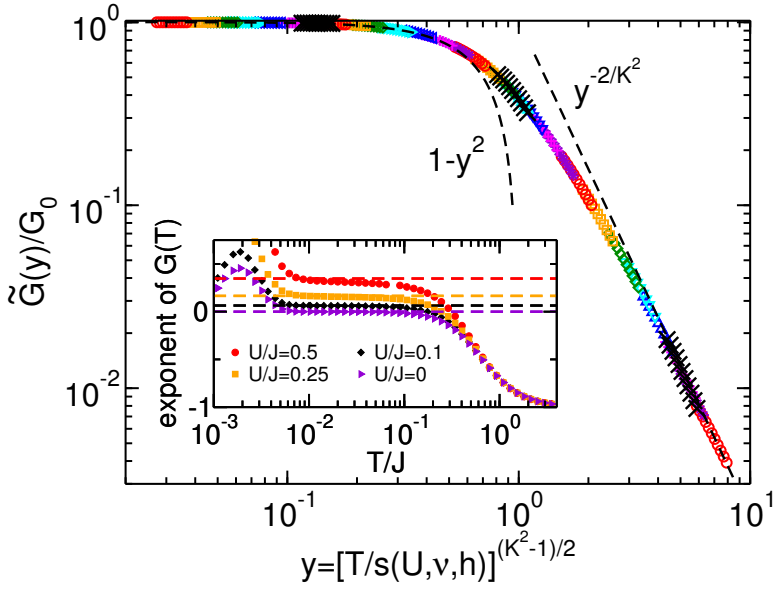


Figure 9.6.: FRG data for the one-parameter scaling of $\tilde{G}(y)$ of the lattice model for $U/J = 0.5$, $\nu = 1/2$, and $N = 10^3$. Different symbols stand for different h increasing from left to right. No fixed point in between the perfect and the steady-state analogue of the open chain ones exist. The crosses were computed for $U/J = 0.85$, $\nu = 1/4$ giving the same K. The scaling function thus depends on U and ν only via K [Kan92]. The prediction of the TL model for $y \to 0$ and $y \to \infty$ with the exact lattice model K is shown as dashed lines. Inset: the effective exponent of $G(T)$ for a strong impurity $h/J = 0.9$ determined by a logarithmic derivative. Dashed lines show the prediction of the TL model with the exact lattice model K.

achieve this we compute $G(T)$ for a variety of h at fixed U and ν. By a one-parameter scaling ansatz $G(T) = \tilde{G}(y)$ [Kan92, Ens05b], with $y = (T/s)^{(K^2-1)/2}$ and the non-universal scale $s(U, \nu, h)$, all data can be collapsed on a single curve continuously connecting the weak ($y \to 0$) and strong ($y \to \infty$) impurity fixed points. This is demonstrated in the main plot of Fig. 9.6, where also different fillings are used.

Spectral Properties

Now we return to the hallmarks found within the TL model for the spectral functions. Can those distinct spectral characteristics of the non-equilibrium steady-state also be found in microscopic models, and can thus be considered universal? To determine the spectral function involves a "double time evolution". First, one for the "center of time" t to push the state into a steady one and afterwards a time evolution of t', with respect to which the Fourier transform can be performed. The limit on the values of t' will limit the "energy resolution" of the Fourier transform. Thus both times have to be very large. To achieve this we consider the *inverse quench* to the one proposed above: instead of turning on the interaction starting with the non-interacting equilibrium state, we focus on the inverse setup by starting in the *interacting* ground state and *time evolving with the non-interacting Hamiltonian*. It turns out (see below) that the spectral characteristics under examination here are also present in this quench setup, rendering this change of perspective a posteriori justified.

For translational invariant system – i.e. bulk properties – it is straight forward to show that $G_t^<(x, t')$ of an arbitrary model does not depend on t and is given by

$$iG_{ss}^<(x, t') = \sum_k e^{-i(\varepsilon_k t' + kx)} n_{ini}(k)/N \tag{9.4.11}$$

with the single-particle dispersion ε_k of the given model. Here $n_{ini}(k)$ is the momentum distribution function in the initial state, and x is the position (in continuous space) or a discrete lattice site. The

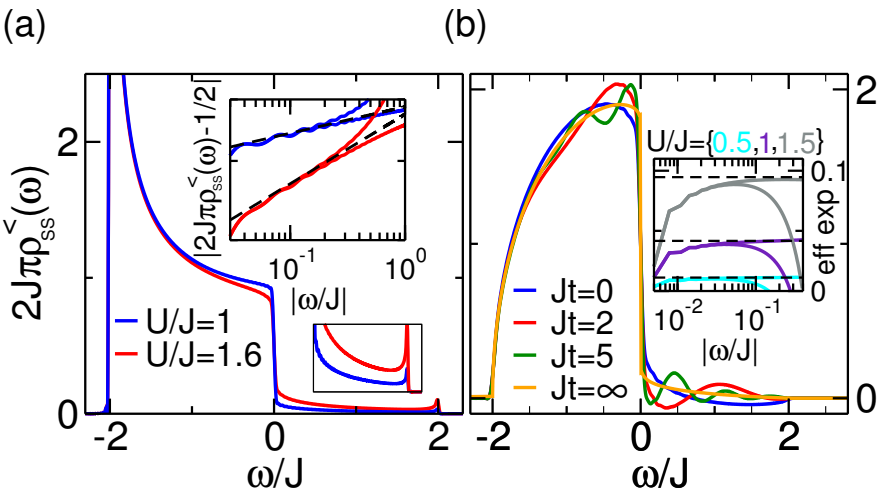


Figure 9.7.: The momentum integrated spectral function for the lattice model of spinless fermions of Eq. (9.1.3) with nearest neighbor interaction U after the inverse quench. Left: $\rho^<_{ss}(\omega)$ of the translational invariant model. Upper inset: $|\rho^<_{ss}(\omega) - \rho^<_{ss}(0)|$ on a log-log scale indicating the power-law behavior with γ_{gs} for $|\omega| \to 0$. The dashed lines are the expected power-laws with K taken from Bethe ansatz [Gia03, Sch05b]. The upper bound over which the power-law manifests depends on U [Kar12b] and sgn(ω). At small $|\omega|$ the power-law is cut off by t'^{-1}. Lower Inset: Zoom into $\omega > 0$. Right: Spectral function at the first site $\rho^<_t(1,\omega)$ for open boundaries with $U/J = 1$ at different t. Inset: logarithmic derivative of $|\rho^<_{ss}(1,\omega) - \rho^<_{ss}(1,0)|$ with respect to $|\omega|$, that is the effective exponent, in the steady-state. The dashed lines indicate the expected exponents.

t independence is particular to the one-particle Green's function; other observables and correlation functions depend on t. The Fourier transformation then gives $\rho^<_{ss}(\omega) = \sum_k n_i(k)\delta(\omega - \varepsilon_k)/N$. The complexity of computing $\rho^<_{ss}(\omega)$ for the inverse quench is thus comparable to the one of computing $n_{ini}(k)$ in the interacting ground state of microscopic models from the Luttinger Liquid class. The latter was recently achieved to very high precision using DMRG [Kar12b]. As $\rho^<_{ss}(\omega)$ "samples" only the equilibrium $n_i(k)$ and for *any model* from the Luttinger Liquid class $|1/2 - n_{ini}(k)| \sim |k - k_F|^{\gamma_{gs}}$ [Gia03, Sch05b] it is evident that the characteristics of $\rho^<_{ss}(\omega)$ are the same as the ones discussed above and thus distinguish this state clearly from equilibrium states. Specifically, we find a finite weight at $\omega = 0$ [in contrast to $\rho^<_{gs}(0) = 0$] which is approached for $\omega \to 0^{\pm}$ following a power-law with interaction dependent exponent (for $\gamma_{gs} < 1$; else $\rho^<_{ss}(\omega) - \rho^<_{ss}(0) \sim -\omega$) [in contrast to the linear behavior of $\rho^<_{th}(\omega)$ around $\omega = 0$].

To visualize this we also show $\rho^<_{ss}(\omega)$ after the inverse interaction quench for the lattice model of spinless fermions given by Eq. (9.1.3) in Fig. 9.7(a). Instead of using $n_i(k)$ we equally efficiently computed $\rho^<_{ss}(\omega)$ by time dependent DMRG[10] and numerical Fourier transformation. Here we can make use of the *non-interacting* time evolution. We then can change perspective and propagate the operators $c_j^\dagger$ and c_j (calculating $e^{iHt}c_j^\dagger e^{iHt'}c_j e^{-iH(t'+t)}$) instead of the wave function's MPS. For such a combination of a (single-particle) operator under the free time evolution it was shown that the time evolution can be done *exactly* with finite bond dimension equal to four [Har09, Mut11]. With this the numerical effort to perform the time evolution reduces from exponential to linear growth in time and times $Jt' \sim \mathcal{O}(10^3)$ (needed for an accurate Fourier transform) become easily accessible.

We finally also study the inverse quench for our lattice model assuming *open boundaries*. Then $G^<_t(j|j',t')$ *depends on* t (as well as on j and j' and not only $j - j'$). We exploit again that the free time evolution is trivial using DMRG and compute $G^<_t(j|j,t')$ at finite t for t' so large that Fourier transformation is meaningful. The limit $t \to \infty$ can be addressed explicitly by calculating $n_{ini}(k)$ of

[10] We only perform the t' evolution at $t = 0$, because of the t independence.

the interacting ground state [Kar12b, Jec13] and using

$$\rho^<_{\mathrm{ss}}(j,\omega) = \frac{2}{N+1}\sum_{n=1}^{N}\sin^2(k_n j)\, n_{\mathrm{ini}}(k_n)\,\delta(\omega-\epsilon_{k_n}) \overset{N\to\infty}{\longrightarrow} \frac{2}{\pi}\frac{1}{|2\sin(k^*(\omega))|}\, W_j(k^*(\omega)), \tag{9.4.12}$$

$$k^*(\omega) = \arccos(-\omega/2), \tag{9.4.13}$$

$$W_j(k) = \sin^2(kj)\, n_{\mathrm{i}}(k), \tag{9.4.14}$$

$$n_{\mathrm{ini}}(k_n) = \frac{2}{N+1}\sum_{j,j'=1}^{N}\sin(k_n j)\sin(k_n j')\,\langle \mathrm{gs}|\, c_j^\dagger c_{j'}\,|\mathrm{gs}\rangle\,, \tag{9.4.15}$$

$$k_n = \frac{\pi}{N+1}n, \qquad n = 1, 2, \ldots, N. \tag{9.4.16}$$

with the initial "pseudo-momentum" distribution[11] function $n_{\mathrm{ini}}(k) = \langle \mathrm{gs}|\, n_k\,|\mathrm{gs}\rangle$. We have to compare this to the 'open boundary' bosonization of the TL model [Gia03, Sch05b] from which we expect $|1/2 - n_{\mathrm{i}}(k)| \sim |k - k_F|^{\gamma_{\mathrm{gs}}}$ (for $\gamma_{\mathrm{gs}} < 1$; else $1/2 - n_{\mathrm{i}}(k) \sim k - k_F$) which implies that $\rho^<_{\mathrm{ss}}(j,\omega)$ of the translational invariant and open boundary case share the same spectral features characteristic for the steady-state. In Fig. 9.7(b) we confirm this prediction of the TL model. We show the evolution of $\rho^<_t(j=1,\omega)$ towards $\rho^<_{\mathrm{ss}}(j=1,\omega)$. We note that only $\rho^<_{\mathrm{ss}}$, not $\rho^<_t$ at finite t, can be measured in 'continuous beam' photoemission spectroscopy [Fre09]; $\rho^<_t$ is merely an auxiliary quantity.

To sum up, we find that the unique LL non-equilibrium steady-state spectral features which are predicted by the Tomonaga-Luttinger model appear to be universal. One should be able to use those to identify this highly interesting steady-state in quenched cold Fermi gases in future radio-frequency spectroscopy experiments [Ste08, Gae10, Fel11].

9.5 Thermalization in One Dimension

In this section, as a secondary objective, we want to present some results on thermalization. The results shown are part of our ongoing research and thus the spirit of this section is rather that of an outlook. So far we studied exclusively effectively non-interacting or integrable models (TL model → effectively non-interacting and nearest neighbor interacting spinless fermions on a lattice → Bethe ansatz solvable). The appearance of LL properties in the steady-state, reached after a quantum quench has been performed, is thus in agreement with the common believe that those systems do not thermalize (for in a thermal state, its finite temperature always cuts off any power-law scaling and leads to asymptotic exponential decay instead of power-laws).

9.5.1 Models and Method

We return to the Hamiltonians of Eqs. (9.1.5) and (9.1.7) and from now on focus on the translational invariant case (next-nearest neighbor XXZ: $J_n = J$, $\Delta_n = \Delta$, $\Delta_{2,n} = \Delta_2$ and extended Hubbard model: $J_n = J$, $U_n = U$, $V_n = V$). Both of those feature a tunable integrability breaking term via Δ_2 and V, respectively. This renders them ideal candidates for studying if and how integrability breaking enforces thermalization. To avoid any finite size effects and to speed up numerics we employ the infinite DMRG procedure of section 5.7. It is important to note that this question was investigated before using DMRG (see e.g. [Kol07, Man07, Sir14, Ess14]), but a truly steady regime of local observables were hardly achieved (on the relevant plot scale). For the time evolution at finite temperature the disentangler of section 5.6.3 is used. The thermal ensemble we compare to (chosen to be canonical as we work at half-filling always) is obtained using infinite DMRG by fixing the conserved energy expectation value after the quench as stipulated by Eq. (9.1.1) for $A = H$. This yields an effective temperature T_{eff} for the reference thermal ensemble $\rho = \exp(-H/T_{\mathrm{eff}})/Z$. For all

[11] pseudo, because the system with boundary is not translational invariant. The k in n_k do thus not correspond to a physical momentum.

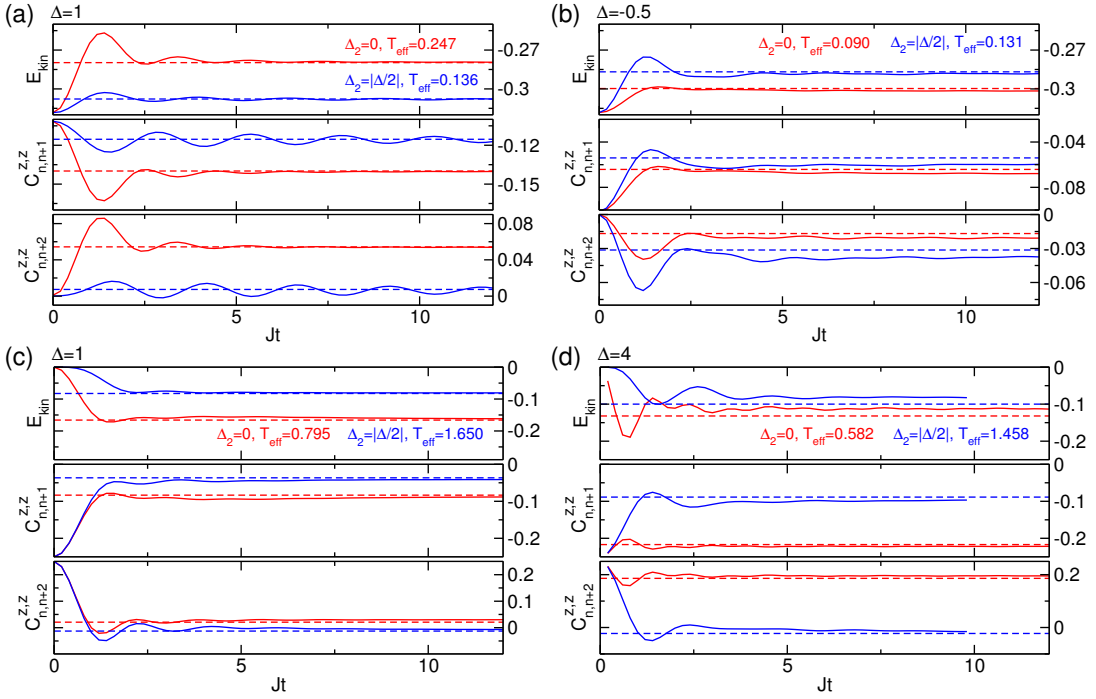


Figure 9.8.: Relaxation dynamics of certain observables in the model defined in Eq. (9.1.5). We start from either the non-interacting ground state [(a) and (b)] or the Néel state [(c) and (d)] and propagate this initial state with the integrable ($\Delta_2 = 0$) or non-integrable ($\Delta_2 = |\Delta/2|$) Hamiltonian of Eq. (9.1.5) for different Δ. For the largest times reachable within our DMRG calculations the expectation values for certain parameters [(a) and (c)] look very close to thermal, while for others [(b) and (d)] this is not the case, regardless of the integrability breaking.

DMRG runs different discarded weights and Trotter steps were compared to ensure the convergence of all results shown in the following (on the scale of their respective plots).

For the remainder of this chapter we will always consider the following quench protocol. Initially the system is prepared in some state $|\Psi(0)\rangle$ or thermal ensemble, which we either choose as

- the non-interacting ground state[12] $|\Psi_0\rangle$ to $H_{\text{Heis}}(\Delta = 0, \Delta_2 = 0)$ or $H_{\text{Hub}}(U = 0, V = 0)$, respectively.
- some explicitly mentioned product state.
- some thermal equilibrium ensemble $\rho = \exp(-H_0/T)/Z$ with respect to the non-interacting Hamiltonian $H_0 = H_{\text{Heis}}(\Delta = 0, \Delta_2 = 0)$ or $H_0 = H_{\text{Hub}}(U = 0, V = 0)$, respectively.

Then we time evolve this state with respect to the full Hamiltonian [given either by Eq. (9.1.5) or Eq. (9.1.7)] at finite (Δ, Δ_2) or (U, V), respectively. With this we can determine the time evolution of different observables supported on a finite subsystem, which we will specify later. The large time asymptotes of these observables can finally be compared to those obtained in the reference thermal ensemble.

[12] We exemplified considering also initial ground states to interacting Hamiltonians that the following statements do not depend on this choice.

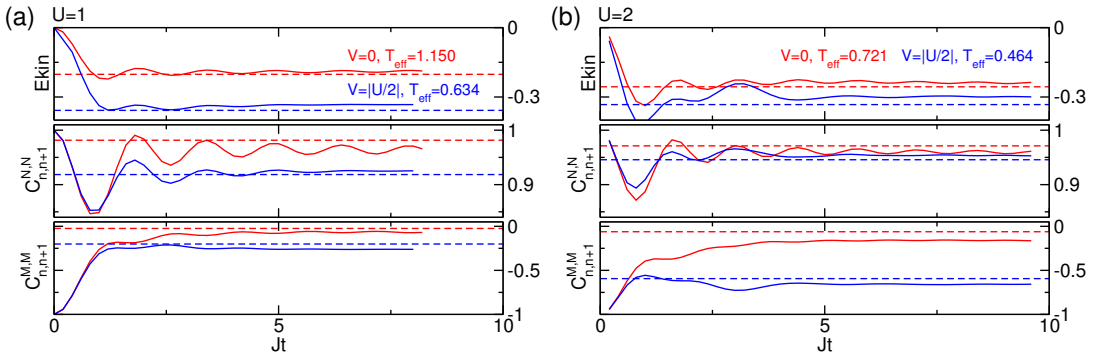


Figure 9.9.: Relaxation dynamics of certain observables in the (extended) Hubbard model. We start from a spin imbalanced state and propagate this initial state with the integrable ($V = 0$) or non-integrable ($V = |U/2|$) Hamiltonian of Eq. (9.1.7) for $U = 1$ (a) and U=2 (b). For the largest times reachable within our DMRG calculations the expectation values seemingly do not approach their thermal expectation value regardless of the integrability breaking.

9.5.2 Time Evolution of Observables

Heisenberg (XXZ) Model

We jump right into the presentation of our results. We show in Fig. 9.8 the time evolution of the expectation value of the kinetic energy $E_{\text{kin}}(t) = \langle H_{\text{Heis}}(\Delta = 0, \Delta_2 = 0)\rangle_{\rho(t)}$ as well as of the spin-spin correlators $C^{z,z}_{n,m} = \langle S^z_n S^z_m\rangle_{\rho(t)}$ for $m = n+1$ and $m = n+2$. For the initial state $|\Psi(0)\rangle$ we choose either $|\Psi_0\rangle$ [Fig. 9.8(a) and (b)] or the Néel product state of $|\ldots\uparrow\downarrow\uparrow\downarrow\ldots\rangle$ [Fig. 9.8(c) and (d)]. Independent of the preparation, we find that for certain parameters of the interactions Δ and Δ_2 the observables appear to relax to thermal values, while for others they are quite far away from their thermal expectation. Importantly, in the second case the observables appear to approach a value inconsistent with the thermal prediction. There appears to be no qualitative difference in the relaxation dynamics of observable in the integrable ($\Delta_2 = 0$) and non-integrable ($\Delta_2 \neq 0$) model. Obviously, using an approach bound to finite times we can never rule out the possibility of a much larger time scale on which the behavior of the observables change again. To further investigate this it might be instructive to consider different models, like the ...

Hubbard Model

The inconclusive behavior of the XXZ model with next-nearest neighbor interaction is not a consequence of considering this particular spin-chain. We find very similar results for the (extended) Hubbard model as well. Fig. 9.9 shows the kinetic energy $E_{\text{kin}}(t) = \langle H_{\text{Hub}}(U = V = 0)\rangle_{\rho(t)}$ as well as correlators of the total occupancy[13] $C^{N,N}_{n,n+1} = \langle N_n N_{n+1}\rangle_{\rho(t)}$ and occupancy imbalance $C^{M,M}_{n,n+1} = \langle M_n M_{n+1}\rangle_{\rho(t)}$ of neighboring sites where $N_n = S^z_{n,\uparrow} + S^z_{n,\downarrow}$ and $M_n = S^z_{n,\uparrow} - S^z_{n,\downarrow}$. The initial preparation is given by an imbalanced spin product state $|\ldots(\uparrow\otimes\downarrow)(\downarrow\otimes\uparrow)(\uparrow\otimes\downarrow)(\downarrow\otimes\uparrow)\ldots\rangle$, where the explicit $\otimes$ is in the sector of $(\sigma\otimes\bar{\sigma})$. Again we find parameter regimes where the considered observables for *both* the integrable and non-integrable model apparently relax to thermal values at large times and also those regimes where this is not the case [only shown in Fig. 9.9]. As this feature appears to show up for different models it might be advisable to change the type of initial preparation. Thus, it is reasonable also in the context of the possible existence of some large time scale on which further relaxation sets in, to ask:...

Does Finite Initial Temperature Help?

We reconsider the setup leading to the results of Fig. 9.8, but now with the initial density matrix given by a thermal equilibrium ensemble $\rho = \exp(-H_0/T)/Z$ with respect to the non-interacting

[13] Here the name "occupancy" becomes plausible only from considering the fermionic language.

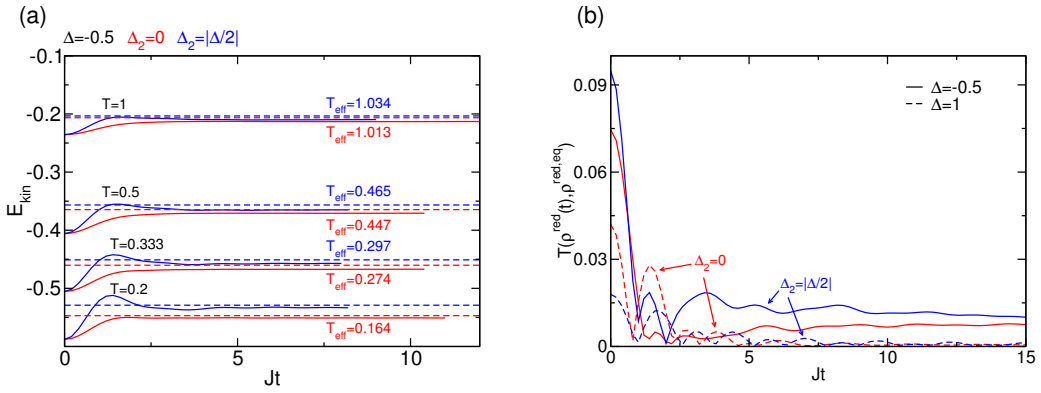


Figure 9.10.: Left: The same as in Fig. 9.8(b) but for an initial preparation given by a thermal state with respect to the non-interacting Hamiltoninan. The initial temperature does not seem to support the thermalization of subsystems in the non-integrable case. Right: The same as in Fig. 9.8(a) and (b) but using the trace distance introduced in Eq. (9.5.1) as a measure of thermalization.

Hamiltonian. The hope would be that the initial temperature will accelerate thermalization. Actually we do not confirm such mechanism. The above made statements hold also for this quench setup. We concentrate on the kinetic energy and the case $\Delta = -0.5$ (where deviations from the thermal values where prominent also for $T = 0$) now and consider different temperatures T for the initial preparation. The results are summarized in Fig. 9.10(a). Again the time dependence of the observable at the largest accessible times scales is weak, but the asymptotic values of observables are generically incompatible with the thermal expectation.

9.5.3 A Single Measure of Thermalization

Above we considered different local observables as measures of thermalization of subsystems. The locality (in real space) of the observables thus defined the length of the subsystem considered. This approach, viewing thermalization in the sense of Eq. (9.1.1), although being a viable one, suffers from the arbitrariness of the observable *choice*. Thus we change perspective in the following and concentrate on thermalization as understood in the light of Eq. (9.1.2). Eq. (9.1.2) is a stronger requirement than Eq. (9.1.1). Furthermore, it removes the arbitrary choice of observables and allows for the definition of a useful single measure of thermalization: the trace distance between the reduced density matrix of the time evolved ($\rho_1 = \rho^{\mathrm{red}}(t) = \mathrm{Tr}_B\,[\rho(t)]$) and the thermal reference ($\rho_2 = \rho^{\mathrm{red,eq}} = \mathrm{Tr}_B\,[\rho^{\mathrm{eq}}]$) ensembles

$$T(\rho_1, \rho_2) = \frac{1}{2}\mathrm{Tr}\left[\sqrt{(\rho_1 - \rho_2)^\dagger(\rho_1 - \rho_2)}\right] = \frac{1}{2}\sum_i |\lambda_i|. \tag{9.5.1}$$

The last equality is a consequence of the hermiticity of reduced density matrices, where λ_i are the eigenvalues of the operator $\rho_1 - \rho_2$ (hermitian but not necessarily positive). The trace distance is a metric in the sense that

$$T(\rho_1, \rho_2) \geq 0\,, \tag{9.5.2}$$
$$T(\rho_1, \rho_2) = 0 \Leftrightarrow \rho_1 = \rho_2\,, \tag{9.5.3}$$
$$T(\rho_1, \rho_2) = T(\rho_2, \rho_1)\,, \tag{9.5.4}$$
$$T(\rho_1, \rho_2) \leq T(\rho_1, \rho_3) + T(\rho_3, \rho_2), \tag{9.5.5}$$

which obviously makes this a good measure for our thermalization question. Additionally, for normalized density matrices $T(\rho_1, \rho_2) \in [0, 1]$. Furthermore, the trace distance can also be related to

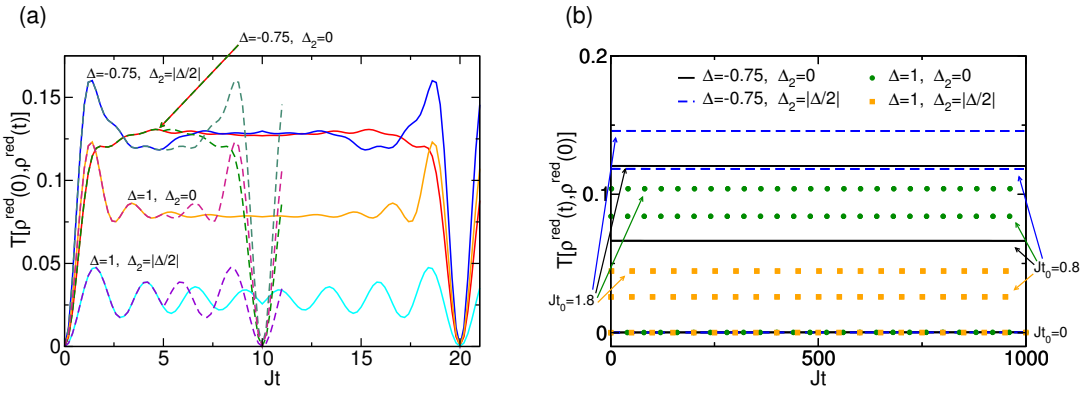


Figure 9.11.: Left: Trace distance of the initial reduced density matrix (determined by the non-interacting ground state) and the time evolved one. After $Jt_f = 5$ or $Jt_f = 10$ the Hamiltonian is switches as $H \to -H$ to perform the inverse time evolution. As the trace distance vanishes at $t = 2t_f$, we show that the initial preparation can be perfectly restored. Right: the same as in (a) but for multiple switching at $Jt = nJt_f$ with $n \in \mathbb{N}$ and $Jt_f = 5$. Considering $T(t_0 + nt_f)$ for different t_0 straight lines show up. This indicates that the time evolved reduced density matrix is periodic even for *very* large times.

the fidelity, defined in Eq. (5.7.3) by

$$1 - F(\rho_1, \rho_2) \leq T(\rho_1, \rho_2) \leq \sqrt{1 - F(\rho_1, \rho_2)^2}. \tag{9.5.6}$$

As we use Vidal's Γ-Λ notation of section 5.1.3, reduced density matrices can be calculated trivially, since we can employ simultaneously left and right normalization for the part to be traced out. In the following we concentrate on the example of the subsystem to consist of two sites only. Fig. 9.10(b) shows the same as considered in Fig. 9.8(a) and (b), but for the trance distance. With this analysis there is no chance of accidentally missing something due to the wrong choice of observables. Remarkably, for $\Delta = 1$ not only some observables, but *the whole reduced density matrix* appears thermal. This is still independent of the integrability of the model. For the less clear case of $\Delta = -0.5$ we can again find no conclusive statements. The trace distance appears to be less relaxed than the corresponding observables, but it is still unclear, whether and how thermalization is reached.

9.5.4 Chaos Induced Thermalization

It was proposed ([Deu91, San10] as well as references therein) that analogous to classical dynamics [Gal10], thermalization is associated to chaos. In this respect one might wonder whether for quantum many-body systems the distance between two initially very close density matrices grows exponentially in time for non-integrable models, while this is not the case for integrable ones. For DMRG small differences due to numerical errors are induced in any time evolution by the method anyway, so one might equivalently ask the question: can one retrieve the initial reduced density matrix $\rho^{\text{red}}(0)$ from the time evolved $\rho(t)$ by evolving backwards in time? We investigate this in Fig. 9.11(a). After a final time t_f the Hamiltonian is suddenly switched as $H \to -H$ to perform the backwards propagation. At time $t = 2t_f$ one finds that regardless of the integrability of the model the density matrix is perfectly retrieved. We generalize this idea by performing multiple switches $H \to -H$ whenever $t = nt_f$ with $n \in \mathbb{N}$. Fig. 9.11(b) shows that the trace distance behaves perfectly periodic, by considering T at times $t_0 + nt_f$ for different t_0. Apparently, no fundamental difference induced by the integrability shows up. Overall, the mechanism for thermalization remains a puzzle.

9.6 Conclusion

Establishing Time Dependent FRG for Closed Systems

In this section we showed how to apply the general FRG framework to the time evolution of closed quantum systems. We outlined and benchmarked different approaches to address this numerically more challenging problem, namely GPU supported calculations as well as Trotter decomposition. The former can be used to tackle general (long-ranged) interactions, while the latter – although restricted to short ranged interactions – is very easy to implement and fast. Comparing the results obtained with (only CPU) and without (additionally GPU) the Trotter decomposition shows that, if done with care, the additional Trotter approximation introduces only a negligible error. Obviously, the FRG treatment itself renders the results approximate, but due to the weak polynomial scaling in both lattice sites as well as maximum time, treating much larger systems and times than, e.g., in a numerical exact DMRG approach, is possible. The developed machinery can straightforwardly be applied to any microscopic lattice Hamiltonian and arbitrary initial preparation (including finite temperature). Employing however higher order truncation schemes unfortunately appears to be impractical with currently available computational resources (as generally for the time dependent FRG treatment).

Results for (Integrable) XXZ model/Spinless Fermions

Integrable models feature particularly constrained dynamics. In these models quenched initial states relax for large times to non-thermal ones, which are of fundamental interest as they cannot be described by the standard ensembles of statistical mechanics. Then the natural question arises: do these steady-states feature particularly interesting physics? We addressed this question for systems showing Luttinger Liquid physics in equilibrium. We provided evidence that the characteristic hallmarks of Luttinger Liquids can also be found in the steady-state reached after an interaction quench for asymptotically large times. Specifically, critical power-laws, incompatible with the thermal asymptotic exponential behavior, show up in a variety of observables. Additionally, we argued that the spectral function can be used to distinguish clearly between an equilibrium setup and a steady-state reached after an interaction quench. The difference between the two should be addressable by future radio-frequency spectroscopy experiments and could thus be used to differentiate between thermal and non-thermal states of the aforementioned type.

Contributions to Thermalization-Debate

The debate about thermalization of closed quantum systems has been reignited by the advances made in the fabrication and control of ultra-cold atoms experiments. Generically, low-dimensional systems in these experiments sometimes show fast thermalization [Hof07], while for other setups appear to relax to non-thermal states [Kin06]. Which systems thermalize and which do not is usually assoziated to the integrability of the system. In one dimension one can treat model Hamiltonians of these systems very efficiently using DMRG. We employed an infinite DMRG code to compare the time evolution of different observables encountered for integrable models to non-integrable ones. We can reach time regimes where the observables do appear to be relaxed. However, regardless of the integrability breaking we find parameter regimes where the long time asymptote of the observables is incompatible with thermal predictions. We scrutinize different initial preparations including finite initial temperature. We then proposed an alternative measure, the trace distance of relaxed and thermal reference reduced density matrix, for thermalization, which is independent of the observable choice. Based on this measure we can draw the same conclusions, where the results however appear less relaxed for the largest times reached. Finally, we shed some light on whether chaos in the sense that initially very close density matrices drift apart exponentially fast within the time evolution, could be attributed to thermalization. Regardless of integrability we find no such mechanism.

Outlook

Many avenues of future research can be envisaged starting from the results presented here. First of all one could further investigate non-thermal steady-states reached in integrable systems, theoretically.

Possibly those could feature unknown physical behavior as they are almost completely unexplored. Experimentally it would be interesting to test the criteria proposed here to distinguish equilibrium and steady-state after a quantum quench by the (momentum resolved) spectral function with future radio-frequency spectroscopy [Ste08, Gae10, Fel11]. As the key signature of the steady-state in this spectral function is so significantly different from those of the equilibrium situation, this could be much easier than trying to follow other routes. Regarding thermalization it would be very interesting if one would succeed in approximating the time scale on which thermalization is supposed to occur. With this one could rule out or make more plausible whether finally relaxation to thermal steady-state sets in, which cannot be observed in current DMRG calculations due to its limitation to intermediate times.

Acknowledgement

We acknowledge very fruitful discussions with Sabine Andergassen, who also provided some equilibrium FRG data used throughout intermediate steps of the code development. Also we would like to thank Christoph Karrasch for helpful discussions regarding DMRG.

References

Part of the results discussed in this chapter were published in

D. M. Kennes and V. Meden
'Luttinger liquid properties of the steady state after a quantum quench'
Phys. Rev. B **88**, 165131 (2013)

D. M. Kennes, C. Klöckner and V. Meden
'Spectral properties of one-dimensional Fermi systems after an interaction quench'
ArXiv 1405.3762 (2014)

Conclusions & Outlook

Chapter 10

Conclusion

10.1 Updated Status Report: Transient Time FRG

The methodical advances aimed at in this thesis were the extension of the real-time formulation of the FRG to (1) open systems at finite temperatures and (2) closed quantum systems in general. We described both of these extensions in the sections 7.2 and 9.3, respectively.

Open Systems at Finite Temperature

For the extension concerning open quantum systems at finite temperatures we have focussed on the example of a charge-fluctuating quantum dot (IRLM $\rightarrow$ Section 3.5), which can be seen as a proof of principle. It was necessary to derive analytic expressions for the Green's functions to describe the dynamics within the FRG, because those are (1) desirable from a viewpoint of numerical efficiency and (2) essential for the important scaling limit, where Cauchy principle valued integrals have to be treated ($\rightarrow$ Section 4.1.2). In passing with this we could exemplify that no subtle problem arises from permuting the limits $N \rightarrow \infty$ and $t \rightarrow \infty$ in the derivation of the steady-state formulation of the functional renormalization group. We benchmarked the functional renormalization group by a complementary real time renormalization group approach, which shows that results are quantitatively reliable for not too large interactions. We restricted ourselves to a first order truncation scheme, where only the leading order on the right hand side of the flow equations is kept. An extension to higher order involves incorporating a non-local retarded and advanced self-energy in time space. This is currently numerically not feasible.

Closed Systems

An extension to closed quantum systems was straightforward, although numerically more demanding. We benchmarked two different approaches to address this, namely GPU supported calculations as well as Trotter decomposition. The former can be used to tackle general (long-ranged) interactions, while the latter – although restricted to short ranged interactions – is very fast. Both give agreeing results if the Trotter decomposition is done with care. The weak polynomial scaling of the approximate functional renormalization group treatment allows to handle much larger systems and times than, e.g., in a numerical exact DMRG approach. Again for not too large interactions FRG was found to give quantitatively correct results for the time evolution of closed quantum systems, which can be seen by comparing to numerically exact DMRG results. The developed machinery can right away be applied to any microscopic lattice Hamiltonian. Again, employing higher order truncation schemes, however, is unfortunately impractical with currently available computational resources.

10.2 Summaries of the Results

We already concluded our findings in each chapter separately. Here for convenience we re-iterate[1] them as an overview.

[1] The summaries are almost literately identical to the summaries of the separate chapters.

10.2.1 Dynamics in Open Quantum Systems

Results for the Bias Driven IRLM

We showed that for the bias driven IRLM analogously to the $T = 0$ case the effect of the two-particle interaction to a very good approximation can be condensed in effective constant Hamiltonian parameters in the transport regime $|\epsilon \pm V/2| \gg T_K$. This facilitates the interpretation of the results to a great deal, as the time evolution of the observables can be understood from the non-interacting case. For finite temperature already this simplified picture gives rise to very rich physics. We have found that different temperature in the left and right reservoir can be used to detune the different contributions found in the dynamics with respect to each other. This cannot be achieved at $T = 0$ and leads to a variety of different dynamical regimes at large times. Where these crossovers from one regime to the other occur are generally described by a power-law in the bare parameters with interaction dependent exponent.

Results for Dissipative Systems

Using a formal mapping between the IRLM and the SBM we have shown that the dynamics encountered in the latter at $T = 0$ are significantly different to what one might expect. Although we reproduce the coherent-to-incoherent transition at $\alpha = 1/2$ found in NIBA and CFT, we showed that the large time dynamics for $1/2 > \alpha > \alpha_c$ in this "coherent" dynamical phase are actually *monotonic*! Only at intermediate times the signature of the coherent dynamics (non-monotonic behavior) can be found. These results lead us to propose a more refined picture of the dynamical phases found, where one differentiates between the asymptotically coherent $\alpha < \alpha_c$ (non-monotonic for all times) and the partially coherent $1/2 > \alpha > \alpha_c$ regime.

Turning to finite T we even more surprisingly found that starting in the partially coherent regime at $T = 0$ elevating temperature drives the system into a regime of asymptotic coherence. Only for even larger T the dynamics finally turns incoherent. This increased coherence at elevated temperature is rather counter-intuitive. All the aforementioned results were not obtained using only the FRG, but also the complementary RTRG approach.

A second interesting application targets quantum quenches where parameters of the Hamiltonian are switched instantly at some time t_q. We have seen using our complementary renormalization group procedures that the non-Markovian memory of the bosonic bath, storing information about the pre-quench history, greatly affects the dynamics after the quench. Because in this example non-Markovian memory plays a major role for the dynamics found, this could be seen as a motivation to a more systematic study of when and why modelling baths as Markovian ones is justified.

10.2.2 Thermoelectric Transport

Results for the IRLM

The FRG has been successfully applied before to the IRLM studying a variety of different aspects. It is well understood that parametric logarithmic divergences showing up in a perturbative treatment are resummed correctly by FRG, motivating the presented thermoelectric study of this model. The results obtained for the IRLM were interpreted using basically non-interacting expressions dressed with the dominant Kondo-like renormalization of the hybridization induced by the reservoirs. With this we could connect our microscopic ansatz to viewpoints attributed to phenomenological thermodynamics. Interestingly, positive interaction (leading to a broader resonance) generally reduces the efficiency encountered in power-engines, while negative interaction (as achievable effectively by including phonons) renders the opposite effect. The flexibility and speed of the FRG is ideal for the posed problem as huge parameter spaces have to be sampled for thermoelectric questions (since usually multiple parameters are optimized). We have also proposed an alternative more "applied" scenario of interest. Here instead of the usual quest for maximum power or efficiency, we search for the optimal efficiency under the constrain of a certain minimum power output. This scenario appears to be of relevance when, e.g., charging applications are envisaged. For this, even in the regime of positive interactions, the general decrease in maximum efficiency can be overcome by an increase in

the power output, yielding a net increase of the achievable efficiency. This part demonstrated some of the impressive key advantages of FRG (flexibility and speed).

Results for the AHM

The AHM features much more complicated physics than the IRLM and thus we applied a second order truncation scheme to handle this problem. This more sophisticated truncation scheme restricts our study to equilibrium, but non-equilibrium FRG results were available from [Laa14]. Similarly to the SIAM studied before in the same framework (truncation scheme, cut-off, channel decomposition, ...) major difficulties show up. It is not possible to reach far into the regime of strong correlations as might be hoped for from an renormalization group approach. For the adiabatic regime this was clear from the beginning as the AHM can then be mapped to the negative-U SIAM. Unfortunately, also for all other cases the range of validity of our FRG approach appears to be limited to small to intermediate interaction strength. For the question of thermoelectric transport we extended an existing approach to compute $G_{c,V}$ from the Matsubara frequency propagator to access all linear response conductances without the need of a possibly ill-posed analytic continuation. Furthermore, we introduced an alternative route based on a Sommefeld expansion. Comparing the conductances obtained by these methods to those from non-equilibrium Keldysh FRG major deviations show up for rather small values of the interaction. As we do not have any non-perturbative benchmark results at hand (e.g. using NRG) at this point it remains an open question, whether either of the FRG approaches yield meaningful results (at least up to intermediate interaction strength). The route to thermoelectric transport at intermediate to large interactions strength is thus blocked. This part demonstrated an unfortunate disadvantage of the FRG. The deep Kondo limit is not accessible; another reminder of the dilemma encountered already for the SIAM.

10.2.3 Dynamics in Closed Quantum Systems

Results for (Integrable) XXZ model/Spinless Fermions

Integrable models feature particularly constrained dynamics. In these models quenched initial states relax for large times to non-thermal ones, which are of fundamental interest as they cannot be described by the standard ensembles of statistical mechanics. Then the natural question arises: do these steady-states feature especially interesting physics? We addressed this question for the particular choice of systems showing Luttinger Liquid physics in equilibrium. We argued that the characteristic hallmarks of Luttinger Liquids can also be found in the steady-state reached after an interaction quench for asymptotically large times. Specifically, critical power-laws, incompatible with the thermal asymptotic exponential behavior, show up in a variety of observables. Additionally, we argued that the spectral function can be used to distinguish clearly between an equilibrium setup and a steady-state reached after an interaction quench. The difference between the two should be addressable by future radio-frequency spectroscopy experiments and could thus be used to differentiate thermal and non-thermal states of the aforementioned type.

Contributions to Thermalization-Debate

The debate about thermalization of closed quantum systems has been reignited by the advances made in the fabrication and control of ultra-cold atoms experiments. Generically, low-dimensional systems in these experiments sometimes show fast thermalization [Hof07], while for other setups appear to relax to non-thermal states [Kin06]. Which systems thermalize and which do not is usually assoziated to the integrability of the system. In one dimension one can treat model Hamiltonians of these systems very efficiently using DMRG. We employed an infinite DMRG code to compare the time evolution of different observables encountered for integrable models to non-integrable ones. We can reach time regimes where the observables do appear to be relaxed. However, regardless of the integrability breaking we find parameter regimes where the long time asymptote of the observables is incompatible with thermal predictions. We scrutinize different initial preparations including finite initial temperature. We then proposed an alternative measure, the trace distance of relaxed and thermal reference reduced density matrix, for thermalization, which is independent of the observable

choice. Based on this measure we can draw the same conclusions, where the results however appear less relaxed for the largest times reached. Finally, we shed some light on whether chaos in the sense that initially very close density matrices drift apart exponentially fast within the time evolution, could be attributed to thermalization. Regardless of integrability we find no such mechanism.

Chapter 11

Outlook

We have already outlined some future avenues of research in each of the result chapters, separately, but at this point we want to add two additional aspects. One regards method development, while the other builds on the results presented.

Method Development: From Transient to Periodically Driven

With the outlined real-time formulation of the functional renormalizationg group it is in principle possible to address arbitrary time-dependent Hamiltonians. For open systems at vanishing temperature this has been done in [Ken12b]. Especially, the intriguing question of quantum quenches can be tackled very efficiently within this method. Another interesting field of research considers periodically time-dependent Hamiltonians, e.g. in quantum pump configurations [Bro98, Alt99, Swi99, Spl06]. Often, the adiabatic limit provides the most clear cut case, because then deviations of the system's behavior from its "steady-state" with respect to the Hamiltonian given at a certain time, are small. In a functional renormalization group study this limit is the numerically most challenging one, because the very small frequency Ω of the adiabatic case gives rise to another, large time scale $\sim 1/\Omega$, which additionally to all other time scales needs to be resolved. For example, in the IRLM this means that the adiabatic limit is realized only if $\Omega \ll T_K$ and to resolve the physics of the pumping process times $\Omega t > 1$ need to be calculated. For the IRLM this right away (1) limits the values which can be chosen to obtain $\Omega \ll T_K$ and (2) renders a study of this setup numerically very demanding. This is exemplified in Fig. 11.1, where we consider the IRLM as introduced in chapter 7, but for a time dependent Hamiltonian with $t_{\text{imp}}(t)/\Gamma = 0.0025 + \Delta t_{\text{imp}}(t)$, $\Delta t_{\text{imp}}(t) = 2.5 \cdot 10^{-4} \sin(\Omega t)$, $\epsilon(t) = -T_K + 0.2 T_K \cos(\Omega t)$ and the adiabatic frequency $\Omega = T_K/100$. The other parameters are $\mu_{\text{L}} = \mu_{\text{R}} = 0$ and $U/\Gamma = 0.2$. This corresponds to a pump setup, in which charge is transported across the dot structure, although there is no bias voltage. The inset shows a zoom into the short to intermediate time regime. The transient behavior is restricted to a finite time interval $\sim 1/T_K$, while the asymptotic periodic behavior is found for $T_K t \gg 1$. We have clearly resolved a complete period of this asymptotic periodic behavior, but running the code for the above plot takes weeks on a single-core machine.

Actually, there is a much more efficient way of handling the periodic problem, if the transient dynamics are not of interest (as it is usually the case when studying quantum pumps). Taking the limit $t_0 \to -\infty$ and considering the differential form of the Dyson equation for the, e.g., retarded Green's function, one realizes that the form of the Dyson equation is of a special type, which can be handled very efficiently within Floquet theory[1]. With this the periodically time dependent problem reduces to a very simple form which is quite similar to its steady-state analogue, where the price to pay is merely that one has to introduce an additional discrete Floquet index, which behaves single-particle like. With this approach one can very quickly tackle the above mentioned adiabatic regime. For example calculating the analogue of Fig. 11.1 takes seconds of CPU time. Furthermore, determining the relevant observables (like the pumped current during one pumping cycle) is very convenient. Additionally, one is of course not restricted to the adiabatic case, basically any periodic time dependency can be covered (although the speed up is, naturally, most prominent in the adiabatic

[1] Which is basically the same as using Bloch theorem for space periodic systems, but in time space.

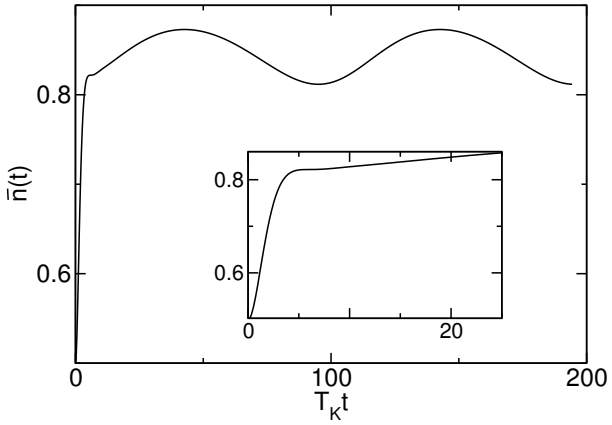


Figure 11.1.: Time evolution of the central site for the IRLM as outlined in chapter 7 under an adiabatic driving. The parameters are chosen as $t_{\mathrm{imp}}(t)/\Gamma = 0.0025 + \Delta t_{\mathrm{imp}}(t)$, $\Delta t_{\mathrm{imp}}(t) = 2.5 \cdot 10^{-4} \sin(\Omega t)$, $\epsilon(t) = -T_K + 0.2\,T_K \cos(\Omega t)$, $\mu_{\mathrm{L}} = \mu_{\mathrm{R}} = 0$, $U/\Gamma = 0.2$ and $\Omega = 0.01\,T_K$. This corresponds to a pump setup, in which charge is transported across the dot structure, although there is no bias voltage. Inset: Zoom into short to intermediate time regime.

setup compared to an explicit time dependent formulation of the functional renormalization group). Together with K. Eissing we follow this line of work currently.

Thermalization in One-Dimensional Systems

Section 9.5 was itself held on the level of an outlook and therefore we want to address some directions of future research here. We already hinted that without the availability of an approximation to the time scale on which thermalization is supposed to occur one can never rule out that the behavior of calculated observables does change on some later time scale not reachable within an algorithm working with finite times (such as DMRG). Aiming at the steady-state of a truly infinite system directly is not possible with nowadays available methods in the non-integrable case, such that the expectation that non-integrable models thermalize can not be tested. Regardless of this, simply stipulating such a large time scale, which protects the made statement about the thermalization of non-integrable systems, is not very satisfying. Understanding its origin is imperative to a deeper understanding of the involved physics. We do however acknowledge that with the usually employed DMRG approach it is impossible to reach the very long time regime, where the times are multiple orders of magnitude larger than the typical (bare) energy scales of the Hamiltonian. We want to stress though that to us, whether non-integrable models in one dimension do thermalize or not, is an open question. There is no conclusive evidence to support the one or the other and future research should tackle this (admittedly difficult) task in an unbiased survey. Either way, even if this very large time scale exists, one should keep in mind, that the intermediate "steady-state" could harbor very interesting physics, similarly to what we studied in the integrable case (no further relaxation is expected) in section 9.4. We also emphasize that one dimensional physics (as hopefully conveyed also in this thesis) is significantly different from its higher dimensional counterparts. For high dimensions one can use dynamical mean field theory, which becomes exact in the limit of infinite dimensions, to map the non-equilibrium problem of thermalization effectively to an impurity problem. These studies favor that thermalization indeed occurs for dimensions in which dynamical mean field theory can accurately be applied [Moe08, Eck09]. Thus even if one dimensional systems would not thermalize generically this would not pose a fundamental problem: contacted baths of higher dimension (which itself could very well thermalize generically) could always drive the thermalization mechanism also in lower dimensions in accordance to what we observe.

Appendix A

List of Acronyms

AHM	single impurity Anderson-Holstein model
CFT	conformal field theory
DMRG	density matrix renormalization group
FRG	functional renormalization group
GF	Green's function
GGE	generalized Gibbs ensemble
GPU	graphics processing unit
IRLM	interacting resonant level model
LL	Luttinger Liquid
MPO	matrix product operator
MPS	matrix product state
NIBA	non-interacting blip approximation
NRG	numerical renormalization group
RLM	resonant level model
RTRG	real time renormalization group
SBM	spin-boson model
SIAM	single impurity Anderson model
SVD	singular value decomposition
TL	Tomonaga-Luttinger

Supplements

Bibliography

[Abr70] M. Abramowitz and I. A. Stegun. *Handbook of Mathematical Functions*. Dover Publications, Inc., New York, 9. edition (1970).

[Alt99] B. L. Altshuler and L. I. Glazman. *Pumping electrons*. Science, **283** 1864 (1999).

[Alv09] A. Alvermann and H. Fehske. *Sparse polynomial space approach to dissipative quantum systems: Application to the sub-ohmic spin-boson model*. Phys. Rev. Lett., **102** 150601 (2009).

[And61] P. W. Anderson. *Localized magnetic states in metals*. Phys. Rev., **124** 41 (1961).

[And04] S. Andergassen, T. Enss, V. Meden, W. Metzner, U. Schollwöck and K. Schönhammer. *Functional renormalization group for luttinger liquids with impurities*. Phys. Rev. B, **70** 075102 (2004).

[And05] F. B. Anders and A. Schiller. *Real-time dynamics in quantum-impurity systems: A time-dependent numerical renormalization-group approach*. Phys. Rev. Lett., **95** 196801 (2005).

[And06] F. B. Anders and A. Schiller. *Spin precession and real-time dynamics in the kondo model:time-dependent numerical renormalization-group study*. Phys. Rev. B, **74** 245113 (2006).

[And08] S. Andergassen, T. Enss, C. Karrasch and V. Meden. *A gentle introduction to the functional renormalization group: The kondo effect in quantum dots*. In B. Barbara, Y. Imry, G. Sawatzky and P. Stamp (eds.), *Quantum Magnetism*, NATO Science for Peace and Security Series, 1–17. Springer Netherlands (2008).

[And11a] S. Andergassen, T. A. Costi and V. Zlatić. *Mechanism for large thermoelectric power in molecular quantum dots described by the negative-u anderson model*. Phys. Rev. B, **84** 241107 (2011).

[And11b] S. Andergassen, M. Pletyukhov, D. Schuricht, H. Schoeller and L. Borda. *Renormalization group analysis of the interacting resonant-level model at finite bias: Generic analytic study of static properties and quench dynamics*. Phys. Rev. B, **83** 205103 (2011).

[Aze12] J. Azema, A.-M. Daré, S. Schäfer and P. Lombardo. *Kondo physics and orbital degeneracy interact to boost thermoelectrics on the nanoscale*. Phys. Rev. B, **86** 075303 (2012).

[Bak75] G. A. Baker Jr. *Essentials of Padé Approximants*. Academic Press New York (1975).

[Bar02] S. E. Barnes and S. Maekawa. *A jordan-wigner transformation for the t - j and hubbard models with holes*. Journal of Physics: Condensed Matter, **14** L19 (2002).

[Bar06] L. Barreira. *Poincaré recurrence: old and new*. World Scientific Publishing Co. Pte. Ltd. (2006).

[Bar13] T. Barthel. *Precise evaluation of thermal response functions by optimized density matrix renormalization group schemes*. New Journal of Physics, **15** 073010 (2013).

[Bat53] H. Bateman and A. Erdélyi. *Higher Transcendental Functions*, volume I. McGraw-Hill New York (1953).

[Bax68] R. J. Baxter. *Dimers on a rectangular lattice*. Journal of Mathematical Physics, **9** 650 (1968).

[Bec85] R. Becker. *Theorie der Wärme*. Springer Verlag, Berlin Heidelberg, 3. edition (1985).

[Ben11] G. Benenti, K. Saito and G. Casati. *Thermodynamic bounds on efficiency for systems with broken time-reversal symmetry*. Phys. Rev. Lett., **106** 230602 (2011).

[Bie09] M. J. Biercuk, H. Uys, A. P. VanDevender, N. Shiga, W. M. Itano and J. J. Bollinger. *Optimized dynamical decoupling in a model quantum memory*. Nature Physics, **458** 996 (2009).

[Blo08] I. Bloch, J. Dalibard and W. Zwerger. *Many-body physics with ultracold gases*. Rev. Mod. Phys., **80** 885 (2008).

[Blu11] C. Blumenstein, J. Schafer, S. Mietke, S. Meyer, A. Dollinger, M. Lochner, X. Y. Cui, L. Patthey, R. Matzdorf and R. Claessen. *Atomically controlled quantum chains hosting a tomonaga-luttinger liquid*. Nat. Phys., **7** 776 (2011).

[Boh07] D. Bohr and P. Schmitteckert. *Strong enhancement of transport by interaction on contact links*. Phys. Rev. B, **75** 241103 (2007).

[Bor07] L. Borda, K. Vladár and A. Zawadowski. *Theory of a resonant level coupled to several conduction-electron channels in equilibrium and out of equilibrium*. Phys. Rev. B, **75** 125107 (2007).

[Bor08] L. Borda, A. Schiller and A. Zawadowski. *Applicability of bosonization and the anderson-yuval methods at the strong-coupling limit of quantum impurity problems*. Phys. Rev. B, **78** 201301 (2008).

[Bor10] L. Borda and A. Zawadowski. *Perturbative treatment of the multichannel interacting resonant-level model in steady-state nonequilibrium*. Phys. Rev. B, **81** 153303 (2010).

[Bou08] E. Boulat, H. Saleur and P. Schmitteckert. *Twofold advance in the theoretical understanding of far-from-equilibrium properties of interacting nanostructures*. Phys. Rev. Lett., **101** 140601 (2008).

[Bra03] S. Braig and K. Flensberg. *Vibrational sidebands and dissipative tunneling in molecular transistors*. Phys. Rev. B, **68** 205324 (2003).

[Bro98] P. W. Brouwer. *Scattering approach to parametric pumping*. Phys. Rev. B, **58** R10135 (1998).

[Bru04] H. Bruus and K. Flensberg. *Many-Body Quantum Theory in Condensed Matter Physics*. Oxford University Press, New York (2004).

[Bul08] R. Bulla, T. A. Costi and T. Pruschke. *Numerical renormalization group method for quantum impurity systems*. Rev. Mod. Phys., **80** 395 (2008).

[Cal07] P. Calabrese and J. Cardy. *Entanglement and correlation functions following a local quench: a conformal field theory approach*. Journal of Statistical Mechanics: Theory and Experiment, **2007** P10004 (2007).

[Caz06] M. A. Cazalilla. *Effect of suddenly turning on interactions in the luttinger model*. Phys. Rev. Lett., **97** 156403 (2006).

[Cor04] P. S. Cornaglia, H. Ness and D. R. Grempel. *Many-body effects on the transport properties of single-molecule devices*. Phys. Rev. Lett., **93** 147201 (2004).

[Cos10] T. A. Costi and V. Zlatić. *Thermoelectric transport through strongly correlated quantum dots*. Phys. Rev. B, **81** 235127 (2010).

[Cra04] N. J. Craig, J. M. Taylor, E. A. Lester, C. M. Marcus, M. P. Hanson and A. C. Gossard. *Tunable nonlocal spin control in a coupled-quantum dot system*. Science, **304** 565 (2004).

[Cro08] G. M. Crosswhite, A. C. Doherty and G. Vidal. *Applying matrix product operators to model systems with long-range interactions*. Phys. Rev. B, **78** 035116 (2008).

[Cur74] F. Curzon and B. Ahlborn. *Efficiency of a carnot engine at maximum power output*. Am. J. Phys., **43** 22 (1974).

[Czy08] G. Czycholl. *Theoretische Festkörperphysik: Von den klassischen Modellen zu modernen Forschungsthemen*. Springer Verlag, Berlin Heidelberg (2008).

[Dal04] A. J. Daley, C. Kollath, U. Schollwöck and G. Vidal. *Time-dependent density-matrix renormalization-group using adaptive effective hilbert spaces*. Journal of Statistical Mechanics: Theory and Experiment, **2004** P04005 (2004).

[DC66] J. Des Cloizeaux and M. Gaudin. *Anisotropic linear magnetic chain*. Journal of Mathematical Physics, **7** 1384 (1966).

[DdS08] L. G. G. V. Dias da Silva, F. Heidrich-Meisner, A. E. Feiguin, C. A. Büsser, G. B. Martins, E. V. Anda and E. Dagotto. *Transport properties and kondo correlations in nanostructures: Time-dependent dmrg method applied to quantum dots coupled to wilson chains*. Phys. Rev. B, **78** 195317 (2008).

[Deu91] J. M. Deutsch. *Quantum statistical mechanics in a closed system*. Phys. Rev. A, **43** 2046 (1991).

[dH34] W. de Haas, J. de Boer and G. van dën Berg. *The electrical resistance of gold, copper and lead at low temperatures*. Physica, **1** 1115 (1934).

[Dom54] C. A. Domenicali. *Irreversible thermodynamics of thermoelectricity*. Rev. Mod. Phys., **26** 237 (1954).

[Doy06] B. Doyon and N. Andrei. *Universal aspects of nonequilibrium currents in a quantum dot*. Phys. Rev. B, **73** 245326 (2006).

[Doy07] B. Doyon. *New method for studying steady states in quantum impurity problems: The interacting resonant level model*. Phys. Rev. Lett., **99** 076806 (2007).

[Dre90] R. M. Dreizler and E. K. U. Gross. *Density functional theory : an approach to the quantum many body problem*. Springer Verlag, Berlin Heidelberg New York London Paris Tokyo Hong Kong Barcelona (1990).

[Duk98] J. Dukelsky, M. A. Martn-Delgado, T. Nishino and G. Sierra. *Equivalence of the variational matrix product method and the density matrix renormalization group applied to spin chains*. EPL (Europhysics Letters), **43** 457 (1998).

[Eck09] M. Eckstein, M. Kollar and P. Werner. *Thermalization after an interaction quench in the hubbard model*. Phys. Rev. Lett., **103** 056403 (2009).

[Egg95] R. Egger and H. Grabert. *Friedel oscillations for interacting fermions in one dimension*. Phys. Rev. Lett., **75** 3505 (1995).

[Egg97] R. Egger, H. Grabert and U. Weiss. *Crossover from coherent to incoherent dynamics in damped quantum systems*. Phys. Rev. E, **55** R3809 (1997).

[Eid13] E. Eidelstein, D. Goberman and A. Schiller. *Crossover from adiabatic to antiadiabatic phonon-assisted tunneling in single-molecule transistors*. Phys. Rev. B, **87** 075319 (2013).

[Eng05] H.-A. Engel and D. Loss. *Fermionic bell-state analyzer for spin qubits*. Science, **309** 586 (2005).

[Ens05a] T. Enss. *Renormalization, conservation laws and transport in correlated electron systems*. Ph.D. thesis, Max-Planck-Institut für Festkörperforschung, Stuttgart (2005).

[Ens05b] T. Enss, V. Meden, S. Andergassen, X. Barnabé-Thériault, W. Metzner and K. Schönhammer. *Impurity and correlation effects on transport in one-dimensional quantum wires*. Phys. Rev. B, **71** 155401 (2005).

[Erd55] A. Erdélyi. *Higher Transcendental Functions*, volume III. McGraw-Hill New York (1955).

[Esp09] M. Esposito, K. Lindenberg and C. V. den Broeck. *Thermoelectric efficiency at maximum power in a quantum dot*. EPL, **85** 60010 (2009).

[Ess12] F. H. L. Essler, S. Evangelisti and M. Fagotti. *Dynamical correlations after a quantum quench*. Phys. Rev. Lett., **109** 247206 (2012).

[Ess14] F. H. L. Essler, S. Kehrein, S. R. Manmana and N. J. Robinson. *Quench dynamics in a model with tuneable integrability breaking*. Phys. Rev. B, **89** 165104 (2014).

[Fab95] M. Fabrizio and A. O. Gogolin. *Interacting one-dimensional electron gas with open boundaries*. Phys. Rev. B, **51** 17827 (1995).

[Fag14] M. Fagotti, M. Collura, F. H. L. Essler and P. Calabrese. *Relaxation after quantum quenches in the spin-$\frac{1}{2}$ heisenberg xxz chain*. Phys. Rev. B, **89** 125101 (2014).

[Fel11] M. Feld, B. Frohlich, E. Vogt, M. Koschorreck and M. Kohl. *Observation of a pairing pseudogap in a two-dimensional fermi gas*. Nature (London), **480** 75 (2011).

[Fil81] V. Filyov, A. Tzvelik and P. Wiegmann. *Thermodynamics of the s-d exchange model (kondo problem)*. Physics Letters A, **81** 175 (1981).

[Fre09] J. K. Freericks, H. R. Krishnamurthy and T. Pruschke. *Theoretical description of time-resolved photoemission spectroscopy: Application to pump-probe experiments*. Phys. Rev. Lett., **102** 136401 (2009).

[Frö10] F. Fröwis, V. Nebendahl and W. Dür. *Tensor operators: Constructions and applications for long-range interaction systems*. Phys. Rev. A, **81** 062337 (2010).

[Gae10] J. P. Gaebler, J. T. Stewart, T. E. Drake, D. S. Jin, A. Perali, P. Pieri and G. C. Strinati. *Observation of pseudogap behaviour in a strongly interacting fermi gas*. Nature Physics, **6** 569 (2010).

[Gal07] M. Galperin, A. Nitzan and M. A. Ratner. *Inelastic effects in molecular junctions in the coulomb and kondo regimes: Nonequilibrium equation-of-motion approach*. Phys. Rev. B, **76** 035301 (2007).

[Gal10] G. Gallavotti. *Statistical Mechanics: A Short Treatise*. Springer Verlag, Berlin Heidelberg New York, 3. edition (2010).

[Gan12] M. Ganahl, E. Rabel, F. H. L. Essler and H. G. Evertz. *Observation of complex bound states in the spin-1/2 heisenberg xxz chain using local quantum quenches*. Phys. Rev. Lett., **108** 077206 (2012).

[Gar85] A. Garg. *Criterion for the observability of macroscopic quantum coherence*. Phys. Rev. B, **32** 4746 (1985).

[Ger00] U. Gerland, J. von Delft, T. A. Costi and Y. Oreg. *Transmission phase shift of a quantum dot with kondo correlations*. Phys. Rev. Lett., **84** 3710 (2000).

[GG98] D. Goldhaber-Gordon, J. Göres, M. A. Kastner, H. Shtrikman, D. Mahalu and U. Meirav. *From the kondo regime to the mixed-valence regime in a single-electron transistor*. Phys. Rev. Lett., **81** 5225 (1998).

[Gia03] T. Giamarchi. *Quantum Physics in One Dimension*. Oxford University Press, New York (2003).

[Gil03] J. Gilewicz and Y. Kryakin. *Froissart doublets in pad approximation in the case of polynomial noise*. Journal of Computational and Applied Mathematics, **153** 235 (2003). Proceedings of the 6th International Symposium on Orthogonal Poly nomials, Special Functions and their Applications, Rome, Italy, 18-22 June 2001.

[Gra85] H. Grabert and U. Weiss. *Quantum tunneling rates for asymmetric double-well systems with ohmic dissipation*. Phys. Rev. Lett., **54** 1605 (1985).

[Hac08] A. Hackl and S. Kehrein. *Real time evolution in quantum many-body systems with unitary perturbation theory*. Phys. Rev. B, **78** 092303 (2008).

[Hal80] F. D. M. Haldane. *General relation of correlation exponents and spectral properties of one-dimensional fermi systems: Application to the anisotropic s=1/2 heisenberg chain*. Phys. Rev. Lett., **45** 1358 (1980).

[Hal81] F. D. M. Haldane. *'luttinger liquid theory' of one-dimensional quantum fluids. i. properties of the luttinger model and their extension to the general 1d interacting spinless fermi gas*. Journal of Physics C: Solid State Physics, **14** 2585 (1981).

[Han06] J. E. Han. *Quantum simulation of many-body effects in steady-state nonequilibrium: Electron-phonon coupling in quantum dots*. Phys. Rev. B, **73** 125319 (2006).

[Han10] J. E. Han. *Nonequilibrium electron transport in strongly correlated molecular junctions*. Phys. Rev. B, **81** 113106 (2010).

[Har09] M. J. Hartmann, J. Prior, S. R. Clark and M. B. Plenio. *Density matrix renormalization group in the heisenberg picture*. Phys. Rev. Lett., **102** 057202 (2009).

[Hat05] N. Hatano and M. Suzuki. *Finding exponential product formulas of higher orders*. In A. Das and B. K. Chakrabarti (eds.), *Quantum Annealing and Other Optimization Methods*, volume 679 of *Lecture Notes in Physics*, 37–68. Springer Berlin Heidelberg (2005).

[Hew93] A. Hewson. *The Kondo Problem to Heavy Fermions*. Cambridge University Press, Cambridge (1993).

[Hew02] A. C. Hewson and D. Meyer. *Numerical renormalization group study of the anderson-holstein impurity model*. Journal of Physics: Condensed Matter, **14** 427 (2002).

[Hof07] S. Hofferberth, I. Lesanovsky, B. Fischer, T. Schumm and J. Schmiedmayer. *Non-equilibrium coherence dynamics in one-dimensional bose gases*. Nature (London), **449** 324 (2007).

[Hon10] C. Honerkamp. *Lecture: Quantum theory of condensed matter ii*. RWTH Aachen (2010).

[Iuc09] A. Iucci and M. A. Cazalilla. *Quantum quench dynamics of the luttinger model*. Phys. Rev. A, **80** 063619 (2009).

[Jak09] S. G. Jakobs. *Functional renormalization group studies of quantum transport through mesoscopic systems*. Ph.D. thesis, RWTH Aachen (2009).

[Jak10a] S. G. Jakobs, M. Pletyukhov and H. Schoeller. *Nonequilibrium functional renormalization group with frequency-dependent vertex function: A study of the single-impurity anderson model*. Phys. Rev. B, **81** 195109 (2010).

[Jak10b] S. G. Jakobs, M. Pletyukhov and H. Schoeller. *Properties of multi-particle green's and vertex functions within keldysh formalism*. Journal of Physics A: Mathematical and Theoretical, **43** 103001 (2010).

[Jay57] E. T. Jaynes. *Information theory and statistical mechanics*. Phys. Rev., **106** 620 (1957).

[Jec13] E. Jeckelmann. *Local density of states of the one-dimensional spinless fermion model*. Journal of Physics: Condensed Matter, **25** 014002 (2013).

[Kan92] C. L. Kane and M. P. A. Fisher. *Transport in a one-channel luttinger liquid*. Phys. Rev. Lett., **68** 1220 (1992).

[Kar08] C. Karrasch, R. Hedden, R. Peters, T. Pruschke, K. Schönhammer and V. Meden. *A finite-frequency functional renormalization group approach to the single impurity anderson model*. Journal of Physics: Condensed Matter, **20** 345205 (2008).

[Kar10a] C. Karrasch. *The Functional Renormalization Group for Zero-Dimensional Quantum Systems in and out of Equilibrium*. Ph.D. thesis, RWTH Aachen (2010).

[Kar10b] C. Karrasch, S. Andergassen, M. Pletyukhov, D. Schuricht, L. Borda, V. Meden and H. Schoeller. *Non-equilibrium current and relaxation dynamics of a charge-fluctuating quantum dot*. EPL (Europhysics Letters), **90** 30003 (2010).

[Kar10c] C. Karrasch, V. Meden and K. Schönhammer. *Finite-temperature linear conductance from the matsubara green's function without analytic continuation to the real axis*. Phys. Rev. B, **82** 125114 (2010).

[Kar10d] C. Karrasch, M. Pletyukhov, L. Borda and V. Meden. *Functional renormalization group study of the interacting resonant level model in and out of equilibrium*. Phys. Rev. B, **81** 125122 (2010).

[Kar12a] C. Karrasch, J. H. Bardarson and J. E. Moore. *Finite-temperature dynamical density matrix renormalization group and the drude weight of spin-1/2 chains*. Phys. Rev. Lett., **108** 227206 (2012).

[Kar12b] C. Karrasch and J. E. Moore. *Luttinger liquid physics from the infinite-system density matrix renormalization group*. Phys. Rev. B, **86** 155156 (2012).

[Kar12c] C. Karrasch, J. Rentrop, D. Schuricht and V. Meden. *Luttinger-liquid universality in the time evolution after an interaction quench*. Phys. Rev. Lett., **109** 126406 (2012).

[Kar13] C. Karrasch, J. H. Bardarson and J. E. Moore. *Reducing the numerical effort of finite-temperature density matrix renormalization group calculations*. New Journal of Physics, **15** 083031 (2013).

[Kas09] V. Kashcheyevs, C. Karrasch, T. Hecht, A. Weichselbaum, V. Meden and A. Schiller. *Quantum criticality perspective on the charging of narrow quantum-dot levels*. Phys. Rev. Lett., **102** 136805 (2009).

[Kas13a] O. Kashuba, D. M. Kennes, M. Pletyukhov, V. Meden and H. Schoeller. *Quench dynamics of a dissipative quantum system: A renormalization group study*. Phys. Rev. B, **88** 165133 (2013).

[Kas13b] O. Kashuba and H. Schoeller. *Transient dynamics of open quantum systems*. Phys. Rev. B, **87** 201402 (2013).

[Kat04] A. A. Katanin. *Fulfillment of ward identities in the functional renormalization group approach*. Phys. Rev. B, **70** 115109 (2004).

[Kel65] L. V. Keldysh. *Diagram technique for nonequilibrium processes*. Soviet Physics JETP, **20** 1018 (1965).

[Ken10] D. M. Kennes and V. Meden. *Relaxation dynamics of an exactly solvable electron-phonon model*. Phys. Rev. B, **82** 085109 (2010).

[Ken11] D. M. Kennes. *A Renormalization Group Approach to the Time Evolution of Correlated Quantum Dots*. Master's thesis, RWTH Aachen (2011).

[Ken12a] D. M. Kennes, S. G. Jakobs, C. Karrasch and V. Meden. *Renormalization group approach to time-dependent transport through correlated quantum dots*. Phys. Rev. B, **85** 085113 (2012).

[Ken12b] D. M. Kennes and V. Meden. *Quench dynamics of correlated quantum dots*. Phys. Rev. B, **85** 245101 (2012).

[Ken13a] D. M. Kennes, O. Kashuba, M. Pletyukhov, H. Schoeller and V. Meden. *Oscillatory dynamics and non-markovian memory in dissipative quantum systems*. Phys. Rev. Lett., **110** 100405 (2013).

[Ken13b] D. M. Kennes and V. Meden. *Interacting resonant-level model in nonequilibrium: Finite-temperature effects*. Phys. Rev. B, **87** 075130 (2013).

[Ken13c] D. M. Kennes and V. Meden. *Luttinger liquid properties of the steady state after a quantum quench*. Phys. Rev. B, **88** 165131 (2013).

[Ken13d] D. M. Kennes, D. Schuricht and V. Meden. *Efficiency and power of a thermoelectric quantum dot device*. EPL (Europhysics Letters), **102** 57003 (2013).

[Ken14a] D. M. Kennes, C. Klöckner and V. Meden. *Spectral properties of one-dimensional Fermi systems after an interaction quench*. ArXiv e-prints 1405.3762 (2014).

[Ken14b] D. M. Kennes, V. Meden and R. Vasseur. *Universal quench dynamics of interacting quantum impurity systems*. ArXiv e-prints 1406.5308 (2014).

[Kin06] T. Kinoshita, T. Wenger and D. S. Weiss. *A quantum newton's cradle*. Nature (London), **440** 900 (2006).

[Koc05] J. Koch and F. von Oppen. *Franck-condon blockade and giant fano factors in transport through single molecules*. Phys. Rev. Lett., **94** 206804 (2005).

[Kol07] C. Kollath, A. M. Läuchli and E. Altman. *Quench dynamics and nonequilibrium phase diagram of the bose-hubbard model*. Phys. Rev. Lett., **98** 180601 (2007).

[Kon64] J. Kondo. *Resistance minimum in dilute magnetic alloys*. Progress of Theoretical Physics, **32** 37 (1964).

[Kön96] J. König, H. Schoeller and G. Schön. *Zero-bias anomalies and boson-assisted tunneling through quantum dots*. Phys. Rev. Lett., **76** 1715 (1996).

[Laa] M. A. Laakso. *Personal communication*.

[Laa14] M. A. Laakso, D. M. Kennes, S. G. Jakobs and V. Meden. *Functional renormalization group study of the andersonholstein model*. New Journal of Physics, **16** 023007 (2014).

[Lan50] C. Lanczos. *An iteration method for the solution of the eigenvalue problem of linear differential and integral operators*. J. Res. Natl. Bur. Stand., **45** 255 (1950).

[Lan09] S. Langer, F. Heidrich-Meisner, J. Gemmer, I. P. McCulloch and U. Schollwöck. *Real-time study of diffusive and ballistic transport in spin-12 chains using the adaptive time-dependent density matrix renormalization group method*. Phys. Rev. B, **79** 214409 (2009).

[Leg87] A. J. Leggett, S. Chakravarty, A. T. Dorsey, M. P. A. Fisher, A. Garg and W. Zwerger. *Dynamics of the dissipative two-state system*. Rev. Mod. Phys., **59** 1 (1987).

[Lei10] M. Leijnse, M. R. Wegewijs and K. Flensberg. *Nonlinear thermoelectric properties of molecular junctions with vibrational coupling*. Phys. Rev. B, **82** 045412 (2010).

[Les98] F. Lesage and H. Saleur. *Boundary interaction changing operators and dynamical correlations in quantum impurity problems*. Phys. Rev. Lett., **80** 4370 (1998).

[Let09] R. Leturcq, C. Stampfer, K. Inderbitzin, L. Durrer, C. Hierold, E. Mariani, M. G. Schultz, F. von Oppen and K. Ensslin. *Franckcondon blockade in suspended carbon nanotube quantum dots*. Nature Physics, **5** 327 (2009).

[Lie72] E. Lieb and D. Robinson. *The finite group velocity of quantum spin systems*. Communications in Mathematical Physics, **28** 251 (1972).

[Los98] D. Loss and D. P. DiVincenzo. *Quantum computation with quantum dots*. Phys. Rev. A, **57** 120 (1998).

[Lut74] A. Luther and I. Peschel. *Single-particle states, kohn anomaly, and pairing fluctuations in one dimension*. Phys. Rev. B, **9** 2911 (1974).

[Mah95] G. D. Mahan and J. O. Sofo. *The best thermoelectric*. Proc. Natl. Acad. Sci. USA, **93** 7436 (1995).

[Mah97] G. Mahan, B. Sales and J. Sharp. *Thermoelectric materials: New approaches to an old problem*. Phys. Today, **50** 42 (1997).

[Man07] S. R. Manmana, S. Wessel, R. M. Noack and A. Muramatsu. *Strongly correlated fermions after a quantum quench*. Phys. Rev. Lett., **98** 210405 (2007).

[McC07] I. P. McCulloch. *From density-matrix renormalization group to matrix product states*. Journal of Statistical Mechanics: Theory and Experiment, **2007** P10014 (2007).

[McC08] I. P. McCulloch. *Infinite size density matrix renormalization group, revisited*. ArXiv e-prints 0804.2509 (2008).

[McL95] R. I. McLachlan. *On the numerical integration of ordinary differential equations by symmetric composition methods*. SIAM J. Sci. Comp., **16** 151 (1995).

[Med99] V. Meden. *Nonuniversality of the one-particle green's function of a luttinger liquid*. Phys. Rev. B, **60** 4571 (1999).

[Med01] V. Meden. *Lecture: Quantenmechanik der vielteilchensysteme*. Georg-August-Universität Göttingen (2001).

[Med05] V. Meden, T. Enss, S. Andergassen, W. Metzner and K. Schönhammer. *Correlation effects on resonant tunneling in one-dimensional quantum wires*. Phys. Rev. B, **71** 041302 (2005).

[Meh06] P. Mehta and N. Andrei. *Nonequilibrium transport in quantum impurity models: The bethe ansatz for open systems*. Phys. Rev. Lett., **96** 216802 (2006).

[Mei92] Y. Meir and N. S. Wingreen. *Landauer formula for the current through an interacting electron region*. Phys. Rev. Lett., **68** 2512 (1992).

[Met12] W. Metzner, M. Salmhofer, C. Honerkamp, V. Meden and K. Schönhammer. *Functional renormalization group approach to correlated fermion systems*. Rev. Mod. Phys., **84** 299 (2012).

[Mit04] A. Mitra, I. Aleiner and A. J. Millis. *Phonon effects in molecular transistors:quantal and classical treatment*. Phys. Rev. B, **69** 245302 (2004).

[Moe08] M. Moeckel and S. Kehrein. *Interaction quench in the hubbard model*. Phys. Rev. Lett., **100** 175702 (2008).

[Moe09] M. Moeckel and S. Kehrein. *Real-time evolution for weak interaction quenches in quenatum systems*. Annals of Physics, **324** 2146 (2009).

[Mon10] H. Monien. *Gaussian quadrature for sums: a rapidly convergent summation scheme*. Math. Comp., **79** 857 (2010).

[Mor94] T. R. Morris. *The exact renormalisation group and approximate solutions*. International Journal of Modern Physics A, **9** 2411 (1994).

[Mur08] P. Murphy, S. Mukerjee and J. Moore. *Optimal thermoelectric figure of merit of a molecular junction*. Phys. Rev. B, **78** 161406 (2008).

[Mut11] D. Muth, R. G. Unanyan and M. Fleischhauer. *Dynamical simulation of integrable and nonintegrable models in the heisenberg picture*. Phys. Rev. Lett., **106** 077202 (2011).

[Neg88] J. W. Negele. *Many-Body Quantum Theory in Condensed Matter Physics*. Addison-Wesley, New York (1988).

[Ngh14] H. T. M. Nghiem and T. A. Costi. *Generalization of the time-dependent numerical renormalization group method to finite temperatures and general pulses*. Phys. Rev. B, **89** 075118 (2014).

[Noz69] P. Nozières and C. T. de Dominicis. *Singularities in the x-ray absorption and emission of metals. iii. one-body theory exact solution*. Phys. Rev., **178** 1097 (1969).

[Oja08] T. Ojanen and A.-P. Jauho. *Mesoscopic photon heat transistor*. Phys. Rev. Lett., **100** 155902 (2008).

[Ons31a] L. Onsager. *Reciprocal relations in irreversible processes. i.* Phys. Rev., **37** 405 (1931).

[Ons31b] L. Onsager. *Reciprocal relations in irreversible processes. ii.* Phys. Rev., **38** 2265 (1931).

[Ort10] P. P. Orth, D. Roosen, W. Hofstetter and K. Le Hur. *Dynamics, synchronization, and quantum phase transitions of two dissipative spins*. Phys. Rev. B, **82** 144423 (2010).

[Ort13] P. P. Orth, A. Imambekov and K. Le Hur. *Nonperturbative stochastic method for driven spin-boson model*. Phys. Rev. B, **87** 014305 (2013).

[Öst95] S. Östlund and S. Rommer. *Thermodynamic limit of density matrix renormalization*. Phys. Rev. Lett., **75** 3537 (1995).

[Oza07] T. Ozaki. *Continued fraction representation of the fermi-dirac function for large-scale electronic structure calculations*. Phys. Rev. B, **75** 035123 (2007).

[Paa05] J. Paaske and K. Flensberg. *Vibrational sidebands and the kondo effect in molecular transistors*. Phys. Rev. Lett., **94** 176801 (2005).

[Pet04] J. R. Petta, A. C. Johnson, C. M. Marcus, M. P. Hanson and A. C. Gossard. *Manipulation of a single charge in a double quantum dot*. Phys. Rev. Lett., **93** 186802 (2004).

[Pet05] J. R. Petta, A. C. Johnson, J. M. Taylor, E. A. Laird, A. Yacoby, M. D. Lukin, C. M. Marcus, M. P. Hanson and A. C. Gossard. *Coherent manipulation of coupled electron spins in semiconductor quantum dots*. Science, **309** 2180 (2005).

[Pla12] J. J. Pla, K. Y. Tan, J. P. Dehollain, W. H. Lim, J. J. L. Morton, D. N. Jamieson, A. S. Dzurak and A. Morello. *A single-atom electron spin qubit in silicon*. Nature Physics, **489** 541 (2012).

[Ple10] M. Pletyukhov, D. Schuricht and H. Schoeller. *Relaxation versus decoherence: Spin and current dynamics in the anisotropic kondo model at finite bias and magnetic field*. Phys. Rev. Lett., **104** 106801 (2010).

[Ple12] M. Pletyukhov and H. Schoeller. *Nonequilibrium kondo model: Crossover from weak to strong coupling*. Phys. Rev. Lett., **108** 260601 (2012).

[Poi90] H. Poincaré. *Sur le problème des trois corps et les équations de la dynamique*. Acta Math., **13** 1 (1890).

[Pol11] A. Polkovnikov, K. Sengupta, A. Silva and M. Vengalattore. *Colloquium*. Rev. Mod. Phys., **83** 863 (2011).

[Poz14] B. Pozsgay, M. Mestyán, M. A. Werner, M. Kormos, G. Zaránd and G. Takács. *Correlations after quantum quenches in the XXZ spin chain: Failure of the Generalized Gibbs Ensemble*. ArXiv e-prints 1405.2843 (2014).

[Ren12] J. Rentrop, D. Schuricht and V. Meden. *Quench dynamics of the tomonagaluttinger model with momentum-dependent interaction*. New Journal of Physics, **14** 075001 (2012).

[Rig06] M. Rigol, A. Muramatsu and M. Olshanii. *Hard-core bosons on optical superlattices: Dynamics and relaxation in the superfluid and insulating regimes*. Phys. Rev. A, **74** 053616 (2006).

[Rig07] M. Rigol, V. Dunjko, V. Yurovsky and M. Olshanii. *Relaxation in a completely integrable many-body quantum system: An ab initio study of the dynamics of the highly excited states of 1d lattice hard-core bosons*. Phys. Rev. Lett., **98** 050405 (2007).

[Rig09] M. Rigol. *Quantum quenches and thermalization in one-dimensional fermionic systems*. Phys. Rev. A, **80** 053607 (2009).

[Ros12] A. Rosch. *Wilson chains are not thermal reservoirs*. Eur. Phys. J. B, **85** 6 (2012).

[Rou13] P. Roura-Bas, L. Tosi and A. A. Aligia. *Nonequilibrium transport through magnetic vibrating molecules*. Phys. Rev. B, **87** 195136 (2013).

[Sal98] M. Salmhofer. *Renormalization*. Springer Verlag, Berlin (1998).

[San10] L. F. Santos and M. Rigol. *Onset of quantum chaos in one-dimensional bosonic and fermionic systems and its relation to thermalization*. Phys. Rev. E, **81** 036206 (2010).

[Sán11] R. Sánchez and M. Büttiker. *Optimal energy quanta to current conversion*. Phys. Rev. B, **83** 085428 (2011).

[Sán13] D. Sánchez and R. López. *Scattering theory of nonlinear thermoelectric transport*. Phys. Rev. Lett., **110** 026804 (2013).

[Sch80a] P. Schlottmann. *Simple spinless mixed-valence model. i. coherent-hybridization states versus virtual-bound states*. Phys. Rev. B, **22** 613 (1980).

[Sch80b] P. Schlottmann. *Simple spinless mixed-valence model. ii. solution of the isolated f-level problem*. Phys. Rev. B, **22** 622 (1980).

[Sch82a] P. Schlottmann. *The kondo problem. i. transformation of the model and its renormalization*. Phys. Rev. B, **25** 4815 (1982).

[Sch82b] P. Schlottmann. *The kondo problem. ii. crossover from asymptotic freedom to infrared slavery*. Phys. Rev. B, **25** 4828 (1982).

[Sch82c] P. Schlottmann. *The kondo problem. iii. the susceptibility and relaxation rate*. Phys. Rev. B, **25** 4838 (1982).

[Sch93] K. Schönhammer and V. Meden. *Correlation effects in photoemission from low dimensional metals*. Journal of Electron Spectroscopy and Related Phenomena, **62** 225 (1993).

[Sch00] H. Schoeller and J. König. *Real-time renormalization group and charge fluctuations in quantum dots*. Phys. Rev. Lett., **84** 3686 (2000).

[Sch05a] K. Schönhammer. *Lecture: Korrelierte elektronen*. Georg-August-Universität Göttingen (2005).

[Sch05b] K. Schönhammer. *Luttinger liquids: the basic concepts*. In D. Baeriswyl and L. Degiorgi (eds.), *Interacting Electrons in Low Dimensions*. Kluwer Academic Publishers (2005).

[Sch06] F. Schwabl. *Statistische Mechanik*. Springer Verlag, Berlin Heidelberg New York, 3. edition (2006).

[Sch08a] T. L. Schmidt, P. Werner, L. Mühlbacher and A. Komnik. *Transient dynamics of the anderson impurity model out of equilibrium*. Phys. Rev. B, **78** 235110 (2008).

[Sch08b] T. Schmiedl and U. Seifert. *Efficiency at maximum power: An analytically solvable model for stochastic heat engines*. EPL (Europhysics Letters), **81** 20003 (2008).

[Sch08c] K. Schreiber. *Nonlinear Eigenvalue Problems: Newton-type Methods and Nonlinear Rayleigh Functionals*. VDM Verlag Dr. Müller (2008).

[Sch09] Schoeller, H. *A perturbative nonequilibrium renormalization group method for dissipative quantum mechanics*. Eur. Phys. J. Special Topics, **168** 179 (2009).

[Sch10] P. Schmitteckert. *Calculating green functions from finite systems*. Journal of Physics: Conference Series, **220** 012022 (2010).

[Sch11a] H. Schoeller. *Lecture: Quantum statistics in nonequilibrium*. RWTH Aachen (2011).

[Sch11b] U. Schollwöck. *The density-matrix renormalization group in the age of matrix product states*. Annals of Physics, **326** 96 (2011). January 2011 Special Issue.

[Sir14] J. Sirker, N. P. Konstantinidis, F. Andraschko and N. Sedlmayr. *Locality and thermalization in closed quantum systems*. Phys. Rev. A, **89** 042104 (2014).

[Sól79] J. Sólyom. *The fermi gas model of one-dimensional conductors*. Advances in Physics, **28** 201 (1979).

[Sot12] B. Sothmann and M. B. ttiker. *Magnon-driven quantum-dot heat engine*. EPL (Europhysics Letters), **99** 27001 (2012).

[Spl06] J. Splettstoesser, M. Governale, J. König and R. Fazio. *Adiabatic pumping through a quantum dot with coulomb interactions: A perturbation expansion in the tunnel coupling*. Phys. Rev. B, **74** 085305 (2006).

[Ste93] J. J. Stewart, Sakurai. *Modern Quantum Mechanics*. Prentice Hall, New Jersey, revised edition (1993).

[Ste08] J. T. Stewart, J. P. Gaebler and D. S. Jin. *Using photoemission spectroscopy to probe a strongly interacting fermi gas*. Nature (London), **454** 744 (2008).

[Suz76] M. Suzuki. *Relationship between d-dimensional quantal spin systems and (d+1)-dimensional ising systems: Equivalence, critical exponents and systematic approximants of the partition function and spin correlations*. Progress of Theoretical Physics, **56** 1454 (1976).

[Swi99] M. Switkes, C. M. Marcus, K. Campman and A. C. Gossard. *An adiabatic quantum electron pump*. Science, **283** 1905 (1999).

[Tay72] J. R. Taylor. *Scattering Theory*. Wiley, New York (1972).

[Tsa05] S.-W. Tsai, A. H. Castro Neto, R. Shankar and D. K. Campbell. *Renormalization-group approach to strong-coupled superconductors*. Phys. Rev. B, **72** 054531 (2005).

[Uhr09] G. S. Uhrig. *Interaction quenches of fermi gases*. Phys. Rev. A, **80** 061602 (2009).

[VdB05] C. Van den Broeck. *Thermodynamic efficiency at maximum power*. Phys. Rev. Lett., **95** 190602 (2005).

[vdW00] W. G. van der Wiel, S. D. Franceschi, T. Fujisawa, J. M. Elzerman, S. Tarucha and L. P. Kouwenhoven. *The kondo effect in the unitary limit*. Science, **289** 2105 (2000).

[Ver04] F. Verstraete, J. J. García-Ripoll and J. I. Cirac. *Matrix product density operators: Simulation of finite-temperature and dissipative systems*. Phys. Rev. Lett., **93** 207204 (2004).

[Ver06] F. Verstraete and J. I. Cirac. *Matrix product states represent ground states faithfully*. Phys. Rev. B, **73** 094423 (2006).

[Vid77] H. Vidberg and J. Serene. *Solving the eliashberg equations by means of n-point padé approximants*. Journal of Low Temperature Physics, **29** 179 (1977).

[Vid03] G. Vidal. *Efficient classical simulation of slightly entangled quantum computations*. Phys. Rev. Lett., **91** 147902 (2003).

[Wan06] J.-S. Wang, J. Wang and N. Zeng. *Nonequilibrium green's function approach to mesoscopic thermal transport*. Phys. Rev. B, **74** 033408 (2006).

[War50] J. C. Ward. *An identity in quantum electrodynamics*. Phys. Rev., **78** 182 (1950).

[Wei] U. Weiss. *Personal communication*.

[Wei86] U. Weiss and H. Grabert. *Effects of temperature and bias on macroscopic quantum coherence*. EPL (Europhysics Letters), **2** 667 (1986).

[Wei87] U. Weiss, H. Grabert and S. Linkwitz. *Influence of friction and temperature on coherent quantum tunneling*. Journal of Low Temperature Physics, **68** 213 (1987).

[Wei12] U. Weiss. *Quantum Dissipative Systems*. World Scientific Publishing Co. Pte. Ltd., fourth edition (2012).

[Whi92] S. R. White. *Density matrix formulation for quantum renormalization groups*. Phys. Rev. Lett., **69** 2863 (1992).

[Whi93] S. R. White. *Density-matrix algorithms for quantum renormalization groups*. Phys. Rev. B, **48** 10345 (1993).

[Whi04] S. R. White and A. E. Feiguin. *Real-time evolution using the density matrix renormalization group*. Phys. Rev. Lett., **93** 076401 (2004).

[Whi05] S. R. White. *Density matrix renormalization group algorithms with a single center site*. Phys. Rev. B, **72** 180403 (2005).

[Wil75] K. G. Wilson. *The renormalization group: Critical phenomena and the kondo problem*. Rev. Mod. Phys., **47** 773 (1975).

[Wou14] B. Wouters, M. Brockmann, J. De Nardis, D. Fioretto and J.-S. Caux. *From Néel to XXZ: exact solution from the quench action*. ArXiv e-prints 1405.0172 (2014).

[Yan12a] H. Yan and H. Guo. *Efficiency and its bounds for a quantum einstein engine at maximum power*. Phys. Rev. E, **86** 051135 (2012).

[Yan12b] H. Yan and H. Guo. *Efficiency and its bounds for thermal engines at maximum power using newton's law of cooling*. Phys. Rev. E, **85** 011146 (2012).

[Zin02] J. Zinn-Justin. *Quantum Field Theory and Critical Phenomena*. Clarendon Press, Oxford, 4. edition (2002).

[Zur03] W. H. Zurek. *Decoherence, einselection, and the quantum origins of the classical*. Rev. Mod. Phys., **75** 715 (2003).

List of Publications

[1] M. A. Raina, D. Kennes, F. Megahed, and T. Gries
'Vliesstoffanalyse mittels digitaler Bildverarbeitung'
Technische Textilien **51**, 186 (2008)

[2] D. M. Kennes and V. Meden
'Relaxation dynamics of an exactly solvable electron-phonon model'
Phys. Rev. B **82**, 085109 (2010)

[3] D. M. Kennes, S. G. Jakobs, C. Karrasch, and V. Meden
'Renormalization group approach to time-dependent transport through correlated quantum dots'
Phys. Rev. B **85**, 085113 (2012)

[4] D. M. Kennes and V. Meden
'Quench dynamics of correlated quantum dots'
Phys. Rev. B **85**, 245101 (2012)

[5] D. M. Kennes and V. Meden
'Interacting resonant level model in nonequilibrium: Finite-temperature effects'
Phys. Rev. B **87**, 075130 (2013)

[6] D. M. Kennes, O. Kashuba, M. Pletyukhov, H. Schoeller, and V. Meden
'Oscillatory dynamics and non-markovian memory in dissipative quantum systems'
Phys. Rev. Lett. **110**, 100405 (2013)

[7] D. M. Kennes and V. Meden
'Luttinger liquid properties of the steady state after a quantum quench'
Phys. Rev. B **88**, 165131 (2013)

[8] O. Kashuba, D. M. Kennes, M. Pletyukhov, V. Meden, and H. Schoeller
'Quench dynamics of a dissipative quantum system: A renormalization group study'
Phys. Rev. B. **88**, 165133 (2013)

[9] D. M. Kennes, O. Kashuba, and V. Meden
'Dynamical regimes of dissipative quantum systems'
Phys. Rev. B. **88**, 241110 (2013)

[10] D. M. Kennes, D. Schuricht, and V. Meden
'Efficiency and power of a thermoelectric quantum dot device'
EPL (Europhysics Letters) **102**, 57003 (2013)

[11] M. A. Laakso, D. M. Kennes, S. G. Jakobs, and V. Meden
'Functional renormalization group study of the AndersonHolstein model'

New Journal of Physics **16**, 023007 (2014)

[12] D. M. Kennes and C. Karrasch
'Extending the range of real time density matrix renormalization group simulations'
ArXiv 1404.3704 (2014)

[13] D. M. Kennes, C. Klöckner, and V. Meden
'Spectral properties of one-dimensional Fermi systems after an interaction quench'
Phys. Rev. Lett. **113**, 116401 (2014)

[14] D. M. Kennes, V. Meden, and R. Vasseur
'Universal quench dynamics of interacting quantum impurity systems'
Phys. Rev. B. **90**, 115101 (2014)

[15] C. Karrasch, D. M. Kennes, and J. E. Moore
'Transport properties of the one-dimensional Hubbard model at finite temperature '
Phys. Rev. B. **90**, 155104 (2014)

[16] D. M. Kennes, M. J. Schmidt, D. Hübscher, and V. Meden
'Renormalization group flows in one-dimensional lattice models: impurity scaling, umklapp scattering and the orthogonality catastrophe'
ArXiv 1409.1671 (2014)

Curriculum Vitae



Dante Marvin Kennes

born on December 21st 1986 in Neuss, Germany

Academic record:

June 2006	Abitur Städtisches Meerbusch Gymnasium, Germany
2006–2009	Bachelor Studies of Physics RWTH Aachen University, Germany
August 2009	Bachelor Thesis Institut für Theorie der Statistischen Physik, RWTH Aachen University, Germany *'Long Time Relaxation of an Electron-Phonon System'* Advisor: Volker Meden
2009–2011	Master Studies of Physics RWTH Aachen University, Germany
February–August 2010	Master Studies of Physics Universidad Autónoma de Barcelona, Spain
September 2011	Master Thesis Institut für Theorie der Statistischen Physik, RWTH Aachen University, Germany *'A Renormalization Group Approach to the Time Evolution of Correlated Quantum Dots'* Advisor: Volker Meden
since 2011	Ph.D. studies Institut für Theorie der Statistischen Physik, RWTH Aachen University, Germany Advisor: Volker Meden
since 2011	Bachelor Studies: Philosophy and Sociology RWTH Aachen University, Germany
March–July 2013	Visiting University of California, Berkeley
Awards	Schöneborn-Award, RWTH Aachen University Springorum Commemorative Medal, RWTH Aachen University Friedrich-Wilhelm-Award, RWTH Aachen University

Thank You!

'Chancen multiplizieren sich, wenn man sie ergreift.'
- Sunzi in *Die Kunst des Krieges*

Neben der "formaleren" Danksagung zu Beginn dieser Arbeit möchte ich an dieser Stelle die Gelegenheit dazu nutzen, bestimmten Menschen zu danken, die mich in der Vergangenheit maßgeblich unterstützt haben.

Als allererstes sei hier mein Doktorvater Volker Meden erwähnt. Volker hat mir über die Jahre (zuerst während der Bachelorarbeit, dann während der Masterarbeit und schließlich während der vorliegenden Dissertation) unzählige Dinge beigebracht, ohne dabei meine eigene Neugier zu mindern. Er hat mich zu jeder Zeit bestärkt, meine eigenen Ideen zu verfolgen, aber an den richtigen Stellen eingegriffen, wenn mehr Erfahrung und Überblick erforderlich war. Aus meiner Sicht eine schwer zu haltende Balance: Vielen Dank!

Ich danke außerdem meinen Kollegen, die zu der angenehmen Arbeitsatmosphäre am Institut beitragen/beigetragen haben. Darunter seien vor allem zum einen meine "alten" Bürokollegen Stephan Grap und Christoph Karrasch und meine "neuen" Bürokollegen Katharina Eissing und Stefan Göttel genannt. Es war ein Traum.

Für die herausragende Zeit nach und während des Studiums bedanke ich mich ausdrücklich bei: David Altmann, Sören Boyn, Andreas Engelhardt, Stefan Göttel, Moritz Küpper, Tobias van Leeuwen, Mathias Mueller, Veronika Bock, Jan Hoffmann, Christoph Hörig, Stephan Grap, Mareike Ahl, Christo-elvis Karrasch, Frank(daTank) Reininghaus, Katharina Eissing, (Bro-)Benedikt Dolzer und (Terefic-)Nick Wawroschek. Außerdem möchte ich auch die "Meerbusch-Crew" nicht unerwähnt lassen, vor allem: Richard Mahr, Robert mit dem Superdaumen, Andrew Feist, Philipp Grimm, Daniel Jäger, Matthias Roggen, Jonathan Meyer, Kerim Ekal, Manu und Victoria Schumann (Frau Vogt). Es sind monumentale Erinnerungen.

Ganz ausdrücklich bedanken möchte ich mich auch bei meiner Freundin Jennifer Arif für ihre einzigartige Unterstützung!

Nicht zuletzt möchte ich die Menschen erwähnen, die wahrscheinlich den größten Einfluss auf mich hatten, meine Familie: Quirin (TheQ), Lieven, Nele und meine Eltern Luc und Annette. Ohne euch wäre nichts von dem hier entstanden.

Erklärung

Hiermit erkläre ich eidesstattlich, dass ich die vorliegende Arbeit selbständig verfasst und dabei nur die angegebenen Quellen verwendet habe. Ferner erkläre ich, dass durch die Veröffentlichung der Arbeit keine Urheberschutzrechte verletzt werden und dass ich bisher keine Promotionsantäge gestellt habe.

Aachen, den 20. Oktober 2014